UNIVERSITY OF LIVERPOOL

Numerical Simulation of Active Cooling Using Porous Metals

Thesis submitted in accordance with the requirements of the University of Liverpool for the degree of Doctor in Philosophy by

Edgar Avalos Gauna

September 2017

Table of contents

Abstract

Porous metals are a novel type of material that possesses many attractive properties such as low density and unique physical, mechanical, thermal, electrical and acoustic properties that make them attractive for a large number of applications. Open-cell porous metals in particular are an innovative solution for thermal control due to their high fluid permeability and good heat transfer capability.

This study investigated the fluid flow and heat transfer behaviour of open-cell porous metals made by space holder methods by numerical simulation. Particular attention was paid to the features of the porous copper manufactured by the Lost Carbonate Sintering process in geometry creation. Three geometrical models were considered: 2D patterned structures of regular struts with different shapes (circle, triangle, square and hexagon), 2D random structures of randomly distributed circular struts, and 3D structures based on the face-centred-cubic arrangement of spheres linked by cylinders.

In the 2D patterned structures, five strut shapes, with a fixed equivalent diameter of 500 μm, in both aligned and staggered arrangements, with porosity ranging from 50%to 80% were studied. In the 2D random structures, the porosity was fixed to 60% and the struts with 10 different diameters were distributed randomly. In the 3D structures, the structural parameters studied were porosity ranging from 50% to 80%, pores size ranging from 400 μm to 1500 μm and metal particle sizes of 30 μm, 50 μm and 70 μm.

In the present study, pressure drop, permeability and form drag coefficient were calculated for all the three geometric models and heat transfer coefficient was calculated for the 3D structures. Copper was selected as the solid structure for all geometric models and water was used as the coolant. The flow rate used was in the range from 0.2 to 1.8 l/min and a constant heat flux was used for the heat transfer analysis on the 3D structures.

For the patterned and the random 2D structures, the pressure drop increased with flow rate displaying a quadratic behaviour that fitted well with Forchheimer's equation. Permeability

increased whereas the form drag coefficient decreased with porosity for the patterned structures. Permeability and form drag coefficient values for the random structures were in a similar range as the patterned structures. The relationship between permeability and form drag coefficient was linear in logarithmic scale. The exponential term changed with strut shape and decreased as the gaps amongst the struts were increased.

For the 3D structures, the pressure drop also increased with flow rate, following Forchheimer's equation. Permeability increased with porosity, pore size and metal particle size, while form drag coefficient decreased with porosity and metal particle size but increased with pore size. The relationship between permeability and form drag coefficient was also linear in logarithmic scale. The exponential term decreased with pore size, approaching to a 0.7 value at bigger pore size, and increased with metal particle size. The heat transfer coefficient increased with increasing flow rate and pore size, and decreased with increasing porosity and metal particle size.

The numerical results for the 3D structures for pressure drop, permeability, form drag coefficient and heat transfer coefficient were compared with experimental data available from previous studies. The numerical results showed the same trends as the experimental results and agreed reasonably well with the experimental data in many cases.

Declaration

This thesis is submitted for the degree of Doctor in Philosophy in the Faculty of Engineering at the University of Liverpool. The research project reported herein was carried out, unless otherwise stated by the author, in the School of Engineering at the University of Liverpool between October 2013 and September 2017.

I confirm that the thesis is my own work, that I have not presented anyone else's work as my own, and that full and appropriate acknowledgement has been given where reference has been made to the work of others.

Edgar Avalos Gauna

September 2017

Acknowledgements

I would like to express my highest gratitude and admiration to Professor Yuyuan Zhao, for his excellent supervision during the PhD programme and for his commitment and support for the competition of this project.

I would like to thank my sponsor in Mexico, CONACyT and SEP for their financial support.

I am forever grateful to my wife Carolina, who joined me on this journey four years ago, has always supported me and has never given up on me.

I am also thankful to my family, especially to my parents Amada and Jaime, who always believed in me and inspired me to pursue this path. I want to thank also to my siblings Yesica and Jaime for their unconditional support and motivation through the years.

I want to also thank Antonia and Carlos and their daughters who have supported Carolina and me in so many ways throughout this journey that culminates with this thesis.

I want also to acknowledge all the support and encouragement received from my friends and colleagues during the PhD.

Finally, I want to thank God for His blessings and for showing me the way.

List of publications

Avalos Gauna, Edgar and Zhao, Yuyuan (2017). “Numerical Simulation of Heat Transfer in Porous Metals for Cooling Applications.” Metallurgical and Materials Transactions B, 48, pp 1925-1932.

Avalos Gauna, Edgar and Zhao, Yuyuan (2016). “Numerical Simulation of Heat Transfer in Porous Metals for Cooling Applications, conference proceeding” THE 8TH INTERNATIONAL CONFERENCE ON PHYSICAL AND NUMERICAL SIMULATION OF MATERIALS PROCESSING

List of tables

List of figures

List of symbols

A	Cross sectional area facing the flow	m^2
A_H	Contact area	m^2
$\overrightarrow{A_i}$	Area vector of a face i	m^2
A_{pl}	Area heated surface	m^2
A_{psc}	Spherical crown projected area	μm^2
A_s	Circular strut area	μm^2
A_{sc}	Spherical cap area	μm^2
A_t	Total area	μm^2
a	Total acceleration of the flow	m^2 / s
a_c	Centre to centre distance between the central sphere and the polar sphere	Mm
a_n	Polygonal strut apothem	Mm
a_p	Atomic packing factor	
B_{sys}	Dummy variable	
C	Forchheimer's coefficient	μm^{-1}
C_f	Drag force coefficient	-
C_p	Specific Heat	kJ / kg· K
c_i	Vector from the centroid of the element to the centroid of the adjacent element that shares that face	
c_0	Kozeny constant	
d	Circular strut diameter	Mm
d_{sp}	Pore diameter for the 3D REVs	Mm
d_{par}	Particle diameter	Mm
dF_x	Net force in the x direction	N
F_d	Form drag force	N
F_T	Total drag force	N

F_v	Viscous drag force	N
f	Volume fraction of the filler material	
f_i	Vector from the centroid of the element to the centroid of that face i	
H	Spherical cap height	Mm
h	Heat transfer coefficient	kW / m^2 ·K
I	Identity matrix	
J	Heat flux	kW / m^2
j	Heat rate	kW
K	Permeability	μm^2
k	Thermal conductivity	W / m ·K
k_0	Thermal conductivity bulk metal	W / m ·K
k_e	Effective thermal conductivity	W / m ·K
k^*	Thermal conductivity porous metal	W / m ·K
L	Length or thickness of the porous media	M
ΔL	Porous media length	M
l	Characteristic length	M
l_a	Path length within a porous media	M
l_b	Side length of the unit cell for the 3D REVs	Mm
l_{cc}	Centre to centre distance for particles in the unit cell	Mm
l_t	Increment of distance at the tangent point of 2 particles in the unit cell	Mm
l_{t*}	Adjusted length for the connecting cylinder	Mm
M	Exponential term for the K and C relationship	
m	Mass	Kg
Nu	Nusselt number	
n	Orthogonal vector	
n_a	Number of sides of the polygon	

n_c	Exponential term to correlate conductivity and relative density	
n^*_{Cu}	Number of copper particles	
$n^*_{K_2CO_3}$	Number of potassium carbonate particles	
n_p	Number of particles inside the unit cell	
ΔP	Pressure drop	MPa
ΔP_a	Pressure drop aligned struts	MPa
ΔP_s	Pressure drop staggered struts	MPa
P	Pressure	Pa
$\tilde{p}$	Pressure at pore level	Pa
Q	Volumetric flow rate	l / min
Q_{m_y}	Volumetric flow rate entering the control volume in the xz plane	l / min
$Q_{m_{y+dy}}$	Volumetric flow rate leaving the control volume in the xz plane	l / min
R	Sphere radius	Mm
Re	Reynold's number	
r	Metal particle radius	Mm
r_c	Connecting cylinder radius	Mm
r_{sc}	Spherical crown radius	Mm
S	Specific surface area	μm^2
T	Temperature	K
T_i	Temperature at starting point	K
T_o	Temperature at the final point	K
T_{pl}	Temperature of the heated surface	K
T_s	Solid temperature	K
T_f	Fluid temperature	K
T_m	Mean temperature of the fluid	K
t	Time	S

u	Darcian velocity	m / s
$\tilde{u}$	Velocity at pore level	m / s
V	Volume	µm^3
V_c	Volume of the unit cell	µm^3
V_p	Volume of a single particle	µm^3
V_v	Void volume	µm^3
V_t	Total volume	µm^3
v	Velocity	m / s
v_f	Fluid velocity	m / s
v^T	Transpose matrix of v	
$\bar{v}$	Mean velocity	m / s
v'	Velocity fluctuations over time	m / s
x	x direction	
x_b	Side length of the 2D REV	Mm
y	y direction	
z	z direction	

β	Variation of B_{sys} per unit of mass $\beta = \frac{dB}{dm}$
∇	Gradient
$\nabla \cdot$	Divergence of
∇^2	Laplace operator
δ_p	Local volume averaged variable
ε	Porosity
λ	Tortuosity
μ	Dynamic viscosity Pa· s
μ_c	Coordination number
$\prod$	Pressure ratio

ρ	Density	kg / m^3
ρ^*	Foam density	kg / m^3
ρ_s	Solid material density	kg / m^3
ρ_f	Fluid density	kg / m^3
σ_{ij}	Cauchy stress tensor	Pa
σ	Stress	Pa
τ	Shear stress	Pa
v	Kinematic viscosity $v = \frac{\mu}{\rho}$	m^2 / s
φ	Rate strain tensor	
$\frac{\partial \vec{v}}{\partial t}$	Local acceleration	
$(\vec{v} \cdot \nabla)\vec{v}$	Convective acceleration	
ω	Rate of strain tensor	
Ω	Orthogonal quality	
φ	Particle size ratio	

Abbreviations

BCC	Body Centred Cubic
FCC	Face Centred Cubic
LB	Lattice Boltzmann
LCS	Lost Carbonate Sintering
LTE	Local Thermal Equilibrium
MHS	Metallic Hollow Sphere
NCX	Nickel – Chrome metal foam
P/M	Powder Metallurgy
PPI	Pores Per Inch
REV	Representative Elementary Volume
SC	Simple Cubic

1 Introduction

Porous metals (the most general term) and metal foams (a special class of porous metal where foaming takes place during the manufacturing process), are metals with pores deliberately integrated in their structure (Zhao, 2013). They are composed of a solid metallic phase and a gaseous phase which, in the end, generates the voids or pores. Depending on how the pores are connected, the cell topology can be considered as closed (no connection among the pores) or open (there exists an internal connected network between the pores)(Ashby *et al.*, 2000). Porous materials have an extensive range of applications in industry. The inclusion of pores allows them to work as flow straighteners, catalytic reactors, pneumatic silencers, mechanical energy absorbers, sound absorbers, orthopaedic uses, etc. The properties and applications of porous metals depend on the materials they are made of as well as the porous structure.

Banhart (2000) for instance distinguished three uses for porous metals. These uses are related to structural and load bearing applications. For instance, for light-weight construction, energy-absorption, and acoustic and thermal control. For the first one, porous metals can take a large volume while maintaining a low weight and a relatively high weight-specific mechanical stiffness. For energy-absorption, porous metals can absorb a large quantity of mechanical energy when deformed due to impact. As for acoustic and thermal control, porous metals due to their internal structure, waves can be damped.

An example of the damping capacity of porous metals can be seen in the golf putters manufactured by Ryobi Corporation in Japan since 2002 (Nakajima, 2007). Figure 1-1 shows a golf putter with the central part made of lotus porous copper with 40% porosity a pore size of 100 μm.

Figure 1-1 Golf putter with the central part made of lotus porous copper, (Nakajima, 2007)

Another example of the uses of porous metals is a vacuum elevator tool manufactured by Shinko wire in Japan. The manufactured tool is used to lift glass panels produced in the floating glass process (Lefebvre *et al.* 2008). The replacement of the full part made by solid metal by the tool made of porous aluminium led to a weight reduction of 50 kg. The core structure of the parts made using porous aluminium can be appreciated in Figure 1-2.

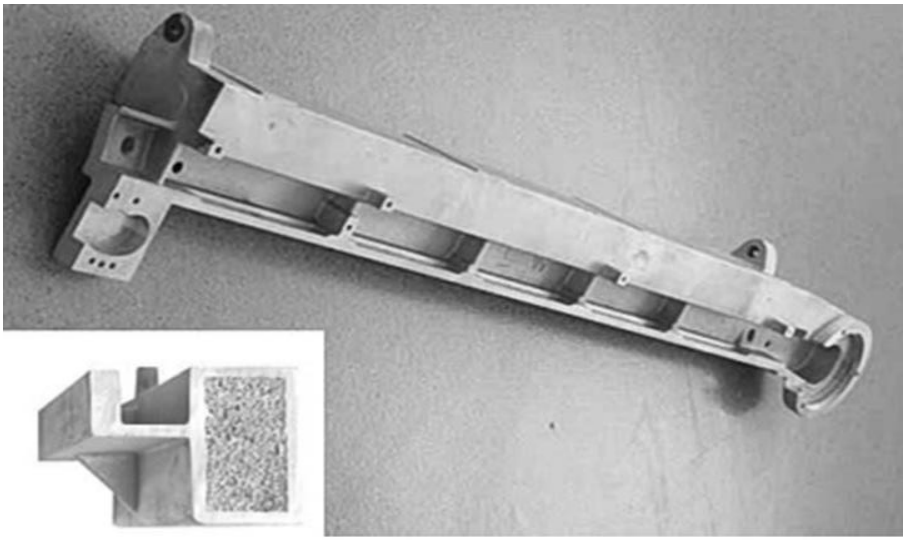

Figure 1-2 Sample of a part made with porous aluminium. The entire part length is 1900 mm; the foam core length is 1580 mm

In particular porous metals have shown to be promising for thermal control applications, due to their high surface area, low density and low thermal resistance. By taking advantage of these different material properties, a wide variety of thermal applications can be realised for this novel type of materials, including heat exchangers and heat sinks for electronic devices and improved cooling methods needed for innovative power systems (Banhart 2000, Clyne *et al.* 2006, Lefebvre *et al.* 2008).

In order to study porous metals, there are two different groups of properties to be considered. First, those properties related with the description of the geometric structure of the foam (pore size, shape and distribution of the cells). Second, the properties intrinsic to the material of which the cell walls are made of such as density, Young's modulus, thermal conductivity, etc. (Gibson and Ashby 1999, Khayargoli *et al.* 2004, Lefebvre *et al.* 2008).

The present study focuses on the numerical analysis of heat transfer and fluid flow in porous copper made by the Lost Carbonate Sintering (LCS) process.

1.1 Background and motivation of the research

There has been a growing demand for better thermal control techniques to prevent electronic equipment from premature failure and to improve their reliability. The trend to make electronic devices smaller and work faster under different circumstances, i.e. the miniaturisation of different components, has resulted in smaller devices experiencing high power densities and hence high heat fluxes (McGlen *et al.* 2004). The current passive cooling techniques are no longer sufficient. Active cooling using metal foams emerges as an effective alternative and provides a promising solution.

When designing heat exchangers using open-cell foams two key properties are important: the heat transfer coefficient (how efficient the amount of heat is transferred) and the pressure drop across the sample (how hard it is to get the fluid to flow through the foam)

(Xiao and Zhao 2013, Saito and de Lemos 2005, Kopanidis *et al.* 2010). The relevant fluid flow and heat transfer properties of porous materials, such as permeability, drag coefficient and convective heat transfer coefficient, have been obtained mainly by experimental means. However, obtaining these properties by experimentation has proven to be expensive, time consuming and not always possible.

Numerical modelling is an alternative approach to analyse different physical aspects of the materials. Numerical modelling can help to obtain a good amount of data in a considerably short period of time with low use of resources in comparison with experimental tests. Numerical studies have shown to be a consistent and effective tool for research.

There are different considerations in the literature in how to tackle the porous material problems numerically. One methodology is to consider the porous media as an arrangement of tube banks in 2D (Chai *et al.* 2010, Papathanasiou *et al.* 2001). Another practice is to create a representative 3D cell structure (Dukhan and Suleiman 2013, Xu and Jiang 2008). A different technique is to create a random walled structure acting as the porous matrix (Geiger *et al.* 2012, Bianchi *et al.* 2015). However, as the structure becomes more complex, the need for computational power increases (Diani *et al.*, 2014).

The numerical approach has been used by a number of researchers to study heat transfer in porous media. For example, Teruel and Rizwan-uddin (2009) numerically calculated the interfacial heat transfer coefficient in porous media. Xin *et al.* (2014) numerically investigated the heat and mass transfer behaviours in porous media for multiphase flow. Hwang and Yang (2012) simulated the heat transfer and fluid flow characteristics in a metallic porous block subjected to a confined turbulent slot jet.

Porous metals made by the Lost Carbonate Sintering Process (LCS) are an ideal medium for use as heat exchangers. LCS porous copper especially, possesses a high thermal conductivity in addition to the high internal surface area and high permeability for fluids (Thewsey and Zhao 2008). LCS porous copper has been studied mainly by experimental methods. For instance, Zhang *et al.* (2009) investigated the heat transfer performance of

LCS porous copper samples with middle range porosity $(57\% - 82\%)$ and pore size ranging from $150 - 1500\mu m$. Is in this porosity range where the porous metal can be considered as an open-cell, lower porosities will create closed cell structures. In their study, the LCS porous copper samples were put inside a test chamber with a heated blocked underneath the chamber with water being pumped inside the chamber as coolant. It was reported that the heat transfer performance was improved by 2 to 3 times compared to cooling with just water inside the testing chamber. They also mentioned that porosity has a significant effect on the heat transfer performance, with 62% being the optimum porosity, whereas pore size has a much less effect. Xiao and Zhao (2013) also analysed the heat transfer performance of LCS porous copper. In their study, they measured the heat transfer coefficient of single and double layered structures. The double layered structures were created by combining two different pore densities inside the same sample. In their experiment they concluded that the double layer samples generally had lower heat transfer coefficients than the single layer structures, due to flow stratification. They also mentioned that placing the high porosity layer of the double layer sample next to the heated block resulted in a much better heat transfer performance than the low porosity facing the heated block. However, information on the heat transfer behaviour of LCS metals is still very limited.

This study is focused on the numerical simulation of heat transfer in open cell structures for cooling applications, with LCS porous copper in mind. The cooling system studied is composed of the porous metal as medium and a fluid used as a coolant flowing through the material. The study was carried out on 2D and 3D structures, using commercial software ANSYS. Pressure drop, permeability, drag force coefficient and heat transfer coefficient were calculated.

1.2 Research aim and objectives

This study provides a numerical approach to analyse and study metal foams manufactured by space holder methods. Particular attention was paid to the LCS porous copper. The aim of the numerical analysis is to help to maximise their heat transfer performance by understanding the effects of porosity, pore size, metal particle size and flow rate on pressure drop and heat transfer coefficient.

The objectives of the research are:

- To develop a geometry generation technique that will account for porosity, pore size and metal particle size of LCS porous samples.
- To obtain reliable data from the numerical model to calculate permeability, form drag coefficient and heat transfer coefficient for porous metals with middle range porosity, i.e. $50\% - 80\%$.
- To analyse the main parameters that have the highest effect on permeability, form drag coefficient and heat transfer coefficient.
- To identify relationships between permeability and form drag coefficient, and permeability and heat transfer coefficient.
- To deliver a reliable numerical model to analyse other porous metals manufactured by space holder methods and different coolants.

1.3 Thesis structure

This thesis is composed of five chapters. Chapter 2 gives a literature review on the topics related to this research. Experimental analysis and numerical simulation of fluid flow and heat transfer in different porous media are reviewed. Specific attention is given to LCS

porous copper and also to the numerical studies related to thermal control. The fluid flow and heat transfer properties of porous media are discussed in detail.

Chapter 3 describes the numerical procedures and the results obtained for 2D structures considered in this research. The geometry creation and the structural considerations needed for the simulations are described in detail. The different techniques used for calculating all the relevant parameters are also presented. The results for permeability and form drag coefficient are presented. The drag distribution is reviewed and compared to other similar studies in the literature.

Chapter 4 describes the numerical modelling methods and the results for a 3D structure. The details related to the geometry creation are explained in full. The results for permeability, form drag coefficient and heat transfer coefficient are presented. Validation with experimental data is also presented. The effects of the structural parameters such as porosity, pore size and metal particle size on fluid permeability and heat transfer coefficient are discussed. The relationship between permeability and drag force is examined. The influence of permeability, porosity, pore size, metal particle size and flow rate on the heat transfer performance is studied.

Chapter 5 presents the conclusions drawn from this study. Important results and findings are summarised. Future work and recommendations are also presented

2 Literature review

2.1 Introduction to porous metals

As a definition, porous metals are a type of material composed of one or more metallic phases, and a gaseous phase which, in the end, generates the voids or pores (Zhao, 2013). Porous metals became useful for engineering applications at the beginning of the 20th century (Lefebvre *et.al* 2008). There are many examples where porous metals play important roles in technology and many technologies depend on or make use of porous metals. Therefore, porous metals have recently attracted considerable attention in both academia and industry. The research made on this novel type of materials has increased considerably in the past few decades. This is due to their exceptional mechanical, thermal, acoustic, electrical and chemical properties (Y. Zhao *et.al* 2005).

Depending on their use, porous metals can have advantages compared to other types of materials. Porous metals have high permeability, good thermal conductivity and high specific strength, just to mention a few properties. Their porous structure provides a unique group of properties not possessed by bulk materials, polymers, glasses or ceramics (Lefebvre, Banhart and Dunand, 2008). For example, for structural applications, the high specific stiffness and high energy absorption capacity are utilised in different applications including building and transport structures against buckling and impact. Another example is that porous metals are thermally and electrically conductive while maintaining their mechanical properties at much higher temperatures than polymers.

Porous metals possess different sets of characteristics. It is possible to classify these properties by two different sets of factors: the ones related to the geometric structure of the foam and the ones that describe the intrinsic properties of the material from which the cell walls are made. For the first case for example, there are studies related to the porosity size,

shape and distribution of the cells. For the other set of characteristics there are studies on density, Young's modulus, thermal conductivity, etc. Tensile strength, energy absorption, flexural strength, electrical and terminal conductivity, are properties related directly to the porous metal constituents. Permeability, sound absorption and heat transfer are mainly related to the geometric structure.

Depending on the connection between pores, a porous metal can be classified as open or closed cell. If the pores are interconnected then it can be considered as open-cell porous metal, otherwise it is a closed-cell porous metal. Closed-cell porous metals are often used as energy absorbers, structural materials, etc. Open-cell porous metals are suitable as sound absorbers, filters, heat exchangers, among many others.

Because of the internal network in the open-cell porous metals, they are permeable materials. This is one of the reasons why most literature focuses on the open-cell porous metals. The open cell structure contains highly desirable qualities for many industrial applications. Its density is lower in comparison to the bulk metal of which they are made. In addition, open-cell porous metals possess high specific surface area and good thermal conductivity (Boomsma *et.al* 2003). Open-cell foams are emerging as an effective material for heat transfer management (Bai and Chung 2011), given the interaction between a fluid and the internal network of the porous metal. The open inner-network part of the pore system is called the effective pore space of the porous metal (Scheidegger, 1957). The effective pore space defines a set of properties or pore parameters that bulk materials do not possess, such as porosity, tortuosity, internal surface area, etc. Different properties of open-cell porous metals such as permeability or heat transfer coefficient can be affected when changing these pore parameters.

2.1.1 Porosity

A porous metal can be defined by two different volumes: the total volume of the porous metal and the volume generated inside the solid due to the voids. This measure of the void

space or pores within the material is known as porosity (Dullien, 1979). A simple approach to determine porosity is by calculating the volume of these empty spaces over the total volume of the porous medium, and it represents a volume fraction (Hahn and Özişik 2012). This equation is more utilised during numerical analysis.

$$\varepsilon = \frac{V_v}{V_t} \tag{2.1}$$

where ε represents porosity, V_v and V_t are volumes of the void part and total geometry respectively. However, this approach requires prior knowledge on the value of V_v which is not easily obtainable. Another approach to estimate the porosity is related to the relative density of the foam (Gibson and Ashby 1999). The relative density is the density of the foam (ρ^*) divided by the actual density of the solid material (ρ_s); then the fraction of pore space in the foam, porosity, is determined experimentally by:

$$\varepsilon = 1 - \frac{\rho^*}{\rho_s} \tag{2.2}$$

Equation 2.2 is the most common way to calculate ε given that most of the literature is based on experimental studies. As it has already been stated, porosity is the measurement of the void space within a material. Pores can be interconnected and they can create interstices. Depending on the density of the number of pores, these interstices can create an internal network of channels where fluids could flow. This internal network depends on the manufacturing technique used to create the porous metal.

2.1.2 Tortuosity

One property that is directly related to the internal network of a porous media is Tortuosity. Tortuosity in porous media is defined as the ratio of the total path length available for flow within the medium to the distance from end to end of the sample (Kopanidis *et.al* 2010):

$$\lambda = \frac{l_a}{L} \tag{2.3}$$

where λ represents the tortuosity of the porous medium, l_a is the path length and L is the length or thickness of the medium. Tortuosity is a dimensionless parameter that is difficult to determine and often is determined experimentally (Diao *et.al* 2015).

There are studies where tortuosity is expressed in terms of other characteristics of the porous media such as experimental porosity, pore diameter or pore shape (Abbas, 2011). One example is the relationship between tortuosity and porosity. Different researchers have attempted to obtain a correlation between these two parameters. Table 2-1 lists some of the relationships found in the literature. All these correlations work under different sets of parameters and frameworks.

Table 2-1 Empirical correlations between porosity and tortuosity, modified from (Abbas 2011)

Correlation	Source
$\boldsymbol{\lambda = 1.5 - 0.5\varepsilon}$	Maxwell, 1873
$\boldsymbol{\lambda = 1 - 0.5 \ln \varepsilon}$	(Weissberg, 1963)
$\boldsymbol{\lambda = 1 - p \ln \varepsilon}$	(Comiti and Renaud 1989)
$\boldsymbol{\lambda^2 = A - n(1 - \varepsilon)}$	(Iversen and Jørgensen 1993)
$\boldsymbol{\lambda = \sqrt{1 - 0.5 \ln(\varepsilon^2)}}$	(Boudreau, 1996)
$\boldsymbol{\lambda = 1 - a\frac{(1-\varepsilon)}{(\varepsilon - \varepsilon_c)^m}}$	(Koponen, Kataja and Timonen, 1997)
$\boldsymbol{\lambda = 1 - p \ln\left(\frac{1}{\varepsilon}\right)}$	(Mauret and Renaud 1997)
$\boldsymbol{\lambda = \varepsilon^{-0.5}}$	Meredith and Tobias 1962 (as cited in Pisani 2011)
$\boldsymbol{\lambda = 1 - 0.49 \ln \varepsilon}$	(Barrande, Bouchet and Denoyel, 2007)

Maxwell's equation has been used as a first approximation to calculate tortuosity for a given porous medium, although Comiti and Renaud's empirical correlation is one of the most invoked models to calculate tortuosity nowadays. For instance, Barrande *et al.* (2007) use it when experimentally studied tortuosity in beds of spherical particles. They proposed a constant value of 0.49 for p. There are other examples where Comiti and Renauds model has been used with different p values. The p factor goes from 0.41 up to 3.2 depending on the medium being analysed (Ghanbarian *et.al* 2013).

Another example is the analysis made by Matyka *et al.* (2008). They studied the tortuosity-porosity relation by numerical means. They used a 2D microscopic model of a porous medium made of a collection of overlapping squares. It was reported that tortuosity is very sensitive to relaxation effects, finite-size, discretisation errors and fluid speed along streamlines.

2.1.3 Specific surface area

The specific surface area is another well-defined feature of porous materials. It is the ratio of the internal network area to the total volume or bulk volume of the porous medium (Scheidegger, 1957). The specific surface area affects many properties such as permeability and is also crucial for many industrial applications. For instance, high specific surface area along with other properties can greatly enhance heat transfer by convection (Bodla *et.al* 2013). According to Collins (1961) and Scheidegger (1957), there are three techniques used for measuring the specific surface area:

1. Adsorption. This method uses the adsortion generated by the internal solid surfaces of the porous metal over a vapour injected to the sample.

2. Quantitative stereology, also known as optical method. This method uses photomicrographs taken of one section of the porous metal to determine the ratio of the circumference of the pores to the total area of the section.
3. Fluid flow. This method uses other parameters such as permeability to calculate the specific surface.

2.2 Manufacturing techniques for porous metals

The aim involved in manufacturing porous metals is to combine the desired attributes of metals with other features obtained from the manufacturing process (Hashim *et al.* 1999). This is why today it is possible to encounter many manufacturing techniques. Some of these techniques used are similar to the ones for foaming aqueous or polymer liquids. Others are specially designed by taking advantage of metal properties such as their sintering capability. Early developments of manufacturing techniques were concentrated on using gas blowing agents for foaming generation within the melted metal.

There are different ways to classify these manufacturing techniques. One of the most widely used way to classify porous metals is the system developed by Banhart (2001), who considered the initial state of the metal used and defined four groups of processes analogous to the four states of matter: liquid metal, solid metal (powdered form), metal vapour or gaseous metallic compounds, and metal ion solution.

Figure 2-1 provides some examples of the methods in the four different categories. A wide range of liquid and solid state techniques are available depending on the desired resulting structure. The following sections will review some of these manufacturing techniques.

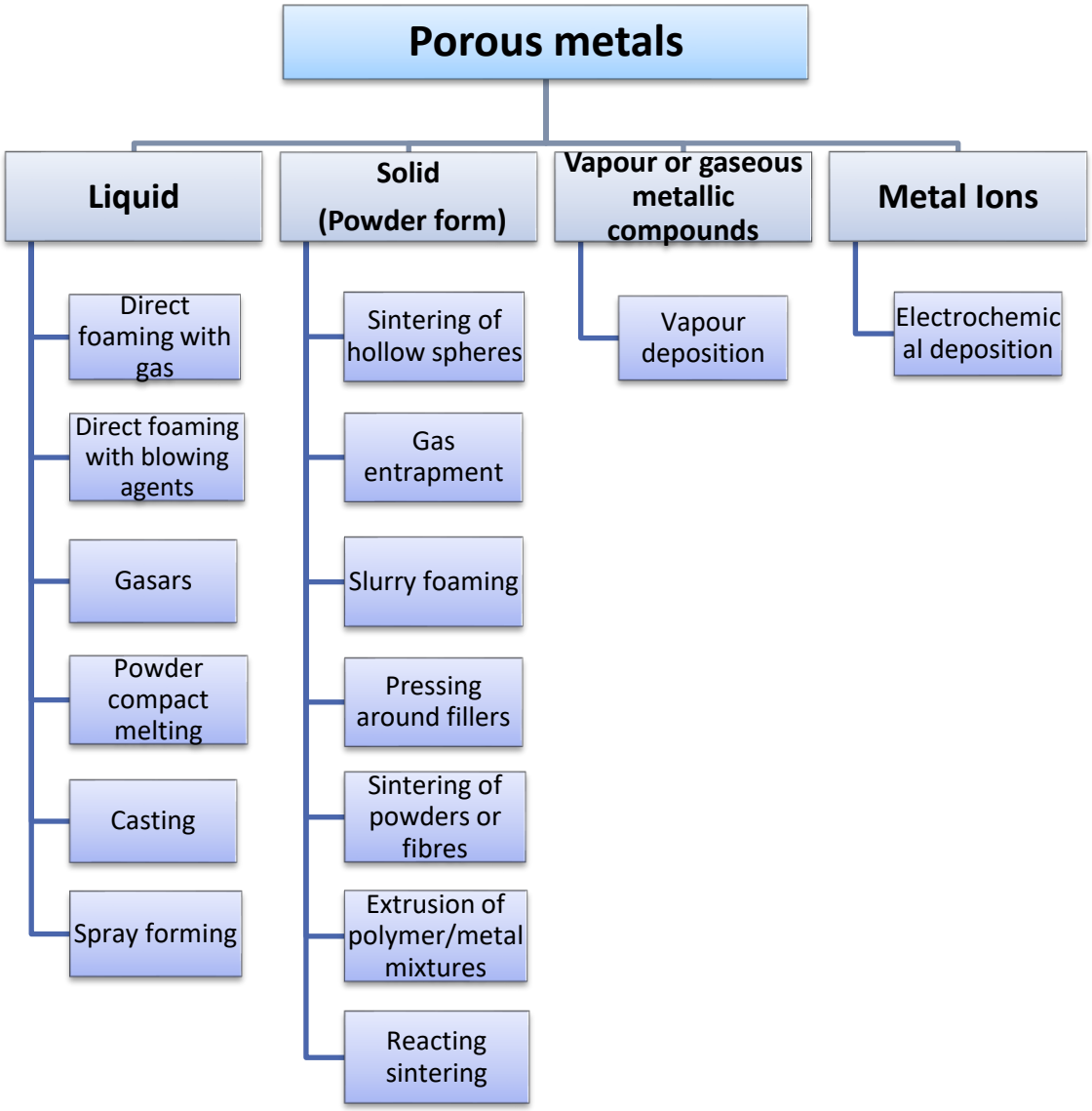

Figure 2-1 Porous metals production techniques (Banhart, 2001)

2.2.1 Liquid state methods

The most common techniques to manufacture porous metals use liquid state metal and can be divided into two groups, according to the source used for creating the pores as shown in Figure 2-2.

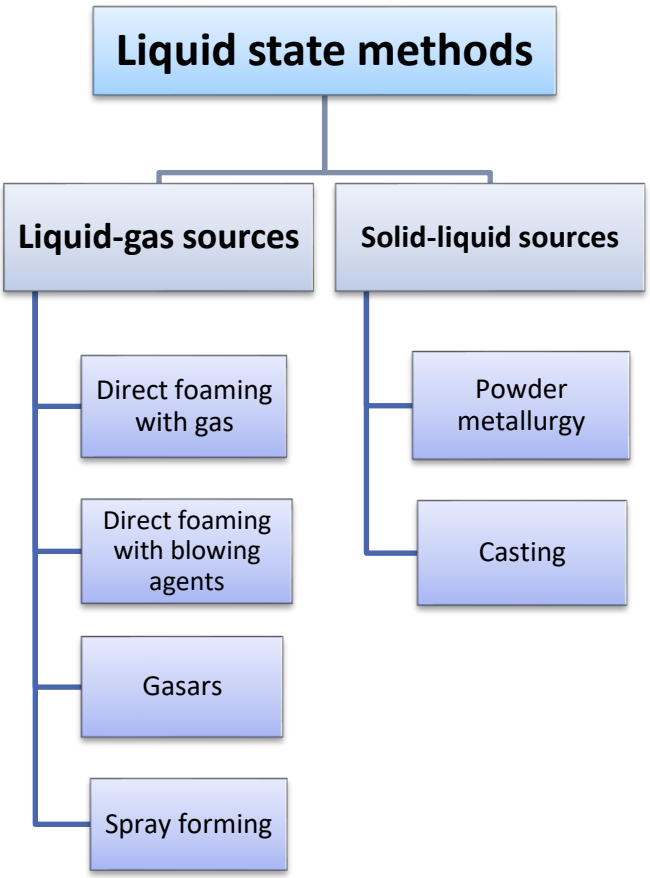

Figure 2-2 Liquid state manufacturing techniques

Some of the techniques are similar; however, the source to create the pores is different. One example of this is direct foaming. This method either injects gas into the melt directly or adds a blowing agent to the liquid melt. The resultant viscous mixture is made of bubbles and metal melt. The bubbles go up to the surface, due to high buoyancy forces creating the foam structure (Banhart, 2001). The foam can be made relatively stable when ceramic particles are present in the melt (Banhart, 2000). This technique has been widely used with aluminium and its alloys. The resulting porosity ranges from 91 to 93% and pore size from 2 mm to 10 mm (Lu, 2011).

Another technique combines hydrogen gas and the metal into a eutectic system. This technique is known as solid-gas eutectic solidification or “Gasars” (Tappan *et al.* 2010). In

order to create a porous metal by this method, the metal is melted in a hydrogen atmosphere under high pressure (up to 50 atm). This will create a mixed melt charged with hydrogen (Banhart, 2001). When the temperature is lowered, a eutectic transition to a heterogeneous system occurs. This leads to directional solidification in the solid-gas system (Baloyo, 2016). As the melt solidifies, gas pores precipitate. The solidification process will entrap them, creating the pore morphology (Banhart, 2000). The pores are elongated and oriented in the direction of solidification as shown in Figure 2-3. Pore diameters range from 10 μm to 10 mm, pore lengths from 100 μm to 30 cm and porosities from 5% to 75 % (Shapovalov in Schwartz *et al.* 1998).

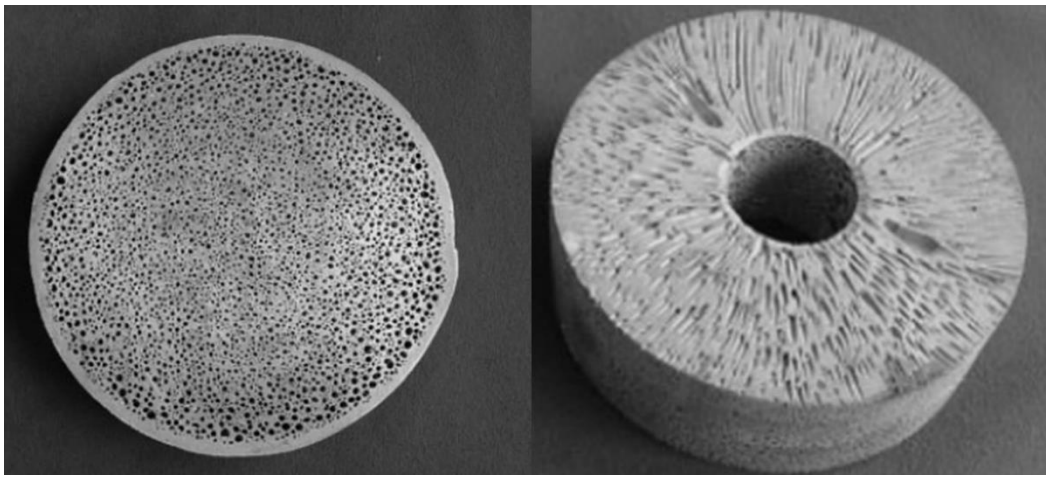

Figure 2-3 Magnesium "Gasar" with axial pores (left) and radial pores (right), (Shapovalov and Boyko 2004)

In spray foaming, the metallic melt is atomised continuously and creates a spray of fast flying small metal droplets (Lu, 2011). The resulting droplets start to build-up progressively in order to solidify and create the porous structure (Hogg *et al.*, 2006). This technique is considered to be an effective alternative due to its production advantages such as higher production rate, low inherent oxide contents and near-net shape products (Wang *et al.*, 2008).

In addition to the above methods, porous metals can also be produced using space holders by a casting technique. The space holding materials can be polymer foams, granules or

hollow spheres (Srivastava and Sahoo 2007). For instance, polyurethane foam can be used as initial matrix during an investment casting process. The pore structure of the precursor foam has to be open for this process, so the foam undergoes a reticulation treatment to remove residual closed cells. The treated foam is filled with a refractory moulding material. After curing, the polymer foam is burned out and the resulting structure is filled with molten melt. Once the melt solidifies, it will replicate the structure of the polymer foam. The investment casting process as shown in Figure 2-4 is a rather expensive process. However it produces high quality metal foams (Zhao, 2013).

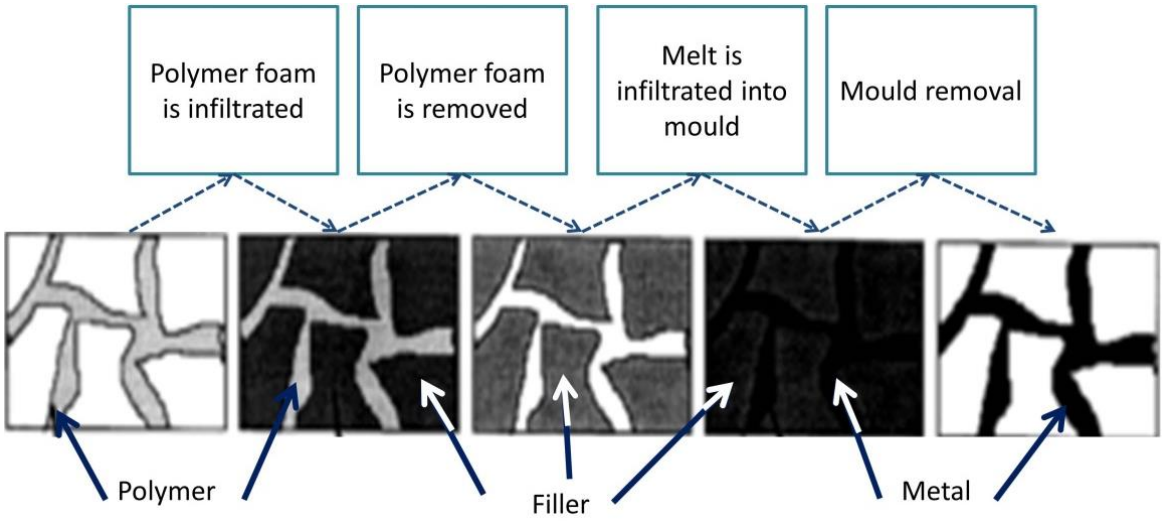

Figure 2-4 Production of metal foams by investment casting (Banhart, 2001)

2.2.2 Solid state methods

There are several techniques to manufacture porous metals using the source material in its solid state, including metallic hollow spheres, space holder fillers, and powder metallurgy, just to mention a few. For the solid state methods, the metal remains solid during the entire manufacturing process and it only experiences other operations (Banhart, 2001).

Using metallic hollow spheres (MHS) for producing hollow sphere structures and composite metal foams is one of the solid state techniques in existence (Behnam *et al.* 2011). The process uses hollow spheres made of copper, nickel, titanium, or steel to create a highly porous structure (Evans *et al.* 1998). Later the spheres are sintered to create bonding among them.

Several solid state methods for producing porous metals are based on the powder metallurgy (P/M) technology. P/M is a manufacturing process making use of metal in powder form. Sometimes, the metal is mixed with a non-metal. They are used as the raw materials to produce porous metals (Liu and Liang 2001). In the P/M methods, the metal is in the form of powder and remains solid throughout the entire process. The most common steps for this technique are shown in Figure 2-5.

The metal powder can also be mixed with other particulate agents (polymer grains, salts, hollow spheres) which are mechanically bonded after pressing. These production techniques can be called space-holder methods (Zhao, 2013). The sintering process occurs at high temperature (slightly lower than the melting point of the metal) to accelerate diffusion among the metal particles. Neck formation will occur at the contact points among adjacent particles at high temperature. With increasing the time, the particle boundary becomes metallurgical bond (Xiao and Zhao 2013). The space holder material is removed During this thermal treatment (Bram *et al.*, 2000).

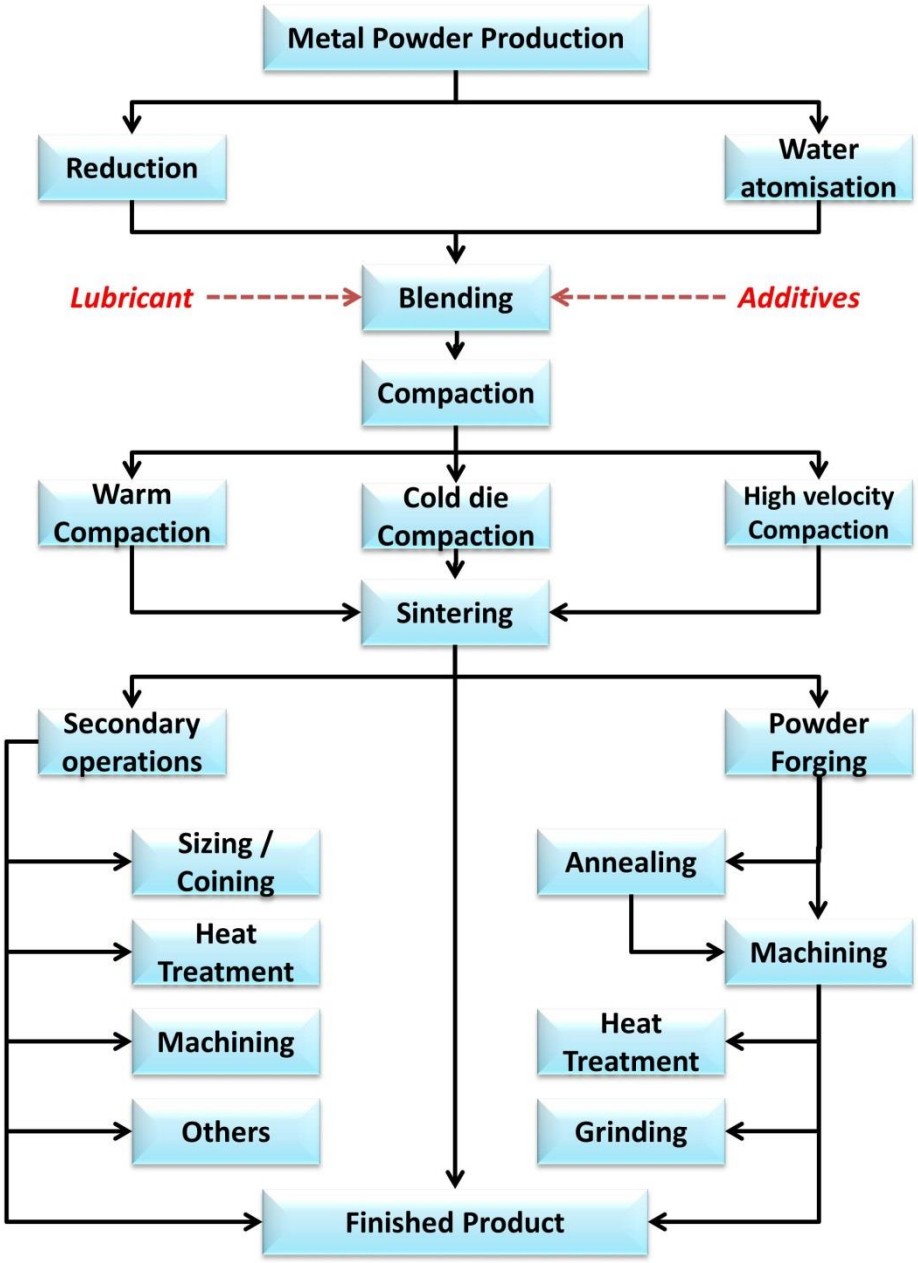

Figure 2-5 Basic steps of powder metallurgy process (Salak, Selecka and Danninger, 2005)

2.2.3 Vapour state methods

Vapour deposition is another technique to manufacture porous metals. Using a vacuum chamber, a cold solid structure is placed to work as a mould. The solid structure mould can

be polyester, polypropylene, polyurethane or an organism composed of cellulose. Glass, ceramics, carbon and minerals can be used as well (Liu and Liang 2001). The metal vapour is produced and condenses over the structure, coating it. Time of exposure and vapour density will determine the thickness of the coating. Finally, the original porous matrix is removed. The resulting structure is an open-cell metal foam with pores having hollow cell edges (Evans *et al.* 1998).

2.2.4 Ion state methods

Porous metals can be manufactured using an electro-deposition technique. The metal needs to be in its ionic state, i.e. a solution of ions in an electrolyte (Banhart, 2001). The metal is electrically deposited onto polymeric foam, similar to the casting technique. Nevertheless, the metal state is different between these two techniques. $Ni - Cr$ alloys and Cu porous metals can be manufactured using this technique (Baloyo, 2016). The resulting porosities will be in the range of $80\% - 99\%$ (Liu and Liang 2001). Nano porous metal foams can be manufactured by this technique at a relatively low cost (Eugénio *et al.*, 2014).

2.2.5 The lost carbonate sintering process

One of the most innovative techniques to obtain porous metals is the method known as Lost Carbonate Sintering (LCS), developed by Zhao and his colleagues (Zhao *et al.*, 2005). It is used for manufacturing open-cell porous metals with a good control over pore size and porosity and is suitable for a range of metals with high melting points. LCS is a space holder method combining two different materials. The first one is a metal powder which will be the matrix and can be Cu, Fe, Ti or Ni. The second one is a carbonate powder. Porous metals with high melting points can be manufactured by the LCS process either via the dissolution route or via the decomposition route.

In LCS, a metal powder and a carbonate powder are first mixed at a given volume ratio. The powder mixture is compacted and then sintered. A porous metal part is finally obtained by removing the carbonate particles from the sintered compact either by decomposition or by dissolution (Zhang and Zhao 2008). The particle size of the metal powder is not critical but the metal particles must be considerably smaller than the carbonate particles. A diagram of this process is shown in Figure 2-6. Porous metals manufactured by this technique can have different porosities, pore sizes and even pore shapes.

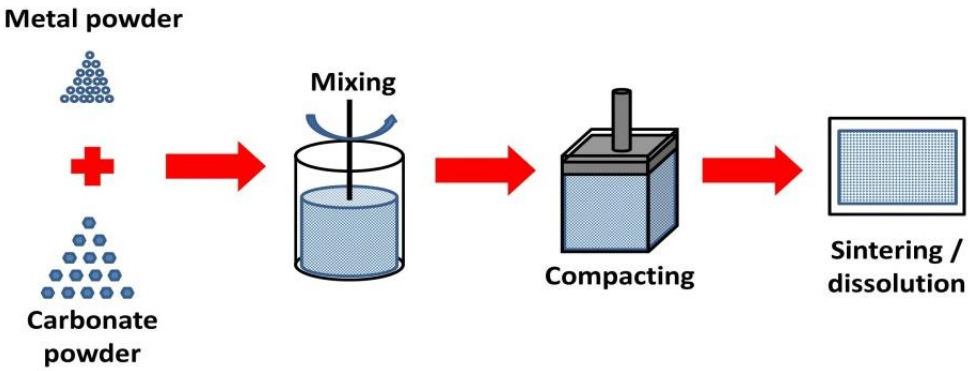

Figure 2-6 Schematic illustration of the LCS process

2.3 Applications of porous metals

Porous metals have an extensive range of applications in industry. This is primarily due to such features as light weight, high specific surface area, high potential to absorb impact energy, high permeability and good acoustic insulating properties. Heat sinks, mechanical energy absorbers, catalytic reactors, biomaterials, pneumatic silencers and heat exchangers are a few examples among many others (Ochiai *et al.*, 2010). Their uses and applications depend on the materials they are made from as well as the porous structure which is related to the manufacturing technique.

For instance, Bram *et al.* (2000) successfully manufactured middle-high porosity range porous parts from titanium, stainless steel and nickel-based super alloys using a space holder technique. Their study showed that these types of porous metals are suitable for uses where good corrosion resistance with sufficient strength is needed. For example, they can be used as some of the assembling components of internal combustion engines such as the inlet and exhaust valves, the connecting rods and gears (Kaczmar *et al.* 2000). Nakajima (2007) studied and analysed lotus type metal foams and their manufacturing techniques and listed some of the uses for these types of porous metals. According to this study, porous metals with directional pores are appropriate for applications including heat sinks, vibration – damping materials, golf putters and artificial teeth.

Porous metals produced by powder metallurgy methods are favourable for use in damping applications, thermal heat exchangers or sound absorbers. This is due to high internal friction and enhanced thermal, acoustic and chemical properties (Zhao, 2013).

Nano-porous metals have higher and desirable properties in comparison to other Nano-porous materials. A brief comparison of some of these properties is shown in Table 2-2. Nano-porous metals have shown to be promising for nanostructured catalysts, hydrogen-storage materials, electromagnetic composites, and lightweight structural materials (Tappan *et al.* 2010).

Table 2-2 Classification of Nano-porous materials, (Lu and Zhao 2004)

	Polymeric	Carbon	Glass	Aluminosilicate	Oxides	Metal
Pore size	Meso-macro	Micro-meso	Meso-macro	Micro-meso	Micro-meso	Meso-macro
Surface area	Low	High	Low	High	Medium	Low
Porosity	>0.6	0.3-0.6	0.3-0.6	0.3-0.7	0.3-0.6	0.1-0.9
Permeability	Low-medium	Low-medium	High	Low	Low-medium	High
Strength	Medium	Low	Strong	Weak	Weak-medium	High
Thermal stability	Low	High	Good	Medium-high	Medium-high	High
Chemical stability	Low-medium	High	High	Low-medium	Medium	Medium
Cost	Low	High	High	Low-medium	Medium	Medium
Life	Short	Long	Long	Medium-long	Long	Long

Srivastava and Sahoo (2007) provided a projection for probable forthcoming applications for porous metals. They cited a survey made by the National Physical Laboratory (UK) of these materials and suggested that most of the potential uses will be in the automotive industry. Overall, porous metals have a variety of thermo-mechanical properties. These properties suggest that they can be used for applications in areas demanding improved dissipation rates for impact, blast or heat removal. The use of porous metals in aircraft technology, like fuselage-production, is already well established (Kaczmar *et al.* 2000). Nonetheless, other industries might find a use for these novel types of materials as shown in Figure 2-7:

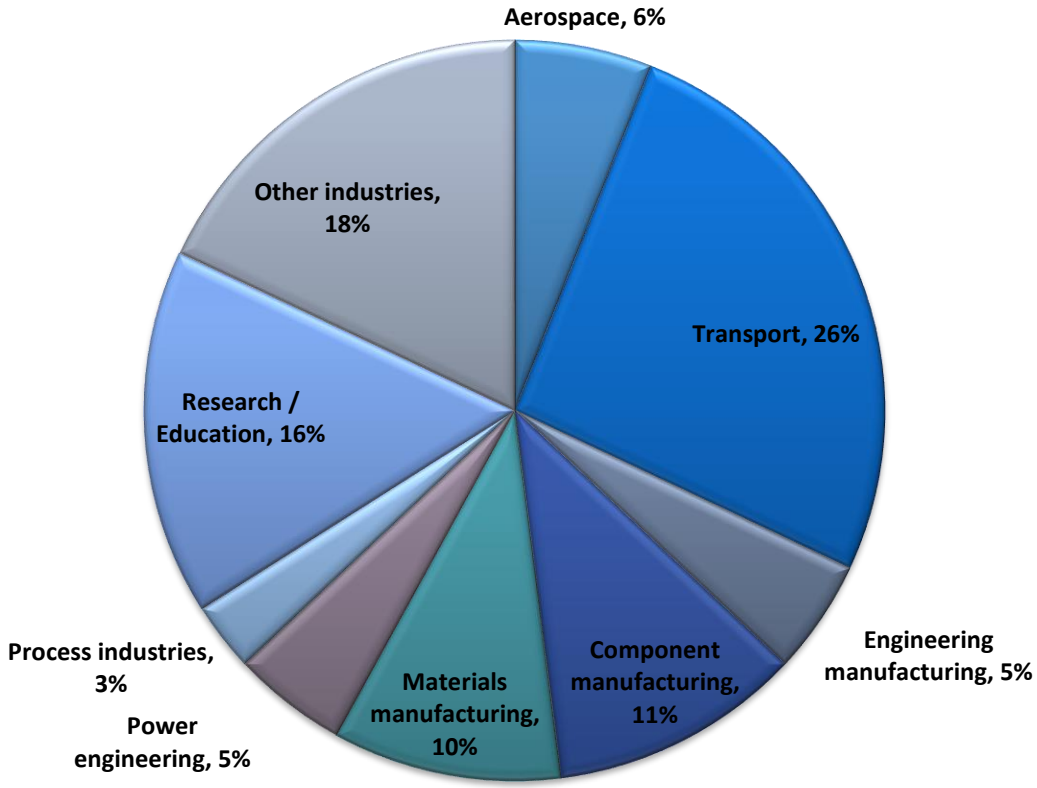

Figure 2-7 Break-up of expected industrial sector requirements for metallic foam

(Srivastava and Sahoo 2007)

Applications of porous metals are highly related to the structure of the material. For example, the open structure allows the interaction between a fluid flowing through the inner channels of the porous metal and energy transfer from the wall to the fluid via forced convection (Mahjoob and Vafai 2008). This is an alternative to the existing cooling techniques, providing an innovative solution to the electronics industry.

2.4 Fluid dynamics in porous media

2.4.1 Darcy's law

Fluids are treated as continuous media, and their motion and state can be specified in terms of the velocity (v), pressure (P), density (ρ), etc., evaluated at every point in space and time (t). The regime of a fluid depends of the relative importance of fluid friction (viscosity) and flow inertia. The fluid flowing during an interval of time Δt may change from one moment to other, or at two different points; however, if it is analysed as a single entity during a long period of time, this flow could be considered as constant. Nevertheless, this situation is no longer valid when the fluid flows through a porous media, thus a new formulation is required.

The study of fluid dynamics through a porous medium can be traced to the 19th century to Henry Philibert Gaspard Darcy, who established the first empirical relationship for such phenomenon (Darcy, 1856). Flow in porous media involves the description of both the media and the flow. Darcy described it as a linear relationship between pressure drop, flow rate and viscosity. At the same time, he found an inverse relationship to a different parameter which he later called permeability (K). Since then, numerous studies and applications have appeared, where fluid flow in porous media plays a major role (Vafai and Tien 1981). According to Darcy's law, permeability can be defined as the rate at which a fluid will flow through a porous medium at a given pressure gradient.

The relationship that Darcy proposed is then:

$$\frac{\Delta P}{\Delta L} = \frac{\mu}{K}\frac{Q}{A} \tag{2.4}$$

where ΔP is the pressure drop, ΔL is the length of the porous medium, μ is the viscosity of the fluid, K is the permeability of the porous medium, Q is the fluid flow rate and A is the

cross sectional area to the flow. This relationship between pressure drop and flow velocity for a porous medium is known as Darcy´s law.

However; Darcy´s law is strictly applicable under the assumption of slow working fluid (Bourantas *et al.*, 2014). This law is reliable when the representative Reynolds number is low so that the flow can be considered as laminar. Deviation from Darcy's law grows as the Reynolds number increases. This will be reviewed in the following section.

2.4.2 Reynold's number

The Reynolds number is a dimensionless parameter that is used for Newtonian fluids to indicate flow situations. It is the ratio between inertial and viscous forces (Duggirala *et al.*, 2008). It is a significant parameter used, e.g. to provide information on the regime of the working fluid, and can be expressed as (Machado, 2012):

$$Re = \frac{v_f l}{v} \tag{2.5}$$

where v_f is the fluid velocity, v is the kinematic viscosity $\left(v = \frac{\mu}{\rho}\right)$, and l is the characteristic length. This parameter is useful when studying fluid dynamics as it offers an indication as to when turbulence will occur. Typically, turbulence might occur at a $Re > 1000$ (Janna, 2016). Yet, this criterion is not precise and turbulence might occur under different scenarios.

Regarding porous media, the transition from laminar to turbulent regimes does not appear at the same Re number as in pipe flows. In addition, the flow behaviour changes in all locations inside the material (Bağci *et al.* 2014). It has been reported that turbulence vortices begin to appear at pore level with a $Re \approx 10$ (Masuoka and Takatsu 1996). The critical Re number in porous materials is a parameter that depends highly on the working fluid and the medium

itself. As a consequence, many values can be found in the literature for the Re number where turbulence is believed to occur within a porous medium (Baloyo, 2016).

This disagreement on the turbulence transition values of Re number is due to the complexity of the geometrical structure of the porous media. This can be appreciated on the different choices of length scale or characteristic length. A few examples of the different length scales available are: particle diameter, square root of permeability, pore diameter, etc. (Karimian and Straatman 2008). Some of the models found in the literature for Re number calculations, as well as the turbulence transition values are presented in Table 2-3.

Table 2-3 Comparison of Reynolds number reported in the literature for numerical analysis

Reference	Definition	Re values considered	
		Laminar	Turbulent
(Hellström and Lundström 2006)	$Re' = \frac{\rho D_p \frac{Q}{A}}{\mu} \frac{1}{1-\varepsilon}$	$(0-10)$	$(10-1000)$
(Papathanasiou, Markicevic and Dendy, 2001)	$Re = \frac{\rho D_p \langle u \rangle}{\mu}$	$(0-1)$	$(1-160)$
(Boomsma, Poulikakos and Ventikos 2003)	$Re = \frac{\rho U K^{1/2}}{\mu}$ $Re = \frac{\rho u D_p}{\mu}$	-	-
(Yang *et al.*, 2013)	$Re_H = \frac{\rho_f (\lvert V_D \rvert) H}{\mu_f}$ $Re_p = \frac{\rho_f \left(\frac{\lvert V_D \rvert}{\varepsilon}\right) d_h}{\mu_f}$	-	10^5
(Bianchi *et al.*, 2015)	$Re = \frac{\rho u d_p}{\varepsilon \mu}$	**Darcian:** $Re \leq 1$~10	**Forchheimer:** 1~$10 < Re \leq 150$ **Post-Forchheimer:** $150 < Re < 300$ **Fully turbulent:** $Re > 300$
(Machado, 2012)	$Re = \frac{vl}{\nu}$ $Re_p = \frac{D_p \rho_{in} u_0}{\mu \left(1 - \frac{\varepsilon}{100}\right)}$	-	$10^1 \leq Re \leq 10^2$~10^3
(B. Goyeau, Songbe and Gobin, 1996)	$Re = \frac{\rho U K^{1/2}}{\mu}$	$Re \leq 20$	$Re > 20$
(Jiang and Lu 2006)	$Re = \frac{\varepsilon \rho u_p d_p}{\mu}$	$4.57 \leq Re$~100	$100 \leq Re \leq 231$
(P. de Carvalho *et al.*, 2015)	$Re = \frac{\rho d_d \lvert \vec{u}_d - \vec{u} \rvert}{\mu}$	**Darcian:** $Re \leq 1$	**Forchheimer:** $1 < Re \leq 150$ **Post-Forchheimer:** $150 < Re < 300$ **Fully turbulent:** $Re > 300$ **Used:** $150 < Re < 2000$
(Karimian and Straatman 2008)	$Re = \frac{\rho V_{int} D_p}{\mu}$	$0.1 \leq Re \leq 120$	-
(Bai and Chung 2011)	$Re = \frac{VH}{\nu_f}$	-	$5x10^3 < Re < 4x10^4$ $1x10^4 < Re < 6x10^4$

Even though there is no agreement on the value when the inertial forces need to be considered when studying fluid flow in porous materials, it is well accepted that the inertial forces begin to appear somewhere in the Re range of 10 to 100.

2.4.3 Forchheimer's equation

For turbulent flow in porous media, both viscous and inertial effects cause a more non-linear behaviour which has to be considered. The inclusion of a second term that accounts for the turbulent effects was first proposed by Jules Dupuit (Boomsma, Poulikakos and Zwick 2003) in the form:

$$\frac{\Delta P}{\Delta L} = \frac{\mu}{K} u + \frac{C_f \rho u^2}{\sqrt{K}} \tag{2.6}$$

where u is the Darcian velocity *(m/s)*, ρ is the fluid's density *(kg/m^3)* and C_f stands for the frictions factor or drag force coefficient. The turbulent effects were widely reviewed by Philipp Forchheimer. In one of his works, he investigated the high velocity fluids flowing through a porous medium. He also proposed the addition of a term to Darcy's law in order to account for the inertial effects creating non-linearity (Jambhekar, 2011). With this inclusion, it is possible to differentiate between a linear or Darcian regime that only accounts for the viscous forces, and a more turbulent or Forchheimer regime (Khayargoli *et al.*, 2004).

The following equation proposed by Forchheimer is generally accepted as the extension to the Darcy equation for high flow rates:

$$\frac{\Delta P}{\Delta L} = \frac{\mu}{K} u + C \rho u^2 \tag{2.7}$$

where C is the Forchheimer's coefficient or form drag coefficient. It is believed that C is fixed for a given class of porous media (Dukhan *et al.* 2014). The linear part of Forchheimer's equation accounts for the viscous forces while the quadratic term accounts for the inertial forces. When studying porous media it is important to properly define K and C. These two

parameters are related to the geometrical structure of the material and the distribution, size and shape of the pores.

2.4.4 Permeability and the form drag coefficient

Permeability is the term that refers to the enablement of Newtonian fluids to flow through the porous medium (Dullien, 1979). Theoretical determination of the permeability is difficult because of the complexity to quantitatively describe the medium in a realistic manner (Adler *et al.* 1990). Permeability is usually related to such parameters as porosity, pore size, tortuosity and/or specific surface area. All these structural parameters vary according to the manufacturing process used. This has created differences in the literature when correlations between permeability and structural parameters have been attempted. One of the existing correlations is the Kozeny-Carman equation (Robert A. Greenkorn, 1983):

$$K = c_0 \frac{\varepsilon^3}{\lambda S^2} \tag{2.8}$$

where K is permeability, S is the specific surface area, λ is tortuosity, ε is porosity and c_0 is known as the Kozeny constant. Clyne *et al.* (2006) used a modified form of equation (2.8) to calculate permeability of different porous materials. Their calculations for specific surface area and permeability were shown to be in good agreement with previous researchers.

This relationship has been studied and modified according to the object of the study. Dukhan *et al.* (2014) used the hydraulic radius theory to determine permeability in the Darcian regime and modified equation (2.8) as follows:

$$K = \frac{\varepsilon^3}{c_0(1-\varepsilon)^2 S^2} \tag{2.9}$$

Because specific surface area is difficult to measure accurately, they used a relation between the surface area of the average particle in the medium and the particle diameter d_{par} $\left(d_{par} = \frac{6}{S}\right)$. Equation 2.9 then yields to:

$$K = \frac{{d_{par}}^2 \varepsilon^3}{36 c_0 (1-\varepsilon)^2} \quad (2.10$$

This inclusion has led to different interpretations from the former correlation. However, Equation 2.10 has become the most well-known model to relate permeability with porous metal properties (Chai *et al.*, 2010).

Boomsma, *et al.* (2003) proposed and idealised an open cell model for numerical analysis of metal foams. They reported that the specific surface area can be increased by increasing the pore diameter, while the opposite will occur by increasing porosity. They also mentioned that this increase of the specific surface area will have a large effect on improving permeability. Permeability and the drag force coefficient are determined from experimental measurements. Hereafter, knowing the pressure drop, the porous media length, viscosity and Darcian velocity are critical to obtain K and C (Naaktgeboren *et al.* 2012).

As the fluid flows through the structure, the pressure changes depending on the porous structure. An example of the pressure drop measured for a Weaire-Phelan base model is presented in Figure 2-8. The change in pressure is due to inertial and viscous effects of the porous structure. The combined resistance is the so called drag force, and it can be divided into two terms as a function of its viscous or inertial behaviour.

$$F_T = F_v + F_d \quad (2.11)$$

where F_T is the total drag, F_v is viscous drag (related to the permeability of the material), and F_d is the form drag (related to the Forchheimer coefficient). At relatively slow flows, the pressure drop is given solely by F_v.

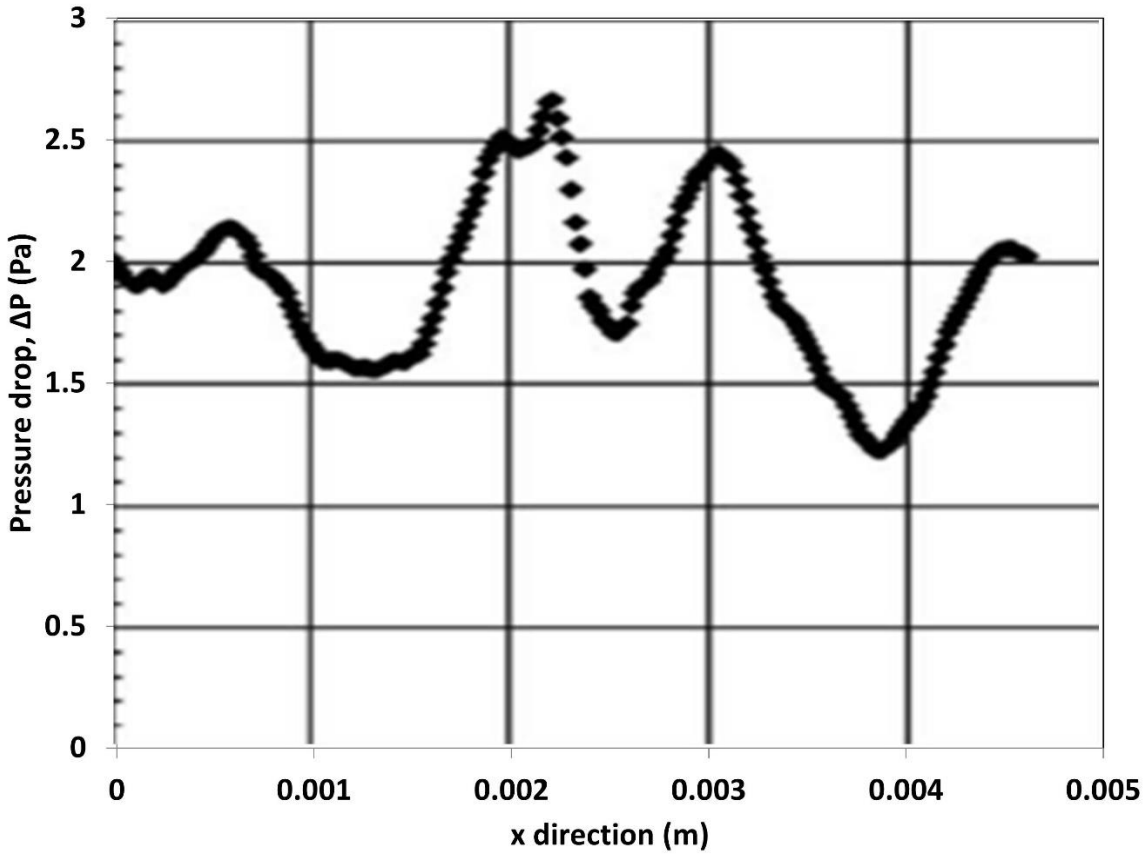

Figure 2-8 Pressure drop versus axial velocity profile measured on a Weaire–Phelan periodic unit cell, (Boomsma *et al.* 2003)

As the flow rate increases, the pressure drop is then due to a sum of both terms (Bağci *et al.* 2014). Della Torre *et al.* (2014) showed evidence of this behaviour. They numerically studied different flow regimes in open-cell foams with high porosities of over 89% and reported that the relative contribution of the viscous drag is more than 50% of the total drag in the laminar regime. At higher velocities, its contribution becomes lower than 25%. Figure 2-9 shows how the inertial effects become more apparent as the Reynolds number increases.

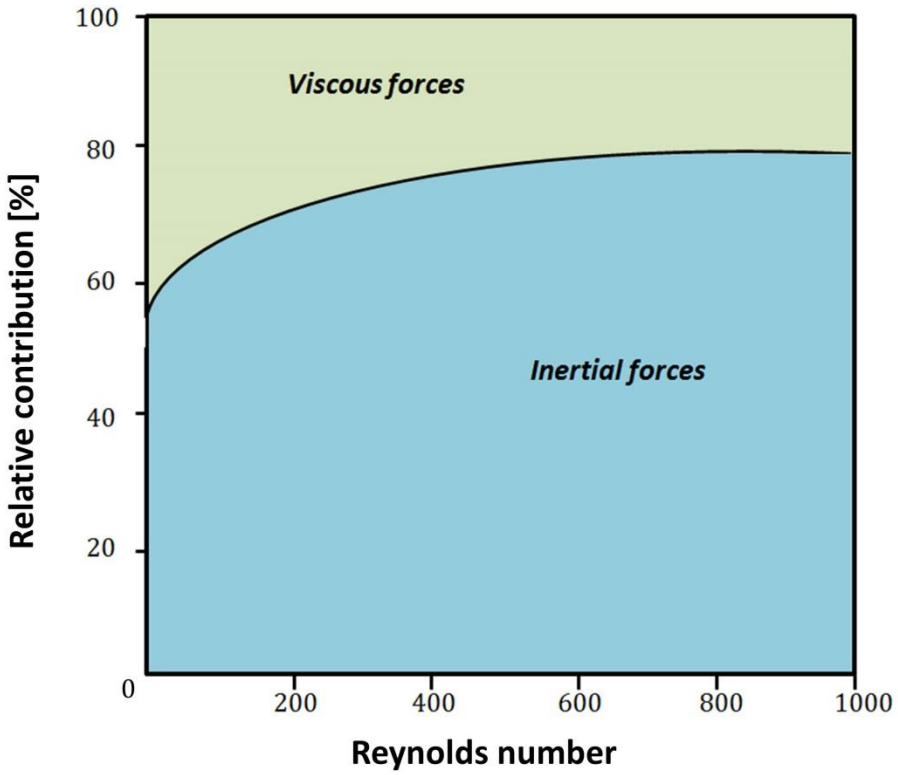

Figure 2-9 Relative contribution of the viscous and inertial forces as function of the Reynolds number, (Della-Torre *et al.*, 2014)

Form drag has proven to be important when measuring the pressure drop. As the velocity increases, so does the form drag. It is believed to be the main mechanism responsible for turbulence generation at pore level.

There are in the literature different attempts to measure the drag force coefficient or friction factor. There are also some attempts to associate it with other porous media parameters such as K. The most commonly known relationship for the Forchheimer coefficient and permeability is the one proposed by Sabri Ergun in 1952 (Jambhekar, 2011, Costa *et al.*, 2015):

$$C = \frac{C_f}{\sqrt{K}} \tag{2.12}$$

where C_f is the drag force or friction factor. Ergun also proposed that the friction factor can be expressed as a function of Reynold's number as in the following correlation (Karimian and Straatman 2008):

$$C_f = \frac{a}{Re} + b \tag{2.13}$$

where a and b are variables that depend on the structure of the porous media. For example, these variables were reported to have values for granular porous media of $a = 150$ and $b = 1.75$. The correlations between K and C, and later C_f and Re, are very popular among researchers, though the fitting parameters a and b depend highly on the type of porous media being studied.

Table 2-4 shows some of the values used for variables a and b found in the literature for metallic foams and porous metals.

Table 2-4 Friction factors found in the literature for porous metals

Reference	Definition	Porous media
(Nakayama *et al.*, 2001)	$C_f = \frac{51.2}{Re} + 1.85$ $C_f = \frac{64}{Re} + 1.62$	Numerical analysis of a porous medium using a periodic array of square cylinders
(Xu and Jiang 2008)	$C_f = \frac{36.4}{Re} + 0.45$	Numerical analysis of water and air flowing within a porous media with pore size ranging from $200\mu m$ to $10\mu m$
(Beugre *et al.*, 2010)	$C_f = 77.85\frac{1-\varepsilon}{Re} + 0.77$	Numerical analysis of a metallic foam made of $Ni - Cr$, the lattice Boltzmann method is employed. The 3D geometry is created using X-ray micro-tomography
(Costa *et al.*, 2015)	$C_f = \frac{111.8}{Re} + 1.85$ $C_f = \frac{165.5}{Re} + 2.04$	Numerical analysis of a small detailed 3-D stacked woven wire regenerator matrix.
(Abbood, 2009)	$C_f = \frac{10.7349}{Re^{0.25}}$	Experimental study for flow through porous media. (crushed silica, crushed coal, glass beads and crushed garnet)
(Naaktgeboren, Krueger and Lage, 2012)	$C_f = \frac{48}{Re}$ $C_f = \frac{64}{Re}$	Analytical and numerical study of flow through a restriction in circular pipe and parallel plates channels.

2.5 Principles of heat transfer in porous metals

Whenever a temperature difference exists in a medium or between media, heat transfer occurs (Incropera *et al.*, 2007). This exchange of energy between systems can be categorised in three different modes, i.e., conduction, convection and radiation. In all three cases, according with the second law of thermodynamics, heat is being transferred from a region of high temperature to a lower temperature region. Therefore it is important to understand the right mechanism of energy transfer:

- Conduction: here the energy is being transferred within a stationary system, i.e., the gradient of temperature is from one point to another inside a system.
- Convection: here the heat is being transferred from a stationary system due to a fluid in motion, e.g. flow within the porous material.
- Radiation: here the energy is being transferred through electromagnetic waves.

Heat transfer in porous metals can be present in any of these three forms. Radiation for instance, is significantly affected by pore size and porosity. Heat transfer by radiation is reduced when pore size or porosity decreases. This is due to the presence of more metal at the cell walls that will work as barriers. However, Zhao *et al.* (2004 b) reported that heat transfer by radiation in porous metals is present only at high temperatures, i.e. 500 – 800 K. At lower temperatures, its influence can be neglected. Therefore, for the study of heat transfer in porous metals at temperatures lower than 500 K, only two of forms are considered, i.e., conduction and convection.

In terms of convection, there are two types, natural convection (generated due to buoyancy forces) and forced convection (when the fluid movement is generated by an external force such as a pump or fan). For the LCS porous copper study, the main heat transfer mechanism is due to forced convection.

2.5.1 Thermal conduction in porous metals

Conduction is a heat flux process where the transfer of energy is done between particles within a substance, from the more energetic to the less energetic. Particles located where the substance is hotter exchange their kinetic and vibrational energies with surrounding particles through random motion and collisions.

A temperature gradient is established with energy being transported constantly in the direction of decreasing temperature. This heat flux occurs in solids, fluids and gases. In order to analyse heat transfer, this process can be described in terms of heat transfer rate,

which is the amount of energy transferred per unit time. For conduction in one-dimensional cases, the rate follows Fourier's law (White, 2011):

$$q = -k\frac{dT}{dx} \tag{2.14}$$

where q is the heat flux i.e., the rate of heat transfer per unit area, $\frac{dT}{dx}$ is the temperature gradient and k the thermal conductivity.

In the literature there are different studies related to the thermal conductivity of porous metals. For example, Muramatsu *et al.* (2013) studied thermal conduction in lotus-type metal foams. They found that reducing the randomness of the pores enhanced thermal conduction and at the same time, pressure drop decreased. These types of metal foams were reported to be advantageous compared to regular metal foams, especially in situations where the volume set for the heat exchanger is limited.

Thewsey and Zhao (2008) measured the thermal conductivity of LCS porous copper. They used an empirical correlation between conductivity and relative density as follows:

$$\frac{k^*}{k_0} = \left(\frac{\rho^*}{\rho_0}\right)^{n_c} \tag{2.15}$$

where k^* and k_0, ρ^* and ρ_0 are the thermal conductivities and densities of the porous metal and the bulk material respectively, and n_c is the exponent that correlates both terms. In their study, $n_c = 2.05$, which is close to the theoretical value of 2.

2.5.2 Convection in porous metals and the heat transfer coefficient

The energy transfer from a stationary system due to a fluid in motion is known as convection. Due to the high surface area of the porous copper, convection will be related to

the permeability of the material and its heat conductivity. The equation for convection is known as Newton's cooling law (Incropera *et al.*, 2007):

$$J = h(T_s - T_f) \tag{2.16}$$

where J is the heat flux, T_s and T_f are the temperatures at the surface and the fluid respectively. In the same way as conduction, the heat flow by convection in a porous metal can be expressed in terms of the contact surface area of the heated source as (Zhang *et al.*, 2009):

$$j = hA_{pl}(T_{pl} - T_m) \tag{2.17}$$

where j is the heat flow, A_{pl} is the contact area between the heat source and porous metal, h the heat transfer coefficient, and $T_{pl}\ and\ T_m$ are the temperature of the heat source and the mean temperature of the fluid inlet and outlet, respectively. Another equation to be considered is the heat flow carried away due to the water in motion inside the porous material, i.e.:

$$j = \rho_f C_p Q(T_o - T_i) \tag{2.18}$$

where C_p is the specific heat of water, Q is the flow rate, ρ_f is the density of water, and T_i and T_o are the temperatures of water inlet and outlet. By combining Equations 2.12 and 2.13 the heat transfer coefficient can be obtained by:

$$h = \frac{\rho C_p Q(T_{out} - T_{in})}{A_{pl}(T_{pl} - T_m)} \tag{2.19}$$

Convection in porous metals has become a recurrent case of study for slow motion fluids, given their wide number of applications in engineering, for example, for geothermal and petroleum reservoirs, in packed bed and nuclear reactors, oil delivery, etc. (Matin and Pop 2013).

Several experimental and theoretical studies are reported in the literature for heat transfer in porous metals. Zaragoza and Goodall (2013) studied open-cell aluminium foams with uniform and non-uniform pore sizes. It was found that non-uniform pore sized samples showed almost twice the heat transfer coefficient as uniform samples. Orientation is shown to be an important factor too. In their study, two sets of samples were considered: large-small pore samples or small-large pore samples, with the flow stream as reference. The resulting heat transfer coefficient is shown to increase by 35% - 40% when using large-small pore samples. This is attributed to the increased resistance to fluid flow of the small-large pore samples at the entrance region. They suggested the use of graded pore structures when designing heat exchangers.

Baloyo and Zhao (2015) studied the heat transfer coefficient of homogeneous and hybrid structures made of LCS porous copper. An optimum porosity of 60% was found for homogenous samples. This porosity improves the heat removal by four times in comparison with an open channel. Hybrid structures were designed by having two different porosities in the whole pore sample. Orientation was also considered during their study. Segmented vertical bilayers with 80% porosity by the water inlet and 40% on the other end were shown to enhance the heat transfer coefficient by up to 5 times in comparison to a homogenous sample.

Dukhan and Al-Rammahi (2012) analysed experimentally and analytically forced convection inside a confined cylindrical isotropic porous medium. It was reported that at low air flow, the model showed good agreement with the experimental data; however differences appeared as the flow rate increased. This was justified in terms of instrumental error measurements. Zhang *et al.* (2009) experimentally studied the heat transfer coefficient of middle range porosity LCS porous copper. In their study, water was used as coolant and the flow rate varied from Darcian to the Forchheimer regime. In their study, porosity and pore size were found to greatly affect the heat transfer coefficient, which increased with porosity until reaching its peak at $\varepsilon \approx 0.62$, then decreased with higher porosities. For the pore size

analysis, three different pore size ranges were tested in their study. The heat transfer obtained from the middle range pore size was 1.5 times higher than the lower and higher pore size ranges.

Heat transfer coefficient has also been studied numerically. For instance, Jiang and Lu (2006) studied convective heat transfer and fluid flow of water through a sintered bronze porous plate. The geometric model consists of homogenous and uniform sized packed particles. In their study, porosity was obtained by changing particle size. From their results, it was observed that the local heat transfer coefficient increased with flow rate. It was also observed that it decreased along the axial direction. Kopanidis *et al.* (2010) examined flow and heat transfer at pore scale level for open-cell metal foams with densities of 10 and 40 PPI (pores per inch). A 3D geometric wire model resembling the Weaire–Phelan structure was presented. It was found that entrance effects, near wall effects and heat conduction through the solid ligaments are significant when calculating heat transfer coefficients using this technique. Teruel and Díaz (2013) conducted a numerical analysis using a symmetric 2D model for middle and high range porosities. The heat transfer coefficient was calculated in terms of a mean logarithmic temperature. It was found that the heat transfer coefficient is sensitive to the 2D model location. Therefore special care should be taken when selecting the location in the porous structure. Moon and Kim (2015) presented a numerical analysis for filled and hollow metal foam ligaments. It was reported that metal foam ligaments enhance heat transfer performance with Reynolds number above 5. Hwang and Yang (2012) simulated fluid flow and heat transfer on a metallic porous block subjected to a confined turbulent slot jet. Their study showed that the average Nusselt number (Nu) increased (about 3 to 5 times) in comparison to fluid channels without the porous block. However, in order to increase the heat removal by conduction, the Reynolds number should decrease.

2.6 Computational fluid dynamics

Computational fluid dynamics (CFD) is a technique using numerical equations to solve fluid dynamics problems which will provide an approximation to the resultant flow fields. With the evolution of technology, this approach has emerged as a reliable tool to analyse systems involving fluid in motion, heat transfer or a chemical reaction. This is a cost-effective way to analyse real flows by numerically solving the Navier-Stokes equations (Sayma, 2009). This technique has been used lately to study porous metals (Lefebvre *et al.* 2008). First, the flow description in the porous metals is assumed to be a Newtonian and incompressible fluid flow under steady-state conditions. Second, depending on the complexity of the structure and the computational resources available, researchers have chosen between 2D and 3D analysis. Finally, analytical and experimental methods have been used to validate numerical solutions.

However, the numerical research made on fluid flow and heat transfer in porous media is limited. This is due to the complexity of the structure of the material and the appearances of new manufacturing methods (Pathak *et al.* 2013). The simulated porous structure is usually described as representative of the real material given its randomness and the complicated network of channels. For instance, Karimian and Straatman (2008) carried out a set of numerical simulations at pore level using laminar flow. They created an idealised pore geometry, developed a permeability model based on the Carman-Kozeny model, and proposed a heat transfer model for foams with interconnected spherical pore structures.

2.6.1 Governing equations

A fluid is anything that flows, usually a liquid or a gas, the latter being distinguished by its great relative compressibility. Fluids are treated as continuous media, and their motion and state can be specified in terms of the velocity (v), pressure (p), density (ρ), etc., evaluated at every point in space and time (t). The regime of a fluid depends on the relative

importance of fluid friction (viscosity) and flow inertia. The fluid flowing during an interval of time Δt may change from one moment to another, or at two different points; however if it is analysed as a single entity during a long period of time, this flow could be considered as constant. Most flows in engineering are turbulent; this regime is irregular and unpredictable. Turbulent eddies create fluctuations in velocity. If the flow is steady and laminar then:

$$v(t) = \bar{v} \tag{2.20}$$

However, for turbulent models, the velocity record includes a turbulent component; this inclusion to the laminar model is commonly called Reynolds decomposition (Tannehill *et al.* 1997):

$$v(t) = \bar{v} + v'(t) \tag{2.21}$$

where $\bar{v}$ is the mean motion and v' is the fluctuating part and they are obtained from:

$$\bar{v} = \frac{1}{\Delta t}\int_{t_0}^{t_0+\Delta t} v(t)dt \tag{2.22}$$

and:

$$v'(t) = v(t) - \bar{v} \tag{2.23}$$

2.6.1.1 Continuity equation

The governing equations for flows are obtained from the conservation laws of mass, momentum, and energy (Haghshenas Fard, 2010). Consider the application of the continuity equation on the pipeline illustrated in Figure 2-10. Fluid enters and leaves the pipeline (control volume) normal to the control surfaces, with inflow velocity denoted by $v_1(r)$, and the outflow velocity by $v_2(r)$, where r is the radial position vector originated at the centreline of the conduit. Both velocities vary across the control volume (Escudier, 1998).

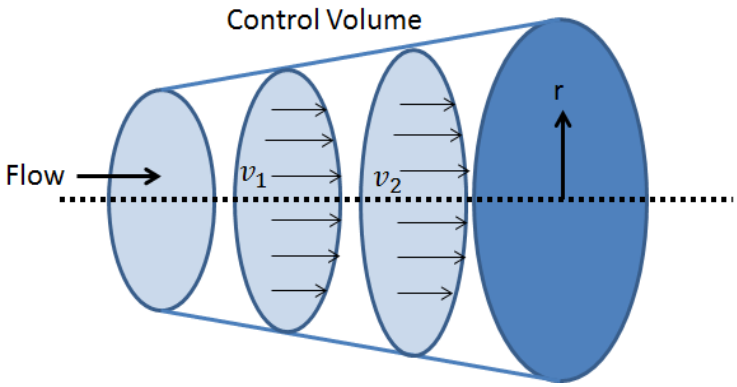

Figure 2-10 Flow rate inside a Control Volume

It is at this point where the continuum assumption takes place. This yields the steady-state continuity equation for an incompressible fluid, which can be written as (Massey, 2006):

$$\int_{A_1} \rho_1 v_1 dA = \int_{A_2} \rho_2 v_2 dA \tag{2.24}$$

where dA represents the derivative of the cross-sectional area from the pipeline. Thus:

$$v_1 A_1 = v_2 A_2 = Q = constant \tag{2.25}$$

where Q is the volumetric flow rate. However, this situation is no longer valid when the fluid flows through a porous medium. When the flow is within a porous material, it becomes unpredictable, thus a new formulation is required (Robert A. Greenkorn, 1983).

Incompressible Newtonian flows at pore-scale level are governed by the Navier-Stokes equations. By considering an infinitesimal element with dx, dy, dz edges inside the control volume like the one shown in Figure 2-11, the volumetric flow rate crossing the plane perpendicular to the y axis at the inlet is assumed to be (Douglas *et al.* 2001):

$$dQ_{m_y} = \rho v_y dA_y = \rho v_y dx dz \tag{2.26}$$

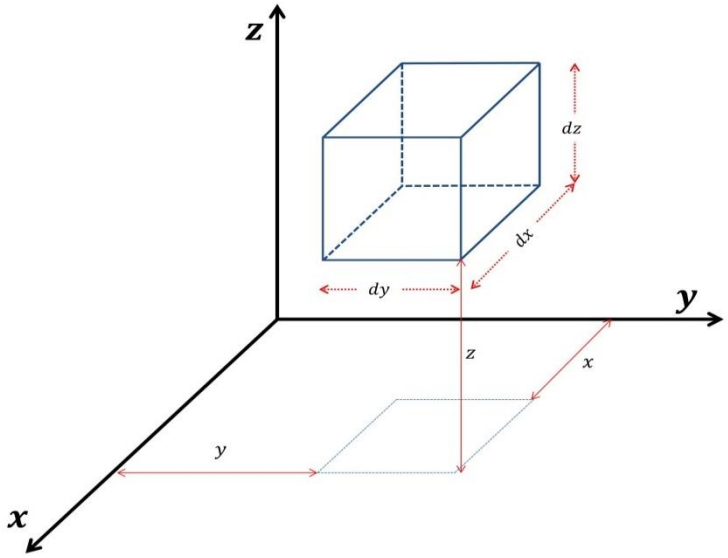

Figure 2-11 Infinitesimal element representation for the continuity equation deduction

Meanwhile the volumetric flow rate at the outlet $(y + dy)$ of the element is calculated by (Crowe *et al.* 2005):

$$dQ_{m_{y+dy}} = \rho v_y dA_y + \frac{\partial}{\partial y}[\rho v_y dA_y]dy = \left[\rho v_y + \frac{\partial}{\partial y}(\rho v_y)dy\right]dxdz \tag{2.27}$$

Thus, the total volumetric flow rate passing inside the element is given by:

$$Q_y^{total} = Q_{m_y} - Q_{m_{y+dy}} = -\frac{\partial}{\partial y}(\rho v_y)dxdydz \tag{2.28}$$

Similar expressions can be obtained for x and z. Thus, the total volumetric flow rate is:

$$Q^{total} = \left[-\frac{\partial}{\partial x}(\rho v_x) - \frac{\partial}{\partial y}(\rho v_y) - \frac{\partial}{\partial z}(\rho v_z)\right]dxdydz \tag{2.29}$$

Equation 2.29 represents the total volumetric flow rate entering and leaving the element in any direction with $\left[-\frac{\partial}{\partial x}(\rho v_x) - \frac{\partial}{\partial y}(\rho v_y) - \frac{\partial}{\partial z}(\rho v_z)\right]$ being the divergence of vector $\vec{v}$ times ρ. Equation 2.29 is later combined with the definition for density that can be expressed as (Fox *et al.* 2010):

$$dm = \rho dV \tag{2.30}$$

where m and V are the mass and volume of the element. The volumetric flow rate can also be calculated in the following way (Janna, 2016):

$$Q^{total} = \frac{\partial}{\partial t}(\rho dV) \tag{2.31}$$

Therefore the final expression for the continuity equation becomes (Emanuel, 2000):

$$\frac{\partial \rho}{\partial t} = -\nabla \rho \vec{v} \tag{2.32}$$

Given the principle of conservation of mass, the continuity equation for an incompressible fluid simplifies to (Shaughnessy *et al.* 2005):

$$\nabla \vec{v} = 0 \tag{2.33}$$

2.6.1.2 Momentum equation

The momentum equation is obtained by using Reynolds transport theorem. The system from Figure 2-11 moves and deforms, but always contains the same number of fluid particles. The total amount of a certain property is given by (Janna, 2016):

$$B_{sys} = \int_{R_{(tot)}} \rho \beta dV \tag{2.34}$$

In this context, B_{sys} is a dummy variable that could represent any of the fluids properties like mass, momentum, etc. β is the variation of B_{sys} per unit mass: $\beta = \frac{dB_{sys}}{dm}$, and $R_{(tot)}$ is the total region occupied by the system. In order to know the rate of change of B_{sys} at a certain time, Equation 2.34 then becomes (Shaughnessy *et al.* 2005):

$$\frac{dB_{sys}}{dt} = \frac{d}{dt}\int_{R_{(tot)}} \rho\beta dV \tag{2.35}$$

Finally, by considering variations at the inlet, outlet and within the control volume, Equation 2.35 becomes (Shaughnessy *et al.* 2005):

$$\frac{dB_{sys}}{dt} = \int_{R_{(tot)}} \frac{\partial}{\partial t}(\rho\beta)dV + \int_{S_{(tot)}} \rho\beta(\vec{v}\cdot n)ds \tag{2.36}$$

where $S_{(tot)}$ is the total surface and n represents the unity vector. By implementing Newton's second law of motion for a system, $\sum F = \frac{dmv}{dt}$, and letting $B_{sys} = m\vec{v}$, Equation 2.36 yields (Crowe *et al.* 2005):

$$\sum F = \frac{d(m\vec{v})_{sys}}{dt} = \int_{CV} \frac{\partial}{\partial t}(\rho\vec{v})dV + \int_{CS} \rho\vec{v}(\vec{v}\cdot n)ds \tag{2.37}$$

Yet, because $\vec{v}$ is a vector that changes in space and time:

$$\vec{v}_{(x,y,z,t)} = \hat{\imath}v_{1_{(x,y,z,t)}} + \hat{\jmath}v_{2_{(x,y,z,t)}} + \hat{k}v_{3_{(x,y,z,t)}} \tag{2.38}$$

the calculation of the total acceleration on the left term in Equation 2.37 is (Janna, 2016):

$$a = \frac{d\vec{v}}{dt} = \hat{\imath}\frac{dv_{1_{(x,y,z,t)}}}{dt} + \hat{\jmath}\frac{dv_{2_{(x,y,z,t)}}}{dt} + \hat{k}\frac{dv_{3_{(x,y,z,t)}}}{dt} \tag{2.39}$$

By solving Equation 2.39, and by using the advection operator $(\vec{v}\cdot\nabla)\vec{v}$ instead of the tensor derivative of ∇u (Zill and Wright 2011), this yields to:

$$\rho\left(\frac{\partial\vec{v}}{\partial t} + (\vec{v}\cdot\nabla)\vec{v}\right) = \int_{CV} \frac{\partial}{\partial t}(\rho\vec{v})dV + \int_{CS} \rho v(\vec{v}\cdot n)ds \tag{2.40}$$

Regarding the right hand side of Equation 2.40, the first term is related to external body forces while the second term represents the surface forces. As the element is so small, only the viscous forces on the surface are considered. To express all the forces over the element, the Cauchy stress tensor is employed (Domingo, 1997). Here, the viscous stresses and the hydrostatic pressure are considered on each side of the control surface (Ortiz Prado *et al.* 2013):

$$\sigma_{ij} = \begin{pmatrix} -P + \sigma_{xx} & \tau_{yx} & \tau_{zx} \\ \tau_{xy} & -P + \sigma_{yy} & \tau_{zy} \\ \tau_{xz} & \tau_{yz} & -P + \sigma_{zz} \end{pmatrix} \tag{2.41}$$

where σ_{ij} is the stress tensor and τ represents the shear stress. Then, the net force in the x direction is given by:

$$dF_x = \left[\frac{\partial}{\partial x}\sigma_{xx} + \frac{\partial}{\partial y}\sigma_{xy} + \frac{\partial}{\partial z}\sigma_{xz}\right] dxdydz \tag{2.42}$$

The same situation happens in the y and z directions. This will lead to 12 partial derivatives that can be easily simplified to the following form (Emanuel, 2000):

$$\left(\frac{dF_x}{dV}\right)_S = -\nabla PI + \nabla \cdot \tau_{ij} + \rho g \tag{2.43}$$

where I is the identity matrix, $\nabla \cdot \tau_{ij}$ is the divergence of the shear stress tensor, ρ is the fluids density and g corresponds to the gravitational acceleration. By linking Equation 2.40 and Equation 2.43 it yields to (Dukhan and Suleiman 2013):

$$\rho\left(\frac{\partial \vec{v}}{\partial t} + (\vec{v} \cdot \nabla)\vec{v}\right) = -\nabla PI + \nabla \tau_{ij} + \rho g \tag{2.44}$$

Assuming the flow is isotropic, the Stokes stress constitutive equation can be implemented, $(\tau = 2\mu\omega)$ (Pino Muñoz *et al.* 2012) to express the stress tensor in terms of dynamic viscosity given that (Malham, 2014):

$$\omega = \frac{1}{2}\left(\nabla v_{i,j} + \nabla {v_{j,i}}^T\right) \tag{2.45}$$

where ω is the rate of strain tensor and v^T is the transposed matrix of v. As the external forces can be neglected for this study, the term ρg will disappear from the formulation (Bianchi *et al.*, 2015). By substituting Equation 2.45 into Equation 2.44 we obtain the final form for the momentum equation.

$$\rho\left(\frac{\partial \vec{v}}{\partial t} + (\vec{v}\cdot\nabla)\vec{v}\right) = -\nabla PI + \nabla\left[\mu\left(\nabla v_{i,j} + \left(\nabla v_{i,j}\right)^T\right)\right] \tag{2.46}$$

where $\frac{\partial \vec{v}}{\partial t}$ and $(\vec{v}\cdot\nabla)\vec{v}$ terms are the local and convective accelerations respectively. The first term denotes a change of velocity due to a change in time, while the second term denotes a change in velocity due to change in space (White, 2011). The right hand side of the equation represents the forces on the element. Finally, the divergence of the Stokes stress tensor is given by $\nabla\tau = 2\mu\nabla\omega = \mu\nabla\cdot\left(\nabla v_{i,j} + \left(\nabla v_{i,j}\right)^T\right)$, and therefore Equation 2.46 becomes:

$$\rho\left(\frac{\partial \vec{v}}{\partial t} + (\vec{v}\cdot\nabla)\vec{v}\right) = -\nabla PI + \mu\nabla^2 v_{i,j} \tag{2.47}$$

Equation 2.47 is the momentum equation for an incompressible fluid flow in a rigid homogeneous porous medium (Saito and de Lemos 2005).

2.6.1.3 Energy equation

For the energy equation, the change of temperature is the main focus of energy transfer. Therefore, a special case of the energy equation is used that only considers low motion fluids and neglects any sort of dissipation. For that Equation 2.14 and Equation 2.18 are employed as (Shaughnessy *et al.* 2005):

$$\rho C_p v\cdot\nabla T = \nabla\cdot(k\nabla T) \tag{2.48}$$

where T is the temperature, C_p is the specific heat and k is the thermal conductivity.

2.6.2 Local volume averaging method

The local averaging method is a technique used to represent the local properties within a small control volume inside the representative elementary volume. To calculate any property or field variable δ, the following expression is employed (Liou, 2005):

$$\langle \delta_p \rangle = \frac{1}{V} \int_{V_p} \delta_p dV \tag{2.49}$$

where V represents the volume and the sub-index p denotes the phase in which the quantity δ_p is defined. In this study, f and s will indicate the fluid and solid phases within the control volume. Therefore, there will be two types of average that will be related through porosity as in Equation 2.1, leading to (Quintard and Whitaker 1994):

$$\langle \delta_p \rangle = \begin{cases} \varepsilon \langle \delta_f \rangle & if\ p = f \\ (1-\varepsilon)\langle \delta_s \rangle & if\ p = s \end{cases} \tag{2.50}$$

When the volume average is used on any transport equation the problem becomes that of solving the average of a gradient (or divergence). In order to interchange integration and differentiation, the spatial averaging theorem is employed (Vafai, 2005):

$$\langle \nabla \delta_p \rangle = \nabla \langle \delta_p \rangle + \frac{1}{V} \int_{A_{pq}} \delta_p n_{pq} dA \tag{2.51}$$

where $p, q \in \{f, s\}, p \neq q$, and n_{pq} is the unit vector oriented from the $p - phase$ to the $q - phase$. Assuming the non-slip condition (Whitaker, 1999) and constant porosity for the purposes of the present study, volume averaging Equation 2.33 and Equation 2.47,results in:

$$\nabla \langle \vec{v} \rangle = 0 \tag{2.52}$$

$$\rho_f\left(\frac{\partial\langle\vec{v}\rangle}{\partial t}+\left(\frac{\langle\vec{v}\rangle}{\varepsilon}\cdot\nabla\right)\langle\vec{v}\rangle\right)=-\varepsilon\nabla\langle P_f\rangle I+\mu\nabla^2\langle\vec{v}\rangle+\frac{1}{V}\int_{A_{fs}}\left(-\tilde{p}n_{fs}+\mu_f\nabla\tilde{u}\cdot n_{fs}\right)dA \tag{2.53}$$

where $\tilde{p}$ and $\tilde{u}$ are velocity and pressure fields at pore level. The complete derivation of Equation 2.53 can be found in Whitaker (1986). At this point supplementary information about velocity and pressure fields is needed in order to solve Equation 2.53. The typical method for seeking closure is to replace the unknown pore-level terms with familiar terms from the extended Darcy equation (Vafai and Tien 1981). Using this methodology the momentum equation can be written with the inclusion of the bulk resistance as follows (Taheri, 2015):

$$\frac{\rho_f}{\varepsilon^2}\left(\frac{\partial\langle\vec{v}\rangle}{\partial t}+(\langle\vec{v}\rangle\cdot\nabla)\langle\vec{v}\rangle\right)=-\nabla\langle P_f\rangle I+\frac{\mu}{\varepsilon}\nabla^2\langle\vec{v}\rangle+F \tag{2.54}$$

where $\langle\vec{v}\rangle$ is the local average Darcian velocity vector and F is the total body force including the resistance from the porous medium and other external forces (Wang *et al.*, 2015). Here, Equation 2.54 offers local volume averaged flow field data throughout the porous media (Sozer and Shyy 2007).

In a similar way, the energy equation is also volume averaged. However, when dealing with porous metals, attention should be paid to the difference between temperature phases, i.e. fluid and solid. In many practical problems, the temperature difference between phases inside the representative elementary volume (REV) should be compared to the overall scale temperature variation across the REV. If the local temperature is much lower compared to total REV, it is suitable to neglect the local temperature variations. Under these conditions, the “local thermodynamic equilibrium” (LTE) is assumed as $\langle T_f\rangle=\langle T_s\rangle=\langle T\rangle$ (Sozer and Shyy 2007). With this in consideration, Equation 2.49 yields to (Liou, 2005):

$$\left[\varepsilon\left(\rho C_p\right)_f+(1-\varepsilon)\left(\rho C_p\right)_s\right]\nabla T=\nabla\cdot(k_e\nabla T) \tag{2.55}$$

where k_e is the effective thermal conductivity. However, if the LTE condition is not achieved, the volume averaging of Equation 2.48 then becomes (Phanikumar and Mahajan 2002):

$$\varepsilon\left(\rho C_p\right)_f\left[\frac{\partial T_f}{\partial t}+\frac{u}{\varepsilon}\cdot\nabla T_f\right]=\nabla\cdot\left(\left(k_e\right)_f\nabla T_f\right)+h_{sf}A_{sf}\left(T_s-T_f\right) \tag{2.56}$$

$$(1-\varepsilon)\left(\rho C_p\right)_s\frac{\partial T_s}{\partial t}=\nabla\cdot\left(\left(k_e\right)_s\nabla T_s\right)-h_{sf}A_{sf}\left(T_s-T_f\right) \tag{2.57}$$

The convective term in Equation 2.56 and Equation 2.57 is used to achieve the coupling between the two phases, i.e. solid to liquid, and the energy transfer due to temperature differences.

2.6.3 Geometrical models

A porous medium consists of a very complex solid matrix making it almost impossible to describe the geometry with an exact technique. However, it is often possible to describe the porous medium as a continuum, where the hydraulic resistance generated in each pore is averaged to a mean pressure drop of the entire medium. Even though the arrangement of pores is random, it is possible to analyse a small portion of it and generalise the results for the complete geometry. Numerical studies have used two different approaches to tackle this issue. The first is the macroscopic approach. This methodology utilises volume-averaged equations to describe the overall flow characteristics. The other methodology is the microscopic approach. Here the researcher uses a specific geometry resembling the porous medium (Krishnan *et al.* 2006). The validity and advantages of both techniques are still under discussion.

For the microscopic approach, there are two major techniques to characterise a porous medium, i.e. 2D and 3D modelling. Even though the 2D approach seems to overlook some

of the important features of a porous medium, interesting results have been obtained via this method. The simplest way to build the porous media is by arranging a group of struts, which are used to represent the porous media as shown in Figure 2-12. Porosity can be changed by simply changing the size of the strut or horizontal distance between strut centres (Saito and de Lemos 2005).

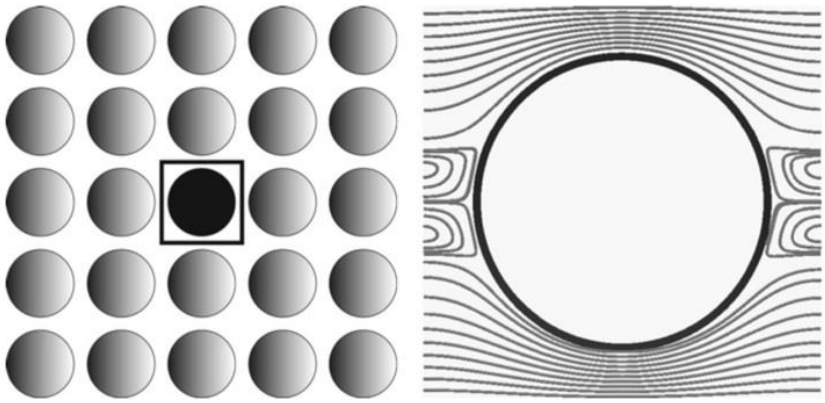

Figure 2-12 2D Arrangement of cylinders and computational box containing one cylinder (left) and streamline plot of flow (right), (Zhu *et al.* 2014)

For instance, Kundu *et al.* (2014) used a periodic array of square cylinders to simulate turbulent flow through porous media. In their case, porosity was varied by changing the size of the fixed struts. It was reported that the macroscopic turbulent kinetic energy and dissipation rate increase with decrease in porosity. This approach was used in a similar way by Pedras and de Lemos (2001). In their study they used an array of elliptic rods to analyse turbulence in a porous medium. The dissipation rate and kinetic energy reported were in good agreement with data from previous studies. Yet, these are not the only models that exist to study porous metals. Another example is the use of a random pattern of cylinders as seen in Figure 2-13. In this case, porosity is achieved by changing the cylinder radius only. The number of struts remains fixed and they do not overlap.

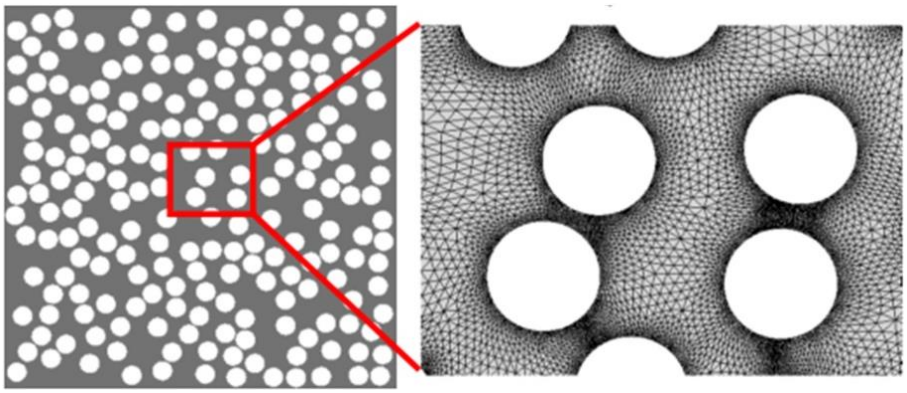

Figure 2-13 2D representation of a fibrous material generated by a Monte Carlo procedure accounting for 200 cylinders (Yazdchi and Luding 2011)

A different approach is using representative 3D models. Such an approach is perfectly capable of representing the real material, but simple enough so it does not require too much time to compute. Arrangements of groups of spheres or different 3D structures have been used. Different techniques are used in the literature to model a porous structure. Some examples of the geometries found in the literature are presented in Table 2-5. It is important to note that most of the geometries found for numerical modelling are related to open-cell structures and one of the main features when deciding for the correct model is porosity.

Table 2-5 Current geometry creation models found in the literature

Reference	Geometrical model	Porous medium	Porosity
(Hellström and Lundström 2006)	2D array of aligned parallel cylinders	-	$40\%, 60\%, 70\%$
(Papathanasiou *et al.* 2001)	2D array of squares and hexagons	Fibrous porous media	$(30\% - 60\%)$
(Machado, 2012)	2D model with random squares distribution.	Micro power plants	$88.5\% , 95\%$
(Karimian and Straatman 2008)	3D model based on interconnected cubes with a spherical hollow space	Graphitic foam	$75\%\ 80\%,$ $85\%, 90\%$
(Jiang and Lu 2006)	3D model with a limited number of identical particles as the porous media	Sintered porous plate channels	$40.2\%, 44.4\%,$ 46.3%
(P. de Carvalho *et al.*, 2015)	3D digital representations were generated using microcomputer tomography scans for open cell metal foams of different grades.	Open-cell metal foams	$88.92\%, 84.65\%,$ 88.62%
(Iasiello *et al.*, 2014)			$89.4\% , 90\%$
(Krishnan *et al.* 2006)	3D model obtained from a solid cube and the subtraction of 5 equally sized overlapping spheres located in a BCC pattern.	Open-cell foam structure	$> 94\%$

(to be continued)

Table 2-5 (Continuation) Current geometry creation models found in the literature

Reference	Geometrical model	Porous medium	Porosity
(Bai and Chung 2011)	3D single sphere- centred tetrakaidecahedron	Open-cell metal foam	$5\ ppi,$ $10\ ppi,$ $20\ ppi,$ $40\ ppi$ $ppi = pores\ per\ inc$
(Duggirala *et al.*, 2008)	3D model obtained from a solid cube and the subtraction of 5 equally sized spheres located in a BCC pattern. In this structure the spheres do not overlap and there are small cylindrical channels crossing the structure that work as the micro-channels.	Activated carbon powder entrapped in a matrix of cylindrical fibres	$41\%,$ $47\%,$
(Yang *et al.*, 2013)	3D periodic arrays of cubic, spherical or ellipsoidal particles	-	$(60\% - 75\%)$

Lately, tetrakaidecahedron has been used to model the geometry (Bai and Chung 2011). This 3D geometry comes as a result of what is better known as Kelvin's conjecture. The best filling arrangement that has minimal surface area of similar cells of equal volume is polyhedrons consisting of eight hexagonal and six quadrilateral faces. In this case, the isoperimetric quotient of the polyhedron is close to 0.753367.

Kopanidis *et al.* (2010) used this structure (Figure 2-14) to simulate flow and heat transfer at pore scale level. They implemented the tetrakaidecahedron and the resulting values were compared with experimental data available in open-cell foams.

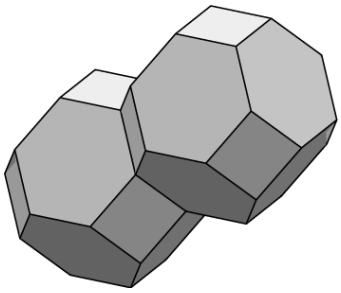

Figure 2-14 Two tetrakaidecahedron united (Kelvin cells) (Boomsma *et al.* 2003)

Their results showed the influence of entrance effects on pressure drop and heat transfer coefficient to be significant. This technique was also used by Boomsma *et al.* (2003). They created a periodic unit volume by joining 8 cells, with the unit cells representing the pores and interstices created by joining other cells to the model. Their numerical simulation results were compared to experiments resulting in good agreement between both techniques.

However, this kind of technique is suitable for structures with high porosity. Besides, the construction of a structure made of several number of this type of cells requires a huge amount of computational resources.

In a similar approach, Dukhan and Suleiman (2013) used Kelvin's cells as a single hollow structure for porosities greater than 90%. In their approach the vertices are used as ligaments which create an assembly similar to the ligaments within open-cell metal foam. The technique used to create this structure is simple. First, a solid cube is subjected to a Boolean operation where eight spheres are subtracted from the corners as shown in Figure 2-15. The centre of each sphere is located in one of the cube's vertices and the radius of the spheres is not larger than half the length of the cube's side.

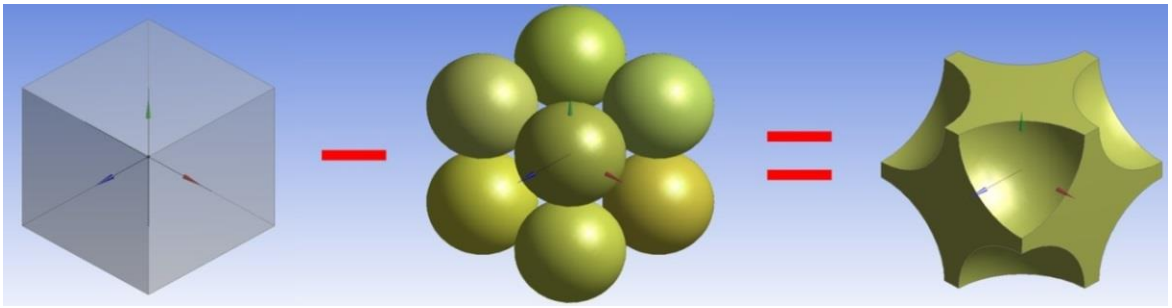

Figure 2-15 First Boolean operation for Kelvin's cell creation (Krishnan *et al.* 2006)

Later, another six spheres are subtracted from the resultant structure. These spheres are located on the planar faces of the remaining body. The distance between the centre of these spheres and the centre of the solid body, as well as the radius of all fourteen spheres are in direct relationship with the desired porosity (Dukhan and Suleiman 2013). The overlapping section will create small spherical caps that will be withdrawn. This geometry modelling is shown in Figure 2-16. This construction is similar to a FCC crystalline structure arrangement.

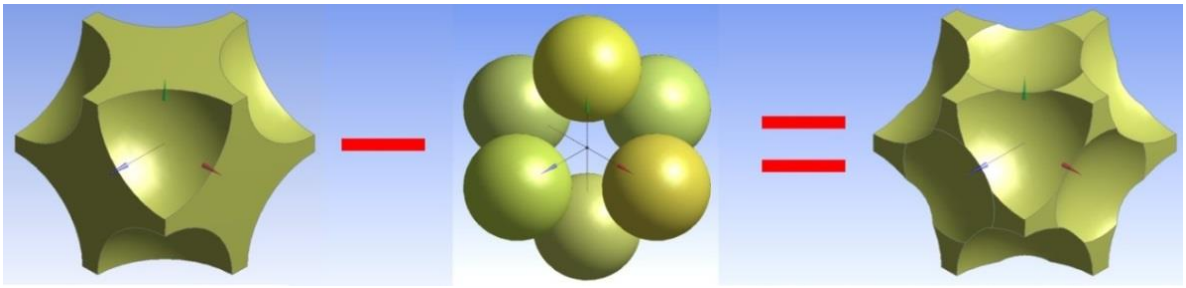

Figure 2-16 Second Boolean operation for Kelvin's cell creation (Dukhan and Suleiman 2013)

The last step is to create a hollow body from the remaining structure. This is easily achieved by subtracting a single sphere which is located in the centre of the structure. It is important to note that this last sphere will have the same radius as the previous ones. The resultant structure has shown to have minimum volume ratio compared to other structures (Krishnan *et al.* 2006).

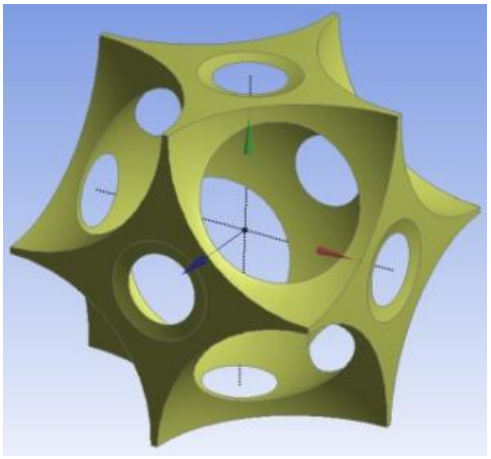

Figure 2-17 Hollow tetrakaidecahedron with a porosity of 92.8% (Dukhan and Suleiman 2013)

Figure 2-17 is the resultant structure, showing a porosity close to 93%. The porosity is determined by considering the original cube as the total space and the remaining structure as the solid matrix. The volume of the remaining structure accounts for overlapping spheres and spherical cap reductions. The porosity can be calculated using the following expression (Dukhan and Suleiman 2013):

$$\varepsilon = \frac{1}{{a_c}^3}\left[\frac{8}{3}\pi R^3 - 2\pi\left(R - \frac{a_c}{2}\right)^2(2R) - \frac{16}{3}\pi\left(R - \frac{a_c\sqrt{3}}{4}\right)^2\left(2R + \frac{a_c\sqrt{3}}{4}\right)\right] \tag{2.58}$$

where a is the centre to centre distance between the central sphere and the polar sphere and R is the radius of any sphere. This technique is suitable for high porosity porous metals.

Xu and Jiang (2008) numerically analysed fluid flow and heat transfer in low porosity porous metals. They used the Simple Cubic (SC) crystal structure as a base model and air as a working fluid. Instead of using the particles as pores, they used the remaining body as the porous structure. With this they achieved porosities closed to 40%. Their results showed that the friction factor calculated for the non-slip flow regime agreed well with the correlation for normal scale porous media.

The use of X-ray computer tomography to characterize foam structures is a common practice (Lefebvre *et al.* 2008). Jaganathan *et al.* (2008) presented a CFD analysis using 3D images from a real fibrous medium to analyse its permeability. They compared their model with an analytical technique. Their results were consistent and in good agreement with previous findings. Scanned 3D geometries seem like the proper approach to tackle the porous media problem by providing a structure close enough to the real material. Nevertheless, this kind of scan generates geometries that require a large amount of computational resources for meshing and simulation processes.

2.7 Current research on heat transfer and fluid flow in porous metals

2.7.1 Fluid flow

Fluid flow in porous media has been analysed experimentally and numerically. Permeability and form drag coefficient are the principal properties measured during these studies. Both parameters describe the resistance for a fluid when flowing through a porous medium. For instance, Papathanasiou *et al.* (2001) investigated numerically the form drag coefficient of fibrous porous media. They employed a 2D model composed of circular struts arranged in a square or hexagonal pattern. They used a low to middle range porosity (30% to 60%) for the geometrical models in their study. The results showed that Ergun's equation is suitable for high porosity structures and Reynolds number below 1. Their model for predicting the form drag coefficient at higher Reynolds number, i.e. $\mathrm{Re} > 1$, fitted better when employing a modified form of the Forchheimer equation than when using Ergun's equation as shown in Figure 2-18.

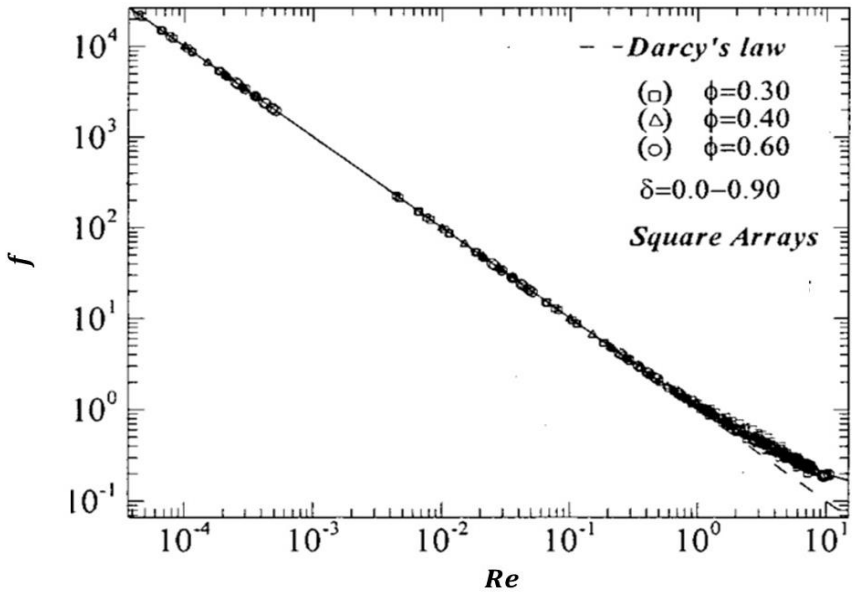

Figure 2-18 Comparison between the numerical results of friction factor considering a porosity of 30%, 40% and 60% and the predictions from the Forchheimer equation over a Reynolds number ranging from 0 to 160 (Papathanasiou *et al.* 2001)

Duggirala *et al.* (2008) numerically analysed pressure drop in fibrous materials with porosity ranging from 40% to 50%. A BCC based model was used and the fibrous materials were included as straight cylinders as shown in Figure 2-19. It was found that the difference in the predicted pressure drop decreased with the number of iterations when compared to experimental data. It was reported that results with residuals below six orders of magnitude will incur in a difference of 30 to 10% for pressure gradient for middle range porosities (47%). It was also found that the difference of pressure drop decreased with flow velocity, and the highest difference for predicted pressure drop occurred at flow velocities closer to 0. Yet, the difference in pressure drop obtained with empirical correlations was between 2% and 20%. For lower porosities (41%), the difference was about 5% to 10% and 2% to 20% for the numerical and empirical approaches respectively.

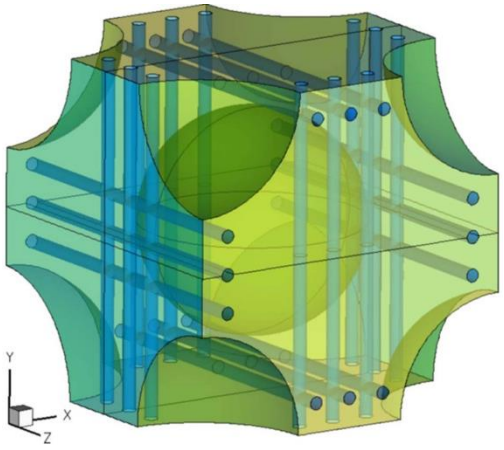

Figure 2-19 Isometric view of the BCC based model employed for pressure drop predictions in micro fibrous materials (Duggirala *et al.*, 2008)

Xu and Jiang (2008) calculated the form drag coefficient in idealized microporous media with the porosity ranging from 34% to 44 % using a numerical approach. They employed air and water as working fluids and used a modified version of Ergun's equation for high Reynolds number ($Re \leq 2000$) flows. Their results fitted well with analytical values.

Porous metals have also been analysed by experimental and numerical means. Boomsma and Poulikakos (2002) studied the effects of pore size and compression on the fluid flow characteristics of water within open-cell aluminium foams. It was reported that post compression samples had steady values for permeability and form drag coefficient when increasing the velocity. It was also mentioned that the permeability of uncompressed samples was sensitive to pore diameter. Decreasing the pore diameter led to higher flow resistance. A transition value of $Re = 26.5$ between flow regimes was reported. Boomsma *et al.* (2003) later provided a numerical analysis of high porosity open-cell foams. The geometric model was based on 8 unit cells joined together, with each unit cell representing a tetrakaidecahedron. A schematic of the final structure can be seen in Figure 2-20. They confirmed that increasing the specific surface area of the sample by increasing pore size will increase the flow resistance, therefore decreasing the permeability.

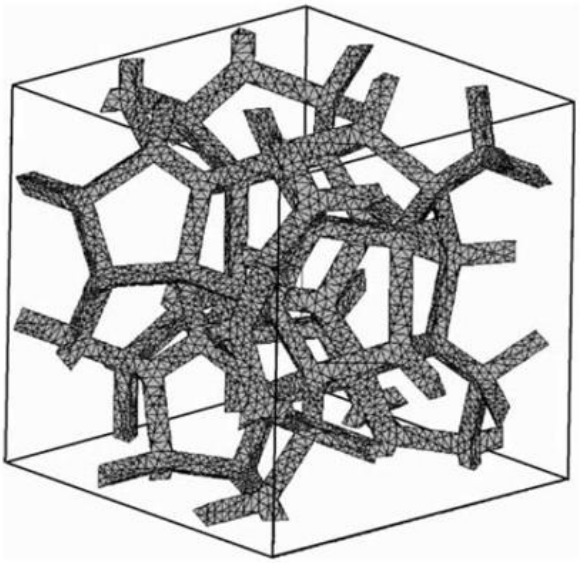

Figure 2-20 Foam structure used in Boomsma's study (Boomsma *et al.* 2003)

Despois and Mortensen (2005) calculated permeability for open-cell foams made of aluminium with porosity between 60% to 90% and pore size between 75 μm and 400 μm. In their study they proposed a "bottleneck" model to calculate permeability by employing the radius of the connections between pores and the foam density. They then normalised the calculated permeability by dividing it by the squared of the pore size. This dimensionless normalised permeability was in the same range (10^{-2} to 10^{-4}) as the experimental data and the evolution model of permeability as presented in Figure 2-21. This model was also used by Krishnan *et al.* (2006) when numerically measuring permeability in open-cell metal foams with porosities of over 94%. Their results were in the same range as microcellular open-pore metal foams with flow rates in the Darcian regime.

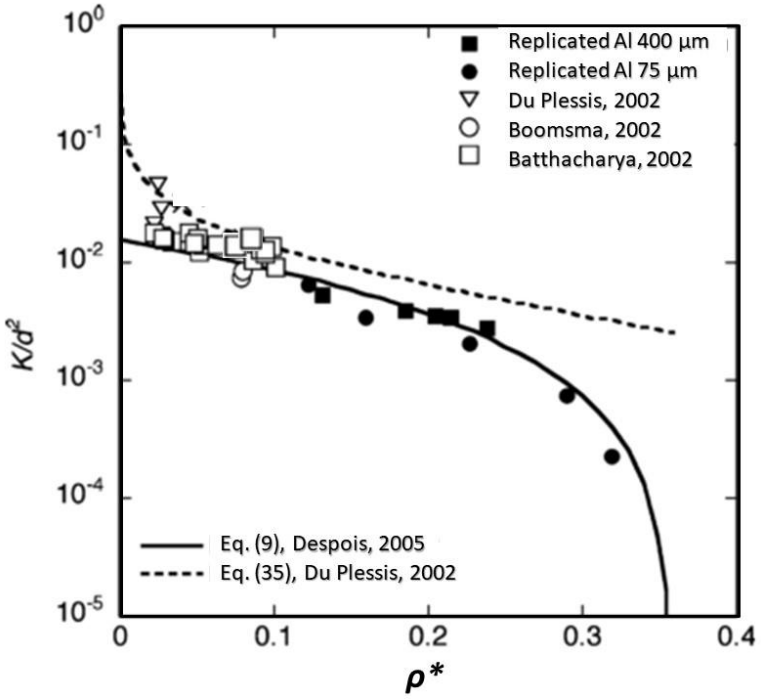

Figure 2-21 Normalised permeability by the pore size squared evolution versus foam density (Despois and Mortensen 2005)

Khayargoli *et al.* (2004) experimentally studied the effects of the microstructure of Nickel-Chrome metal foams (NCX) on permeability and form drag coefficient. In their study, pressure drop increased with increasing flow velocity and decreasing pore diameter. Permeability increased with porosity in a power law trend. The form drag coefficient decreased with increasing porosity in a power law relation. However, their study showed that permeability increased with increasing pore diameter. This is opposite from that previously reported by other researchers. This difference was explained by the different degrees of homogeneity of the microstructure of the metal foams.

Beugre *et al.* (2010) analysed incompressible flow in a Ni-Cr metal foams (RCM-NCX-1116) using the Lattice Boltzmann (LB) numerical approach. It was reported that pressure drop increased with velocity in a quadratic manner. It was also mentioned that the LB technique was a suitable method for the microscopic approach to numerically analyse porous metals, but, time consuming in comparison to other numerical techniques.

Chai *et al.* (2010) also studied fluid flow within a disordered porous media using the LB method. In their study they considered the existence of three different flow regimes depending on the Reynolds number, i.e. linear behaviour $(Re{\sim}0)$, a cubic behaviour corresponding to the transition regime $(Re \leq 1)$ and a quadratic behaviour corresponding to the Forchheimer regime $(Re > 1)$. They used a 2D distribution of random cylinders as shown in Figure 2-22. They found that the Carman–Konezy equation is inaccurate in predicting permeability of disordered porous media. They reported that the change in flow regime occurs over a range of Reynolds number from 3 to 9. The transition regime was found to be sufficiently small, and therefore can be neglected.

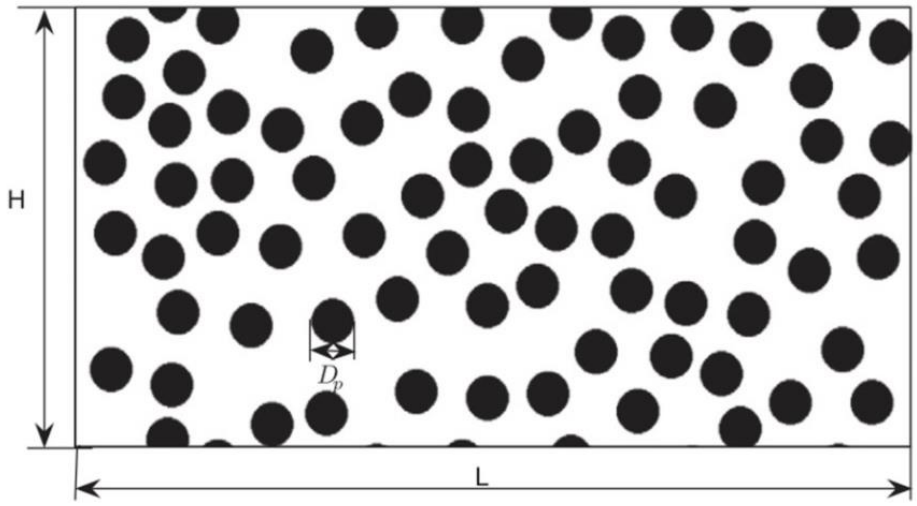

Figure 2-22 Disordered porous media (Chai *et al.*, 2010)

Bağcı *et al.* (2014) analysed the different regimes for low flow inside metal foams and experimentally measured pressure drop. It was reported that a single sample can exhibit different values of permeability and Forchheimer coefficient depending on the flow regime. A modified Reynolds number was employed accounting for the metal foam porosity and a transition value of $Re = 28$ was reported, which is different from other studies in the literature.

De Carvalho *et al.* (2015) investigated oil separation inside metal foams. In their study, the structure of open cell metal foam was created using 3D digital microcomputer tomography. It was reported that pressure drop was highly affected by the foam thickness. Pore scale modelling is demonstrated to be a valid tool to capture the flow field and model oil separation inside open cell metal foams.

Zhu (2013) experimentally studied LCS porous copper properties. It was reported that the lowest pressure drops for air were obtained with the samples with smaller pore sizes and higher porosities, as observed in Figure 2-23. It was also reported that permeability increased with porosity and copper particle size, but decreased with pore size. The samples with the smaller pore sizes gave the highest permeability values. The effect of extending the sintering time for the porous copper samples on permeability was small.

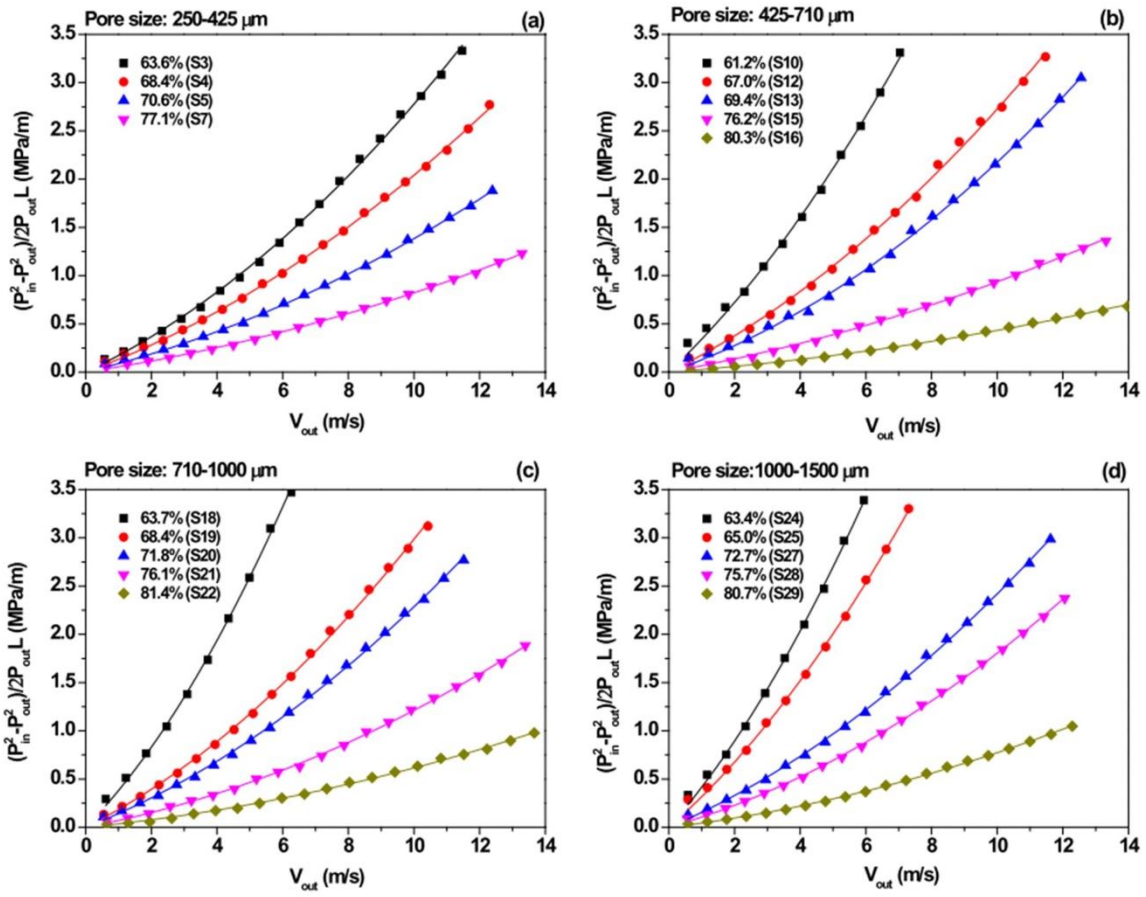

Figure 2-23 Variations of pressure drop versus outlet velocity for different pore sizes and porosities (shown in the figure) (Xiao, 2013)

2.7.2 Thermal control

Current electronic systems pose a serious challenge to thermal control, mainly due to the increase in density of microelectronic devices (Leong and Jin 2006). Porous metals have shown to be a promising type of material for thermal control applications. Compared to bulk metals, open-cell porous metals have shown to be ideally suited for use in compact heat exchangers (Diani *et al.*, 2014), due to their high surface area, low density and low thermal resistance. Forced convection in porous metals has many engineering applications, such as in heat exchangers for electronics, packed bed regenerations, and heat transfer enhancement (Hwang and Yang 2012). The heat transfer occurs between the high surface area of the open channels and the cooling fluid. By allowing fluids to flow through the

porous metals, excess heat can be dissipated (Clyne *et al.*, 2006). Generally, a liquid coolant is preferred over air for this type of applications due to better thermal conductivity (Boomsma *et al.* 2003). However, it is important to bear in mind that the heat transfer performance of porous metals is influenced significantly by their structure and the metal used. Thus, many recent studies have emerged on the properties of porous metals for thermal applications (Mahjoob and Vafai 2008).

Ejlali *et al.* (2009) numerically analysed two different samples of high porosity metal foam. They compared their potential use, as extended surfaces instead of fins, in heat removal from geothermal power plants and showed that the porous metals work better as heat exchangers than fins, and at no excess cost.

Teruel and Díaz (2013) numerically calculated the interfacial heat transfer coefficient in porous metals employing a 2D arrangement of squares as a representative elementary volume (REV). It was reported that the difference between the numerical method and the experimental data was about 20% for lower porosities (55%). For larger porosities, i.e. 75% and 91%, the difference was about 5%. Special attention was recommended when employing 2D REV, as the heat transfer coefficient varies with the position at which it is being measured, as exemplified in Figure 2-24.

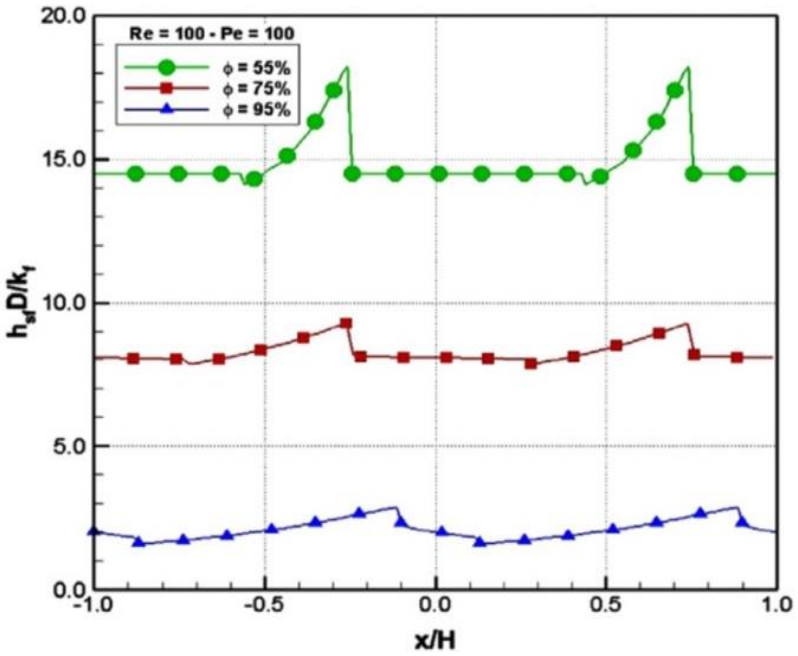

Figure 2-24 Modified heat transfer coefficient as a function of its position within REV for samples with different porosities (shown in the picture) (Teruel and Díaz 2013)

Experimental tests have been used primarily to analyse the heat transfer performance of porous metals. For example, Phanikumar and Mahajan (2002) provided an experimental analysis of high porosity metal foams with different pore sizes (measured in pores per inch, PPI). Examples of the aluminium specimens used in their study are shown in Figure 2-25. Nickel was also used in their study. Local thermal equilibrium was found to be justified for air when the flow velocity is relatively low and for water regardless of flow velocity, due to the higher thermal conductivity of water. In order to identify the thermal performance of the different materials, a dimensionless enhancement factor was defined as the ratio of the Nusslet number of the material and the Nusslet number of an empty channel. Using the enhancement factor, Aluminium samples provided the best heat transfer enhancement. The enhancement factor was up to 16 for aluminium-water combinations and 4 times for aluminium-air. The nickel-water enhancement factor was reported as 9.5. It was stated that the enhancement of the thermal conductivity of a system can be achieved when the thermal conductivity of the solid is higher than the thermal conductivity of the fluid.

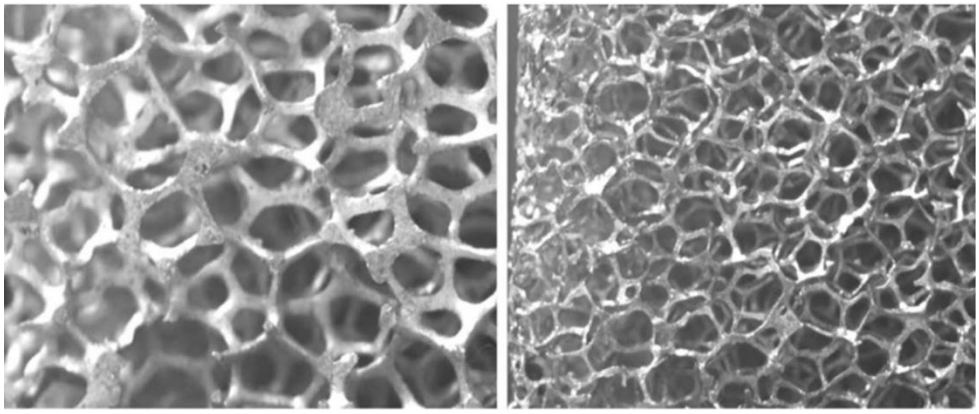

Figure 2-25 Metal foam samples with pores of 5 PPI (left) and 40 PPI (right)
(Phanikumar and Mahajan 2002)

Bhattacharya *et al.* (2002) measured the effective thermal conductivity, permeability and form drag coefficient of high porosity metal foams. Aluminium and reticulated vitreous carbon (RVC) were selected as the foams and their porosity was over 90%. It was reported that heat transfer enhancement exists only when the thermal conductivity of the metal foam or carbon foam is higher than the thermal conductivity of the fluid alone. While analysing the enhancement of heat transfer among different combinations, aluminium foam and water exhibited the highest thermal conductivity, while the combinations of RVC with air or water provided no enhancement at all. The resulting values of effective thermal conductivity can be seen in Table 2-6.

Table 2-6 Effective thermal conductivity of foam-fluid systems (Bhattacharya *et al.* 2002)

PPI	Porosity	Al - air	Al - water	RVC - air	RVC - water
		($^{W}/_{m\,K}$)	($^{W}/_{m\,K}$)	($^{W}/_{m\,K}$)	($^{W}/_{m\,K}$)
5	0.971	2.7	3.7		
5	0.9664			0.164	0.73
5	0.946	4.6	5.4		
5	0.905	6.7	7.65		
10	0.9724			0.15	0.722
10	0.949	3.9	4.8		
10	0.909	6.7	7.6		
20	0.978	2.2	3.05		
20	0.9615			0.17	0.743
20	0.949	4	4.95		
20	0.906	6.9	7.65		
40	0.972	2.5	3.3		
40	0.9681			0.16	0.727
40	0.952	3.9	4.75		
40	0.937	4.5	5.35		

Lu *et al.* (1998) investigated the uses of metal foams as compact heat exchangers. In their paper they presented an analytical model based on the cross-flow of cylinder banks. Even though the model oversimplifies the real structure of the porous metals, their results showed good agreement with data available for open-cell metal foams. Ejlali *et al.* (2009) investigated the heat transfer and fluid flow properties of a metal foam heat exchanger cooled by high speed air. It was reported that metal foam heat exchangers had a superior Nusselt number (between 2 to 3 times greater) compared to conventional finned surfaces under similar circumstances (material weight and pressure drop).

Dukhan and Chen (2007) studied the heat transfer performance of blocks made of aluminium foam, with air as coolant. They found that the temperature decreases exponentially with increasing distance from the heat source whereas the temperature increases with lower porosity, due to the increase in conduction through the solid materials and not letting the air flow properly. Mancin *et al.* (2010) also studied aluminium foams and

forced convection with air. They experimentally measured the heat transfer coefficient at high porosities. Different pore densities where analysed. It was reported that at high porosities, i.e. 90% to 96%, the heat transfer coefficient increases slightly with decreasing porosity. For example, decreasing the porosity from 96% to 90% increased the local heat transfer coefficient around 1.3 to 1.7 times. Zaragoza and Goodall (2013) also analysed the potential of aluminium foams as heat exchangers subjected to forced convection. Aluminium has shown to be a good option due to its high thermal conductivity.

There are other porous metals with as good or even better thermal performance. A clear example is porous copper due to its high thermal conductivity, internal surface area and permeability for fluids (Zhang *et al.*, 2009). Mancin *et al.* (2012) analysed heat transfer and pressure drop by forced convection in high porosity copper foams. It was observed that the heat transfer coefficient does not depend on the imposed heat flux but rather on the flow rate. Chiba *et al.* (2004) calculated the heat transfer coefficient for lotus-type porous copper samples, and found that it was 4 times greater than conventional grooved fins and 1.3 greater than conventional micro-channel heat sinks.

LCS porous copper has gained a lot of attention because of its high heat transfer coefficient. Experimental research for this material has been carried out in the University of Liverpool. For instance, Thewsey and Zhao (2008) measured the effective thermal conductivity of LCS porous copper. In their study, 10 porous copper samples were used, with porosity ranging between 64% and 85%, and with three pore size ranges, i.e. 425 μm to 710 μm, 710 μm to 1000 μm, and 1000 μm to 1500 μm. It was found that the thermal conductivity of porous copper increased with relative density whereas pore size has no effect. The relation between thermal conductivity and relative density follows a power law with the exponential term between 2.05 and 2.96. Xiao (2013) studied the fluid flow and heat transfer performance of different porous metal specimens. The results showed that permeability increased with porosity and metal particle size, whereas it decreased with pore size. Thermal conductivity decreased with metal particle size, but increased with pore density and pore size.

Zhang *et al.* (2009) studied the heat transfer performance of LCS porous copper, with porosity ranging from 57% to 82% and pore size ranging from 150 μm to 1500 μm. In their study, the LCS porous copper samples were placed into a purpose built chamber with a heated plate that was located underneath the samples. Water was pumped into the chamber at different flow rates (0.3 l/min to 2.0 l/min) and an input heat flux of 1.3 MW/m^2 was used. It was reported that the porous copper samples enhanced the heat transfer performance by 2 to 3 times compared to an empty channel. The heat transfer coefficient increased with flow rate and porosity showed significant effects as shown in Figure 2-26. An optimum porosity of 62% was reported to give peak enhancement to the heat transfer coefficient. Pore size was reported to have fewer effects on the heat transfer performance.

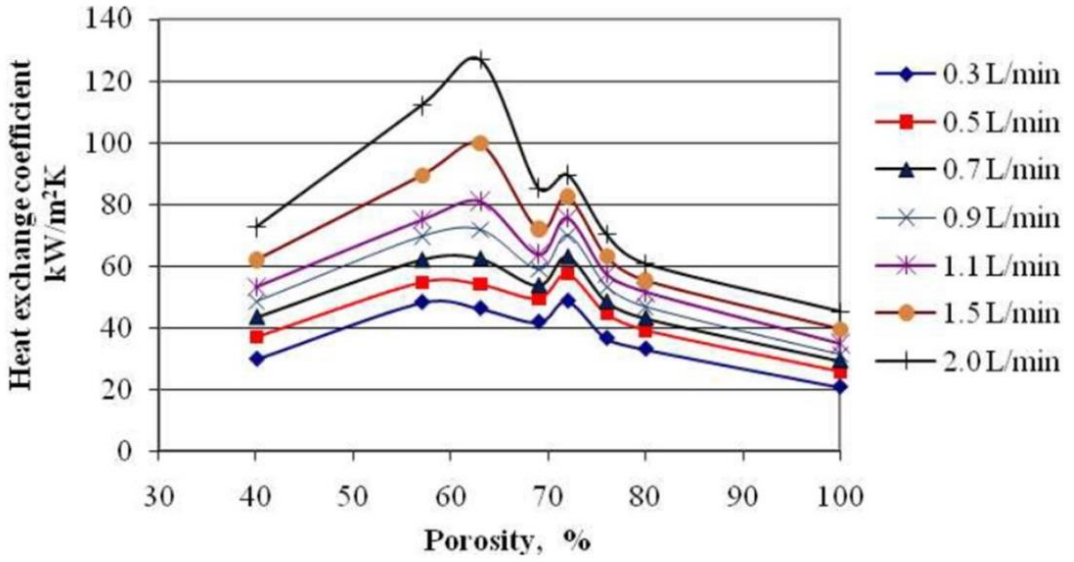

Figure 2-26 Heat transfer coefficient versus porosity of LCS porous copper samples at different flow rates with pore size of 425 to 710 μm and input heat flux of 1.3 MW/m^2
(Zhang *et al.*, 2009)

Zhu and Zhao (2013) studied the heat transfer properties of LCS porous copper with homogenous and hybrid structures in active cooling. Porosity and pore size were in the same ranges as in Thewsey and Zhao's (2008) analysis. A purpose built chamber was employed in their studies. The porous copper samples were put into the chamber while heated underneath. Water was pumped into the chamber to remove the heat from the

samples. Their results showed that the heat transfer coefficient for this material is 5-8 times better compared to an empty channel cooling system. It was also reported, that the heat transfer coefficient decreased linearly with increasing porosity. A different behaviour was observed with increasing flow rate, as the heat transfer coefficient increased in a parabolic manner.

Baloyo (2016) explored the behaviour of non-homogeneous LCS porous copper structures. The structures were made of two layers of LCS porous copper with different porosities. The resulting heat transfer coefficients for two different flow rates are shown in Figure 2-27. An optimum heat transfer was found at 60% porosity for homogenous structures. For bilayer structures the heat transfer coefficient increased almost every time the higher porosity was placed facing the flow. The 80%-40% bilayer structure displayed the best heat transfer performance overall.

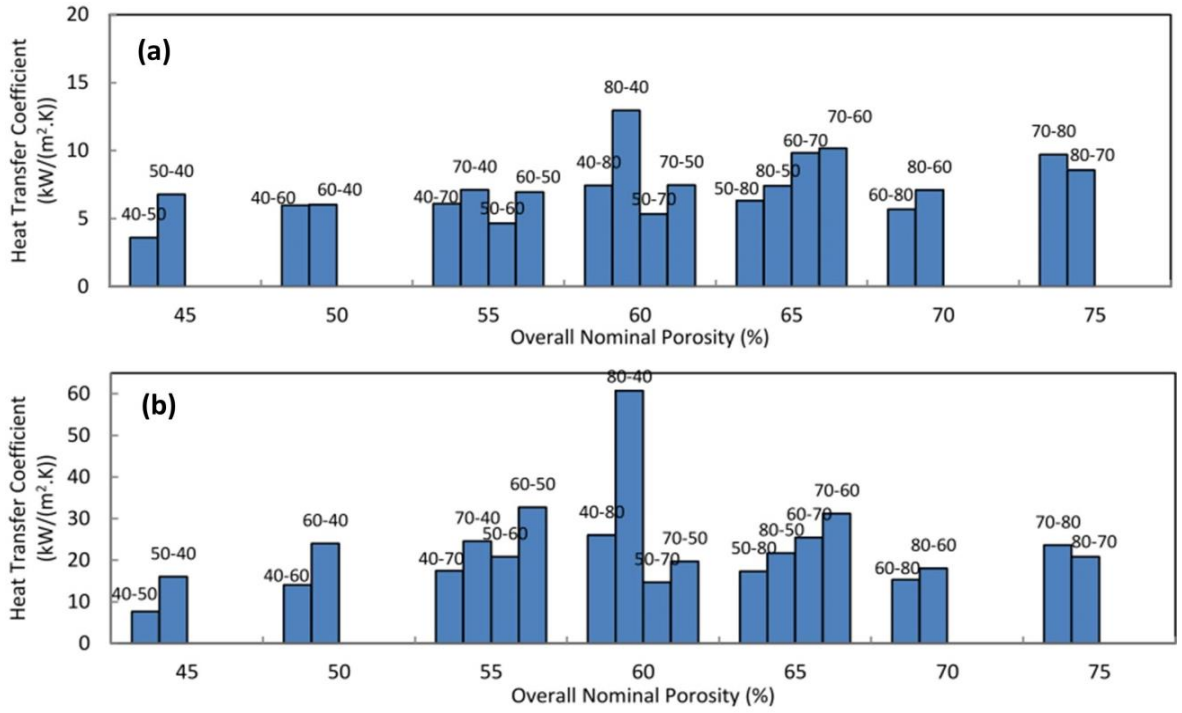

Figure 2-27 Heat transfer coefficient variations for LCS porous copper bilayer structures (layer porosity is indicated at the top of the bars with the first number corresponds to the layer facing the water flow rate) with different porosities (averaged from the layers, indicated in the axis) and flow rates of (a) 0.28 l/min and (b) 1.12 l/min (Baloyo, 2016)

2.8 Summary

Porous metals are a novel and complex types of structures made using innovative techniques and different types of materials. Most of the research conducted on these types of materials is focussed on their manufacturing techniques and their characterisation. Properties like Young's modulus, sound absorption, thermal conductivity, heat transfer coefficient or permeability are the emphases of the research made on porous metals.

Heat disipation is among the many applications with major interest for porous metals. LCS porous copper has been shown to be an excellent material for thermal control. However, most of the information obtained for this material for active cooling is mainly from experimentation and LCS porous copper creates structures with a middle range of porosities, i.e., between 40% and 80%. In addition, the number of connections between the pores is not as high as in other open-cell metal foams. Considerations on the inertial effects of fluid flow on permeability and heat transfer performance of LCS porous copper have become a challenging task. Numerical simulation has become a more suitable approach.

In this study, a numerical approach is proposed to understand how this kind of material works and finally to optimise its capabilities in active cooling. A representative volume element (RVE) approach is adopted to study the inner structure of the porous metal with different structural parameters, such as pore size, porosity and metal particle size.

3 Numerical modelling of fluid flow in 2D structures

The numerical model presented in this chapter is intended to study the effects of porosity and pore shape on pressure drop in open-cell porous metals. The numerical modelling is carried out on two dimensional (2D) geometric models. ANSYS workbench and Fluent in its version 14.5.7 were used to create the geometries, construct the meshing and run the simulations. The permeability and form drag coefficient were calculated.

3.1 Geometry creation

In this study, the geometries were created using ANSYS Workbench-design modeller. Different geometry models were tested in the process of this research. However, only two sets of models are reported in the present study: patterned 2D structures and a random 2D structure.

3.1.1 Patterned 2D porous structures

For the patterned 2D structures, the geometry was constructed by arranging solid geometrical shapes in a pattern, as illustrated in Figure 3-1. In this setup, the struts will act as the matrix of the porous metal while the open space, represented by the grey zone acts as the interconnected pores, where the fluid is in motion.

Two arrangements for the struts: aligned and staggered, also known as squared and hexagonal arrays, respectively, were reported in the literature (Papathanasiou *et al.* 2001). The aligned struts resemble a structure with directional pores and the staggered pattern is similar to an open-cell structure with a more tortuous path for the fluid.

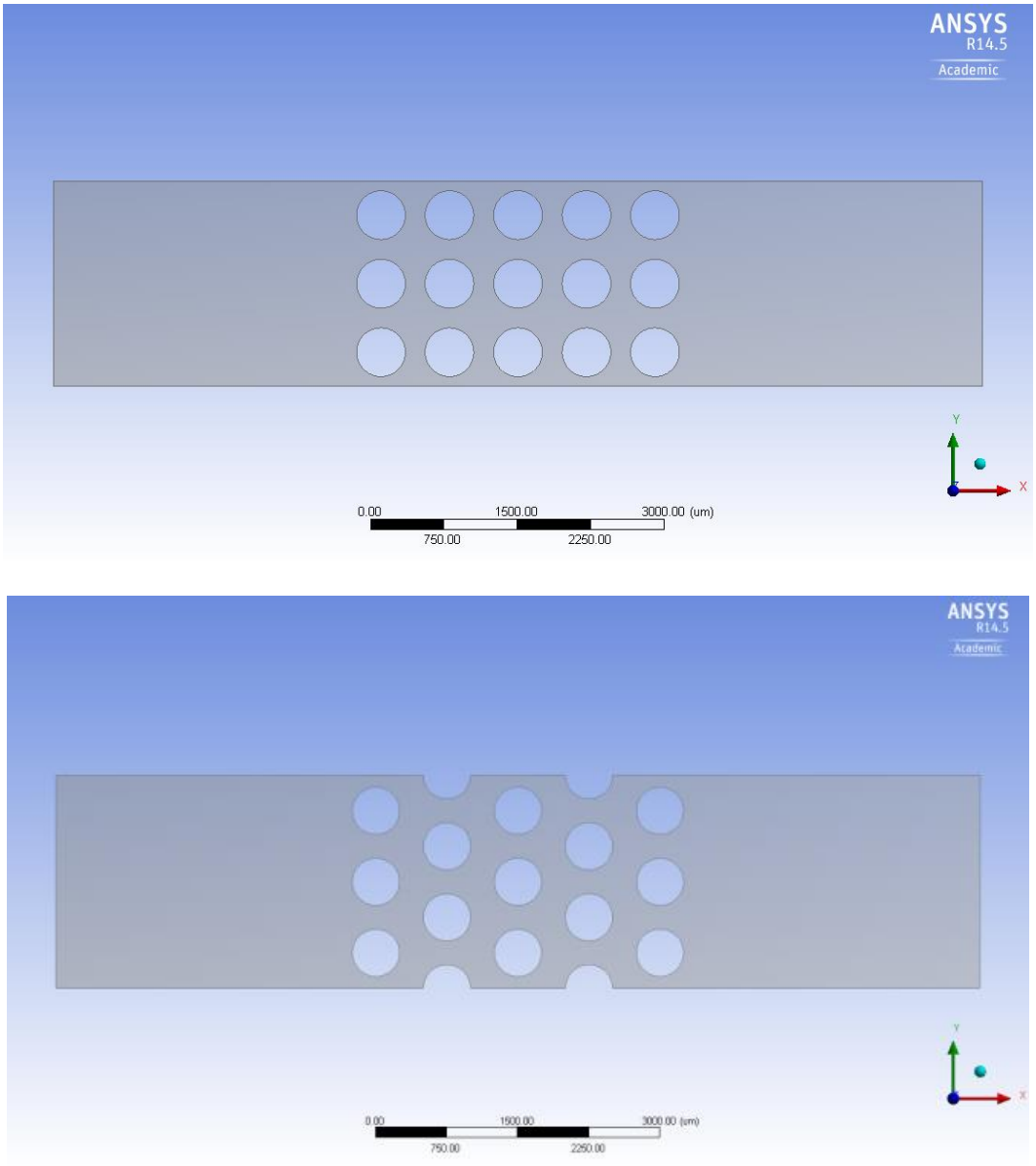

Figure 3-1 Geometrical model in 2D with circular aligned struts (top) and staggered struts (bottom)

An example of the implementation of these arrangements was given by Papathanasiou *et al.* (2001) in their study of fibrous porous media. Porosity and pore size were related to the strut size and strut spacing. In their model they implemented both arrangements but only considered circular struts. Kundu *et al.* (2014) on the other hand, utilized staggered squared struts in order to study turbulence through an isotropic porous media. Yet, the reason for the strut shape selection was not explained in the literature. In this study, both the aligned and

staggered arrangements with different strut shapes will be used to analyse the pressure drop in open-cell porous metals.

3.1.1.1 Strut shapes

Pores inside LCS porous metals have irregular shapes (Figure 3-2) due to the filler material particles and the sintering process. Some of the pores have rounded shapes while others are close to rounded polygons with a number of sides.

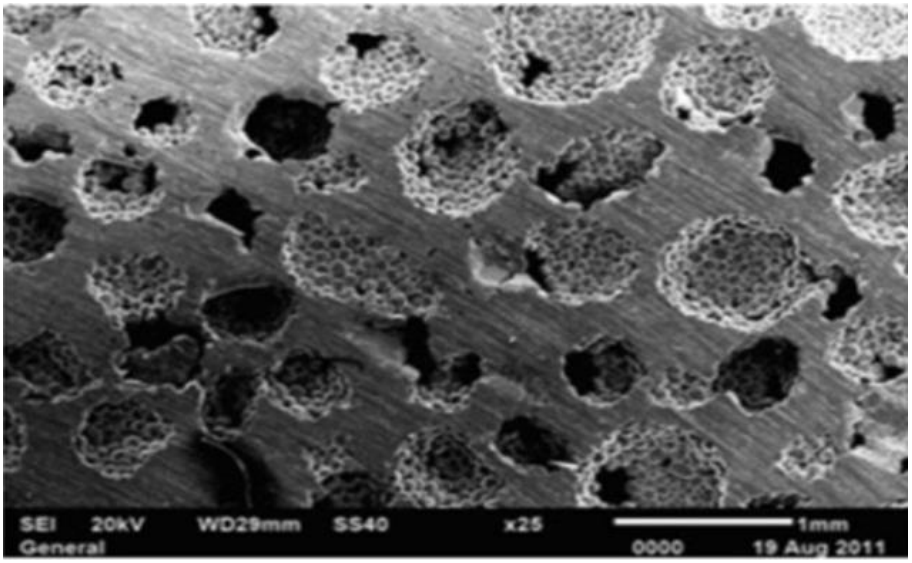

Figure 3-2 Microscopic photograph showing irregular shapes of pores at pore level in LCS porous copper (Xiao and Zhao 2013)

Therefore it is necessary to analyse different strut shapes to simulate open-cell porous metals with different pore features. The geometrical shapes used in this study for the struts are circles, triangles, squares, rotated squares and hexagons, as shown in Figure 3-3.

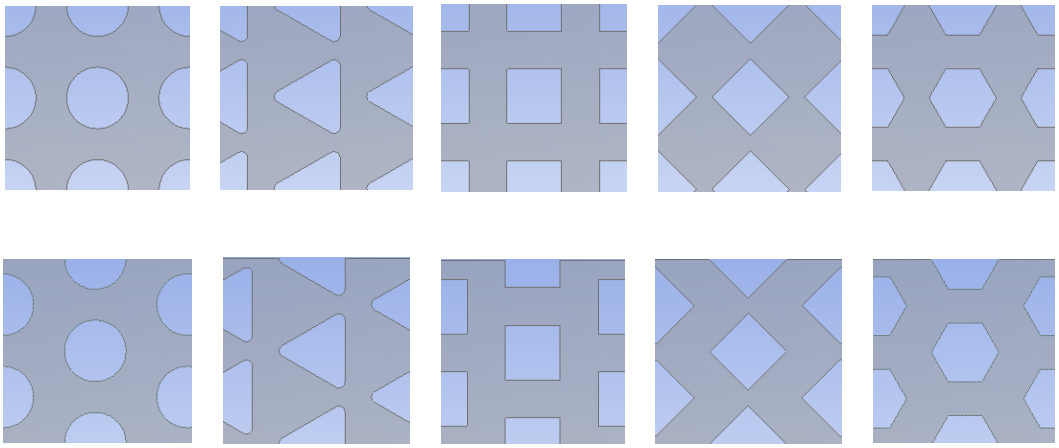

Figure 3-3 Aligned (top) and staggered (bottom) 2D patterned structures used in the numerical analysis, from left to right: circles, triangles, squares, rotated squares and hexagons

3.1.1.2 Representative elementary volume

A representative elementary volume (REV) is defined as the smallest volume or region over which a measurement of certain property can be made and can be considered as representative of the whole (Hill, 1963). Particularly for porous media it is important to understand the property of interest to study (Costanza-Robinson *et al.* 2011). In this case, porosity is the main feature that is going to be considered during the 2D simulations. In order to achieve porosity, the REV must contain an equal number of struts regardless of strut shape or orientation. In the literature it has been well stablished to use 2 sets of arrangements when modelling porous media in 2D due to the low computer resources needed and the acceptable data obtained: aligned struts and staggered struts (Faiz, 2014). For this study, the REV for the aligned and staggered struts is shown in Figure 3-4.

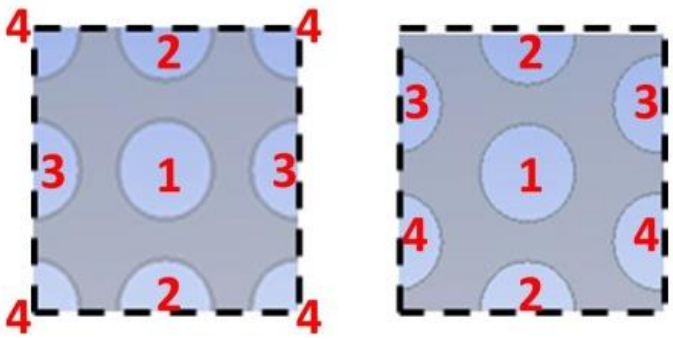

Figure 3-4 REVs of aligned (left) and staggered (right) struts

The porosity of the 2D structure can be calculated from the REV using the following expression:

$$\varepsilon = \frac{A_v}{A_T} = \frac{A_T - A_S n_S}{A_T} \tag{3.1}$$

where ε is porosity, A_v and A_T are the void and total areas respectively, A_S is the area of a strut and $\mathrm{n_S}$ is the number of struts in the REV (4 in both cases).

Given that the REV is a square as shown in Figure 3-4, the side length of the REV, x_b, is related to the strut area and porosity, ε, by:

$$x_b = \sqrt{A_T} = \sqrt{\left(\frac{4A_s}{1-\varepsilon}\right)} \tag{3.2}$$

For circular struts, $A_s = \frac{\pi}{4} d^2$, where d is the diameter of the circle. This yields a simpler equation relating REV side length (x_b) to strut diameter and porosity:

$$x_b = d\sqrt{\left(\frac{\pi}{1-\varepsilon}\right)} \tag{3.3}$$

Equation 3.3 is employed in order to determine the side length of the 2D REVs.

In the present analysis, 4 different strut shapes were employed: circular, triangular, squared, and hexagonal. In order to compare these shapes, their areas are kept as constant, equivalent to the area of a circle with a diameter of 500 μm. There is therefore a relationship between the circular strut diameter and the apothem of the polygonal struts as:

$$\frac{\pi}{4}d^2 = {a_n}^2 n\, tan\left(\frac{\pi}{n_a}\right) \tag{3.4}$$

where d is the diameter of the circle, a_n and n_a are the apothem and number of sides respectively of a given polygon. The apothem (a_n) of the polygon of same area as a circle of diameter d is achieved by:

$$a_n = \frac{d}{2}\sqrt{\left(\frac{\pi}{n_a\, tan\left(\frac{\pi}{n_a}\right)}\right)} \tag{3.5}$$

Table 3-1 lists the values for the apothem and side length for the polygons used (triangle, square, and hexagon) equivalent to a circular strut with a fixed $500\ \mu m$ diameter.

Table 3-1 Apothems and side lengths of polygons for an equivalent diameter of 500 μm

Sides	Apothem $(\boldsymbol{\mu m})$	Side length $(\boldsymbol{\mu m})$
3	194.39	626.66
4	221.56	443.12
6	238.08	274.91

In the present analysis, two different orientations of the squared struts were considered. The first has one side of the squared struts (aligned and staggered) perpendicular to the flow stream, designated as squared struts. The second has the squared struts rotated 45

degrees, i.e., one of the vertexes of the squares is now facing the flow stream. The second set was designated as rotated squares in this study. Ten different patterned structures, i.e., five aligned shapes and five staggered shapes were used for each analysis, as shown in Figure 3-3.

3.1.1.3 Strut spacing

Porosity is the main parameter to be considered in the geometry creation. Here, the target porosity will be achieved by changing the distance between the struts. Increasing the distance will increase the gap between the struts and therefore will increase the porosity. To achieve a low porosity, the spacing between the struts needs to be reduced. If the porosity is too low, strut overlapping can occur, depending on strut arrangement, and strut shape.

To avoid strut overlapping, the gap amongst the struts is considered. The gap is defined as the vertical distance of an opening between two struts. The opening considers the two closest points between the struts. The smallest gap amongst the struts is calculated by subtracting the apothem of the struts from the length of the spacing which in turn are calculated by employing Equation 3.3 and Equation 3.5. The gaps for the patterns with different strut shapes and porosities can be seen in Table 3-2. The negative values indicate strut overlapping and therefore a closed-cell structure. The gaps are different for the different strut shapes. For the same porosity, the patterns with the widest to the smallest gaps are: squares, hexagon, circle triangle and rotated squares. The minimum porosity to maintain open cell, i.e. a gap mayor than zero, for hexagon, circle triangle and rotated squares are: 15%, 25%, 50%, and 55% respectively. The regular square pattern has the widest gap among the other shapes. This strut shape showed to remain as an open-cell structure regardless of porosity.

The different gap values for different strut shapes showed that not all shapes are suitable for a wide range of porosities. However, for a middle range of porosities (50 to 80%), it is possible to use all the patterned structures to numerically calculate pressure drop.

Table 3-2 Gap (μm) values for all different strut shapes and porosities

Porosity (ε)	Circle	Triangle	Rot Square	Square	Hexagon
10%	-32.9	-133.1	-159.6	24	-9.1
15%	-19.4	-119.6	-146	37.5	4.5
20%	-4.6	-104.8	-131.2	52.3	19.3
25%	11.7	-88.5	-115	68.5	35.5
30%	29.6	-70.6	-97	86.5	53.5
35%	49.6	-50.6	-77	106.5	73.5
40%	72.1	-28.1	-54.6	128.9	95.9
45%	97.5	-2.7	-29.2	154.4	121.3
50%	126.7	26.5	0	183.5	150.5
55%	160.6	60.4	33.9	217.4	184.4
60%	200.6	100.4	74	257.5	224.5
65%	249	148.8	122.3	305.9	272.8
70%	309	208.8	182.4	365.9	332.9
75%	386.2	286	259.6	443.1	410.1
80%	490.8	390.7	364.2	547.7	514.7
85%	644.1	543.9	517.5	701	668
90%	901.2	801.1	774.6	958.1	925.1
95%	1481.7	1381.5	1355	1538.6	1505.5

The side length of the REV is the sum of two strut diameters (or side lengths) plus two gaps. Geometries with different porosities can be created by employing the values presented in Table 3-2. An example of how strut spacing increases with increasing porosity, when the area of the struts is fixed, can be appreciated in Figure 3-5.

Particular attention was made when creating the REVs with the triangular struts. Specifically the corners of the triangular struts were rounded in the geometry creation process. This is to reduce the high instability in the meshing process and later on the simulations, caused by

the sharp edges of the original structure. The change of the shapes was considered in the strut spacing calculations.

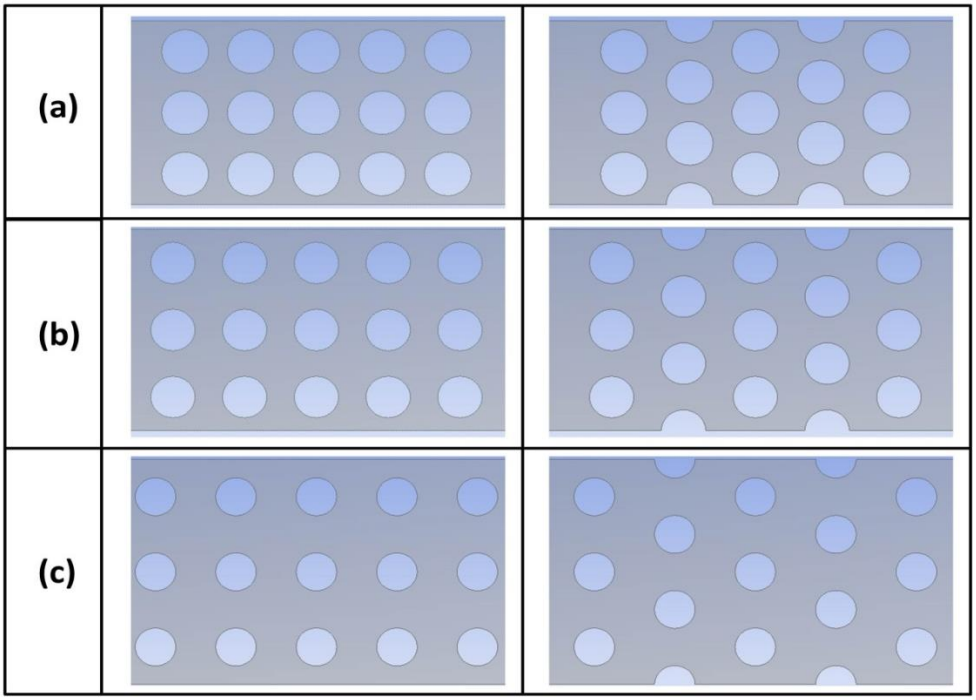

Figure 3-5 Aligned (left) and staggered (right) circular struts with different porosities: (a) 60%, (b) 70% and (c) 80%

3.1.2 Random 2D porous structure

A random 2D structure was created to simulate a porous medium. To create this structure, a program was coded using Visual Basic for Applications (VBA) and Excel. The geometry consists of circles distributed randomly in a confined domain. Porosity, strut size, length and height of the domain, are specified before starting the program. An example of the final structure is shown in Figure 3-6, where the green zone represents the fluid area.

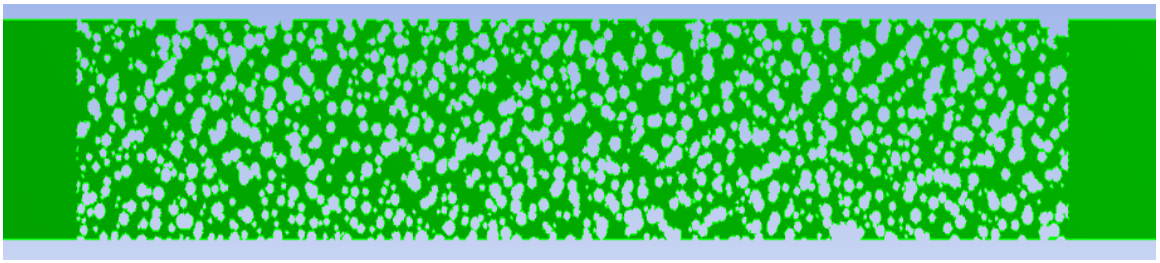

Figure 3-6 Random structure of a porous medium with a strut size ranging between 200 and 500 µm and porosity of 60%

The geometry creation process is divided into two parts. The first part uses a program coded in VBA (Appendix A) to create text files containing the strut locations and sizes. The second part creates the domain in ANSYS – Design – modeller and then employs the text files to create the struts within the domain.

For the first part, porosity, strut size range, the length and height of the domain are specified. For this study only 10 different strut sizes are used. The positions and sizes of the struts change with each iteration of the program that creates the struts.

The program made in VBA considers a domain with the specified length and height. Then it randomly selects a strut diameter from the strut size range and positions the strut inside the domain. The program stores the area of each strut added to the domain. The process continues until the specified porosity value is reached.

In positioning the struts, some of the struts might overlap. The program does not consider the total strut area for the final calculation of porosity. Instead, the program includes extra struts (20% or more) to address the overlapping issue. The positions of the resulting struts are stored in text files as shown in Figure 3-7 as an example. These text files are used by ANSYS to create the struts. The number of text files depends on the number of struts generated, because the 3D curve tool inside ANSYS - Design modeller can only read a maximum of 2000 coordinate lines. To avoid conflict with geometry creation, a maximum of

1000 lines was set for each text file. A new text file is generated when 1000 lines are reached.

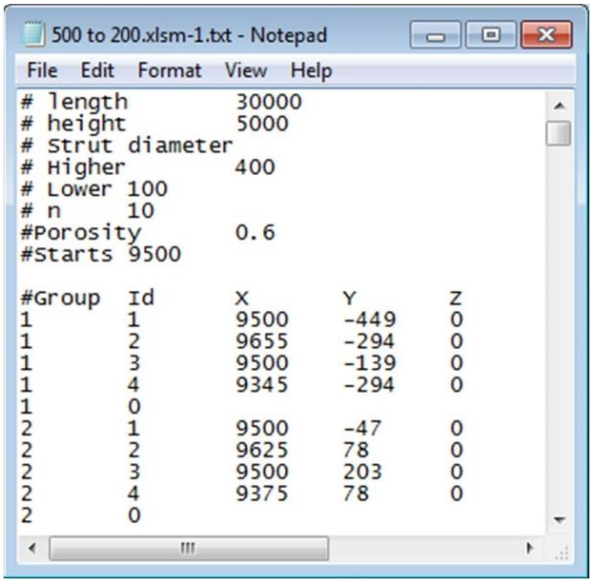

Figure 3-7 Example of the output text file obtained from the program coded to create random struts

The first text file includes all the specified values at the top. The information needed to create the struts is stored under 5 labels: Group, Id, X, Y and Z. The Group label indicates the strut. The Id label indicates the coordinate. In ANSYS, 5 code lines are needed to create a closed circular shape,. The first 4 (numerated from 1 to 4) correspond to the coordinates located on the perimeter of the circle and the last one, has a value of zero indicating a closed shape. The last 3 columns indicate the coordinates used to create the strut in the X, Y and Z axis. By specifiying the Z axis as cero, the curves generated are in the XY plane.

The 3D curve tool inside ANSYS - Design modeller is used to read the coordinate files to create line bodies inside a solid domain. The line bodies are transformed into solid shapes and are removed using the removal tool from the solid domain. The final structure as shown in Figure 3-6 was created.

3.2 Governing Equations and boundary conditions

Fluid flow in porous structures is described by the volume averaged Navier-Stokes Equations. The standard $\mathrm{k}-\varepsilon$ model was set for all the simulations, due to its robustness, computational time, efficiency and suitability for different engineering flow calculations. The fluid used in this study was water and the solid struts were set to be copper. The steady state condition was selected. The Navier-Stokes Equations, i.e. continuity and momentum Equations used in the present analysis are:

$$\nabla\langle\vec{v}\rangle = 0 \tag{2.34}$$

$$\rho\left(\frac{\partial\vec{v}}{\partial t} + (\vec{v}\cdot\nabla)\vec{v}\right) = -\nabla PI + \nabla\left[\mu\left(\nabla v_{i,j} + \left(\nabla v_{i,j}\right)^{T}\right)\right] \tag{2.48}$$

The boundaries of the computational domain can be seen in Figure 3-8. The upper and lower sides of the whole geometry were set as symmetric. The no-slip and no penetration boundary condition was used on the strut walls and enhanced wall treatment was also activated. For the random structure, all the random distributed struts were set as walls.

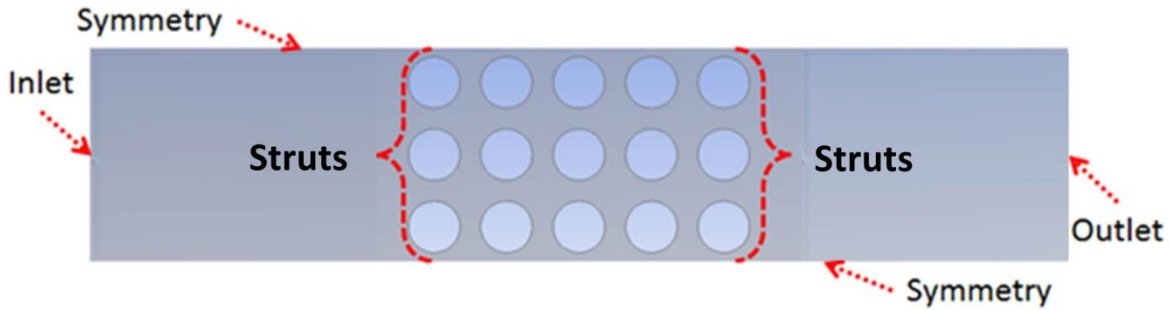

Figure 3-8 Boundary conditions used for the 2D analysis

3.3 Mesh generation and mesh quality

In this study, the governing equations were solved by discretizing the flow domain. This created a finite set of elements for which variables of interest were calculated. The elements have different shapes to adjust to the geometry. In the 2D analysis, there are three different types of elements: triangles, squares and quadrilaterals as shown in Figure 3-9. The domain containing these elements forms the mesh.

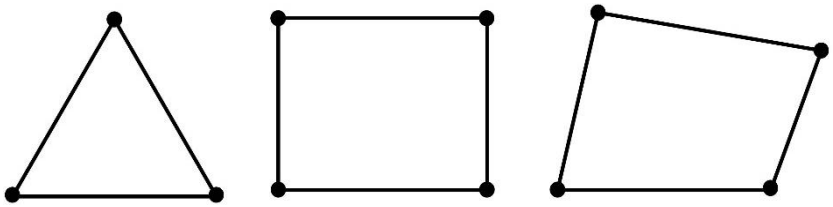

Figure 3-9 2D element forms, from left to right: 3-noded triangle, 4-noded square and 4-noded quadrilateral

To obtain accurate results, the flow behaviour and the quality of the mesh have to be taken into account in mesh generation. It is important to identify the regions where large gradients of pressure and temperature exist and to have a large number of elements in these regions. It is also essential to have a high quality mesh to improve the convergence time and reliability of the model. In ANSYS as well as in Fluent, there are different parameters that help to measure the quality of the mesh. The most common parameter to determine mesh quality is the orthogonal quality (Ω), which is a measure of how good an element is for further use by ANSYS and it is defined by (ANSYS, 2013):

$$\Omega = \frac{\vec{A}_i \cdot \vec{f}_i}{|\vec{A}_i||\vec{f}_i|} \tag{3.6}$$

and

$$\Omega = \frac{\vec{A}_i \cdot \vec{c}_i}{|\vec{A}_i||\vec{c}_i|} \tag{3.7}$$

where $\vec{A}_i$ is the area vector of a face i, $\vec{f}_i$ is a vector from the centroid of the element to the centroid of that face i and $\vec{c}_i$ is a vector from the centroid of the element to the centroid of the adjacent element that shares that face. The orthogonal quality is calculated using both Equation 3.6 and Equation 3.7and the lower value between them is the resulting orthogonal quality of the element analysed. The orthogonal quality is calculated for every single element of the mesh, ranging from 0 to 1. The closer it gets to 1 the better the element quality is. The overall orthogonal quality of the geometry is an average of the quality of all elements. For complex structures, it is not possible to obtain a high element quality over all the elements within the mesh; therefore the average orthogonal quality is considered. The mesh in the regions closer to the struts where sharp edges exist was refined using the process called smoothness. Two examples of the resulting meshes for the aligned and staggered patterns with circular struts can be appreciated in Figure 3-10.

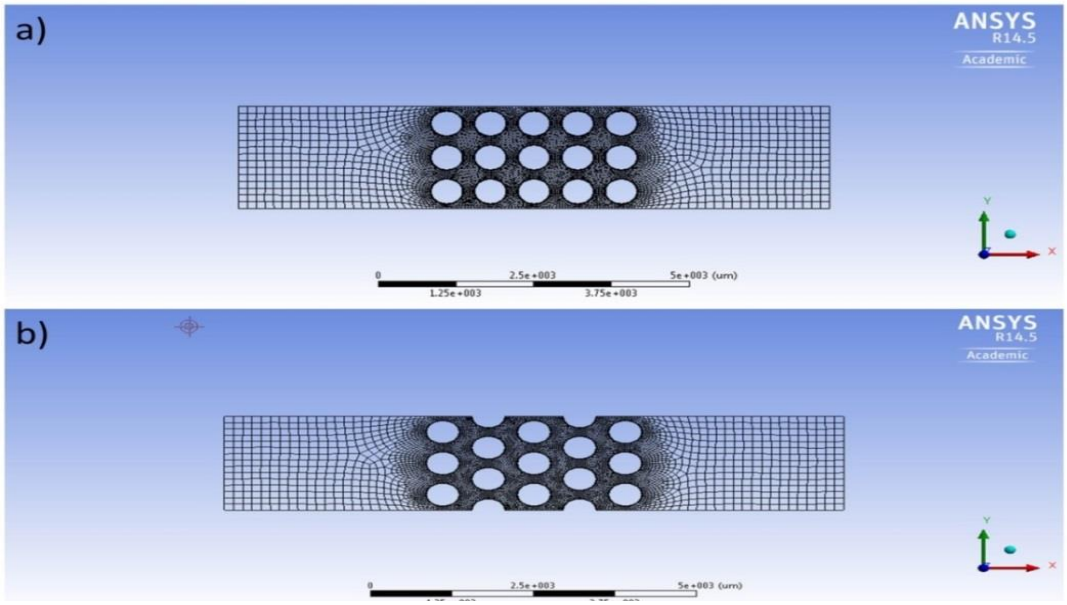

Figure 3-10 Mesh lattice for a 2D analysis, a) aligned, b) staggered circular struts, (to be continued)

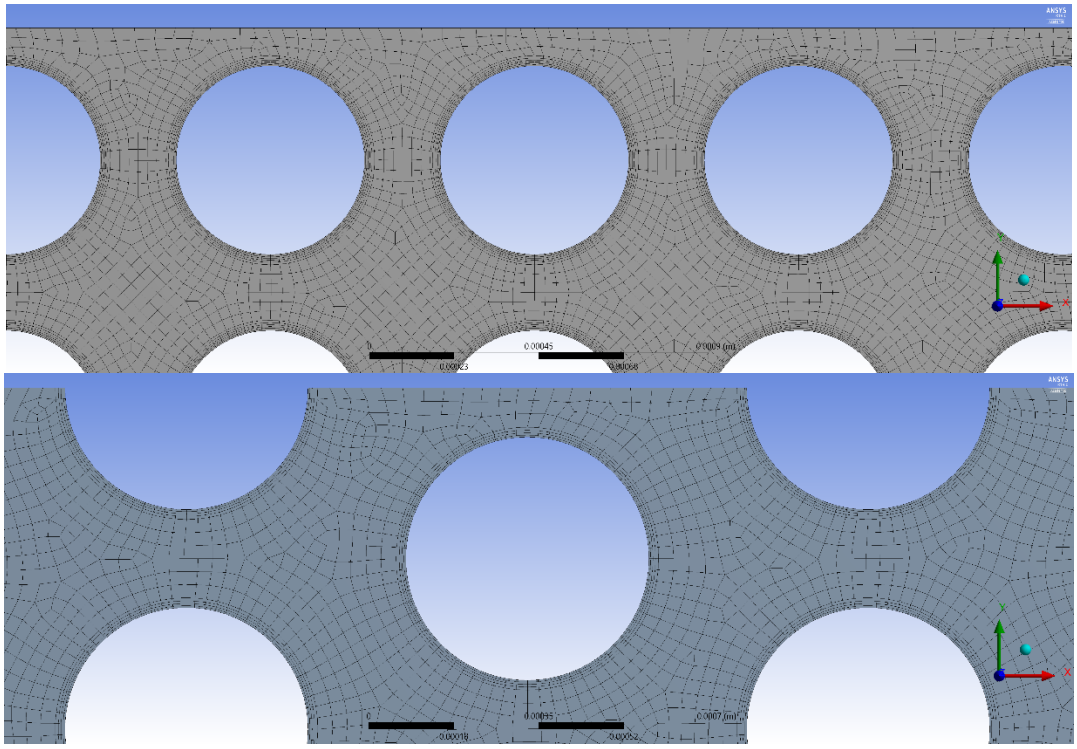

Figure 3-10 (Continuation) Zoom in Mesh lattice for a 2D analysis, aligned (top), and staggered circular struts (bottom)

In the smoothness process, more elements were created close to the walls, because pressure drop and heat transfer are more significant in these areas. For the patterned structures, the wall faces were divided into smaller elements using the edge sizing tool. It is important to select the appropriate number of divisions, because a large number of cells do not necessarily mean better results and an excessive number of elements will increase the computational time for each simulation. For the circular struts, a total of 72 divisions, i.e. 5 degrees apart, around each circle were used. For half circles, only 36 divisions were used. A similar process was used for the other strut shapes. The number of divisions remained as 72 along the strut perimeter, regardless of the total number of strut sides. The number of divisions was equally divided for each side in all geometrical shapes. For triangular struts, the number of divisions per strut side is 24. For squared struts, each side has 18 divisions while one side of the hexagonal struts has 12 divisions. Whit all these improvements, the

average orthogonal quality of the patterned structures is over 0.99 with poor elements above 0.5.

For the random structure a simpler approach was used due to the complexity of the domain. The default meshing tools were used, and the grid of the mesh was set with a medium value. The resultant mesh can be seen in Figure 3-11. The overall orthogonal quality for this mesh is close to 0.95, with poor elements above 0.4.The meshing process for the random structures was 3 times longer than the patterned structures.

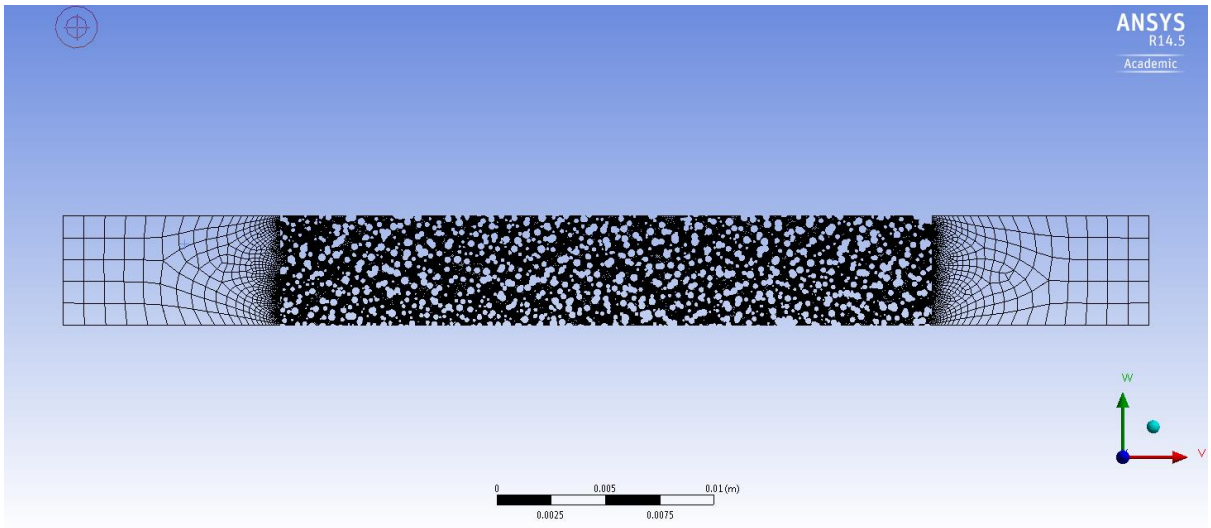

Figure 3-11 Mesh lattice for a 2D random structure with porosity of 60% and pore size ranging from 200-500μm

3.4 Simulations and convergence criteria

The most common convergence criterion requires that the scaled residuals (the difference between the new result and the previous calculation in each iteration) decrease to 10^{-3} for all equations. In this analysis, the numerical computations were considered to be converged when all the residuals of the variables were lowered by six orders of magnitude (i.e. $\leq 10^{-6}$). In order to improve accuracy further, double precision was used in all the simulations.

3.5 Normalised pressure drop

Pressure was measured throughout the whole domain with the highest pressure belonging to the inlet of the porous structure as shown in Figure 3-12 for all the patterned structures as well as the random structures. Pressure drop was measured at different flow rates and at a fluid temperature of 300K.

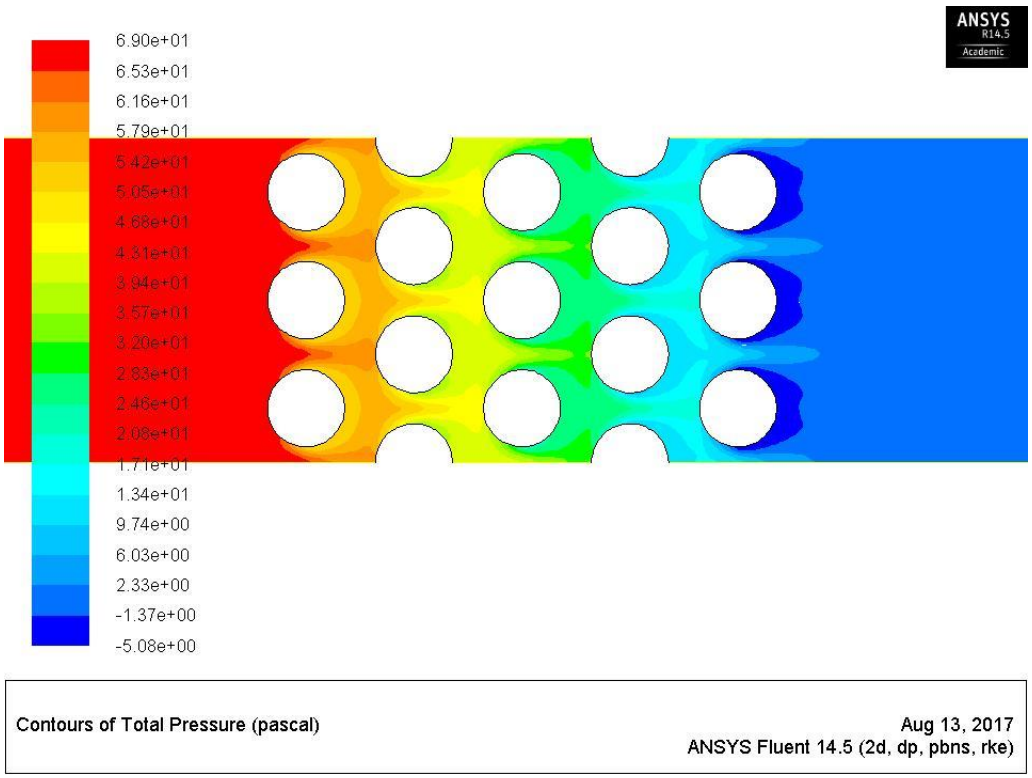

Figure 3-12 Pressure contours on a 2D staggered pattern with circular struts and 60% porosity

Pressure drop and flow velocity are correlated either by Darcy's law,

$$\frac{\Delta P}{L} = \frac{\mu}{K} u \tag{3.8}$$

or by the Forchheimer equation:

$$\frac{\Delta P}{L} = \frac{\mu}{K}u + C\rho u^2 \tag{3.9}$$

where ΔP is the pressure, ρ is the fluid density, L is the length of the porous medium, C is the Forchheimer's coefficient or form drag coefficient, μ is the viscosity of the fluid, K is the permeability of the porous medium, and u is the Darcian velocity.

The applicability of the correlations depends on the flow regimes encountered. Based on the Reynolds number (Re), Darcy or creeping flow $(Re < 10)$ or Forchheimer flow $(Re > 10)$ applies. Darcy's law only accounts for low motion fluids. Forchheimer's equation needs to be used for high velocity flows to account for the inertial effects generated within the porous structure. In this study, Forchheimer equation was used to analyse the pressure drop in the geometries created. The pressure values were normalised against the length of the REVs for convenience of analysis.

Darcian velocity, the only parameter that is not related to the porous structure, is varied from test to test. Darcian velocity can be obtained from the volumetric flow rate (Q) divided by the cross-sectional flow area of the porous medium (Darcy, 1856). In this study, the flow rate considered for the numerical analysis ranged from 0.2 L/min to 1.6 L/min, corresponding to Darcian velocities of 0.03 m/s to 0.27 m/s.

3.5.1 Patterned structures

The pressure drops were measured for different strut shapes with a wide range of porosities (60% to 80%). Both aligned and staggered arrangements were considered in the simulations. The length-normalised pressure drops for the aligned struts were plotted against Darcian velocity and the results can be seen in Figure 3-13.

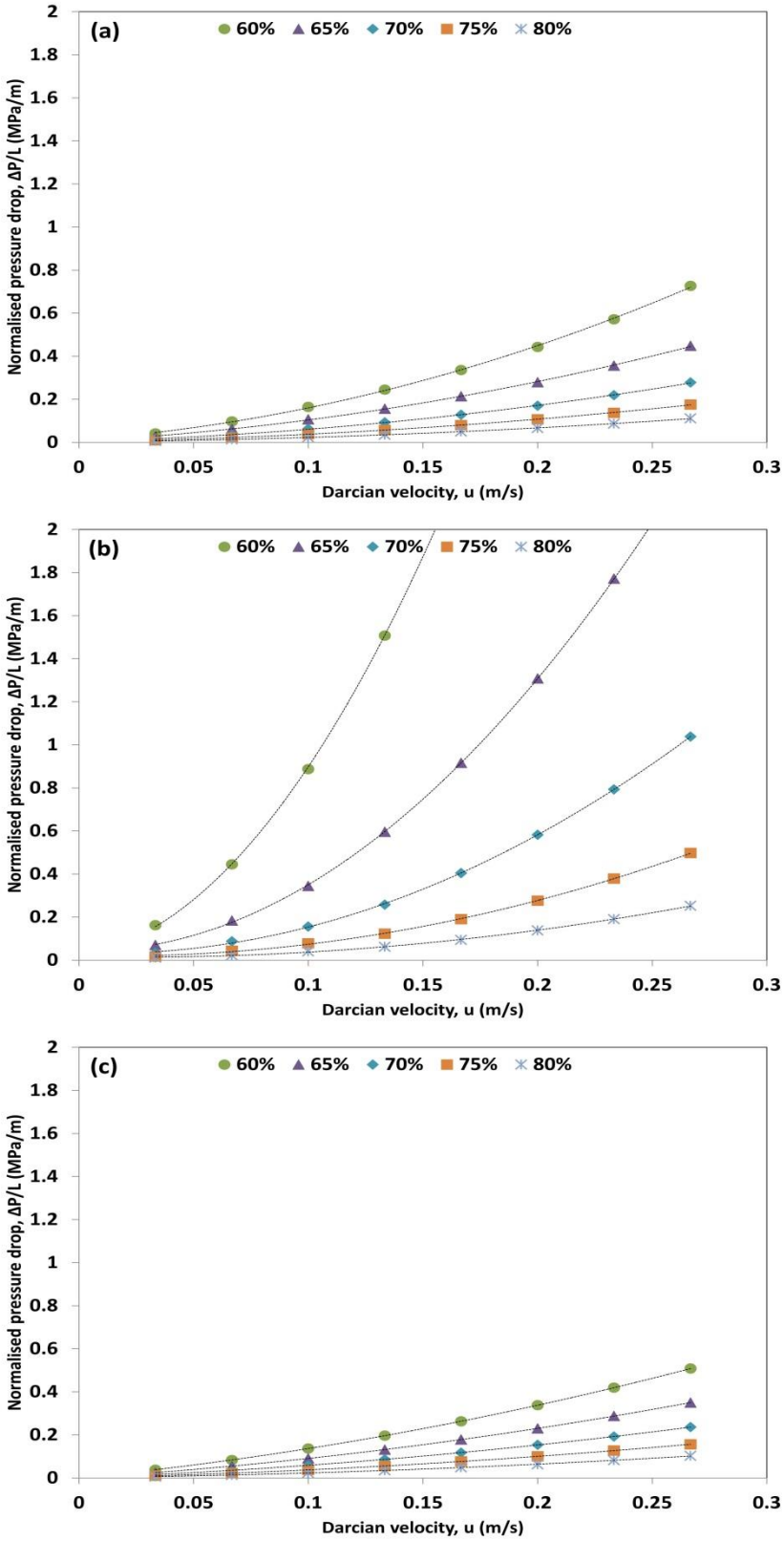

Figure 3-13 Length-normalised pressure drop versus Darcian velocity for middle range porosities (60% to 80%) for (a) circular, (b) triangular, (c) squared, (d) rotated square and (e) hexagonal aligned struts (to be continued)

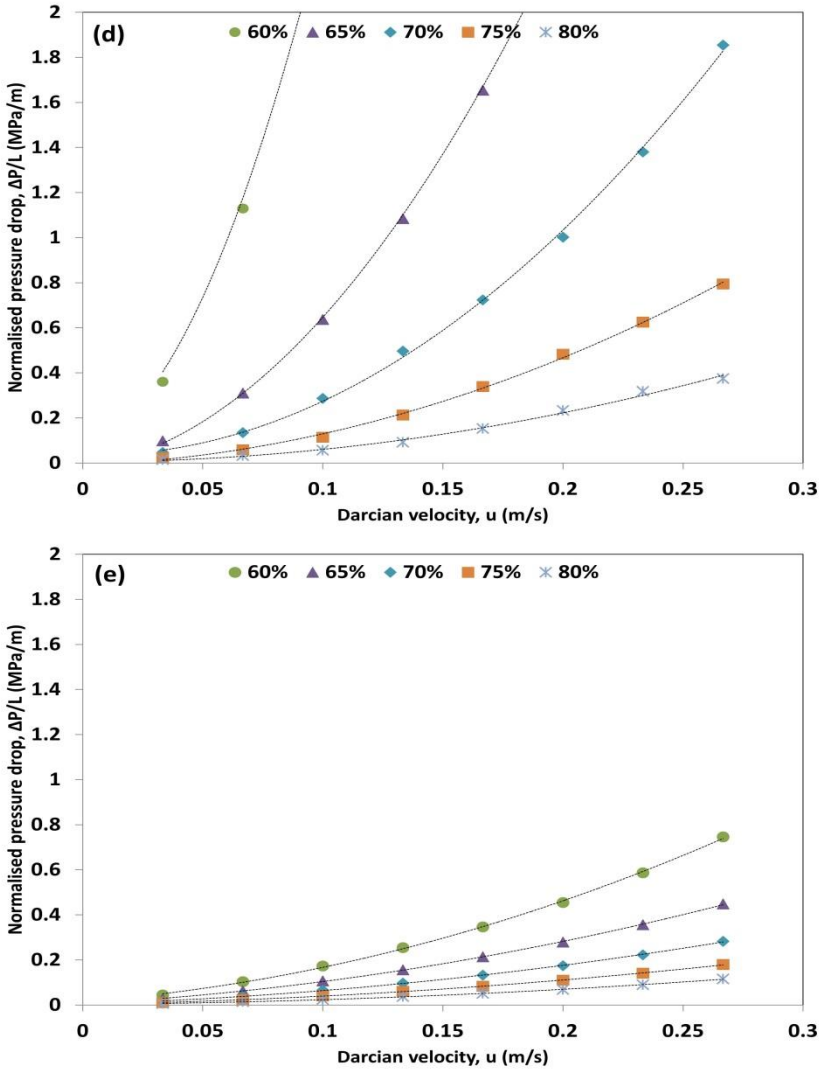

Figure 3-13 (Continuation) Length-normalised pressure drop versus Darcian velocity for middle range porosities (60% to 80%) for (a) circular, (b) triangular, (c) squared, (d) rotated square and (e) hexagonal aligned struts

The numerical results showed that the pressure drop increased with increasing flow rate for all the aligned structures regardless of the strut shape. A quadratic trend is evident, indicating that the flow is in the Forchheimer regime. This quadratic behaviour is due to the inertial effects becoming more dominant (Yang *et al.* 2013, Kundu *et al.* 2014). Bağci *et al.* (2014) reported that the Forchheimer regime starts at a flow velocity about 0.02m/s. The

current study considered Darcian velocities from 0.03 to 0.27 m/s, so the pressure drop dependence on velocity is second order as shown in Figure 3-13.

The triangular and rotated square aligned patterns exhibited the highest pressure drops as shown in Figure 3-13 (b) and Figure 3-13 (d). The pressure drop values for the circular, squared and hexagonal struts are similar, although hexagonal struts showed slightly higher values than the other two. Baloyo (2016) also reported that pore structure has a significant effect on pressure drop and consequently affects the flow regime.

The structures with lower porosities, due to the reduction of strut spacing, have higher pressure drop as shown in Figure 3-13. Mancin *et al.* (2010a) reported a similar behaviour for high porosity aluminium foams. In their study, when the porosity was decreased the pressure gradient was increased. This is because lowering the porosity leads to a reduction in the void space inside the porous material due to an increase of solid material and thus higher pressure drops arise.

The length-normalised pressure drop was plotted against Darcian velocity for the staggered patterns and the resulting graphs are shown in Figure 3-14.

The pressure drop values for the staggered patterns also presented a quadratic trend. Once again the triangular and rotated square struts showed the highest pressure drops. The numerical pressure drop values for the staggered arrangements are somewhat higher than the pressure drop obtained for the aligned struts. Papathanasiou *et al.* (2001) observed when numerically studying fibrous media using 2D patterned circular struts that the staggered arrangements exhibited higher pressure drops and higher friction factors. They attributed the difference in pressure drop to more uniform distribution of the flow as the channels are more open, leading to a less contracting / expanding character. In addition, the tortuous paths created by staggering the struts inside the REVs, increasing mixing and wall friction (further analysis in section 3.10). The tortuous paths contrast with what could be called directional pores in the aligned struts structures.

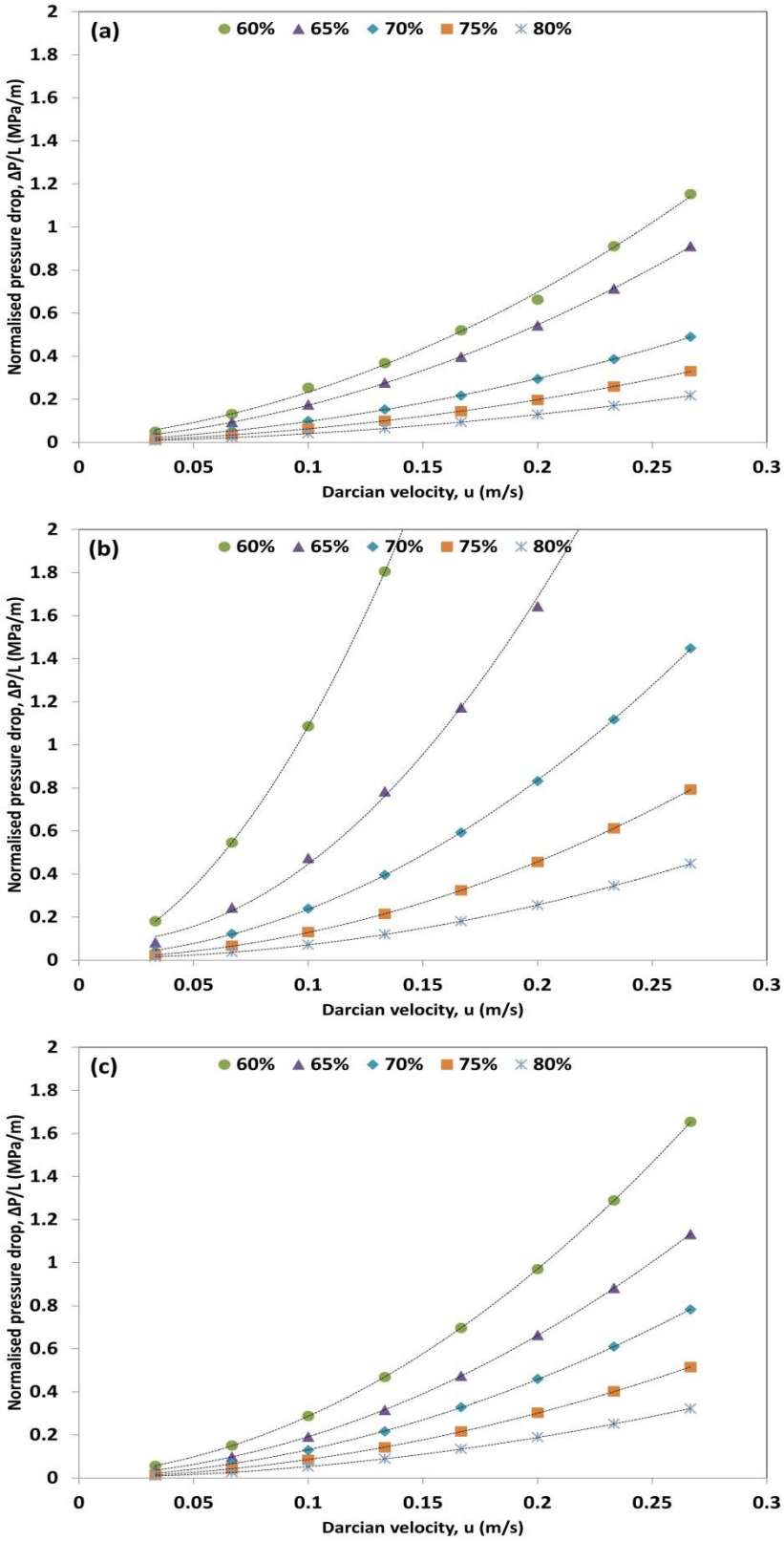

Figure 3-14 Length-normalised pressure drop versus Darcian velocity for middle range porosities (60% to 80%) for (a) circular, (b) triangular, (c) squared, (d) rotated square and (e) hexagonal staggered struts (to be continued)

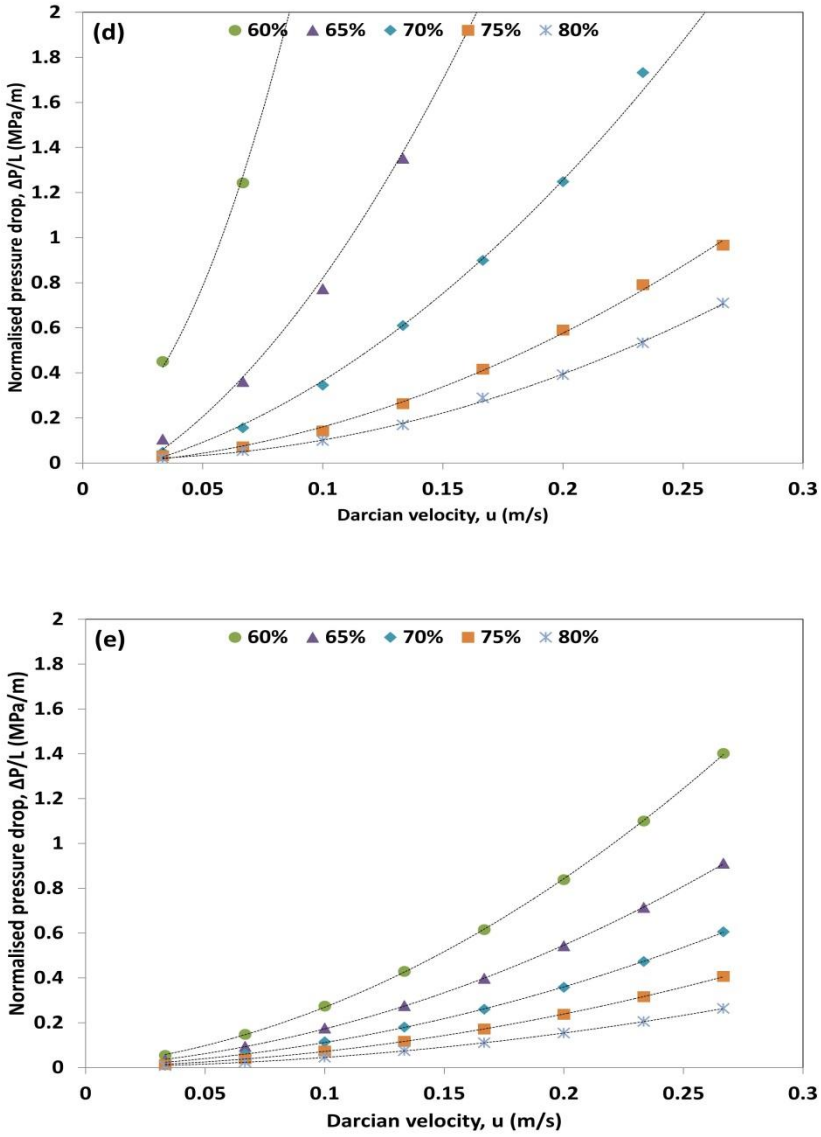

Figure 3-14 (Continuation) Length-normalised pressure drop versus Darcian velocity for middle range porosities (60% to 80%) for (a) circular, (b) triangular, (c) squared, (d) rotated square and (e) hexagonal staggered struts

In both the aligned and staggered arrangements, circular struts showed the lowest pressure drop for all the simulations. This can be explained by the smoothness of the perimeter of the circle where there are no sharp edges, in contrast with the other shapes that have sharp edges in the vertex. In addition, it is important to consider the frontal surface area facing the flow. For instance, squares and rotated squares have the same features and yet rotated squares showed pressure drops 6 to 10 times higher than the regular squares. The

difference between the rotated squares and the other strut shapes can be explained in terms of the gap created amongst the struts. Because of the rotation, the projected area of the rotated square struts is much larger than those of other strut shapes. As a consequence the gap for the fluid flow is much smaller, leading to much higher pressure drops. Despois and Mortensen (2005) observed that for lower porosities, the bottleneck created between pores increases the pressure drop.

In general, the highest pressure drop was obtained at the lowest porosity in the middle porosity range (60% to 80%) for all strut shapes. Further reduction in porosity is expected to result in larger pressure drops. In order to corroborate this, a lower range of porosities, 40% and 50%, were also considered in the present study. However, only certain strut shapes can be considered due to the overlapping effect explained in section 3.1.1.4. The length-normalised pressure drops for circular, squared and hexagonal struts with low porosity are shown in Figure 3-15.

In the middle range porosity (60% to 80%), the pressure drops for circular, squared and hexagonal aligned struts are very similar. For example, the difference in the normalised-pressure drop between the squared struts and the circular struts is from 1% to 45%, depending on the flow rate and porosity. In the porosity range of 40% to 60%, however, the difference in pressure drop amongst the strut shapes becomes more evident. This can be explained by the different gaps. For instance, the gap for the squared struts is almost twice the gap for the circular struts, leading to pressure drop values of the circular struts being three times larger.

The length – normalised pressure drops for staggered patterns in the low porosity range are shown in Figure 3-16. The pressure drop increased in all cases when compared with their aligned counterparts. The pressure drop for the staggered struts increased about 25% at low flow rates and almost 125% at higher flow rates, compared with the aligned struts. This difference in pressure drop can be explained by the change in flow direction.

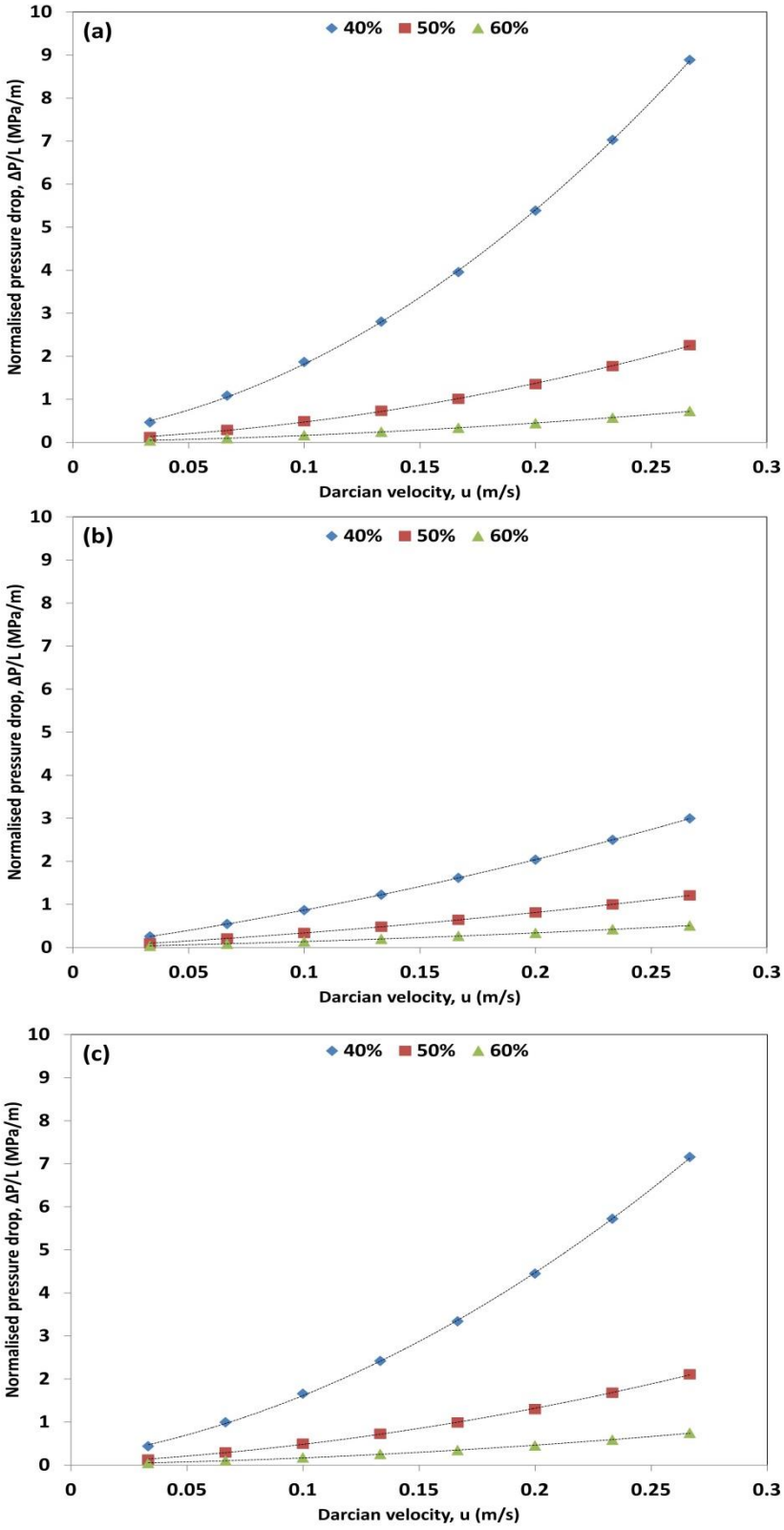

Figure 3-15 Length-normalised pressure drop versus Darcian velocity for low range porosities (40% to 60%) for (a) circular, (b) squared and (c) hexagonal aligned struts

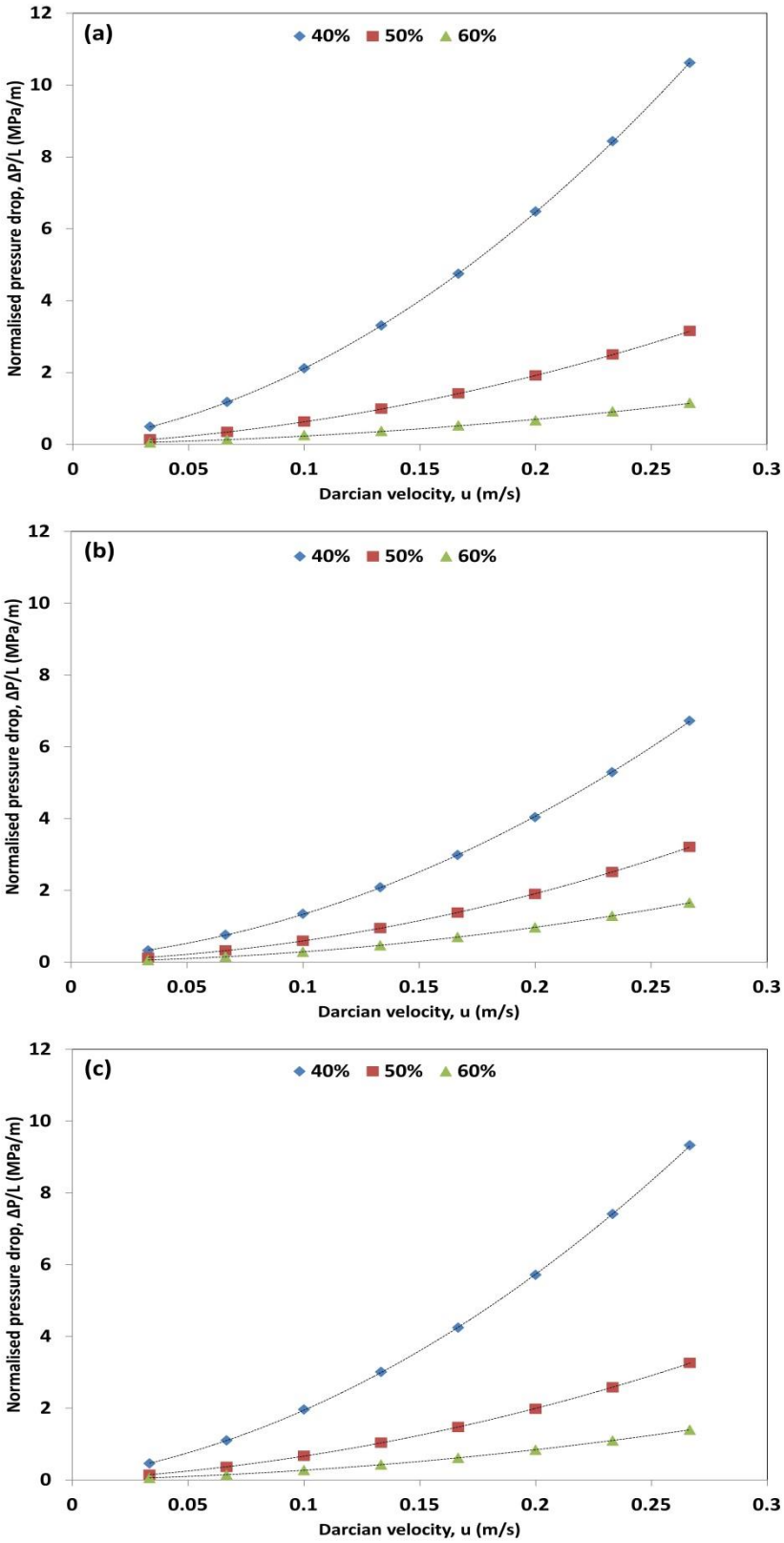

Figure 3-16 Length-normalised pressure drop versus Darcian velocity for low range porosities (40% to 60%) for (a) circular, (b) squared and (c) hexagonal staggered struts

In order to fully compare the pressure drops between the aligned and staggered arrangements, a dimensionless pressure drop ratio is defined as follows:

$$\prod = \frac{\Delta P_s}{\Delta P_a} \tag{3.10}$$

where ΔP_s and ΔP_a are the pressure drops for the staggered and aligned structures respectively. The pressure drop ratios for different porosities are shown in Figure 3-17. It can be seen that $\prod > 1$ as the pressure drop for the staggered structures is always higher for all strut shapes.

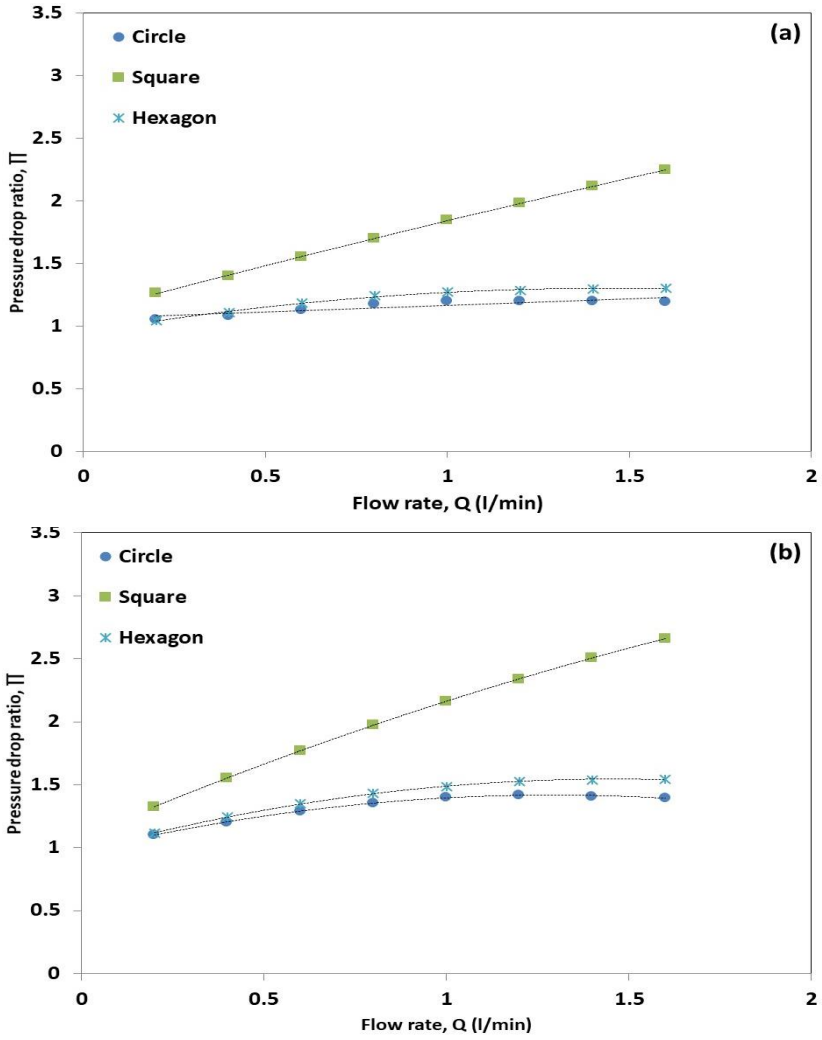

Figure 3-17 Pressure ratios between aligned and staggered patterns versus flow rate of circular, squared and hexagonal struts at different porosities: (a) 40%, (b) 50% (c) 60%, (d) 65%, (e) 70%, (f) 75% and (g) 80% (to be continued)

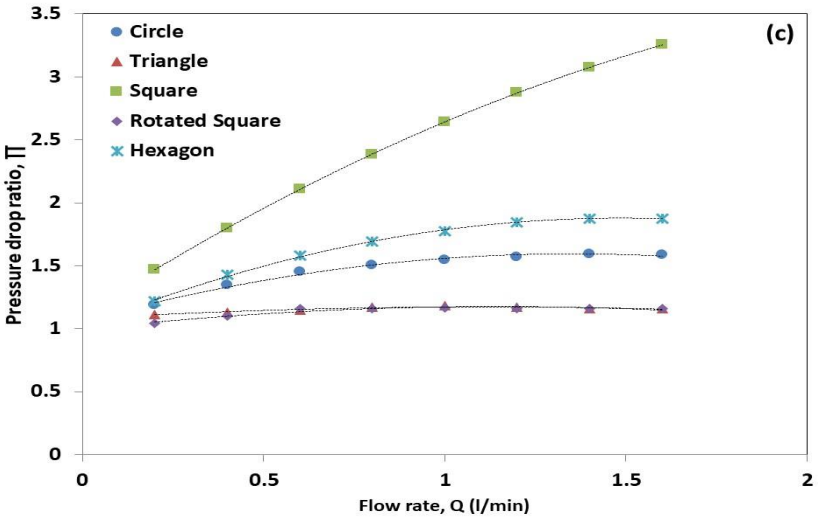

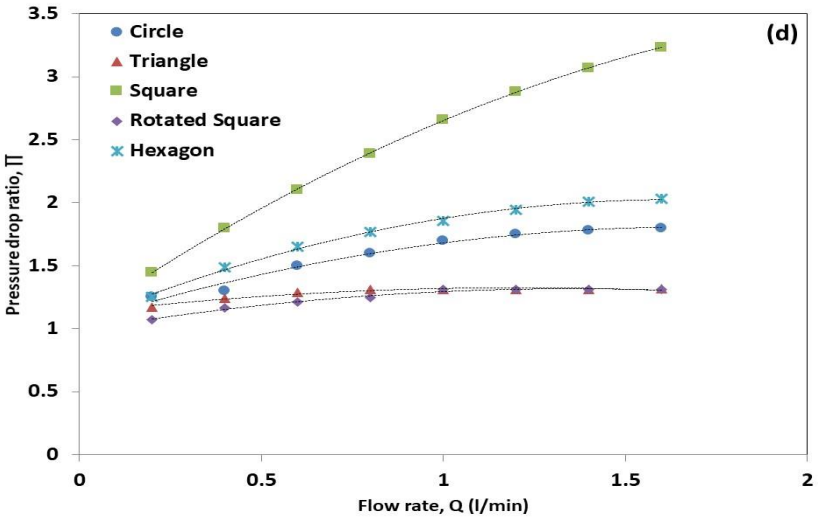

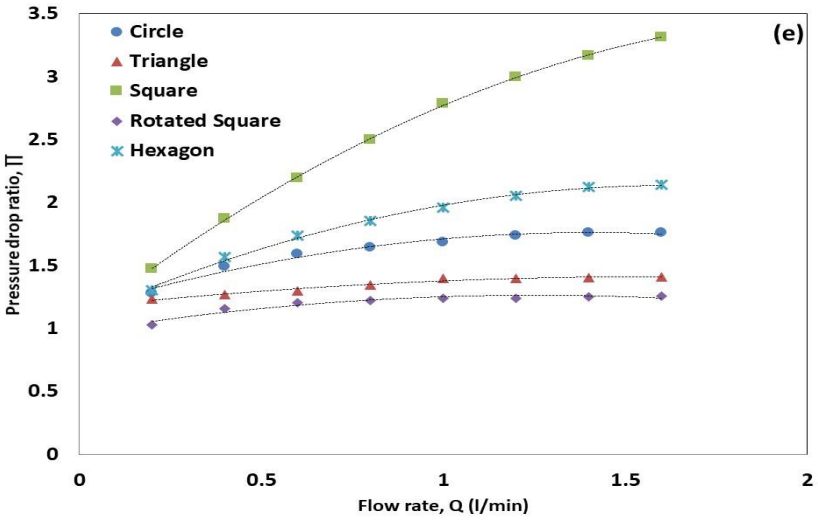

Figure 3-17 (Continuation) Pressure ratios between aligned and staggered patterns versus flow rate of circular, squared and hexagonal struts at different porosities: (a) 40%, (b) 50% (c) 60%, (d) 65%, (e) 70%, (f) 75% and (g) 80% (to be continued)

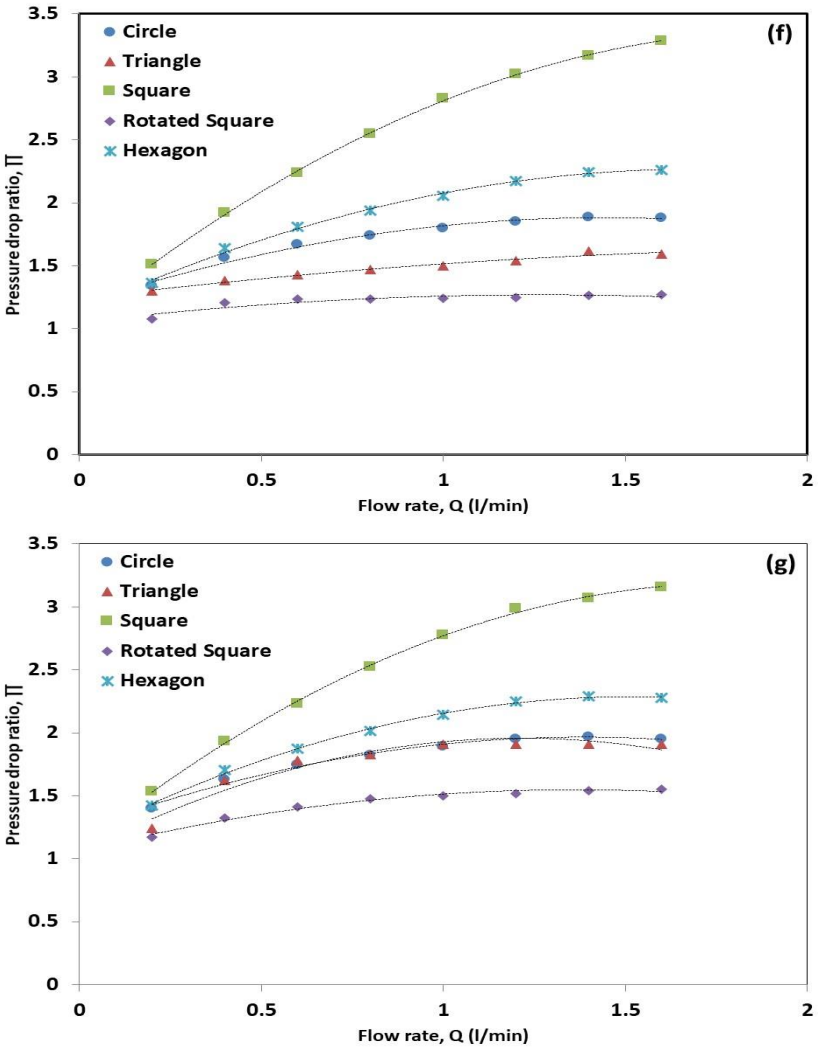

Figure 3-17 (Continuation) Pressure ratios between aligned and staggered patterns versus flow rate of circular, squared and hexagonal struts at different porosities: (a) 40%, (b) 50% (c) 60%, (d) 65%, (e) 70%, (f) 75% and (g) 80%

Figure 3-17 shows that the pressure drop ratio increases with flow rate. At low flow rate, the pressure ratio is between 1.1 and 1.5 for all strut shapes regardless porosity and for higher flow rates, the pressure ratio is increased between 1.4 and 3.4. In most of the cases the pressure ratio stabilises at higher flow rates (Q > 1.2 l/min).

It can also be seen that the pressure ratio was highly affected by the strut shape. The strut shape with the lowest pressure ratio was the rotated squares, followed by triangles, circles, hexagons and squares. The squared struts displayed the highest pressure drop ratio with

1.4 for the lowest flow rate and up to 3.4 for the highest flow rate. Except for the squared struts, the pressure ratio remained between 1.1 and 1.4 at low flow rate and increased to 1.2 to 2 for the higher flow rates. The difference in pressure ratio between the strut shape is due to the different effects on the flow path.

Porosity also affects the pressure ratio for the 2D patterned structures. It is shown that pressure ratio increases when porosity is increased, especially at higher flow rates. Increasing porosity leads to less tortuous paths in the aligned arrangements compared with a low porosity structure.

3.5.2 Random structures

Pressure drop was measured for two different random 2D structures with a similar porosity of 60%. The flow rate considered ranged from 0.2 l/min to 1.8 l/min. Strut size used ranged from $200 - 500\mu m$. Pressure drop was numerically calculated and plotted against Darcian velocity, as shown in Figure 3-18.

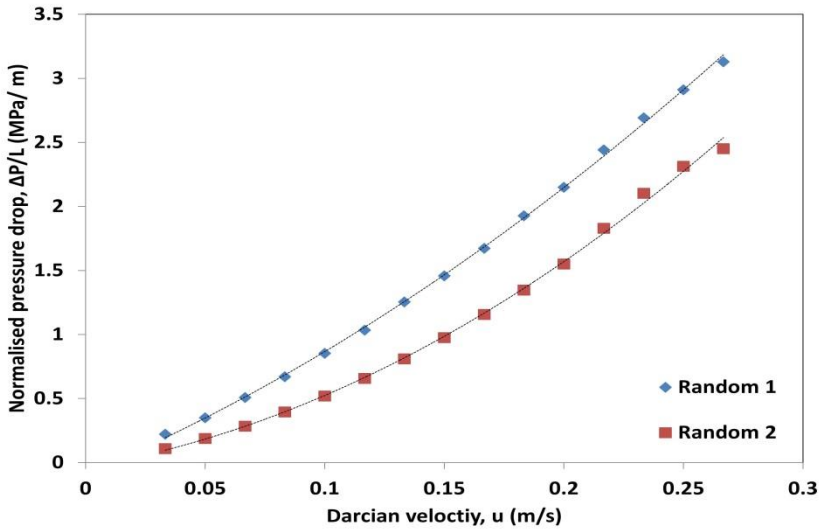

Figure 3-18 Length-normalised pressure drop versus Darcian velocity for 2D random structures with porosity of 60% and pore size ranging from 200-500 µm

Pressure drop increased with increasing Darcian velocity. The pressure drops are in a similar range as the triangular and rotated square patterned structures, but much higher than the other patterns, indicating higher resistance. Koponen *et al.* (1997) reported that using a 2D random structure using square struts had 1.5 times higher pressure drop compared to a 2D arrangement of aligned squares with similar porosity. They attributed this difference between the random model and the patterned model to the restrictions on the flow caused by the randomness of the structure such as dead-end pores ore narrow passages.

There is a big difference in pressure drop values between the two random structures. It indicates that the pressure drop is extremely sensitive to the structure.

Finally, it is worth to mention that the simulation time for the random structure (considering geometry creation, mesh generation and calculations) was three times longer than those used for the patterned structures.

3.6 Permeability

3.6.1 Patterned structures

In this study, permeability for the patterned structures was calculated using Forchheimer's equation. In order to obtain permeability and form drag coefficient more conveniently Equation 3.22 can be rearranged to obtain a linear relationship as follows:

$$\frac{\Delta P}{uL} = \frac{\mu}{K} + C\rho u \tag{3.11}$$

If $\frac{\Delta P}{uL}$ is plotted against u, the values for K can be obtained from the interception of the resulting trend line with the y axis and C can be obtained from the slope of the trend line.

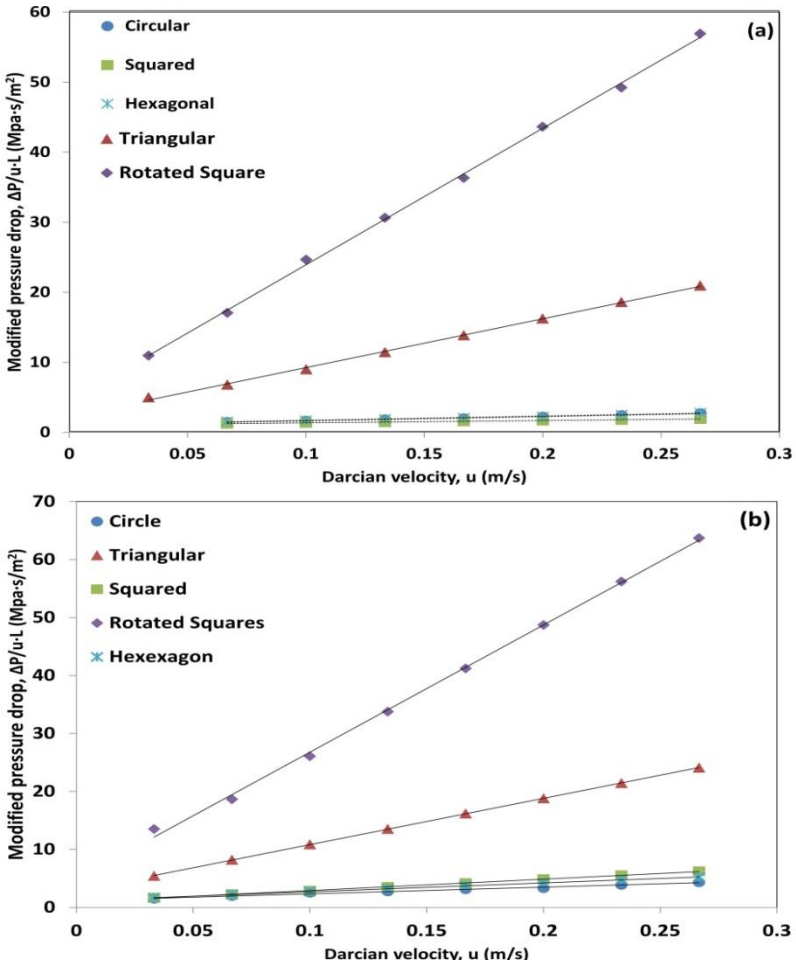

Figure 3-19 Modified pressure drop vs Darcian velocity for (a) aligned and (b) staggered struts with porosity of 60%

Figure 3-19 shows the plots of the modified pressure drop (ΔP/u·L) versus Darcian velocity (u) for the patterned structures of a porosity of 60%. This process was performed for all geometrical shapes in both aligned and staggered arrangements for all the other porosities.

Table 3-3 lists the permeability and form drag coefficient values for all the strut shapes in both aligned and staggered patterns. 576 simulations were carried out in order to gather all the data needed to complete Table 3-3. The results were used to analyse the effects of porosity and strut shape on permeability and form drag coefficient. The results of the form drag coefficient will be analysed in the following section.

Table 3-3 Permeability and form drag coefficient of 2D geometrical shapes

		Aligned		Staggered	
Porosity	**Strut shape**	**Permeability**	**Form drag coefficient**	**Permeability**	**Form drag coefficient**
		K (x10 $^{-10}$ m^2)	*C (x10 ^{4} m^{-1})*	*K (x10 $^{-10}$ m^2)*	*C (x10 ^{4} m^{-1})*
40%	Square	1.72	1.25	1.76	5.48
	Hexagon	1.13	4.75	1.17	7.44
	Circle	0.95	8.3	0.95	10.93
50%	Square	4.19	0.62	4.45	3.15
	Hexagon	3.45	1.51	3.43	3.01
	Circle	3.47	2.01	3.39	3.32
60%	Triangle	4.6	6.96	3.52	7.99
	Square	9.61	0.32	10.33	1.95
	Rot Square	2.15	19.28	2.09	21.99
	Hexagon	8.91	0.6	8.53	1.53
	Circle	9.76	0.62	8.4	1.16
65%	Triangle	11.22	3.07	8.98	3.99
	Square	14.1	0.26	16.32	1.47
	Rot Square	8.5	5.71	7.24	6.88
	Hexagon	13.37	0.38	12.93	1.08
	Circle	14.3	0.36	13.82	1.01
70%	Triangle	20.59	1.45	13.71	2.06
	Square	21.03	0.2	24.8	1.12
	Rot Square	16.6	2.7	14.06	3.24
	Hexagon	20.56	0.27	19.45	0.79
	Circle	26.29	0.24	22.08	0.52
75%	Triangle	32.85	0.74	23.93	1.24
	Square	31.63	0.16	37.1	0.82
	Rot Square	30.33	1.31	23.78	1.61
	Hexagon	31.6	0.19	30.4	0.59
	Circle	43.68	0.16	36.46	0.36
80%	Triangle	42.45	0.38	36.03	0.77
	Square	48.24	0.12	55.85	0.58
	Rot Square	40.86	0.67	33.34	1.26
	Hexagon	50.77	0.15	47.51	0.44
	Circle	76.23	0.1	61.83	0.24
85%	Triangle	65.84	0.23	52.9	0.49
	Square	81.63	0.11	85.8	0.38
	Rot Square	60.1	0.4	47.96	0.75
	Hexagon	77.28	0.12	59.94	0.3
	Circle	155.2	0.07	110.71	0.16

The relationships between permeability and porosity for aligned and staggered patterns are displayed in Figure 3-20. Porosity, or strut spacing, has a significant effect on permeability. By increasing the distance among the struts or increasing porosity, permeability increased, especially rapidly at higher porosities. This is because a higher porosity means less geometrical surfaces opposing to the fluid stream and more spacing among the struts for the flow, leading to higher permeabilities. The permeability increased exponentially with porosity, agreeing with the trend reported in the literature (Bhattacharya *et al.* 2002, Karimian and Straatman 2008).

Strut shape and arrangement also have an influence on permeability. For each arrangement, the circular struts show the highest permeability among all shapes, while rotated squares show the lowest permeability. Triangular struts also show low permeability but are superior to the rotated squares. Squared and hexagonal struts have better permeability than triangular struts. The hexagonal and squared struts have similar permeabilities when aligned but are noticeably different when staggered. The aligned arrangement has a higher permeability than the staggered pattern for any strut shape.

There was limited analysis in the literature on different strut shapes. Most of the studies concentrated only on one type of strut, either squared or circular (Papathanasiou *et al.* 2001, Hellström and Lundström 2006 Yazdchi and Luding 2011, Pisani 2011, Li *et al.* 2014). Nonetheless, some studies used 2D arrangements of different structural shapes to represent the porous media and investigated their properties such as permeability. Circular and ellipsoidal pores have shown to have less turbulent effects and better permeability (Pedras and de Lemos 2001, Yang *et al.* 2013).

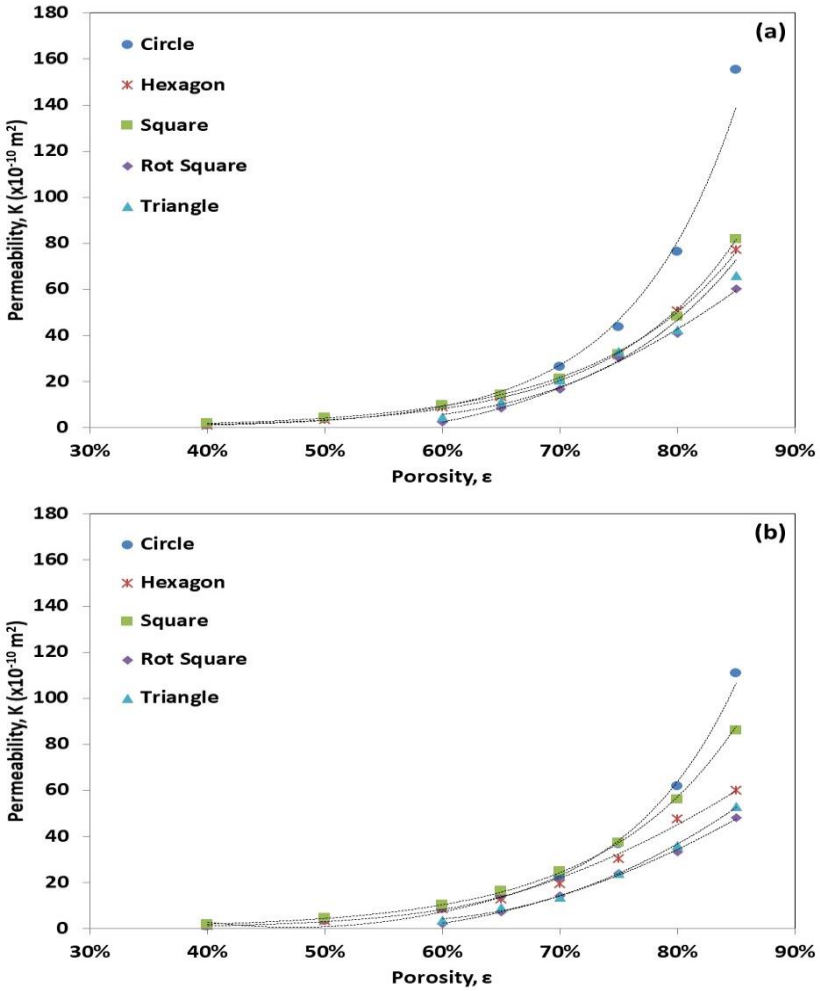

Figure 3-20 Relationship between permeability and porosity of (a) aligned and (b) staggered 2D structures

3.6.2 Random structures

Permeability and the form drag coefficient were also obtained for the random structures using the same method as with the patterned structures. The resulting plots can be observed in Figure 3-21. The resulting values of permeability and form drag coefficient are presented in Table 3-4. 30 simulations were carried out in order to obtain all the necessary data.

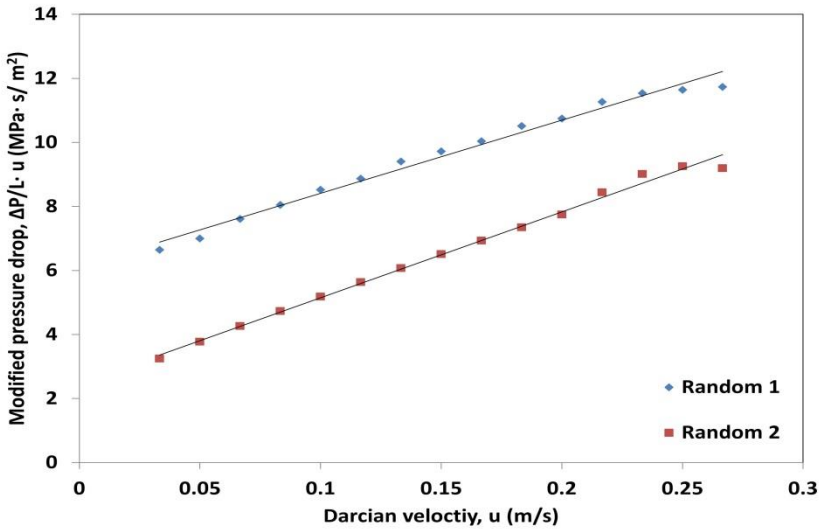

Figure 3-21 Modified pressure drop vs Darcian velocity for 2D random structures

Table 3-4 Permeability and form drag coefficient of the random structures

	K (x 10^{10} m^2)	C (x 10^4 m^{-1})	R^2
Random 1	1.55	2.11	0.98
Random 2	3.9	2.63	0.99

The values of permeability for the random structures were lower than those obtained for the patterned structures with circular, triangular, hexagonal and square struts. However, the permeability obtained for the random structures was in the same order as for the rotated squares.

3.7 Form drag coefficient (C)

The relationship between form drag coefficient and porosity is shown in Figure 3-22. Form drag coefficient decreases with porosity, especially rapidly for rotated squares and triangular struts.

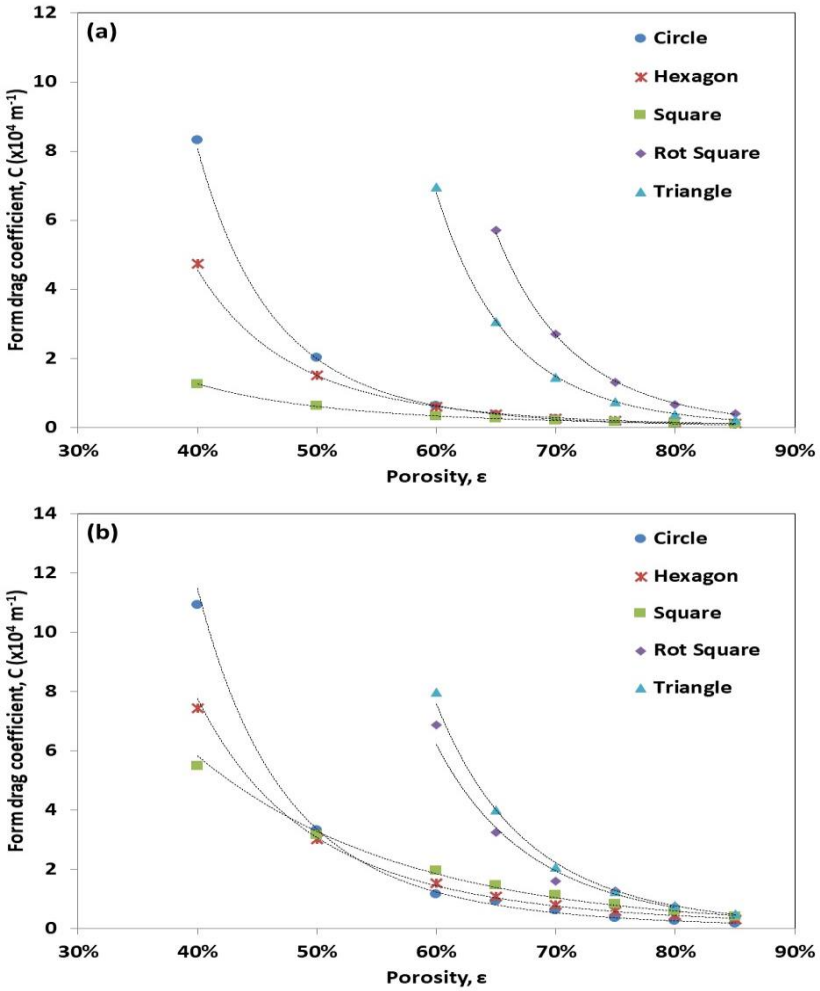

Figure 3-22 Relationship between form drag coefficient and porosity of (a) aligned and (b) staggered 2D structures

The squared, hexagonal and circular struts have smaller values for the form drag coefficient due to large gaps. The staggered patterns showed larger form drag coefficients than the aligned structures.

Strut shape also affects the form drag coefficient. Rotated squares and triangular struts exhibited the highest form drag coefficient regardless of the arrangement due to the small gaps between the struts. For the circular, squared and hexagon struts the form drag coefficient changed depending on the strut arrangement. For the aligned patterns, the squared struts showed the smallest form drag coefficient followed by the hexagonal and circular struts. The aligned arrangement functions as directional pores, therefore the straight

channels created by the squared struts help to reduce the form drag created within the structure. For the staggered structures however, circular struts showed the smallest form drag coefficient. This can be related to the smoothness of the surface of the circular struts and the change in flow direction created by the squares leading to higher values of form drag coefficient. In general, staggered arrangements showed higher drag form coefficients than the aligned patterns.

For the random structures, the form drag coefficient values are above the form drag coefficients obtained for circular, hexagonal and squared struts but several times below the triangular and rotated squares struts.

3.8 Relationship between *K* and *C*

The relationship between permeability K and form drag coefficient C is shown in Figure 3-23. Both permeability and form drag coefficient are a function of porous structure. Low permeability is due to reduce strut spacing inside the REVs, which increases the form drag coefficient as well. With high porosity, the strut spacing increases leading to an increase in permeability and a decrease in form drag coefficient. Permeability and form drag coefficient leads have a negative correlation.

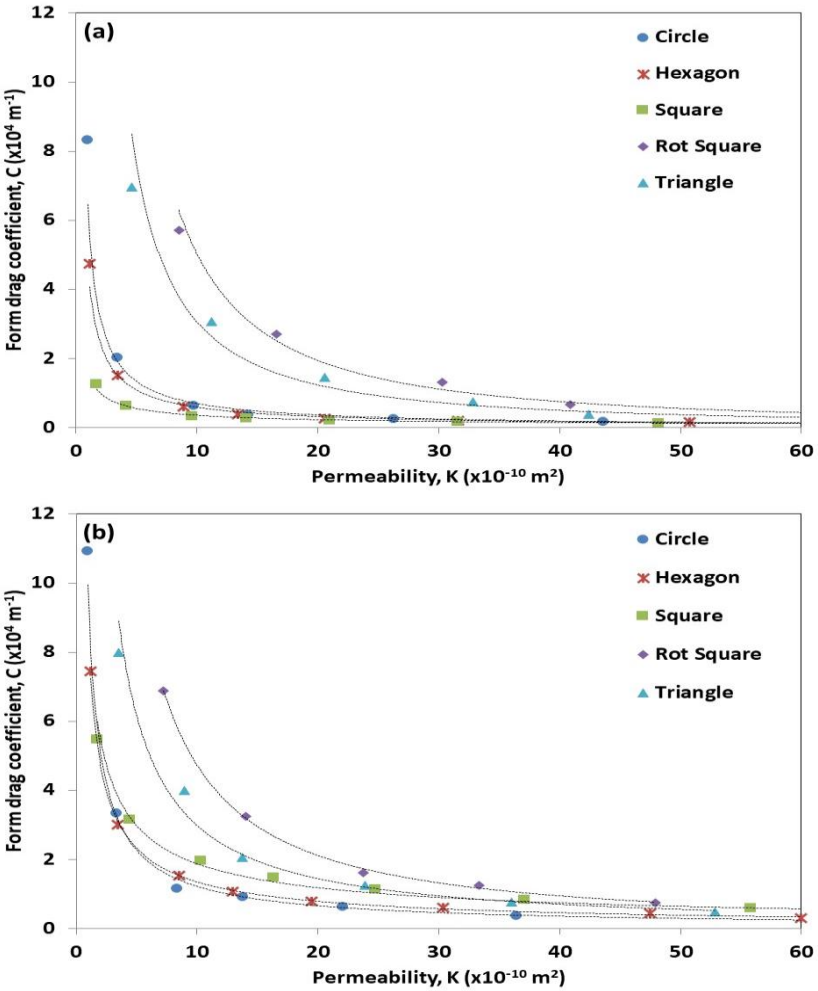

Figure 3-23 Relationship between form drag coefficient and permeability for (a) aligned and (b) staggered 2D structures

In the literature, permeability and form drag coefficient are often related in terms of the expression proposed by Ergun (Mancin *et al.* 2010, Costa *et al.* 2015):

$$C = \frac{C_f}{\sqrt{K}} \tag{3.12}$$

where C_f represents the drag force coefficient or non-Darcy coefficient. Although this relationship is applicable for packed beds, it has to be modified for other porous media (Li and Engler 2001) and different empirical models can be found in the literature.

It is clear that the data in the current study do not follow Equation 3.25, but can be described in the following form:

$$C = C_f K^{-M} \tag{3.13}$$

where M is a constant for any fixed pore size. In order to use Equation 3.26, the relationship between permeability and form drag coefficient is plotted in the logarithmic scale as shown in Figure 3-24.

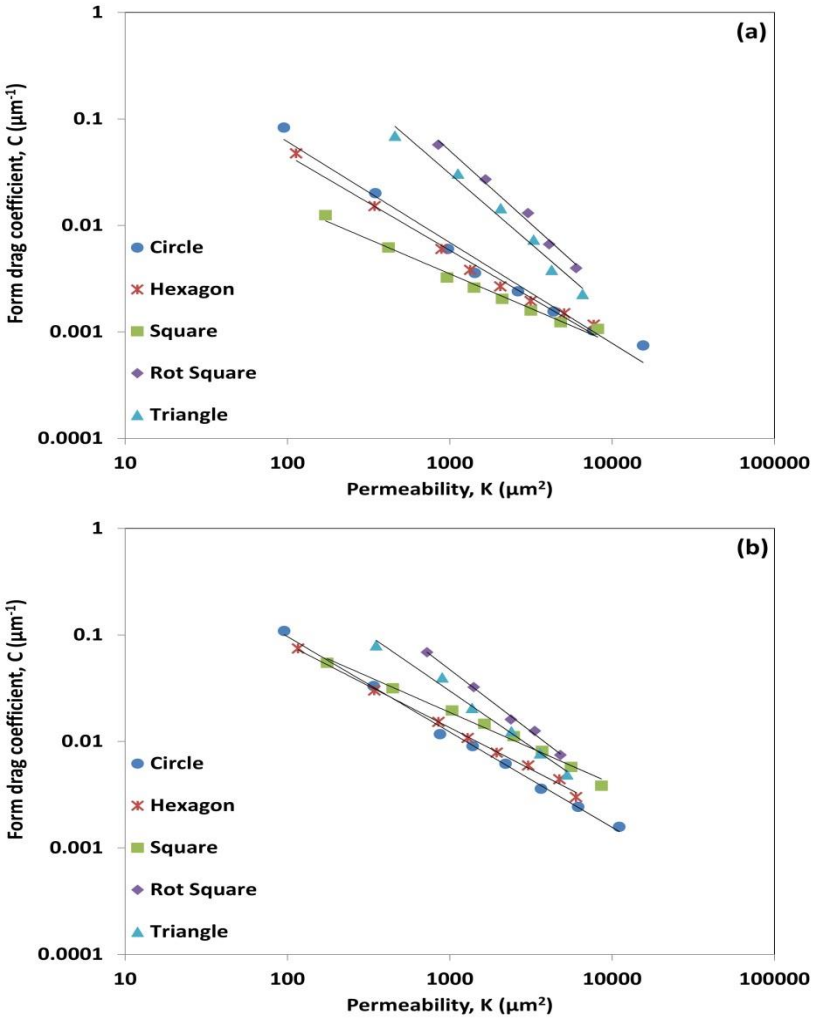

Figure 3-24 Form drag coefficient versus permeability log-log plot for (a) aligned and (b) staggered structures

The values for the exponential term M and the drag force coefficient C_f calculated from linear regressions are presented in Table 3-5. The results show that in both aligned and

staggered arrangements the exponential term diverges from the Ergun's value of 0.5. However, squared struts showed the closest exponential term to Ergun's value with 0.65 for the aligned patterns and 0.67 for the staggered patterns. The smallest drag force coefficients were obtained for the aligned patterns.

Table 3-5 Exponential term and drag force coefficient values for 2D patterned structures

	Aligned			Staggered		
Shape	***M***	**C_f**	**R^2**	***M***	**C_f**	**R^2**
Circle	0.95	2.11 e-5	0.98	0.9	1.07 e-4	1
Hexagon	0.89	5.63 e-5	0.99	0.78	1.21 e-3	1
Square	0.65	4.9 e-3	0.99	0.67	1.79 e-2	0.99
Rot Square	1.32	4.4e-8	0.98	1.08	8.32 e-6	1
Triangle	1.16	1.38 e-6	0.98	1.05	1.12 e-5	0.99

Cooper *et al.* (1999) proposed a correlation for anisotropic porous media which described permeability-form drag coefficient relationship as follows:

$$C = \frac{10^{-3.25} \cdot \lambda^{1.943}}{K^{1.023}} \tag{3.14}$$

where λ represents the tortuosity of the porous media. In order to use Equation 3.27, here tortuosity is considered as 1 for the aligned patterns. To approximate tortuosity value for the staggered patterns, the changes on flow direction are considered. Assuming that the direction changes are of 45 degrees just for simplicity, the increase in tortuosity is proximately 1.4. The C values are calculated by Equation 3.27 using $\lambda = 1$ and $\lambda = 1.4$ and are also shown in Figure 3-25.

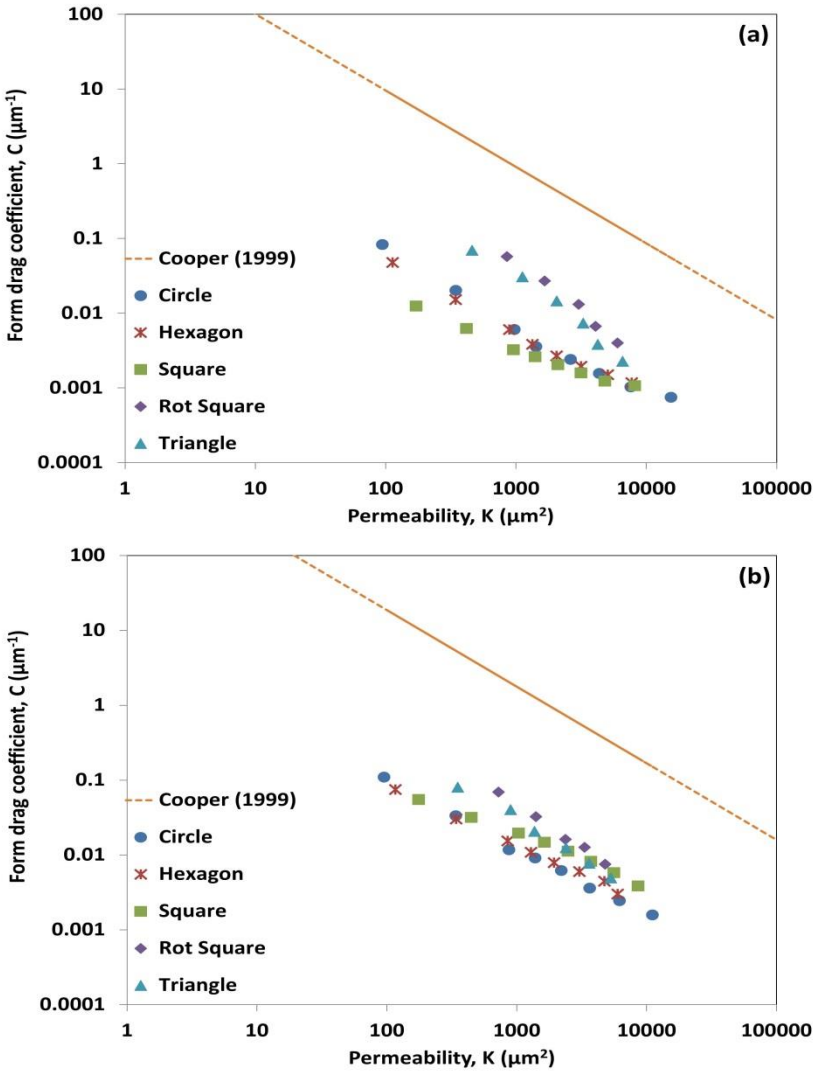

Figure 3-25 Relationship between permeability (K) and the form drag coefficient (C) with comparison to Cooper *et al.* (1999) for (a) aligned and (b) staggered patterns

The plots show that the C values for the 2D patterns used in the present study were much lower than Cooper's prediction. The difference is more than 10 times. Li and Engler (2001) proposed three main reasons for the variety of results and empirical models to correlate permeability and form drag coefficient: geometry composition, the number of parameters considered and flow changes with respect to the pore channels. In this case, geometry composition seems to be the main reason for the difference with the literature.

3.9 Drag force

Two types of drag, viscous and form drag (inertial), contribute to the total drag force. In open-cell metal foams with high porosity it was reported that the contribution of viscous drag is about 50% at low flow rates and decreases to only 25% at high flow rates (Della-Torre *et al.*, 2014).

The drag contributions of the viscous and form drag for the 2D patterned structures were numerically obtained from the force report in Fluent, which allows the calculation of the forces at a specified wall zone (the struts in this case). The viscous drag (F_v) and form drag (F_d) for the aligned structures are shown in Figure 3-26 and Figure 3-27respectively.

As the flow rate increases, both the viscous drag and form drag increase with the form drag increasing more rapidly. A linear trend is shown in Figure 3-26 for the viscous drag, while for all different strut shapes a quadratic behaviour for the form drags is shown in Figure 3-27. This means that as the flow velocity increases the inertial forces contribute more to the pressure drop.

Increasing porosity led to a decrease in both viscous and form drag. However, for the triangular and squared struts, the decrease in form drag with increasing porosity is more evident than the other strut shapes. The maximum amounts of decrease in form drag are 60%for the rotated squares, followed by 50% for the triangular struts and 25% for the circle, hexagon and square struts.

Circle, hexagon and square struts have similar form drags with the square struts having the smallest form drag amongst all strut shapes.

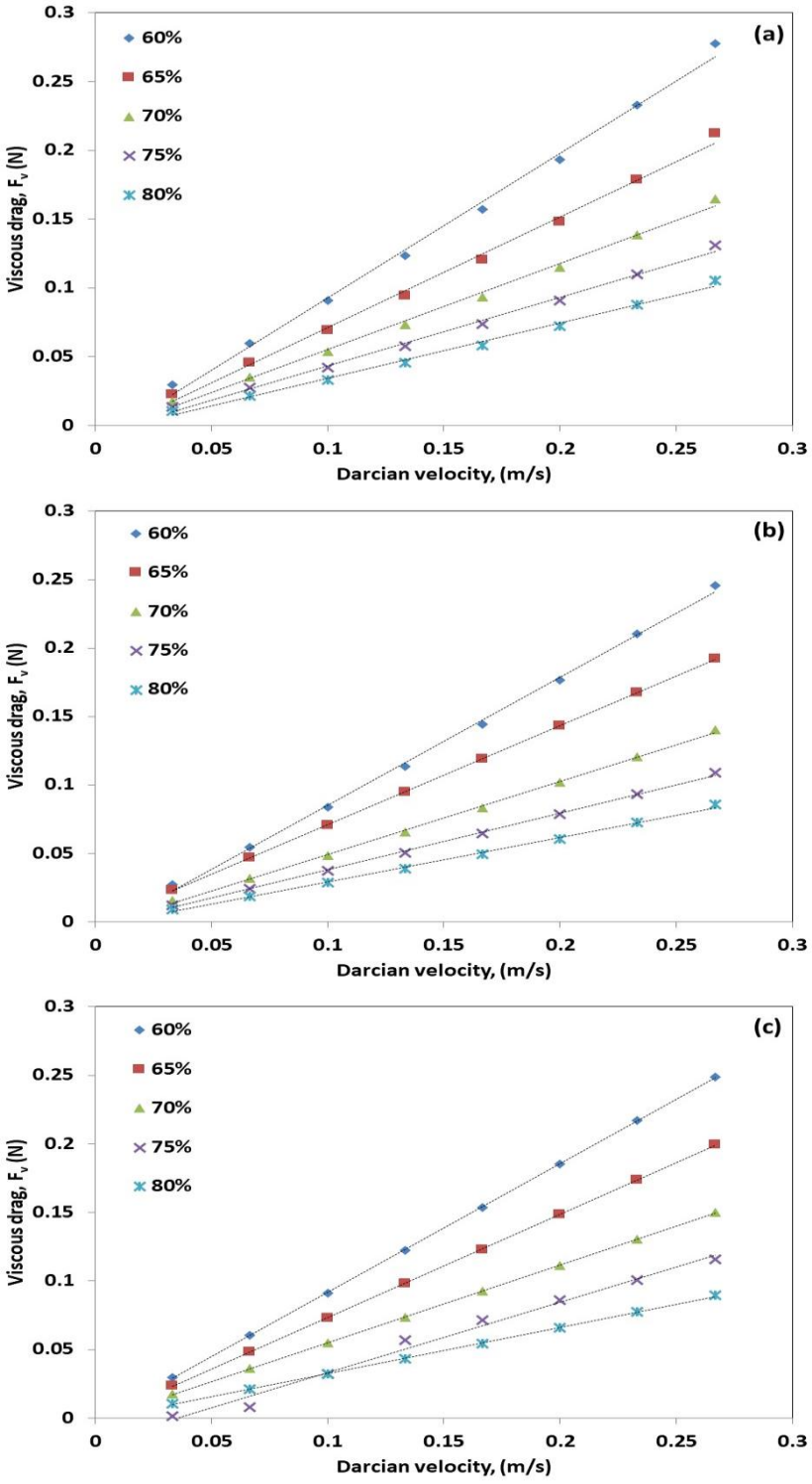

Figure 3-26 Viscous drag measurements for the 2D aligned structures for (a) circular, (b) hexagonal, (c) squared, (d) triangular and (e) rotated square struts at different porosity (shown in the picture) (to be continued)

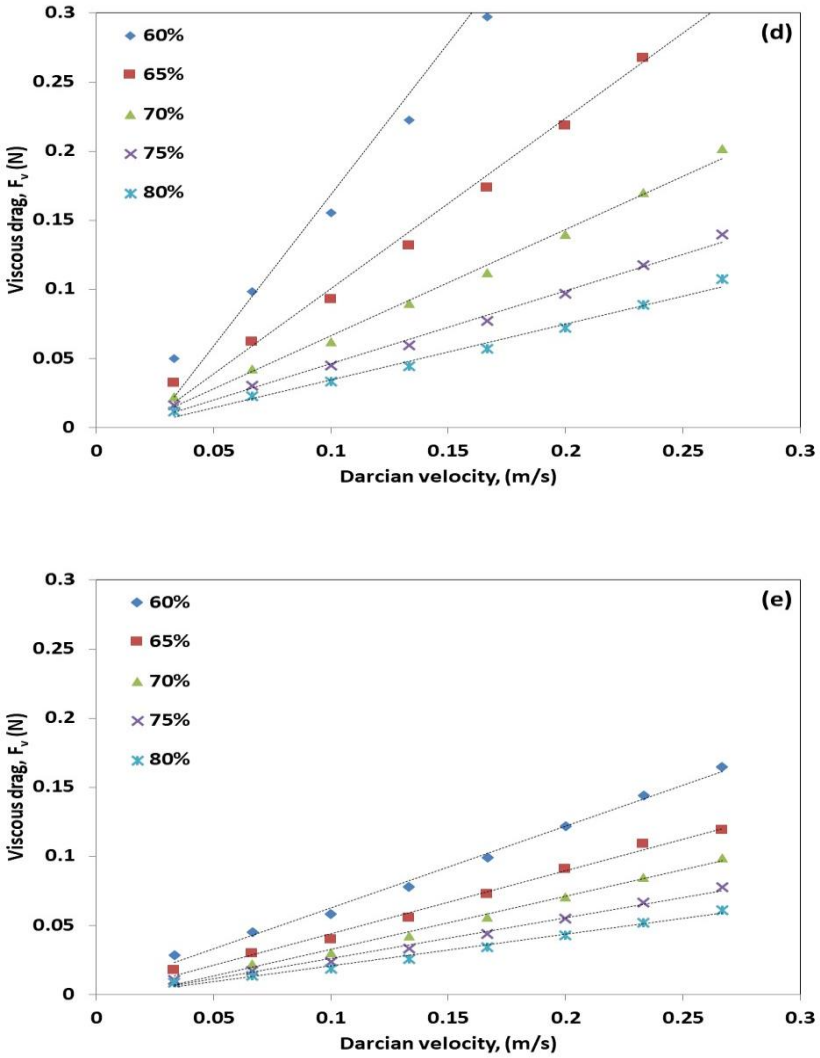

Figure 3-26 (Continuation) Viscous drag measurements for the 2D aligned structures for (a) circular, (b) hexagonal, (c) squared, (d) triangular and (e) rotated square struts at different porosity (shown in the picture)

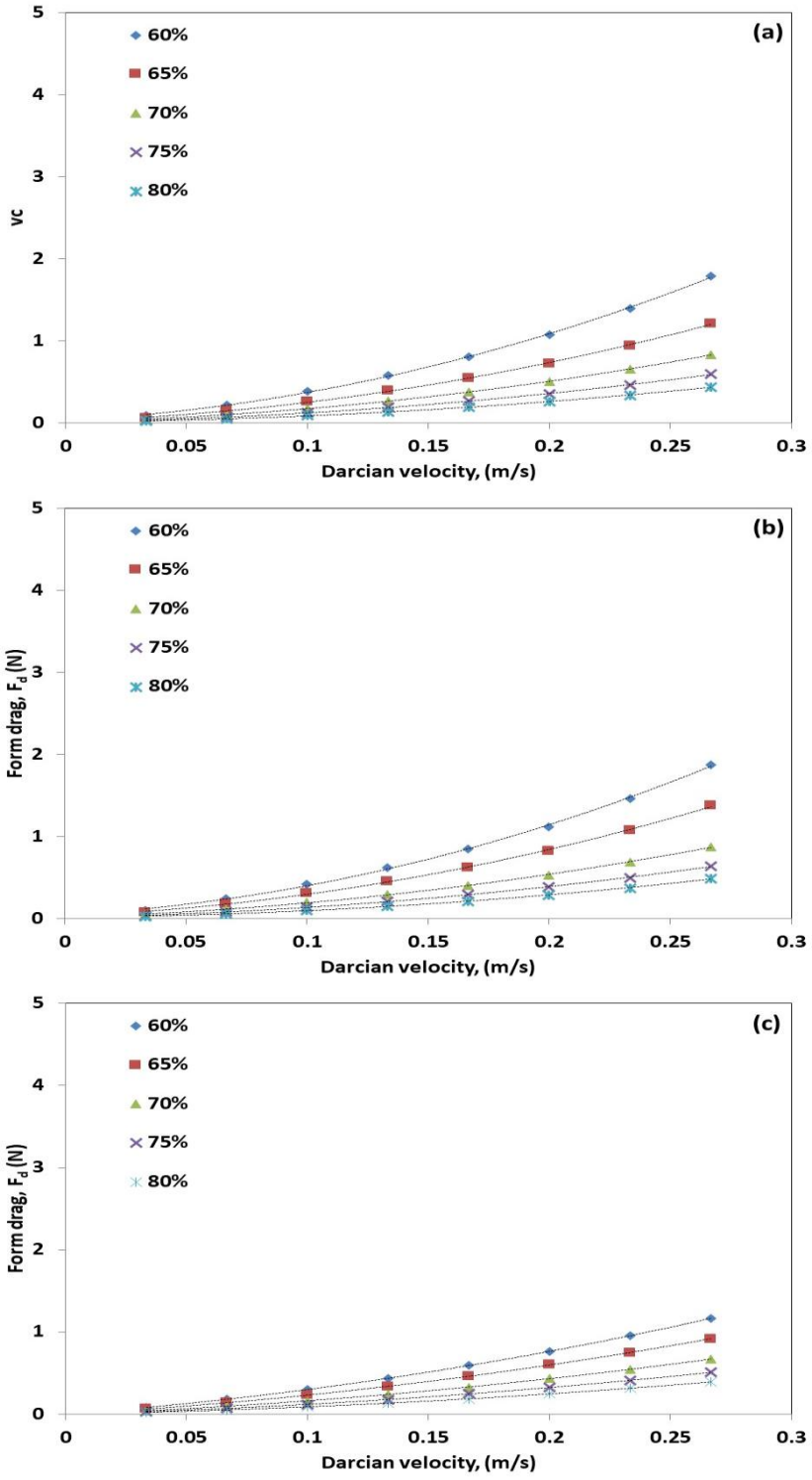

Figure 3-27 Form drag measurements for the 2D aligned structures for (a) circular, (b) hexagonal, (c) squared, (d) triangular and (e) rotated square struts at different porosity (shown in the picture) (to be continued)

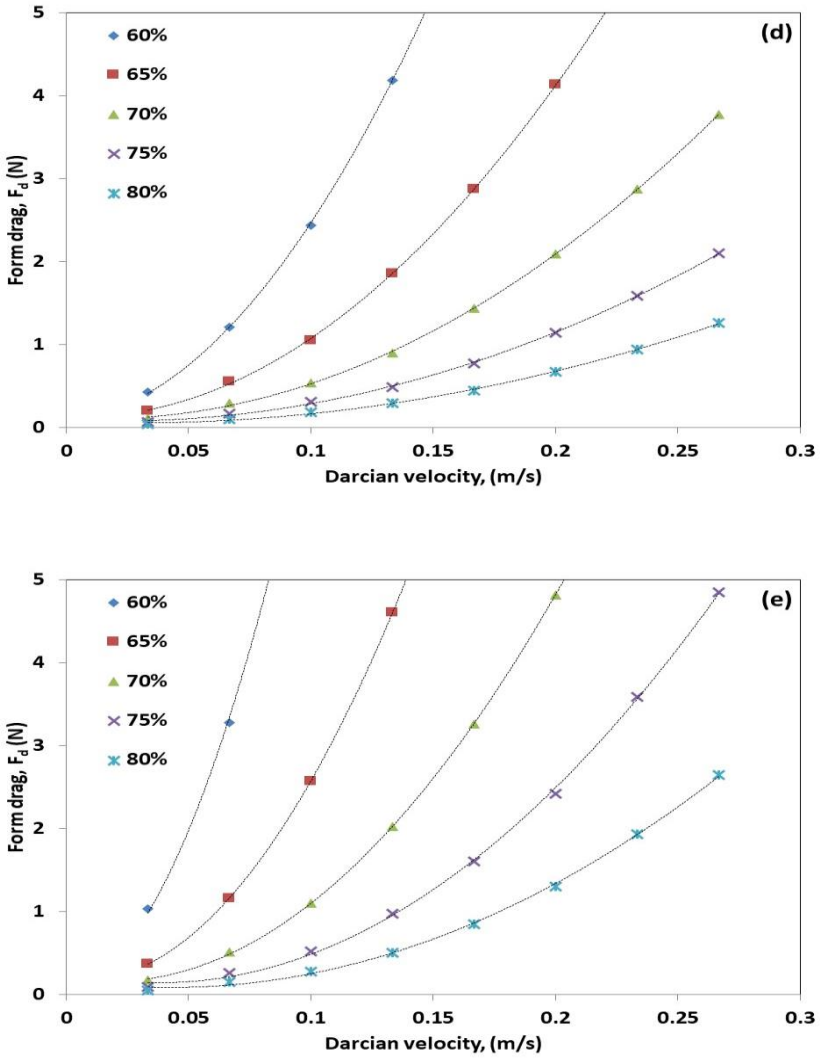

Figure 3-27 (Continuation) Form drag measurements for the 2D aligned structures for (a) circular, (b) hexagonal, (c) squared, (d) triangular and (e) rotated square struts at different porosity (shown in the picture)

The viscous drag and form drag coefficient for the staggered patterns are shown in Figure 3-28 and Figure 3-29 respectively. Analogous to the viscous drag for the aligned patterns, almost all strut shapes for the staggered patterns, except for the staggered square struts, showed a linear relationship with Darcian velocity. The staggered square struts showed a different behaviour at a Darcian velocity above 0.1m/s, where the viscous drag decreases drastically. This can be explained by the increase in turbulence due to the changes in flow direction, leading to the formation of more eddies. When porosity is increased to 80%, the viscous drag for the staggered squares almost reaches a value of zero.

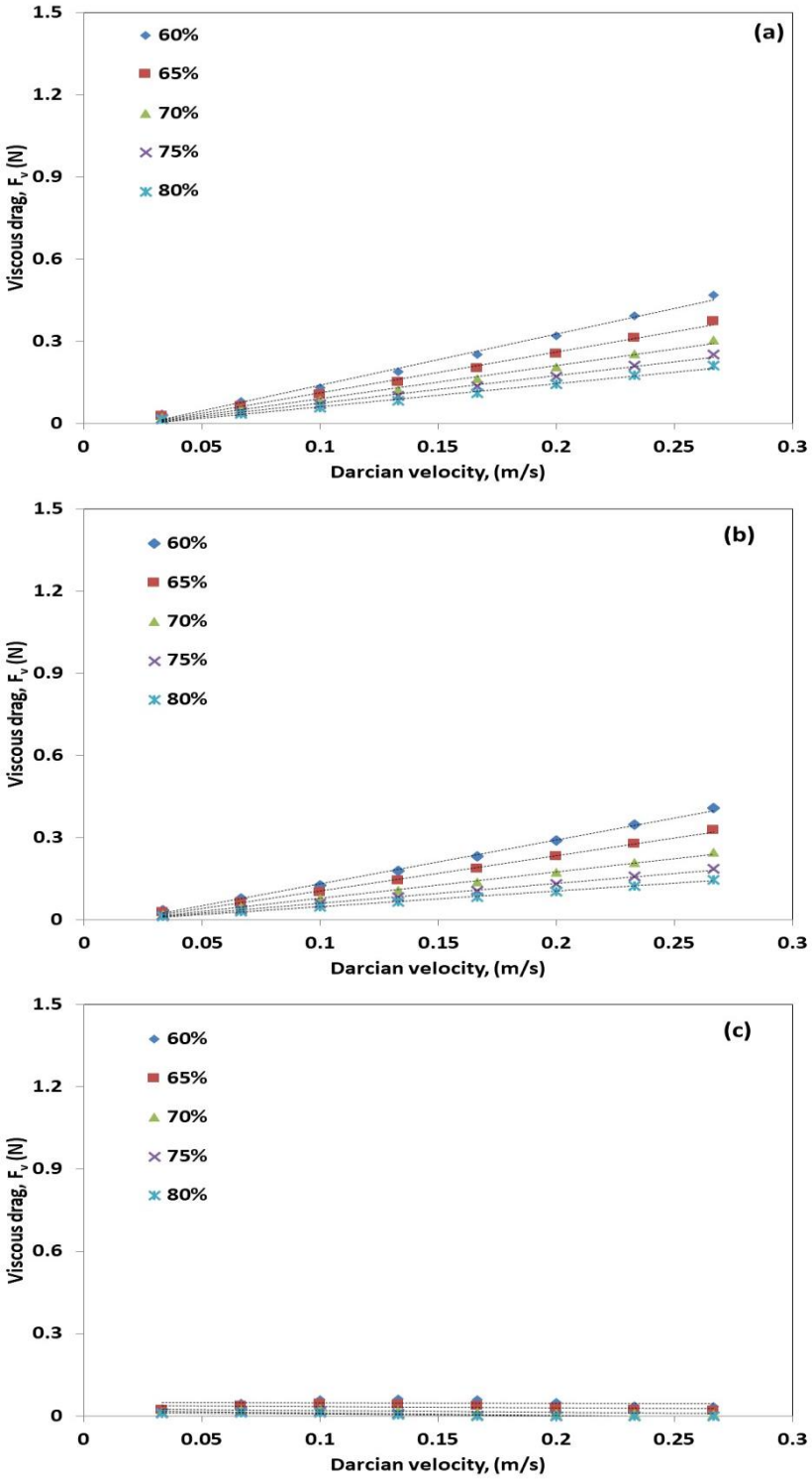

Figure 3-28 Viscous drag measurements for the 2D staggered structures for (a) circular, (b) hexagonal, (c) squared, (d) triangular and (e) rotated square struts at different porosity (shown in the picture) (to be continued)

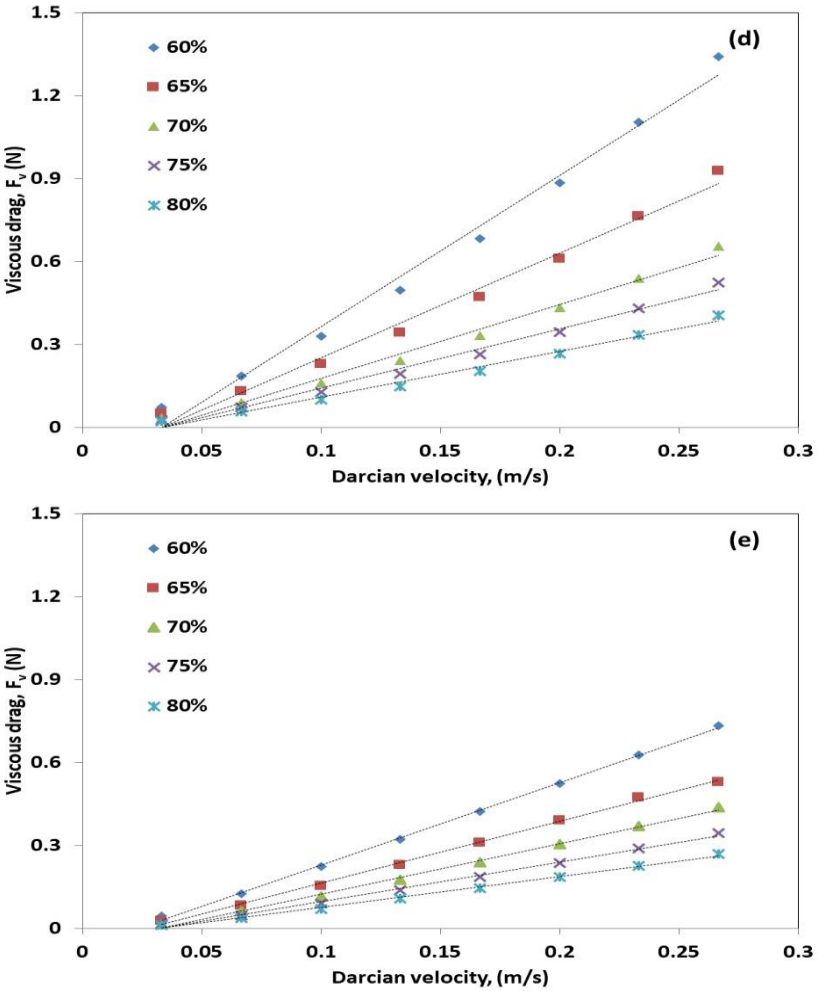

Figure 3-28 (Continuation) Viscous drag measurements for the 2D staggered structures for (a) circular, (b) hexagonal, (c) squared, (d) triangular and (e) rotated square struts at different porosity (shown in the picture)

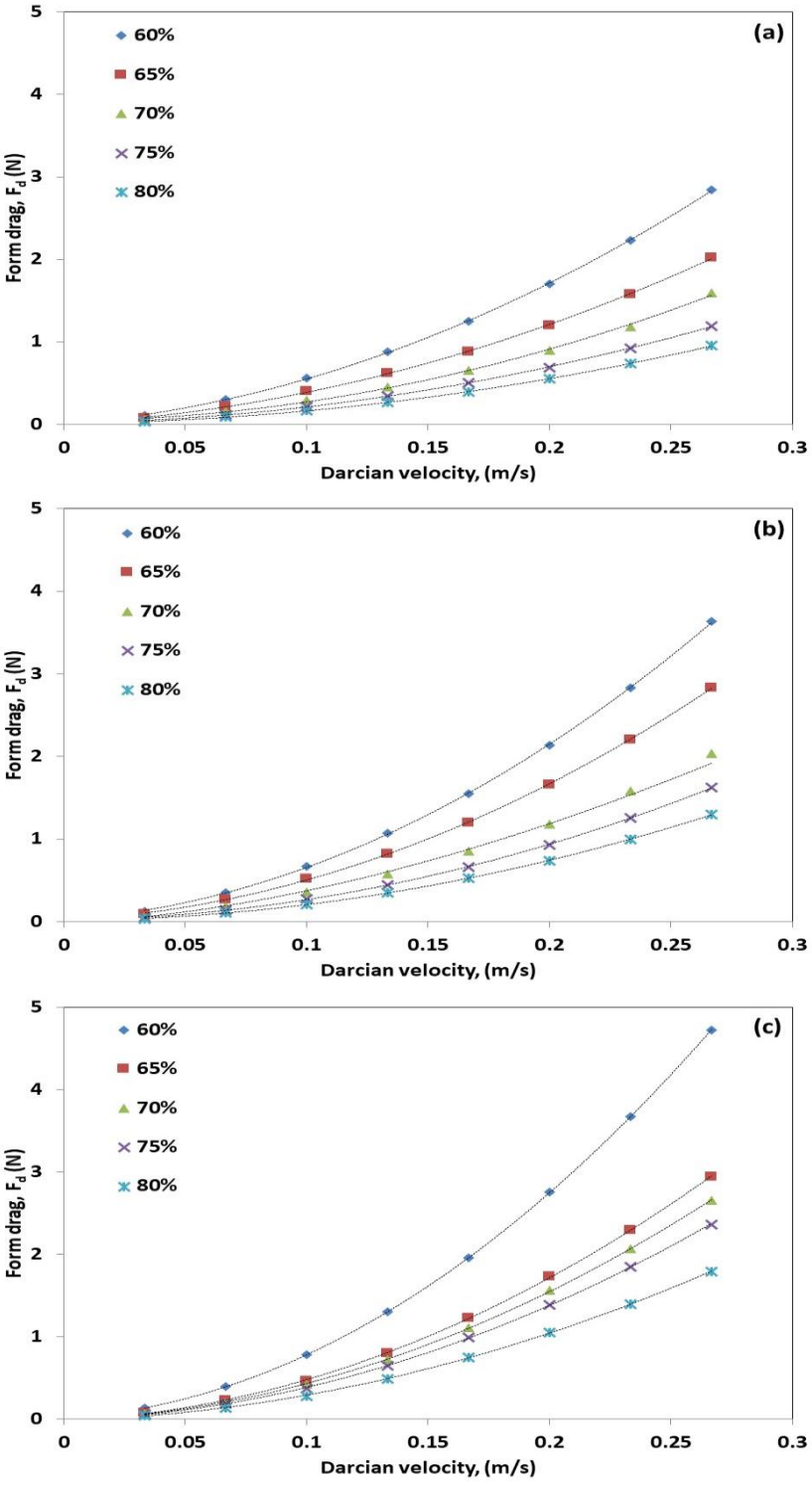

Figure 3-29 Form drag measurements for the 2D staggered structures for (a) circular, (b) hexagonal, (c) squared, (d) triangular and (e) rotated square struts at different porosity (shown in the picture) (to be continued)

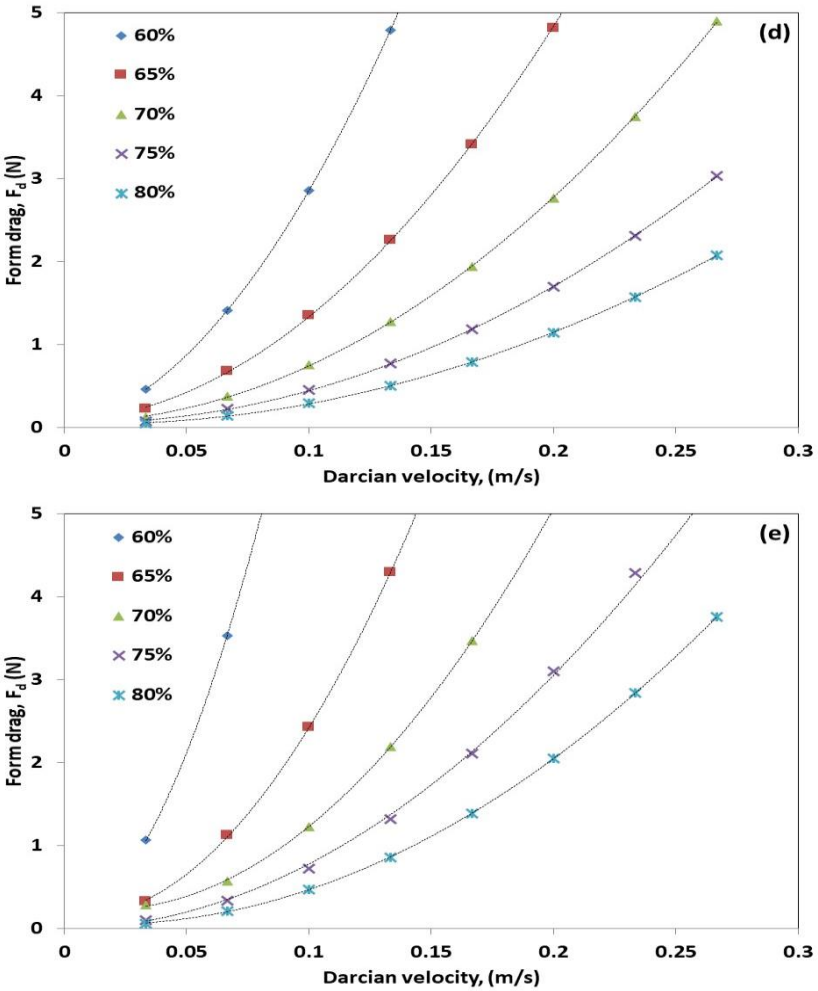

Figure 3-29 Form drag measurements for the 2D staggered structures for (a) circular, (b) hexagonal, (c) squared, (d) triangular and (e) rotated square struts at different porosity (shown in the picture)

The form drag for the staggered arrangements as shown in Figure 3-29 has a similar behaviour as in the aligned patterns. Porosity and strut shape affected form drag in a similar manner. However, the form drag for the staggered patterns is higher than the aligned patterns because of a more tortuous path in the staggered arrangements.

Figure 3-30 displays the relative contribution of form drag for all the shapes and patterns used as a function of Darcian velocity. Increasing flow velocity increased the form drag contribution. The relative distribution of form drag converges as the flow rate increases for all strut shapes because the inertial force has higher influence on the total drag force at high

flow rates. For example, the circular aligned struts showed viscous forces accounting for almost 25% to 35% of the total drag at a Darcian velocity below 0.05 m/s; as the flow rate increases, this contribution reduces to 15% to 20%.

The relative contribution of form drag decreases considerably with porosity for the staggered patterns as seen in Figure 3-30 (d) and Figure 3-30 (e). This is similar to what has been reported in the literature (Della-Torre *et al.*, 2014). As porosity increases by 5%, the relative contribution of form drag decreases by 2% up to 5% at low flow velocities and less than 2% at higher flow velocities in most of the strut shapes.

The shapes that exhibited the largest form drag contribution were the staggered squares and the rotated squares in both arrangements with the aligned rotated squares being higher. For the aligned rotated squares, almost all drag is considered as form drag at high flow rate. This is mainly because the rotated squares exhibited the largest projected area amongst all strut shapes, leading to very small gaps for the flow stream. Circular, hexagonal and triangular struts in both arrangements showed similar relative form drag contributions in most cases (65% to 85%) although the triangular struts have higher pressure drop.

Considering the arrangement of the struts, the lowest relative contribution of form drag was obtained on the aligned struts, because they function as directional channels. The aligned squared struts have the largest gap among all the strut shapes. In contrast, the staggered patterns offered higher resistance to the flow, because there is a change in flow direction every time the flow faces with a strut.

In general these results are similar to the data reported by Della-Torre *et al.* (2014). In their study for open cell foams, the relative contribution of form drag ranged from 50% to 80% from a low Reynold's number ($Re \approx 0$) to much higher Reynold's numbers ($Re > 800$). They concluded that at high Reynolds number, form drag was the major contributor to pressure drop within a porous medium.

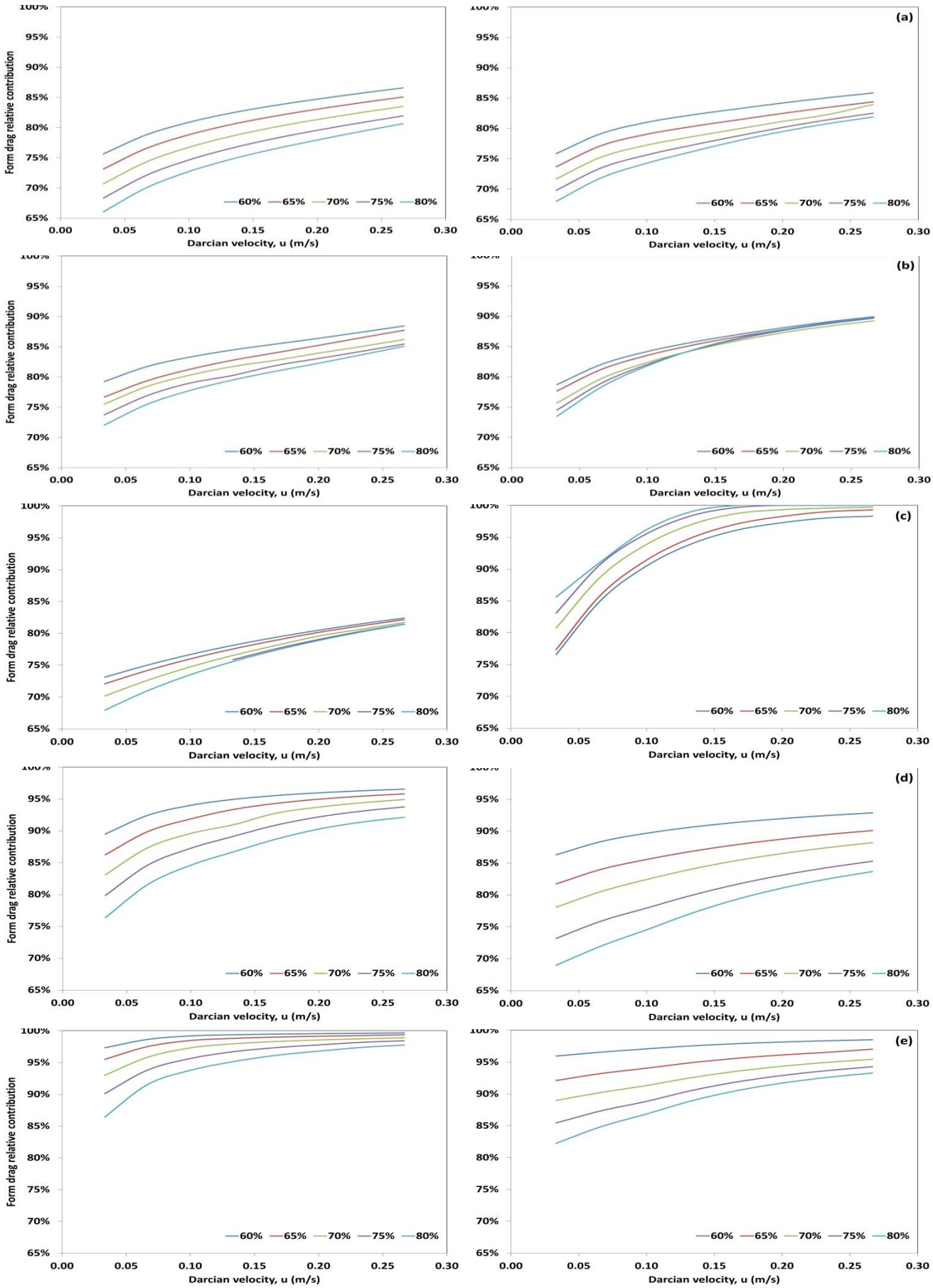

Figure 3-30 Form drag relative contribution versus flow rate for aligned (left) and staggered (right) patterns considering middle range porosities (60 to 80%) in all strut shapes: (a) ciruclar, (b) hexagonal, (c) squared, (d) triangular and (e) rotated squares

3.10 Summary

Two different 2D structures, i.e. patterned and random, were created to simulate fluid flow through porous metals. For patterned structures, five different strut shapes were used: circular, triangular, squared, rotated square and hexagonal. Two different patterns were also implemented: aligned and staggered. A random structure was created by the use of an algorithm.

Pressure drop was measured for both patterned and random structures for a wide range of flow velocities and porosities. For all the structures studied, pressure drop increases with increasing flow rate or decreasing porosity. The pressure drop increases with Darcian velocity in a quadratic behaviour, showing that there is turbulence occurring in the flow and inertial forces need to be accounted for. The permeability and form drag coefficient of each structure were calculated from the pressure drop values. This was carried out by rearranging Eq.3.22 into Eq.3.24 and implementing linear regression. The correlation factor obtained for the fitted regressions were close to $R^2 \geq 0.99$ in almost all the cases, confirming that the flow was in the Forchheimer regime.

The effects of porosity (strut spacing), strut shape and strut arrangement on permeability and form drag coefficient were analysed. Permeability increases with porosity whereas form drag coefficient decreases with porosity. Circular, squared and hexagonal struts have similar permeability and form drag coefficient values, with some differences at the low porosity of 40%. Triangular struts and rotated squares have low permeability and high form drag coefficient due to larger inertial effects.

The relationship between permeability and form drag coefficient was linear in logarithmic scale. The exponential term and the drag force coefficient were calculated. The empirical models in the literature are found not suitable for the current analysis, because they consider different geometries or require variables that are not available in the current study.

The drag force for the aligned and staggered patterns was also analysed. The total drag force was divided into: viscous drag and form drag. From these results, the relative form drag contribution was then calculated and plotted. The relative form drag contribution increased with flow rate for all cases. However, this increasing behaviour for the relative contribution of the form drag is more evident when choosing the staggered pattern.

The contribution of form drag decreased with porosity in all cases. At low flow rate, the change in form drag contribution is up to 5% every time porosity is increased by 5%, while for higher flow rates the decrease in form drag contribution is less than 2%.

Strut shape also affected the relative contribution of form drag. Hexagonal and circular struts showed similar relative contribution of form drag. Triangular struts, and rotated squares, showed the highest values of form drag even at low flow rates. The aligned squared struts had less form drag contribution than the other strut arrangements, because they created directional pores decreasing mixing in the flow stream. In contrast, the rotated squares exhibited the highest form drag contribution; because the high projected area of the struts generated more turbulence.

The pressure drop in the 2D random porous structure is in a similar range as in the triangular and rotated squares arrangements. However, the geometry creation and numerical analysis showed to be difficult and time consuming.

In conclusion, the analysis of 2D structures provides some insights into the pressure drop in porous structures, as it shows the same quadratic trend against Darcian velocity as in experimental analysis. However, the 2D models do not fully capture some of the structural characteristics such as tortuosity, pore size and metal particle size. In addition, the 2D models cannot be used to simulate conduction and convection simultaneously for the heat transfer analysis.

4 Numerical modelling of fluid flow and heat transfer in 3D structures

4.1 Introduction

This chapter presents the numerical modelling of 3D structures to simulate porous metals manufactured by the space holder technique. A representative example of this technique is the LCS process. Porous metals made by the LCS process have open-cell structures and middle range porosities $(40\% - 80\%)$. Some examples of the samples used in previous studies can be appreciated in Figure 4-1.

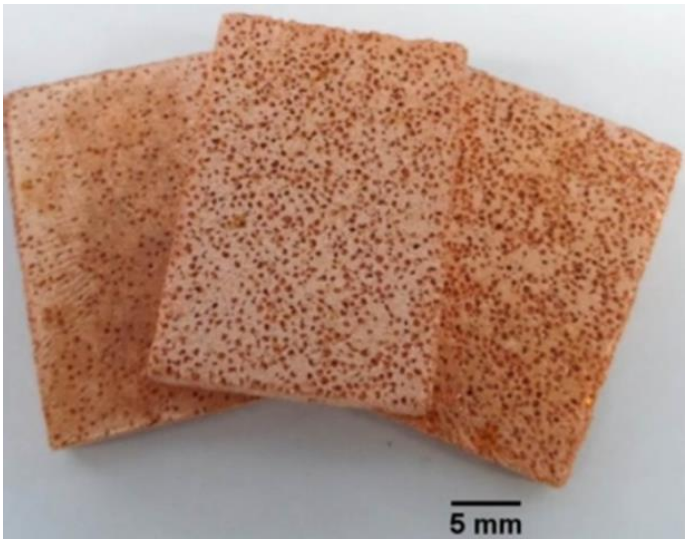

Figure 4-1 LCS porous copper samples with different porosities (Left to right: 50%, 60%, 70%; Pore size: 425-710 μm) (Baloyo, 2016)

In order to capture the main features of these porous metal samples, the characteristics considered in this study are presented in Table 4-1, which are the experimental values used by Baloyo (2016). Some of these parameters are not constant. Specifically, porosity changes from sample to sample, pore size has a range and metal particle size also has a range. In the geometry modelling, however, these parameters are considered as fixed for each sample. Porosity, pore size and metal particle size were considered to fit the parameters of

Table 4-1. The geometric parameters will be explained in the following sections of this chapter.

Table 4-1 Features of experimental samples

Characteristic	Measurements
Length [cm]	3
Height [cm]	0.5
Width [cm]	2
Porosity	$50\% - 80\%$
Pore size [μm]	$(250 - 425)$ $(425 - 710)$ $(710 - 1000)$ $(1000 - 1500)$
Metal particle size [μm]	$(30 - 70)$

ANSYS workbench and Fluent, version 14.5.7, were used throughout the simulation process and geometry creation. Simulations were carried out for fluid flow and heat transfer. The pressure drop and temperature values were used to calculate permeability, form drag coefficient and heat transfer coefficient. The numerical results obtained in the analysis were compared with experimental data. The geometry creation and simulation processes, and the results and their discussion are presented in the following sections.

4.2 Geometry creation

4.2.1 Crystalline structure based models

ANSYS workbench-Design modeller was employed to create the 3D structures. The LCS porous copper properties listed in Table 4-1 were considered. For each structural parameter a fixed value within the range of the real material was used. For example, pore size in the real material is categorised in four different ranges. For the 3D structures created in the numerical model, the selected pore size values were fixed at: 400 μm, 600 μm, 800 μm, 1000 μm and 1500 μm. Porosity had fixed values of 50%, 60%, 65%, 70%, 75% and 80%. The selected metal particle sizes were 30 μm, 50 μm and 70 μm. A simple unit cell model was chosen for the geometry construction.

It is possible to use unit cells based on the crystalline structures to simulate porous structures. Simple cubic (SC), body centred cubic (BCC) and face centred cubic (FCC) structures, as shown in Figure 4-2, are the most common unit cells.

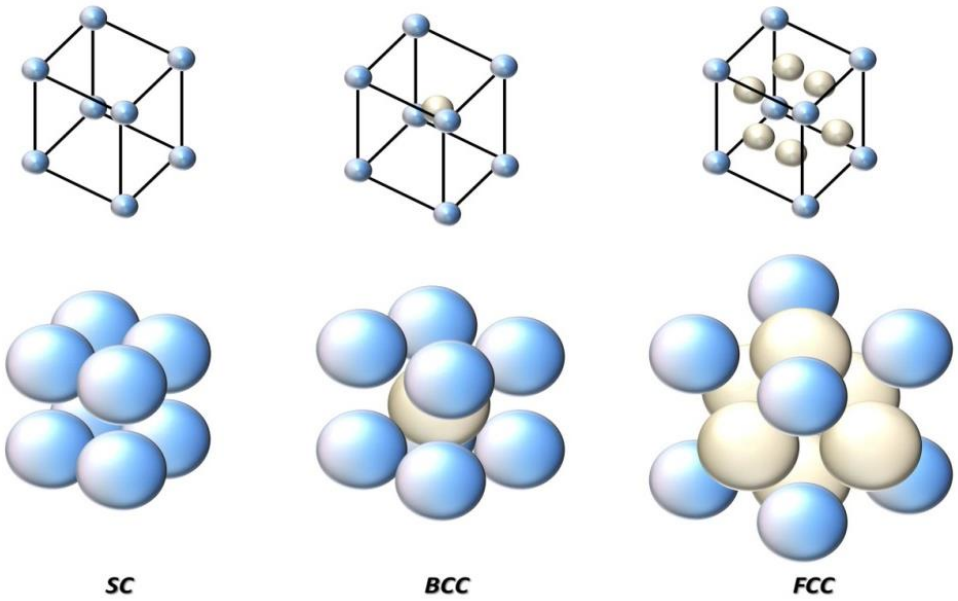

Figure 4-2 Crystalline structures used to simulate porous media in the literature

Porous structures can be created in three different ways by employing this approach. The first way is using the particles of the crystalline structure as the walls of the porous media. In other words, the empty space surrounding the spheres acts as the void volume. This technique is often used to simulate porous media with directional pores, e.g. in Xu and Jiang (2008) and Yang *et al.* (2013). The second way is using the particles as solid removal tools in the geometry creation process in order to create filament structures. The resulting geometry is used frequently to simulate open-cell metal foams with high porosities and minimal specific surface areas (Krishnan *et al.* 2006, Dukhan and Suleiman 2013). The third way is arranging the pores of the porous media as the atoms of the crystalline structure are arranged. The first way is used for low porosities (40% or less) while the second way is used for high porosities (90% or more). The third approach is less frequently used but is suitable for the middle range porosities.

Arranging pores as the atoms in a crystalline unit cell is an appropriate approach for the LCS porous copper given its porosity range. However, not all crystalline structures are suitable. The LCS porous copper has a tortuous arrangement of voids. The FCC arrangement seems to be the most appropriate option, because its atomic packing factor is close to the middle range of the porosity of the LCS porous copper. Therefore, the FCC based model was selected as the unit cell in this study.

4.2.2 Unit cell design

The particles in a FCC unit cell are arranged in a way that will create a non-linear path along the particles, i.e. pore space, for the running fluid. The atomic packing factor (a_p) of the FCC arrangement, or the porosity, can be calculated by the following expression:

$$a_p = \frac{n_p \cdot V_p}{V_c} \tag{4.1}$$

where n_p represents the number of particles in a unit cell, V_p is the volume of a single particle and V_c is the volume of the unit cell. The number of particles contained in a FCC unit cell is 4, which is easily appreciated in Figure 4-3.

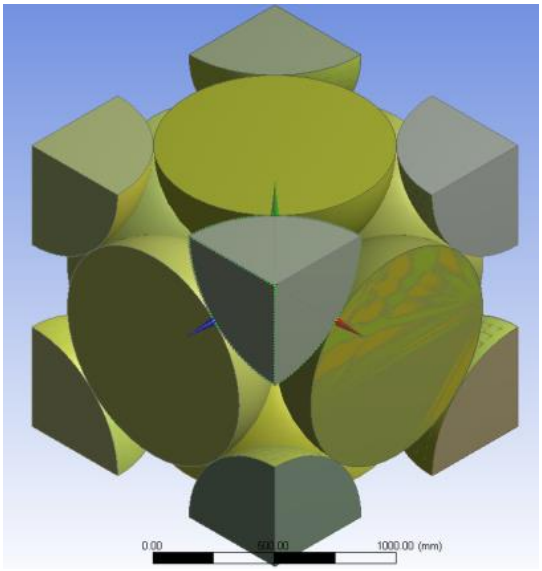

Figure 4-3 FCC particle arrangement

However, the LCS porous copper with the features as described in Table 4-1 can achieve a wide range of porosities from 50% to 80%, while the atomic packing factor of the FCC, a_p, is fixed at 74%. In order to achieve the full porosity range, the FCC model is modified so the distance between the spheres centres changes according to porosity. In other words, if the desired porosity is less than 74%, the distance between the particles is increased; if the chosen porosity is higher than 74%, the distance is decreased, meaning that the spheres will start to overlap.

In the 3D model, the diameter of the spheres will be used to determine the spacing between the spheres. This spacing will then be used to determine the size of the unit cell, one of the faces of which is shown in Figure 4-4. Here R represents the radius of the spherical particle and l_c is the side length of the unit cell. By using Pythagoras's theorem we obtain the following expression:

$$l_b = 2\sqrt{2}R = \sqrt{2}d_{sp} \tag{4.2}$$

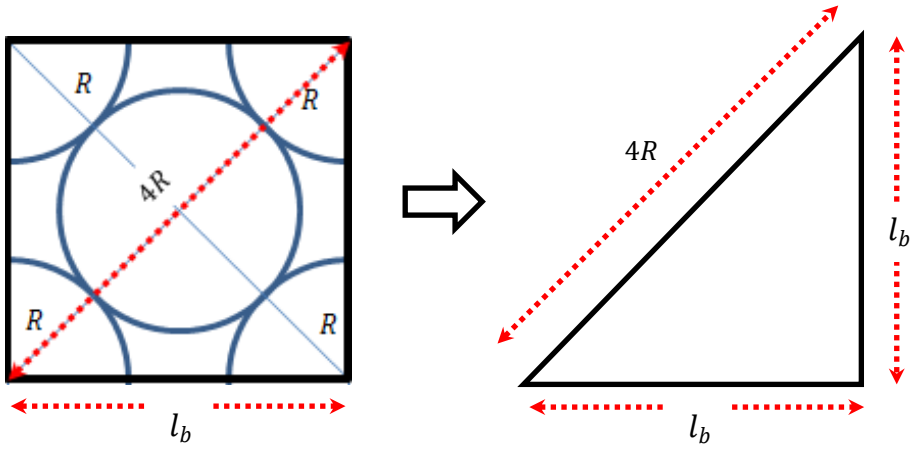

Figure 4-4 FCC cube length calculation

where d_{sp} is the diameter of a single sphere. Equation 4.2 applies to the unit cell where the particles are in contact. It provides a first base to the geometry construction. From Figure 4-4 it can be seen that the corner particles touch with the central particle along the diagonals. These touching points can be separated to change the porosity. In other words, the distance between the particles can be increased according to the desired porosity value. This increment is designated as l_t. Equation 4.2 can be modified to facilitate porosity change:

$$l_b = \sqrt{2}\left(d_{sp} + l_t\right) \tag{4.3}$$

The size of the unit cell containing all particles depends on the particle size and l_t which is related to porosity.

Combining Equation 4.1 with Equation 4.3 gives the modified atomic packing factor or porosity as:

$$a_p = \frac{4 \cdot \left(\frac{4}{3}\pi R^3\right)}{\left(\sqrt{2}\left(d_{sp} + l_t\right)\right)^3} = \frac{4\sqrt{2}}{3}\pi\left(\frac{R}{d_{sp} + l_t}\right)^3 \tag{4.4}$$

At this point, it is better to consider the particles as the pores or the potassium carbonate (K_2CO_3) particles used to create the pores. Therefore, $a_p = \varepsilon$ is the porosity and d_{sp} corresponds to the diameter of the potassium carbonate particles. Rearranging Equation 4.4 yields the distance between particles as:

$$l_t = d_{sp}\left[\sqrt[3]{\frac{\pi}{\left(3\sqrt{2}\right) \cdot \varepsilon}} - 1\right] \tag{4.5}$$

4.2.3 Coordination number and connecting cylinders calculations

In order to maintain the pore structure as open, cylinders are introduced to connect the pores. The centre line of each cylinder is collinear with the sphere centres.

The use of connecting cylinders is a realistic way to simulate the interstices formed in the LCS porous metals, where the filler material (K_2CO_3) particles only touch at certain points. The metal particles surrounding the filler particles cannot fill all the interstices and connecting channels between the pores are formed (Zhao *et al.*, 2005), as exemplified in Figure 4-5.

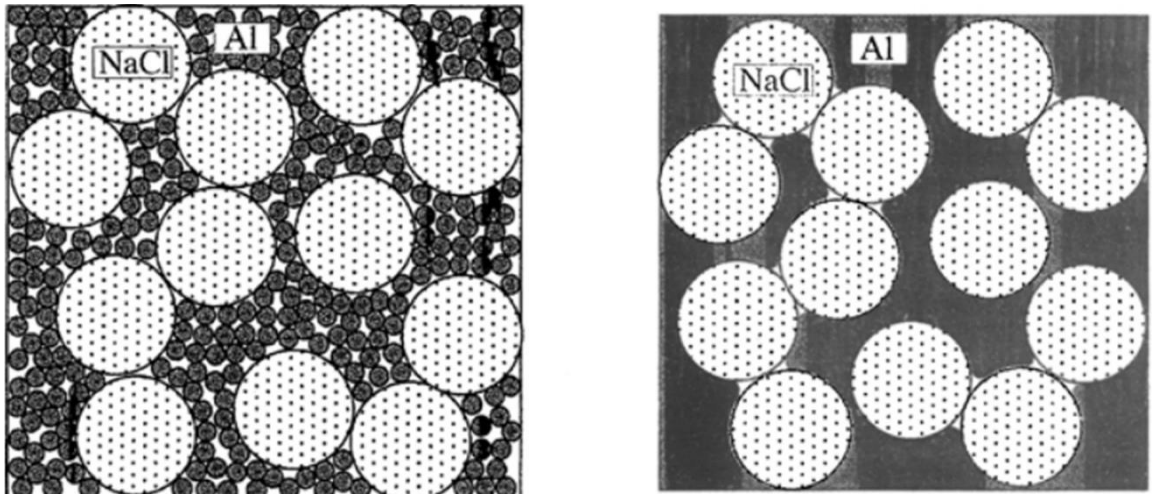

Figure 4-5 Diagrams of pore formation in Al foam from Al / NaCl powder mixture (left) to the compacted and sintered preform (right) (Zhao, 2003)

However, by including the cylinders into the model, a different issue arises. The porosity will be increased from the calculated value of Equation 4.5. Moreover, the FCC model needs to account for the number of real connections that exist between the pores in the LCS porous copper. In real material, the number of connections depends on the filler particle size, the metal particle size and porosity, while in the FCC model the number of connections remains at 12. To address both issues, the method proposed by Zhao (2003) will be used to calculate the coordination number in the LCS porous copper structures. The following factors are taken into account:

- The coordination number of the real material
- The potassium carbonate particle (K_2CO_3) size

- The metal particle (Cu) size
- All particles are considered to be spherical and have fixed sizes

Figure 4-6 depicts the interaction between the K_2CO_3 particles and the Cu particles in the manufacturing process and shows how a connecting channel is formed. Here H is the height of the spherical crown and A_{sc} its surface area, shaded in Figure 4-6. The size of the connecting channel is determined by the spherical crown. The lower case letters in Figure 4-6 represent geometric points used for creating line segments, which will be used to calculate H and A_{sc}.

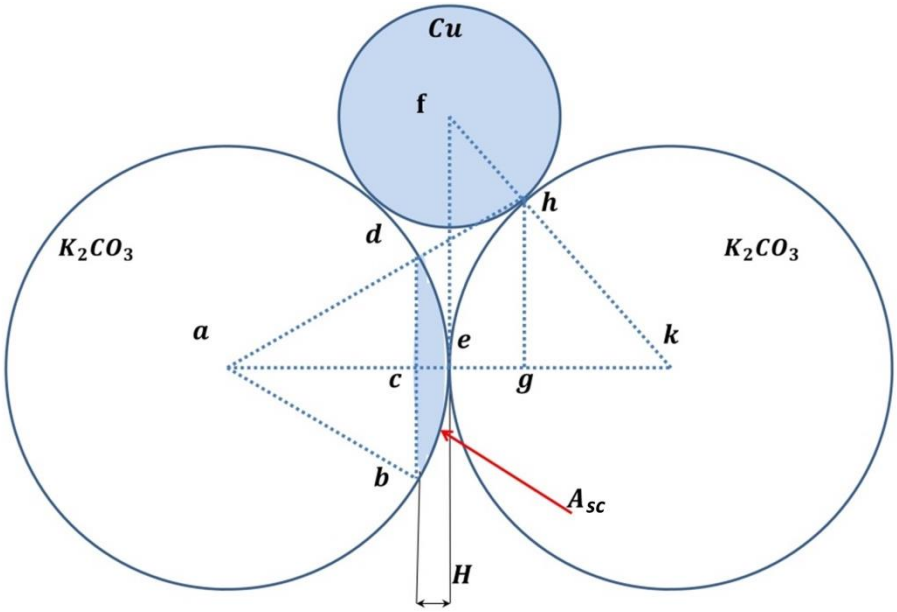

Figure 4-6 Contact between particles in Cu / K_2CO_3 powder mixture

First the $\overline{gk}$ segment in Figure 4-6 is solved. There are two similar triangles, Δkgh and Δkef, giving $\frac{\overline{hk}}{\overline{fk}} = \frac{\overline{gk}}{\overline{ek}} = \frac{\overline{gh}}{\overline{ef}}$. Given that $\overline{ek} = R$, $\overline{hf} = r$, and $\overline{fk} = r + R$, where r and R are the radii of the Cu and K_2CO_3 particles, respectively. $\overline{gk}$ can therefore be obtained by:

$$\overline{gk} = \frac{R^2}{r+R} \tag{4.6}$$

$\overline{gh}$ can simply be calculated by using the Pythagorean Theorem:

$$\overline{gh} = \sqrt{\left(\overline{gk}\right)^2 + \left(\overline{hk}\right)^2} = \left(\frac{R}{r+R}\right)\sqrt{r(2R+r)} \tag{4.7}$$

As $\overline{ag} = \overline{ak} - \overline{gk}$ then:

$$\overline{ag} = 2R - \overline{gk} \tag{4.8}$$

Once again, using the Pythagorean theorem, $\left(\overline{cd}\right)^2 + (\overline{ac})^2 = \left(\overline{ad}\right)^2 = R^2$. From another pair of similar triangles, $\Delta\mathrm{acd}$ and $\Delta\mathrm{agh}$, ,we have the following $\frac{\overline{ac}}{\overline{ag}} = \frac{\overline{ad}}{\overline{ah}} = \frac{\overline{cd}}{\overline{gh}}$. Using the above relationship $\overline{ac}$ can be calculated by:

$$\overline{ac} = \frac{R(R+2r)}{\sqrt{R^2+6Rr+5r^2}} \tag{4.9}$$

From Figure 4-6 it is appreciated that: $\mathrm{H} = \mathrm{R} - \overline{\mathrm{ac}}$. Combining this expression with Equation 4.9 and using a simplified variable: $\varphi = \frac{R}{r}$, gives:

$$H = R\left(1 - \frac{(\varphi+2)}{\sqrt{\varphi^2+6\varphi+5}}\right) \tag{4.10}$$

where φ is the $\mathrm{K_2CO_3} - \mathrm{to} - \mathrm{Cu}$ particle size ratio, i.e., the ratio between the diameters of the $\mathrm{K_2CO_3}$ and Cu particles.

The surface area of the sphere crown is given as follows:

$$A_{sc} = 2\pi RH = 2\pi R^2 \left(1 - \frac{(\varphi + 2)}{\sqrt{\varphi^2 + 6\varphi + 5}}\right) \tag{4.11}$$

The spherical crown area (A_{sc}) will be used later to calculate the coordination number, i.e. the real number of contact points that exist between the particles in the powder compact used for producing porous metals. At low porosities, there are fewer contact points between the particles. As porosity increases, the number of contact points also increases. This is different from the FCC model which has 12 contact points regardless of porosity.

The model proposed by Zhao (2003) is employed here to calculate the number of contact points in a Cu / $\mathrm{K_2CO_3}$ powder mixture. Considering a powder mixture of Cu / $\mathrm{K_2CO_3}$ having a unit net volume, if it is assumed that $\mathrm{K_2CO_3}$ has a volume fraction of f (also represents the effective porosity of the porous Cu), then the volume fraction of Cu is $(1 - f)$. The number of $\mathrm{K_2CO_3}$ particles, $n^*_{K_2CO_3}$, and the number of Cu particles, n^*_{Cu}, in the Cu / $\mathrm{K_2CO_3}$ mixture of unit volume are therefore:

$$n^*_{K_2CO_3} = \frac{f}{\frac{4}{3}\pi R^3} \tag{4.12 a}$$

$$n^*_{Cu} = \frac{1 - f}{\frac{4}{3}\pi r^3} \tag{4.12 b}$$

The total surface area of all the K_2CO_3 and Cu particles in the Cu / K_2CO_3 mixture per unit volume is therefore:

$$S = n^*_{K_2CO_3} 4\pi R^2 + n^*_{Cu} 4\pi r^2 = \frac{3f}{R} + \frac{3(1-f)}{r} \tag{4.13}$$

Direct contact between two spherical K_2CO_3 particles in the Cu / K_2CO_3 mixture will form a neck, which will result in a window between the two resultant primary pores in the porous Cu sample. Every K_2CO_3 sphere crown potentially in contact with another K_2CO_3 particle can be treated as a contact point. The total number of such contact points is (Zhao, 2003):

$$N^* = \frac{n^*_{K_2CO_3} \cdot S_{K_2CO_3}}{A_{sc}} \tag{4.14}$$

where $S_{K_2CO_3}$ is the surface area of a single K_2CO_3 particle. The density of such contact points per unit surface area is therefore:

$$\lambda = \frac{N^*}{S} \tag{4.15}$$

The average number of K_2CO_3 / K_2CO_3 contacts on a single K_2CO_3 particle in the Cu / K_2CO_3 powder mixture can be calculated by (Diao, Xiao and Zhao, 2015):

$$\mu_c = \lambda S_{K_2CO_3} = \frac{2R}{H\left(1 - \varphi + \frac{\varphi}{\varepsilon}\right)} \tag{4.16}$$

This averaged number of contact points is also called the coordination number. It depends not only on φ, but also on the volume fraction of the $\mathrm{K_2CO_3}$ in the mixture or the porosity ε.

To calculate the cylinder radius (r_c), the projected area of the sphere crown $\left(A_{psc}\right)$ needs to be calculated as shown in Figure 4-7.

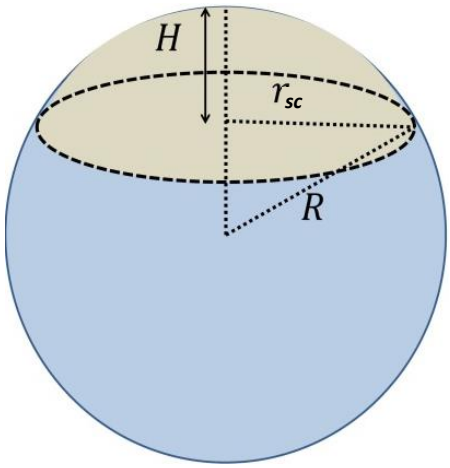

Figure 4-7 Spherical crown terms

The projected area of the sphere crown can be obtained from the radius of the sphere crown $\mathrm{r_{sc}}$, $\left(\mathrm{A_{psc}} = \pi \mathrm{r_{sc}}^2\right)$, which can be obtained using the height of the sphere crown (H):

$$r_{sc} = \sqrt{H(2R - H)} \tag{4.17}$$

Equation 4.17 can be obtained by using the Pythagorean theorem in Figure 4-7 and solving for r_{sc}. As the number of sphere crowns on any of the K_2CO_3 particles is μ, the total projected area created by the windows between the K_2CO_3 particles is: $\mu_c A_{psc}$.This total projected area

can be divided by the 12 contact points of the FCC structure to give the area of each of the 12 windows. This area can be taken as the cross sectional area of the connecting cylinders. The following expression can therefore be used to calculate the radius of the cylinders (r_c):

$$r_c = \sqrt{\frac{\mu_c \cdot A_{psc}}{12\pi}} \tag{4.18}$$

With the inclusion of the cylinders in the unit cell, porosity will increase. This change is barely noticeable with large particles, but can be significant for smaller particles. Therefore the cylinder length (l_t) needs to be adjusted to obtain an accurate porosity. The new cylinder length (l_{t*}) is specific for each unit cell and is obtained by trial and error for each of the geometries used in the present study. As an example,

Table 4-2 provides the calculations made for the geometries with a pore size of 400 μm, different metal particle sizes and different porosities. It can be seen from the actual porosity column that porosity increases with the addition of the cylinders in all cases. For porosities above 74% however, the cylinder length becomes negative, meaning that the particles overlap. In order to avoid confusion, the distance between the particle centres is used instead and is designated as the length between centres (l_{cc}). This new parameter included in Table 4-2 can be calculated by considering the radius of the two particles plus the cylinder length. This process was performed for the other geometries. In this study, the pore diameters were chosen to be: 400 μm, 600 μm, 800 μm, 1000 μm and 1500 μm. The selected values for the metal particle size were 30 μm, 50 μm and 70 μm. For porosity, the following fixed values were chosen: 50%, 60%, 65%, 70%, 75% and 80%. In total 90 different unit cells were created by employing the same procedure to calculate the parameters in Table 4-2.

Table 4-2 Parameters used to construct the unit cells with a pore size of 400 and different porosities and metal particle sizes.

ε	Cu diameter [μm]	μ_c	H [μm]	r_{sc} [μm]	A_{psc} [μm^2]	φ	$\mu \cdot A_{psc}$ [μm^2]	r_c [μm]	l_t [μm]	Actual Porosity	l_{t*} [μm]	l_{cc} [μm]
50%	30	2.58	10.82	64.90	1.32E+04	13.33	3.41E+04	24.95	55.94	51.4%	60.6	460.60
	50	2.94	15.10	76.24	1.83E+04	8.00	5.37E+04	30.08		52.3%	63.87	463.87
	70	3.29	18.10	83.13	2.17E+04	5.71	7.15E+04	34.24		53.2%	67.15	467.15
60%	30	3.74	10.82	64.90	1.32E+04	13.33	4.95E+04	40.82	29.06	61.4%	32.7	432.70
	50	4.18	15.10	76.24	1.83E+04	8.00	7.64E+04	43.54		62.3%	35.44	435.44
	70	4.60	18.10	83.13	2.17E+04	5.71	9.98E+04	21.83		63.1%	38.29	438.29
65%	30	4.52	10.82	64.90	1.32E+04	13.33	5.98E+04	36.22	17.76	66.2%	20.69	420.69
	50	4.99	15.10	76.24	1.83E+04	8.00	9.11E+04	41.01		67.1%	23.11	423.11
	70	5.42	18.10	83.13	2.17E+04	5.71	1.18E+05	45.01		67.9%	25.71	425.71
70%	30	5.51	10.82	64.90	1.32E+04	13.33	7.28E+04	51.45	7.57	70.9%	9.57	409.57
	50	5.98	15.10	76.24	1.83E+04	8.00	1.09E+05	24.19		71.6%	11.61	411.61
	70	6.41	18.10	83.13	2.17E+04	5.71	1.39E+05	33.32		72.4%	13.95	413.95
75%	30	6.79	10.82	64.90	1.32E+04	13.33	8.98E+04	44.94	-1.7	75.4%	-0.88	399.12
	50	7.22	15.10	76.24	1.83E+04	8.00	1.32E+05	49.17		76.0%	0.7	400.7
	70	7.61	18.10	83.13	2.17E+04	5.71	1.65E+05	52.76		76.7%	2.7	402.7
80%	30	8.53	10.82	64.90	1.32E+04	13.33	1.13E+05	26.96	-10.18	79.6%	-11.01	388.99
	50	8.83	15.10	76.24	1.83E+04	8.00	1.61E+05	36.95		80.1%	-9.97	390.03
	70	9.10	18.10	83.13	2.17E+04	5.71	1.98E+05	43.96		80.7%	-8.3	391.7

An example of the final unit cell structure is shown in Figure 4-8. The unit cell represents a structure with 50% porosity and 800 μm pore diameter. The copper particle size used is 70 μm. The diagram on the left shows the solid walls while the diagram on the right shows how the pores are interconnected by cylinders.

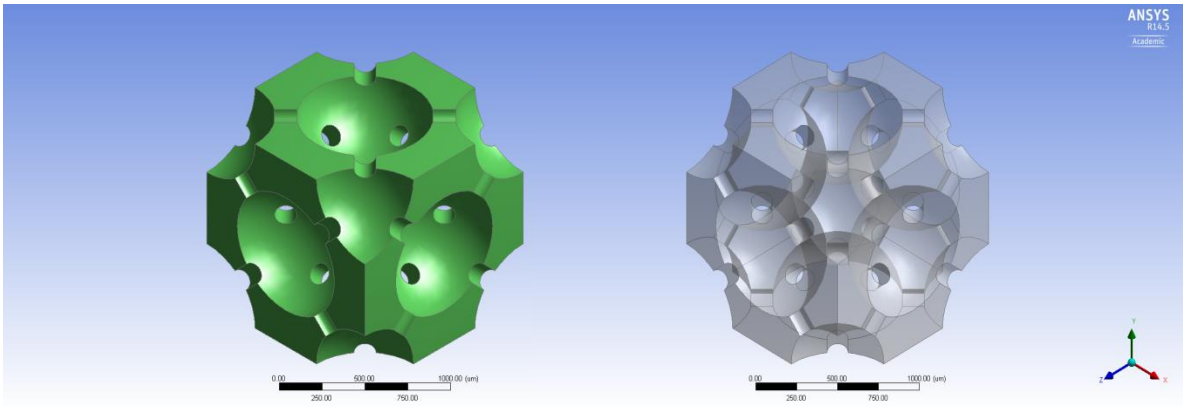

Figure 4-8 Isometric view of a 3D Unit cell with a porosity of 50%, pore size of 800 μm and metal particle size of 70 μm

The unit cells with porosity of 80% showed some limitations for some particle size ratios (φ). As the pore size ratio increases, it becomes more complex to achieve the right values for the cylinder radius and cylinder length. The situation becomes worse for unit cells with pore sizes of 800, 1000 and 1500 μm. This is mainly because the pore size is too big in comparison to the metal particle size, creating an overlapping region much bigger than the calculated cylinder radius (r_c). Therefore, some of the results for these unit cells are not presented.Table 4-3 shows a full list of the geometrical values obtained for all unit cells. Only coordination number, cylinder radius and length between particle centres are presented as these parameters are the main values needed to achieve a specific porosity value.

Table 4-3 Geometric parameters used for the creation of unit cells for different pore sizes, porosities and metal particle sizes

		Pore size of 400 µm			Pore size of 600 µm			Pore size of 800 µm			Pore size of 1000 µm			Pore size of 1500 µm		
ε	*Cu diameter [µm]*	μ_c	r_c [µm]	l_{cc} [µm]	μ_c	r_c [µm]	l_{cc} [µm]	μ_c	r_c [µm]	l_{cc} [µm]	μ_c	r_c [µm]	l_{cc} [µm]	μ_c	r_c [µm]	l_{cc} [µm]
50%	30	2.58	30.08	460.6	2.39	37.42	688.6	2.29	43.56	916.75	2.24	48.94	1144.4	2.16	60.36	1714.50
	50	2.94	37.76	463.87	2.64	47.33	691.85	2.49	55.34	919.85	2.39	62.36	1147.60	2.26	77.21	1717.60
	70	3.29	43.54	467.15	2.88	54.96	695.10	2.67	64.51	923.10	2.54	72.88	1150.80	2.36	90.57	1720.80
60%	30	3.74	36.22	432.7	3.50	45.29	647.2	3.38	52.87	861.75	3.31	59.51	1076.05	3.21	73.56	1612.45
	50	4.18	45.01	435.44	3.81	56.89	649.85	3.62	66.81	864.30	3.50	75.49	1078.60	3.34	93.82	1614.95
	70	4.60	51.45	438.29	4.11	65.62	652.60	3.85	77.47	866.97	3.69	87.83	1081.20	3.47	109.70	1617.45
65%	30	4.52	39.82	420.69	4.27	49.98	629.47	4.13	58.46	838.33	4.05	65.88	1047	3.94	81.57	1569.20
	50	4.99	49.17	423.11	4.60	62.48	631.70	4.39	73.59	840.47	4.27	83.30	1049.05	4.09	103.80	1571.20
	70	5.42	55.88	425.71	4.92	71.76	634.15	4.64	85.03	842.80	4.47	96.64	1051.30	4.23	121.13	1573.25
70%	30	5.51	43.96	409.57	5.24	55.42	613.2	5.11	64.99	816.9	5.02	73.35	1020.45	4.91	91.02	1529.90
	50	5.98	53.82	411.61	5.59	68.86	614.93	5.38	81.41	818.50	5.24	92.37	1021.90	5.06	115.49	1531.20
	70	6.41	60.75	413.95	5.91	78.66	617.00	5.63	93.65	820.33	5.45	106.77	1023.63	5.21	134.41	1532.70
75%	30	6.79	48.81	399.12	6.55	61.93	597.95	6.42	72.86	796.95	6.34	82.41	995.8	6.23	102.55	1493.60
	50	7.22	59.15	400.70	6.87	76.32	599.13	6.67	90.67	797.82	6.55	103.21	996.50	6.38	129.62	1494.00
	70	7.61	66.20	402.70	7.16	86.58	600.70	6.90	103.71	799.12	6.74	118.70	997.60	6.51	150.31	1494.75
80%	30	8.53	54.71	388.99	8.37	70.00	583.32	8.28	82.75	777.83	8.23	93.87	972.15	8.15	117.31	1458.40
	50	8.83	65.40	390.03	8.58	85.33	583.75	8.45	102.05	777.93	8.37	116.67	972.15	8.25	147.46	1458.40
	70	9.10	72.40	391.70	8.78	95.91	584.80	8.61	115.80	778.50	8.50	133.27	972.40	8.34	170.11	1458.40

4.2.4 Representative elementary volume

Before starting with the numerical analysis it is important to determine the number of unit cells needed to achieve accurate results. For this purpose, 1, 2, 5 and 8 unit cells were joined together and tested for pressure drop and heat transfer coefficient calculations (see sections 4.4 and 4.5 for calculation details). The geometries used can be seen in Figure 4-9. The pattern tool inside Design modeller was employed to create the additional unit cells.

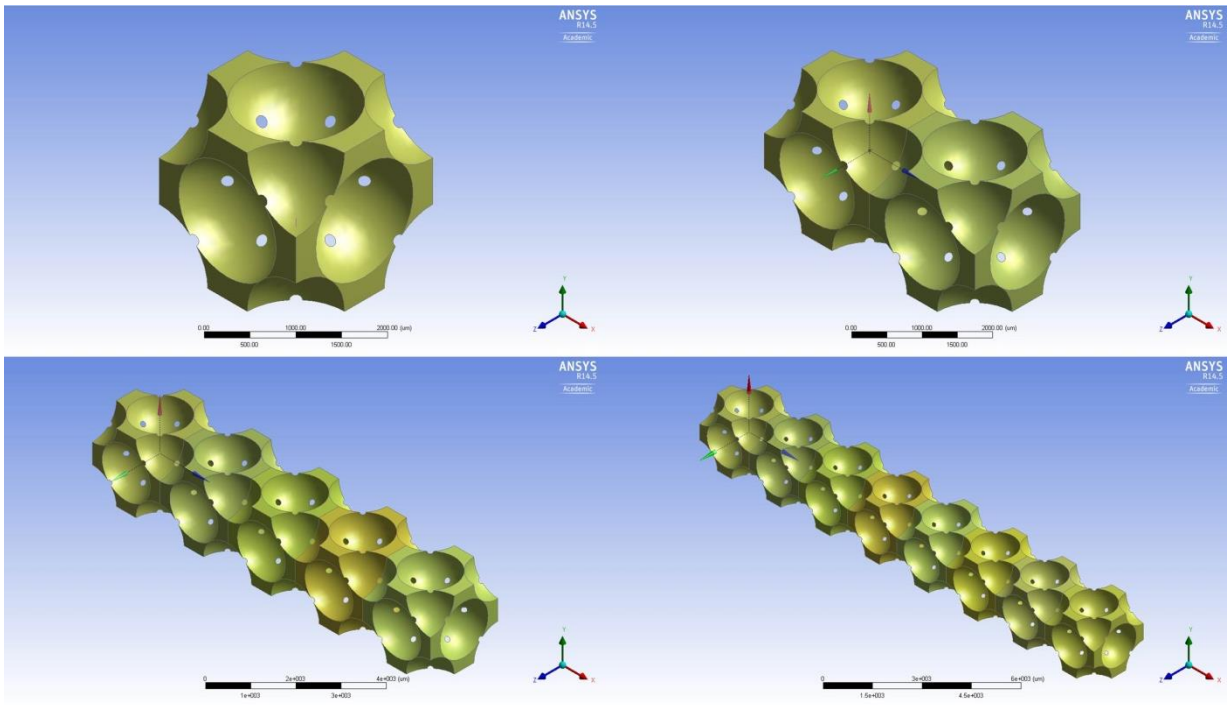

Figure 4-9 Representative elementary volumes with different numbers of unit cells

The predicted values of pressure drop and heat transfer coefficient versus the number of unit cells can be appreciated in Figure 4-10. It is shown that the normalised-pressure drop is not much affected by the number of unit cells over all the flow rates tested. Kopandis et al. (2010) attributed this almost asymptotical behaviour to the use of the fixed inlet boundary condition leading to a fully developed fluid at the entry region. The normalization of the

pressure values also reduces the effects of the length of the porous metal which is related to the number of unit cells employed during the numerical analysis.

The heat transfer coefficient showed a different behaviour. The heat transfer coefficient decreased when the number of unit cells was increased. The difference between one unit cell and two unit cells is between 35% and 15%, depending on the flow rate. As the flow rate increases, the difference of the heat transfer coefficient between the numbers of unit cells decreases. Nonetheless, the heat transfer coefficient approaches a steady value when five or more unit cells were used. The difference of heat transfer coefficient between 5 unit cells and 8 unit cells is about 5% for the low flow rates and about 2% for the higher flow rates.

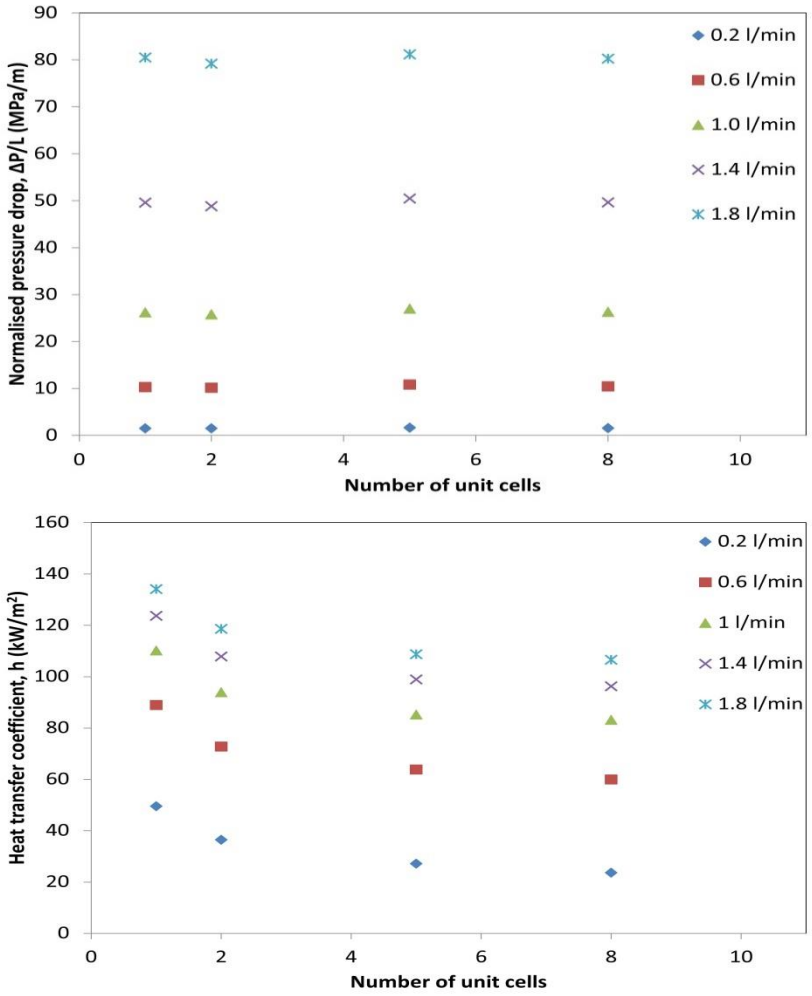

Figure 4-10 Normalised pressure drop (top) and heat transfer coefficient analysis (bottom) versus number of unit cells at different flow rates

It is advisable not to employ an excessive number of unit cells as they will require more simulation time. Dukhan and Suleiman (2013) carried out a numerical analysis of flow in porous media in the entry region. Their numerical results for pressure drop and velocity stabilised after 5 unit cells. Therefore, for the rest of the analysis in this study, the number of unit cells used for all geometries will be set to 5. These 5 unit cells are joined to form the 3D representative elementary volume (REV).

4.3 Governing equations and boundary conditions

The governing equations are similar to the equations presented in Chapter 3. The heat conduction equation for the solid parts is (Jiang and Lu 2006):

$$\nabla \cdot (k_s \nabla T_s) = 0 \tag{4.19}$$

and the energy equation for the fluid is:

$$\rho C_p v \cdot \nabla T = \nabla \cdot \left(k_f \nabla T_f\right) \tag{2.49}$$

The governing equations for an uncompressible fluid in motion can be solved when the boundary conditions and the initial conditions are specified. The fluid in this study is water and the solid material is copper. The standard $\mathrm{k} - \varepsilon$ model was used in all the simulations, with enhanced wall treatment activated. The energy calculation option was also activated in the simulations. At the solid-fluid interface, the non-slip condition was used and the temperature and heat flux rate were maintained.

The boundaries used for the numerical analysis can be seen in Figure 4-11. The computational domain is an assembly of three parts: the REV, which is made of 5 unit cells;

the solid heated block that is made of solid copper having the same length as the REV; and the fluid channel, which is composed of three different fluid parts, upstream, interior and downstream. The downstream channel has the same length as the upstream channel. The flow stream channel used is long enough for the fluid to fully develop. All solid bodies are highlighted in blue, while the fluid space is shown as translucent.

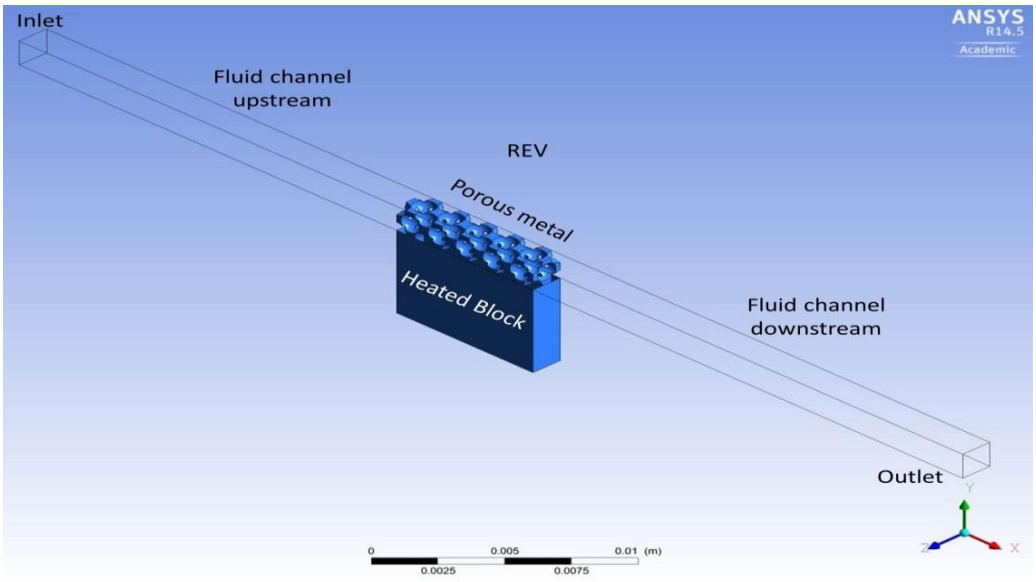

Figure 4-11 Boundary conditions used for the 3D structure

The model comprised of one velocity inlet set at the entrance of the flow channel and a pressure outlet at the end of the same channel. The volumetric flow rate used in the numerical analysis ranged from 0.2 l/min to 1.8 l/min. A constant heat flux is set at the boundary of the heated block (J = 250 kW/m^2). The heat is being transferred from the heated block underneath the REV via conduction. The heat is removed from the REV by forced convection. The left and right sides of the whole geometry were set as symmetrical. The initial temperature for the whole geometry was set as $300\ \mathrm{K}$. All the governing equations were solved numerically inside the simulation domain. Rigorous numerical computations were performed for a wide range of porosity (50% to 80%), pore size $(400\mu\mathrm{m} - 1500\mu\mathrm{m})$, metal particle size $(30\mu\mathrm{m} - 70\mu\mathrm{m})$ and flow rate (0.2 l/min to 1.8 l/min).

4.4 Mesh quality and convergence criterion

Similar to the 2D analysis, the governing equations were solved by discretising the flow domain in several control volumes. The default meshing tools were used. In the sizing pane, the relevance centre was changed to fine in order to have smaller elements where needed. Smoothing and face swapping are tools that complement the mesh generation process by increasing the quality of the final mesh. In this case, only smoothing was used to reposition the nodes with lower quality. A Multi-Zone method was included for the heated block part, because it has a regular shape. The Multi-Zone method creates a mesh with pure hexahedral elements. By implementing all the aforementioned techniques the quality of the mesh was improved and the accuracy was enhanced in the heat transfer interface near the heated block. There are five different interfaces in the connections panel: the pore walls with the fluid inside the porous metal, the REV wall with the upstream, the REV wall with the downstream, the heated block with the REV wall, and the heated block with the fluid inside the REV. These regions are where heat transfer takes place. To make sure the analysis results are comparable, the number of faces was set to be the same for all simulations. For a REV with 5 unit cells, the number of faces for each interface is shown in Table 4-4.

Table 4-4 Number of faces for each interface inside the numerical domain

Connection	Contact	Target
Pore-Fluid (interior)	214	214
REV-Fluid (upstream)	4	4
REV-Fluid (downstream)	4	4
Heated block-REV	1	36
Heated block-Fluid (interior)	1	1

The overall orthogonal quality for the 3D structures was close to 0.99 with a small number of poor elements of 0.3. In order to improve the quality of these elements, the smooth/swap mesh tool in Fluent was used. An example of the final mesh can be seen in Figure 4-12.

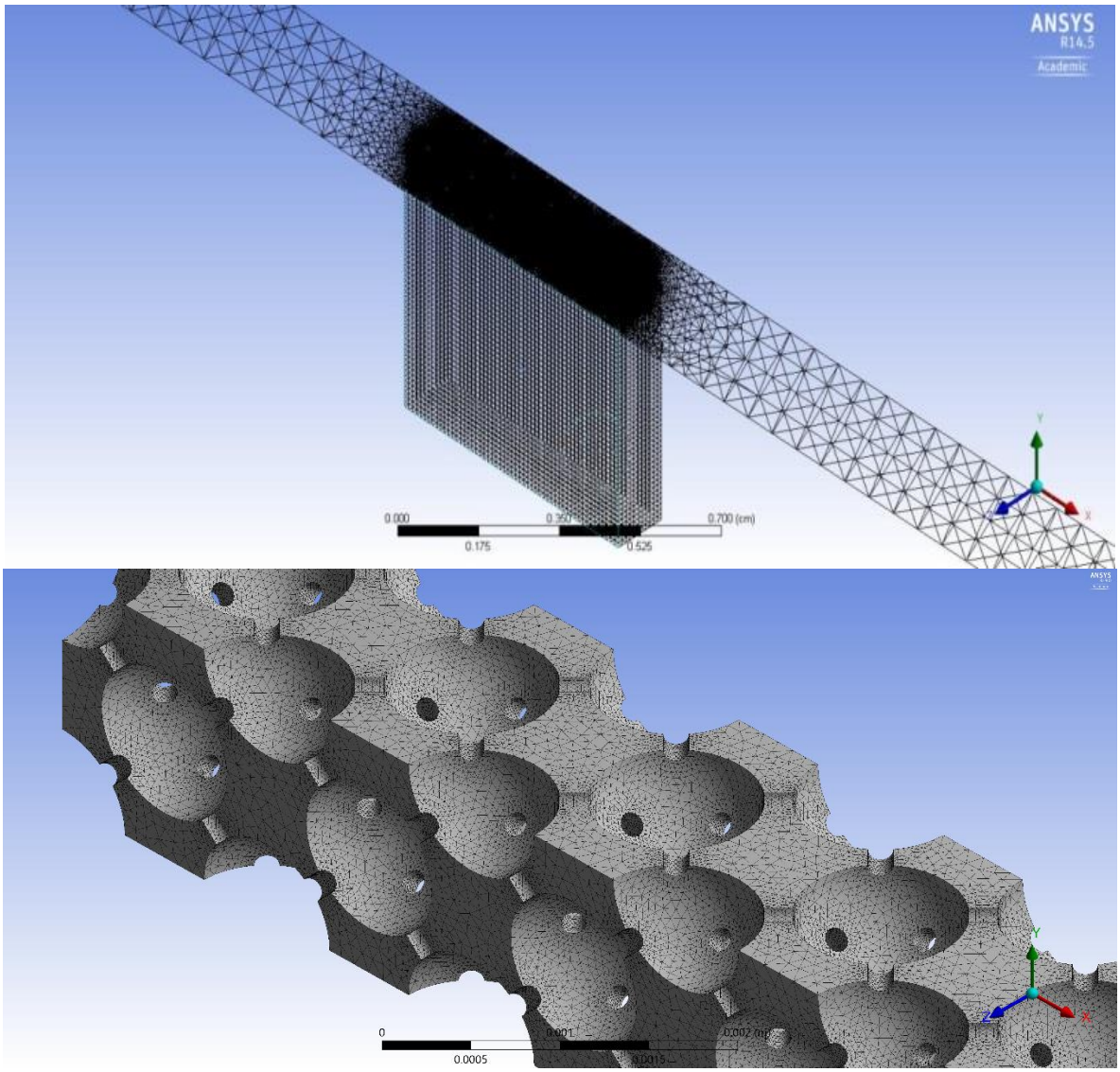

Figure 4-12 Example of the mesh used for the 3D REV structures (top) and local mesh used for the 3D REV (bottom)

The numerical computations were considered to be converged when all the residuals of the variables were below 10^{-6}. Double precision was active in all simulations in order to improve accuracy.

4.5 Fluid flow

4.5.1 Normalised pressure drop

For the pressure drop calculations, the characteristics of the 3D REVs used were: pore diameters of 400 μm, 600 μm, 800 μm, 1000 μm and 1500 μm; metal particle size of 30 μm, 50 μm and 70 μm and porosity of 50%, 60%, 65%, 70%, 75% and 80%. The volumetric flow rate used ranged from 0.2 l/min to 1.8 l/min corresponding to a Darcian velocity from 0.03 m/s to 0.3 m/s. From the numerical analysis, the pressure drop between the inlet and outlet of the porous structure (REV) was calculated and then normalised using the length of the REV. The normalised-pressure drop (ΔP/L) for the 3D structures with a metal particle size of 30 μm was plotted against Darcian velocity as shown in Figure 4-13.

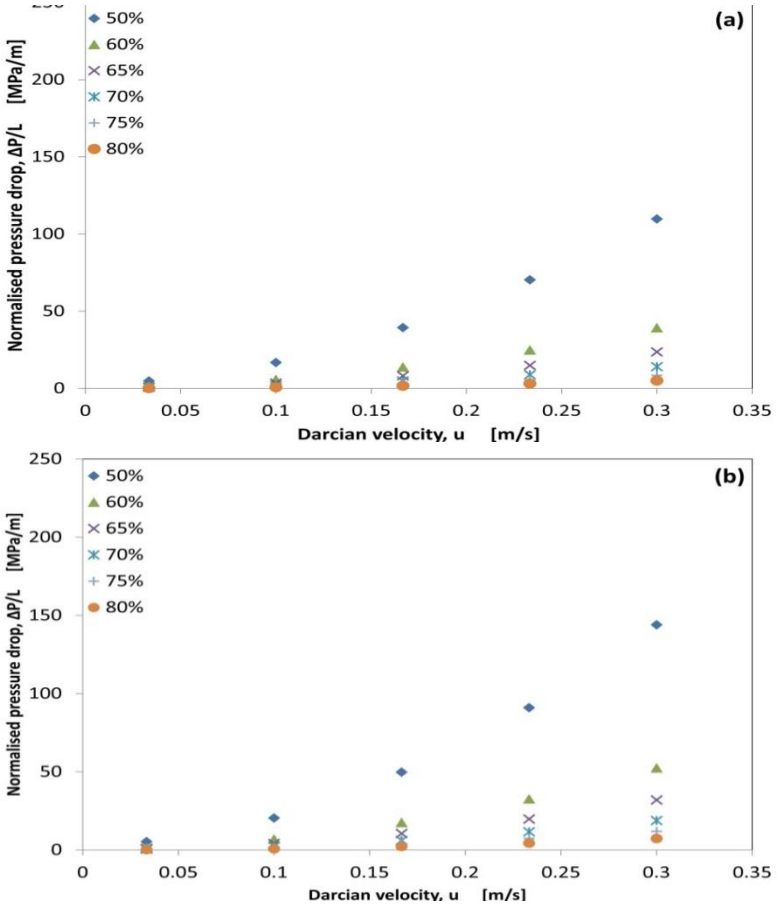

Figure 4-13 Length-normalised pressure drop (ΔP/L) versus Darcian velocity (u) for 3D REVs with porosity ranging from 50% to 80%, metal particle size of 30 μm, and pore size of: (a) 400 μm, (b) 600 μm, (c) 800 μm, (d) 1000 μm and (e) 1500 μm (to be continued)

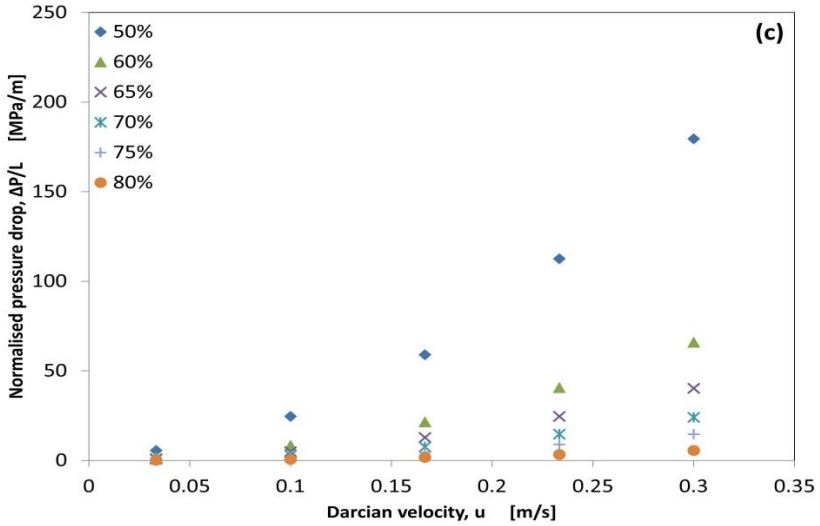

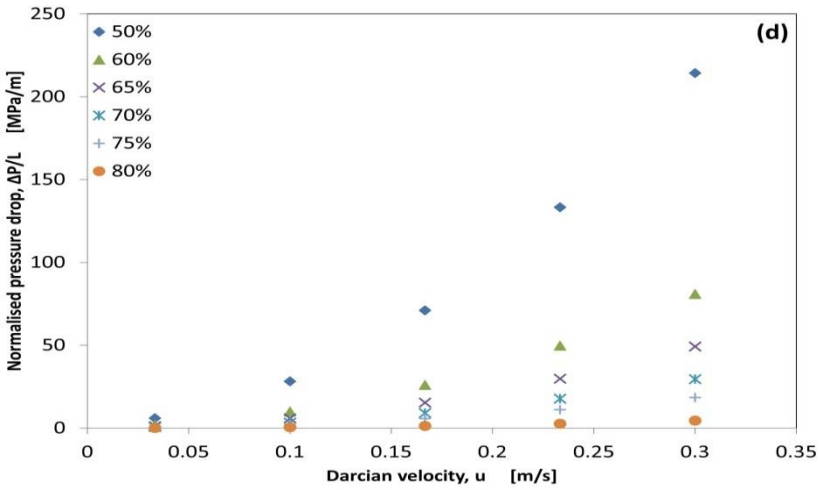

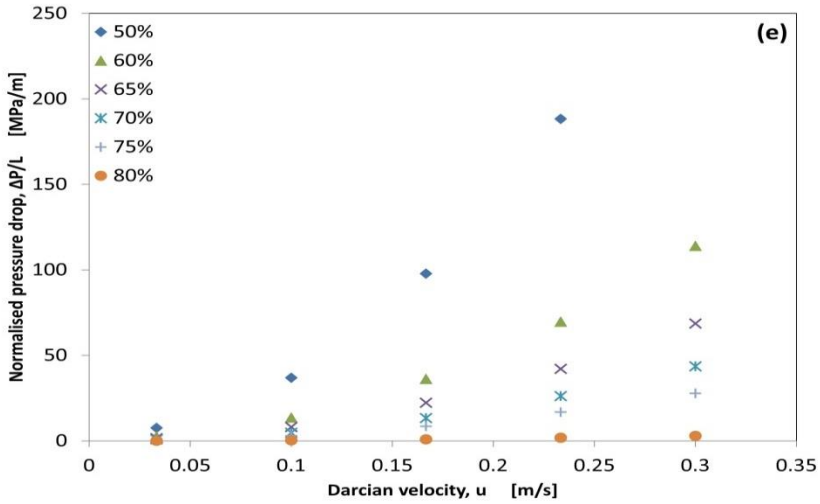

Figure 4-13 (Continuation) Length-normalised pressure drop (ΔP/L) versus Darcian velocity (u) for 3D REVs with porosity ranging from 50% to 80%, metal particle size of 30 μm, and pore size of: (a) 400 μm, (b) 600 μm, (c) 800 μm, (d) 1000 μm and (e) 1500 μm

Several observations can be made from the results for the normalise-pressure drop. First, the pressure drop increased in with increasing fluid velocity, following a quadratic behaviour in all cases. This means that the fluid is no longer in the Darcian regime and there are inertial effects occurring on the flow stream. Therefore, the flow can be considered to be in the Forchheimer regime. Second, the plots showed a negative relation between pressure drop and porosity. For all cases pressure drop decreased with increasing porosity. This was expected as high porosity structures have less surface area in the solid material, generating less drag force against the fluid. The highest pressure drop was obtained with a combination of the lowest porosity (50%) and pore size of 1500 μm. In contrast, the structure with the highest porosity gave the lowest pressure drop in all pore size categories. Third, there is positive relationships between the pressure drop and pore size, i.e., when the pore size is increased, the pressure drop also increases.

Similar behaviours were observed for the REVs with metal particle sizes of 50 μm and 70 μm as shown in Figure 4-14 and Figure 4-15 respectively. Pressure drop also increased in a quadratic fashion with increasing Darcian velocity. Increasing porosity also led to a decrease in the pressure drop. In addition, pore size also affected pressure drop in a positive manner.

Increasing the metal particle size from 30 μm to 50 μm and then to 70 μm led to decreases in the pressure drop because the cylinder diameter is increased with larger metal particles. The highest normalised pressure drops registered in Figure 4-13, Figure 4-14 and Figure 4-15 were over 250 MPa/m, 120 MPa/m and 60 MPa/m respectively.

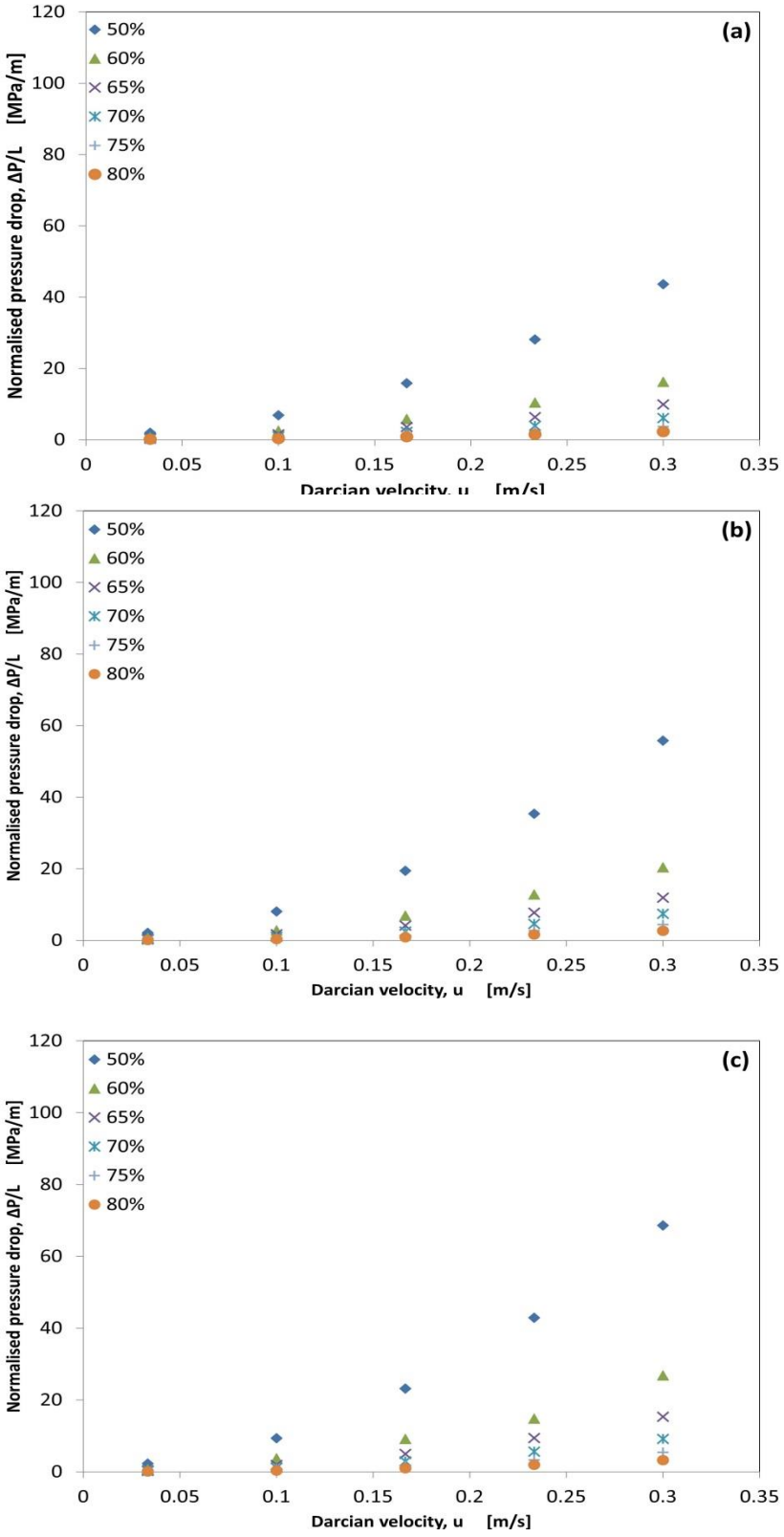

Figure 4-14 Length-normalised pressure drop (ΔP/L) versus Darcian velocity (u) for 3D REVs with porosity ranging from 50% to 80%, metal particle size of 50 μm, and pore size of: (a) 400 μm, (b) 600 μm, (c) 800 μm, (d) 1000 μm and (e) 1500 μm

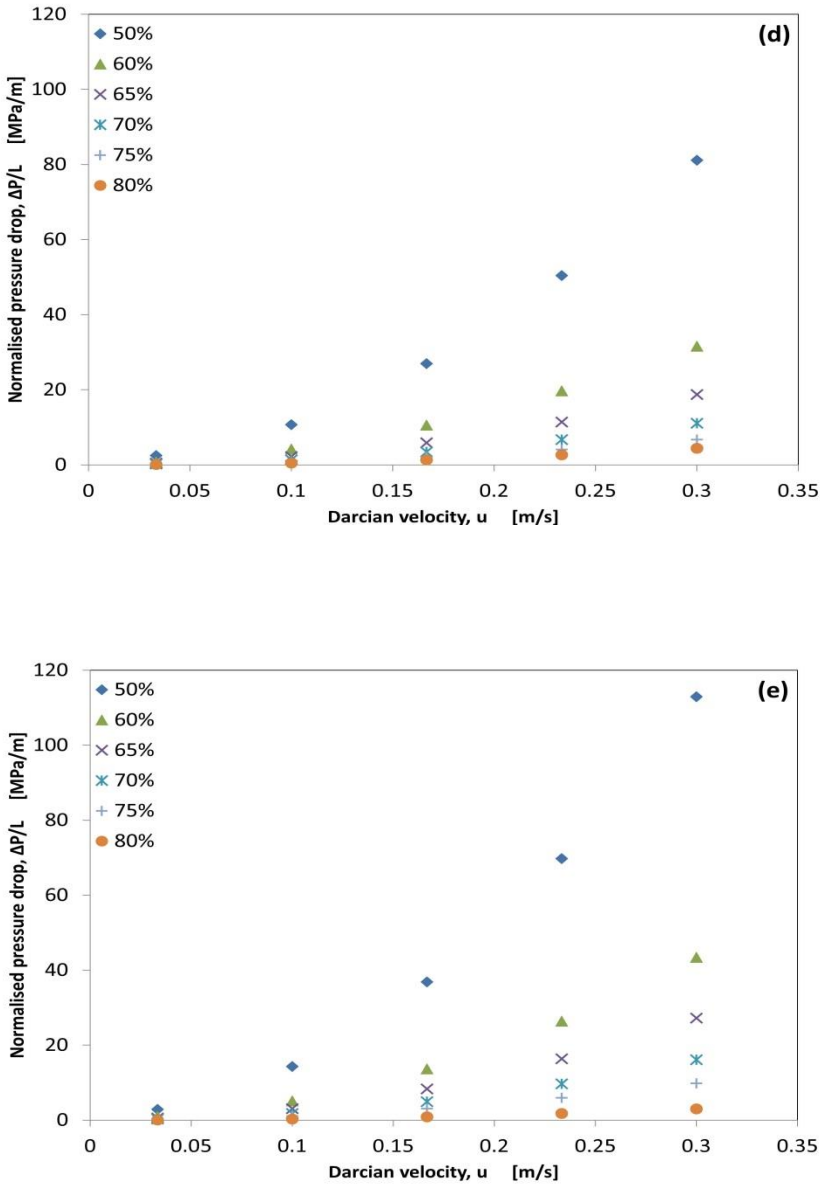

Figure 4-14 (Continuation) Length-normalised pressure drop (ΔP/L) versus Darcian velocity (u) for 3D REVs with porosity ranging from 50% to 80%, metal particle size of 50 µm, and pore size of: (a) 400 µm, (b) 600 µm, (c) 800 µm, (d) 1000 µm and (e) 1500 µm

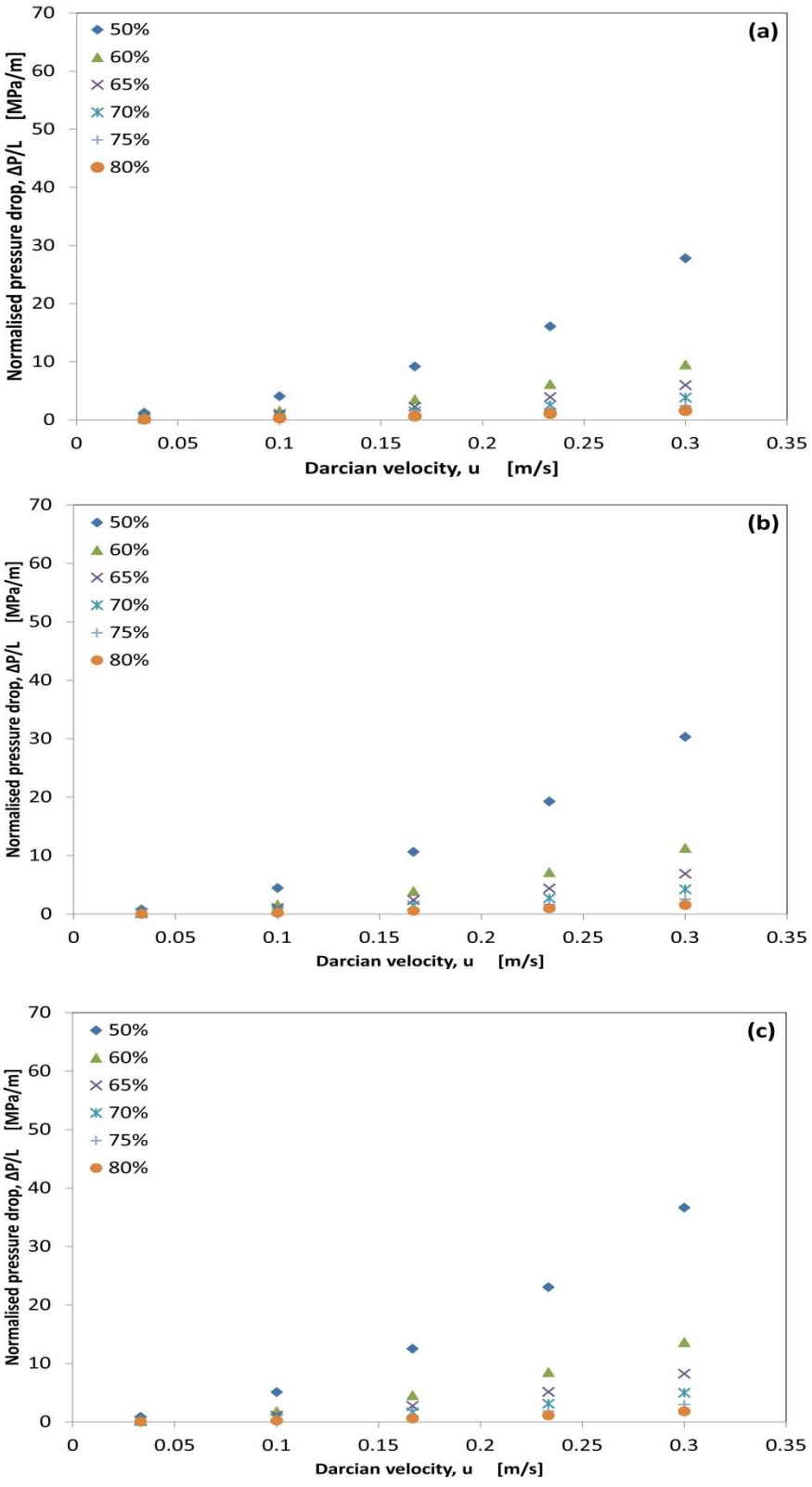

Figure 4-15 Length-normalised pressure drop (ΔP/L) versus Darcian velocity (u) for 3D REVs with porosity ranging from 50% to 80%, metal particle size of 70 μm, and pore size of: (a) 400 μm, (b) 600 μm, (c) 800 μm, (d) 1000 μm and (e) 1500 μm (to be continued)

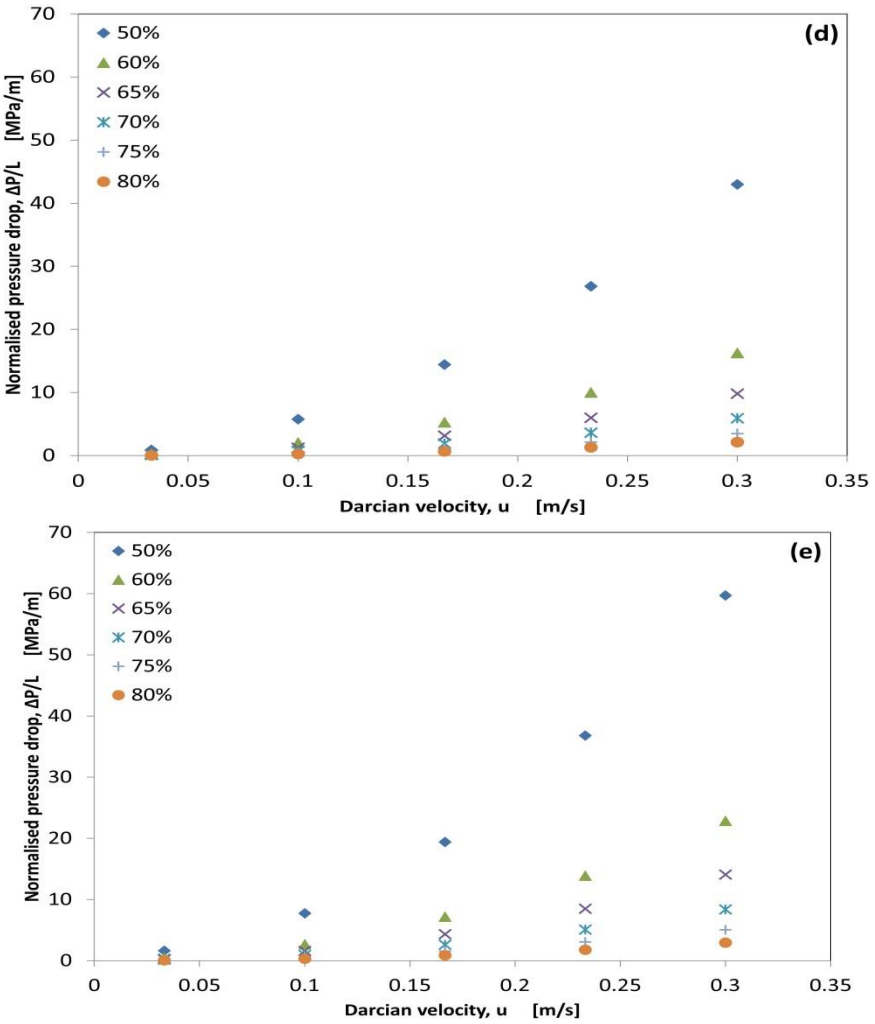

Figure 4-15 (Continuation) Length-normalised pressure drop (ΔP/L) versus Darcian velocity (u) for 3D REVs with porosity ranging from 50% to 80%, metal particle size of 70μm, and pore size of: (a) 400 μm, (b) 600 μm, (c) 800 μm, (d) 1000 μm and (e) 1500 μm

The numerical results of the normalised pressure drop were compared with experimental data obtained by Baloyo (2016) for LCS porous copper samples. The results for the metal particle sizes of 30 μm, 50 μm and 70 μm are shown in Figure 4-16, Figure 4-17, and Figure 4-18 respectively. In general, the numerical results are in similar ranges as the experimental data. However, there are some differences between the two sets of data.

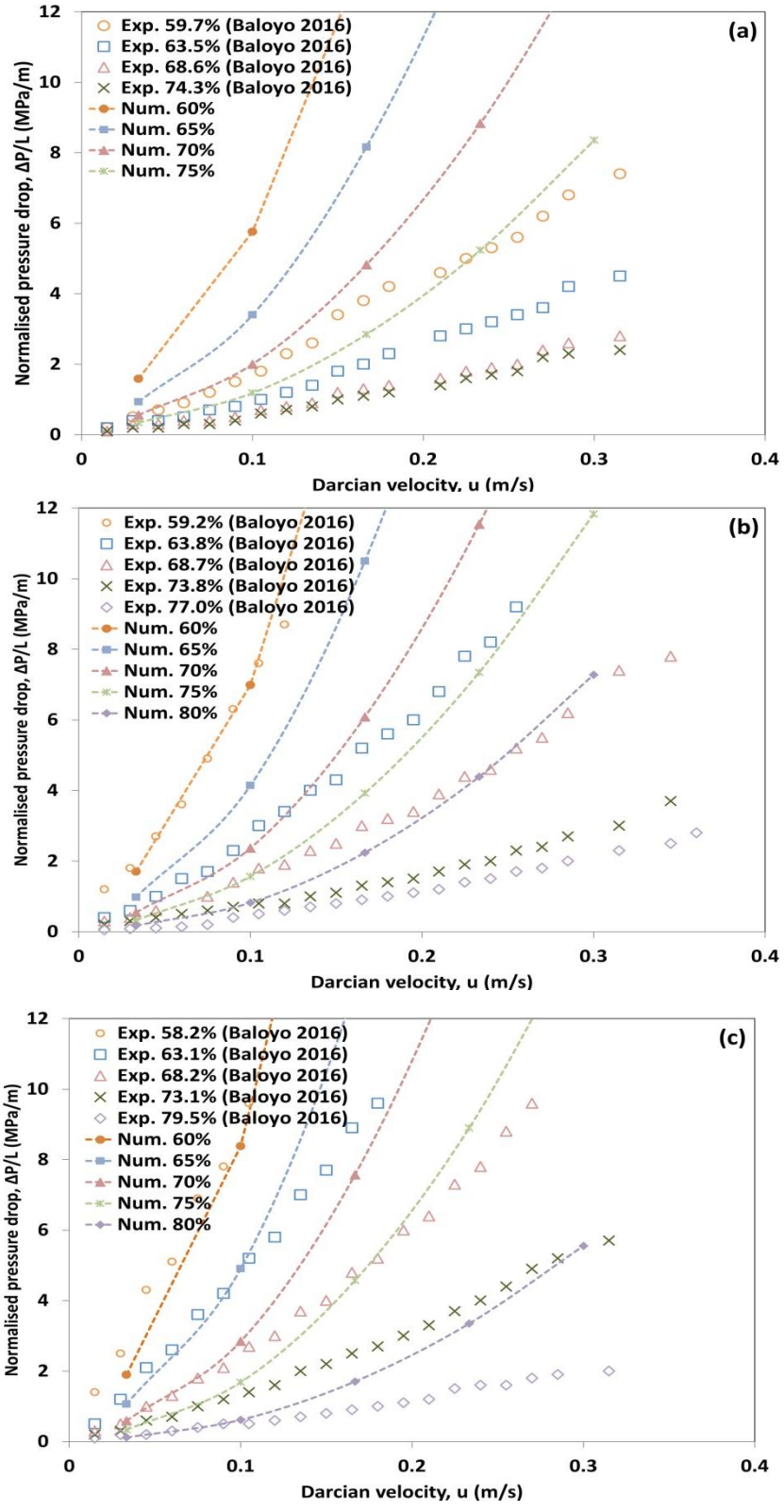

Figure 4-16 Normalised pressure drop compared with experimental data for 3D REVs with a 30 μm metal particle size, different porosities (shown in the figure) and different pore sizes: (a) exp. 250-450 μm and num. 400 μm, (b) exp. 450-710 μm and num. 600 μm, (c) exp. 710-1000 μm and num. 800 μm, and (d) exp. 1000-1500 μm and num. 1000 μm (to be continued)

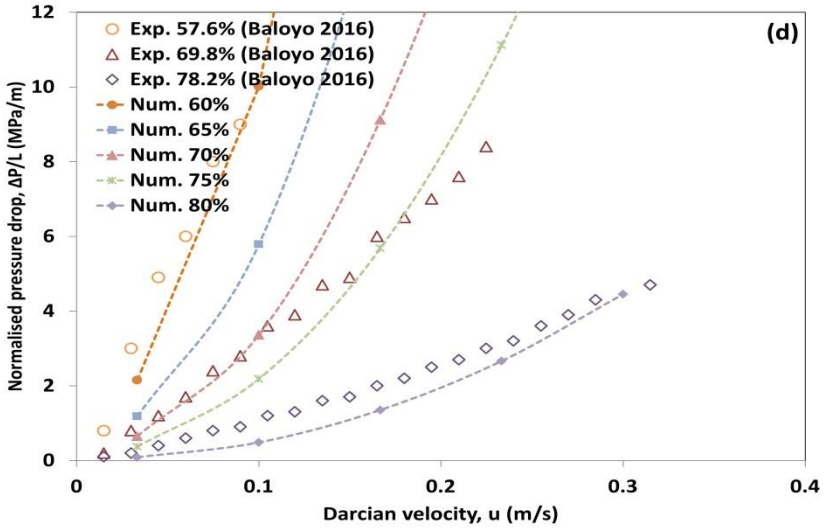

Figure 4-16 (Continuation) Normalised pressure drop compared with experimental data for 3D REVs with a 30 µm metal particle size, different porosities (shown in the figure) and different pore sizes: (a) exp. 250-450 µm and num. 400 µm, (b) exp. 450-710 µm and num. 600 µm, (c) exp. 710-1000 µm and num. 800 µm, and (d) exp. 1000-1500 µm and num. 1000 µm

The numerical results with a metal particle size of 30 µm showed the same increasing trend as for the experimental data. At a Darcian velocity below 0.1 m/s, the normalised pressure drop agrees well with the experimental values. In some cases, as in Figure 4-16 (d) for the high porosity of 80%, the trend between the numerical and experimental values is very similar, even at high flow rates. In most cases, however, as Darcian velocity increases, the numerical pressure drop increases more rapidly than the experimental data. A particular case is observed in Figure 4-16 (a) where the normalised pressure drops diverge considerably from the experimental data. The differences between the numerical and the experimental values can be attributed to the difference in porosity, pore size and metal particle size of the experimental values. These differences were observed to affect the normalised pressure drops. The experimental values were obtained from materials with variable porosity and pore size in ranges as shown in Figure 4-16, while the numerical analysis used fixed porosity, pore size and metal particle size values.

The normalised pressure drops with metal particle sizes of 50 μm and 70 μm were also compared to the experimental data as shown in Figure 4-17 and Figure 4-18 respectively. The results in particular are in good agreement for porosity between 65% and 80% and Darcian velocity below 0.2 m/s in most of the cases. However, the numerical values do not fit completely with the experimental data. The 3D REVs with a porosity of 50% and pore size of 600 μm and higher have a normalised pressure drop lower than the experimental data. In these cases, does not fit as well as in the case of the metal particle size of 30 μm. Similar trends between the numerical and experimental results are also shown in Figure 4-18. In general the numerical results agreed better with the experimental data at small pores, especially at low flow velocities. When pore size is increased, the difference between the numerical results and the experimental data becomes evident.

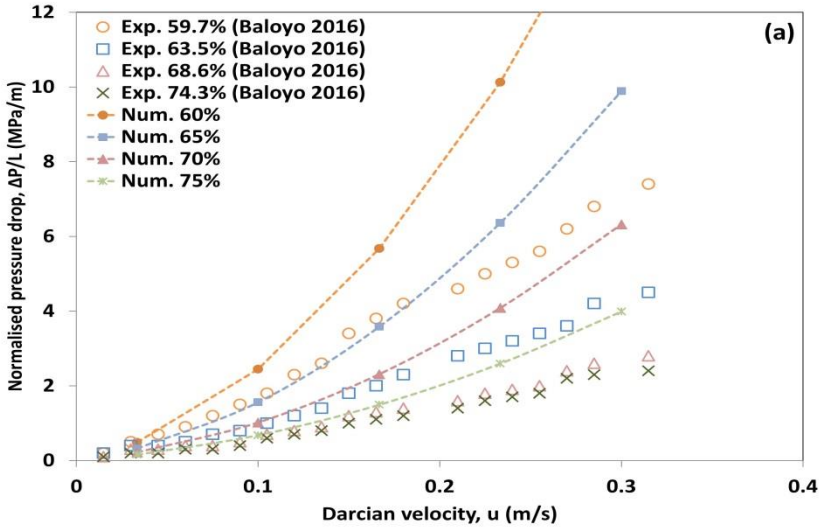

Figure 4-17 Normalised pressure drop compared with experimental data for 3D REVs with a 50 μm metal particle size, different porosities (shown in the figure) and different pore sizes: (a) exp. 250-450 μm and num. 400 μm, (b) exp. 450-710 μm and num. 600 μm, (c) exp. 710-1000 μm and num. 800 μm, and (d) exp. 1000-1500 μm and num. 1000 μm (to be continued)

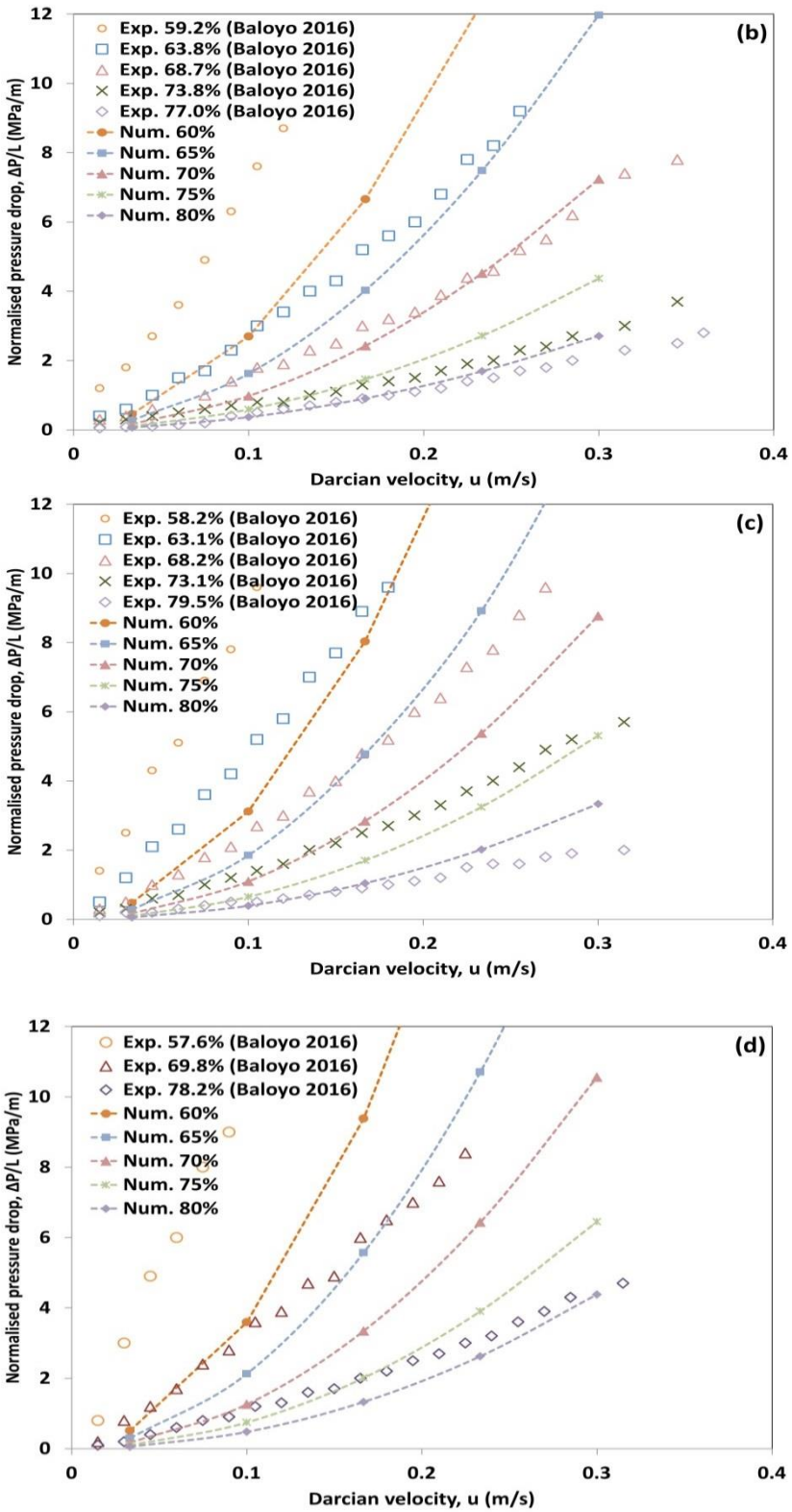

Figure 4-17 (Continuation) Normalised pressure drop compared with experimental data for 3D REVs with a 50 µm metal particle size, different porosities (shown in the figure) and different pore sizes: (a) exp. 250-450 µm and num. 400 µm, (b) exp. 450-710 µm and num. 600 µm, (c) exp. 710-1000 µm and num. 800 µm, and (d) exp. 1000-1500 µm and num. 1000 µm

The numerical results showed that pressure drop decreases with pore size, which agrees with some observations (Boomsma and Poulikakos 2002), but disagrees with the data of Baloyo (2016) which reported that the pressure drop increases with increasing pore size.

In principle the numerical model is a good representation of the experimental data. Although the 3D REVs are created with parameters similar to the real material, the 3D REVs are a simplification of the real material. The real material has variable parameters (porosity, pore size and metal particle size), while the 3D REVs possess fixed values for all these parameters. In addition, the real material is more tortuous than the REVs. The change in flow direction was shown to increase the pressure drop as mentioned in Chapter 3.

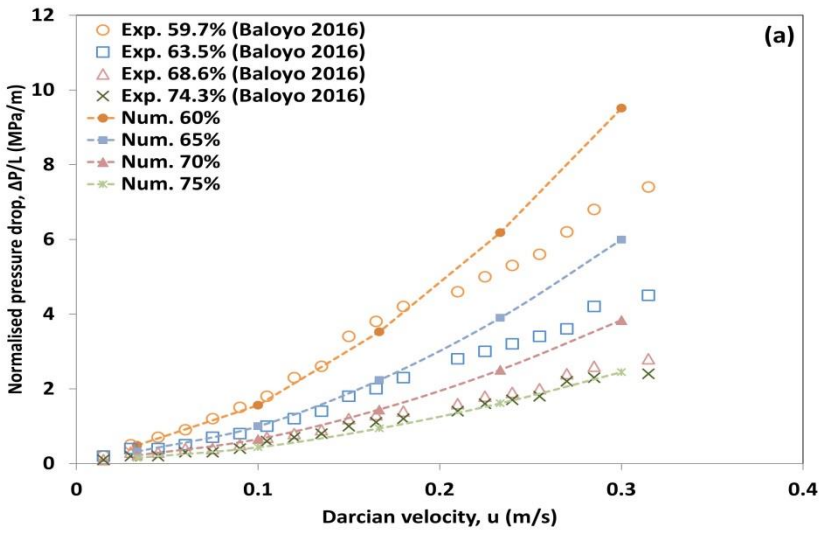

Figure 4-18 Normalised pressure drop compared with experimental data for 3D REVs with a 70 µm metal particle size, different porosities (shown in the figure) and different pore sizes: (a) exp. 250-450 µm and num. 400 µm, (b) exp. 450-710 µm and num. 600 µm, (c) exp. 710-1000 µm and num. 800 µm, and (d) exp. 1000-1500 µm and num. 1000 µm (to be continued)

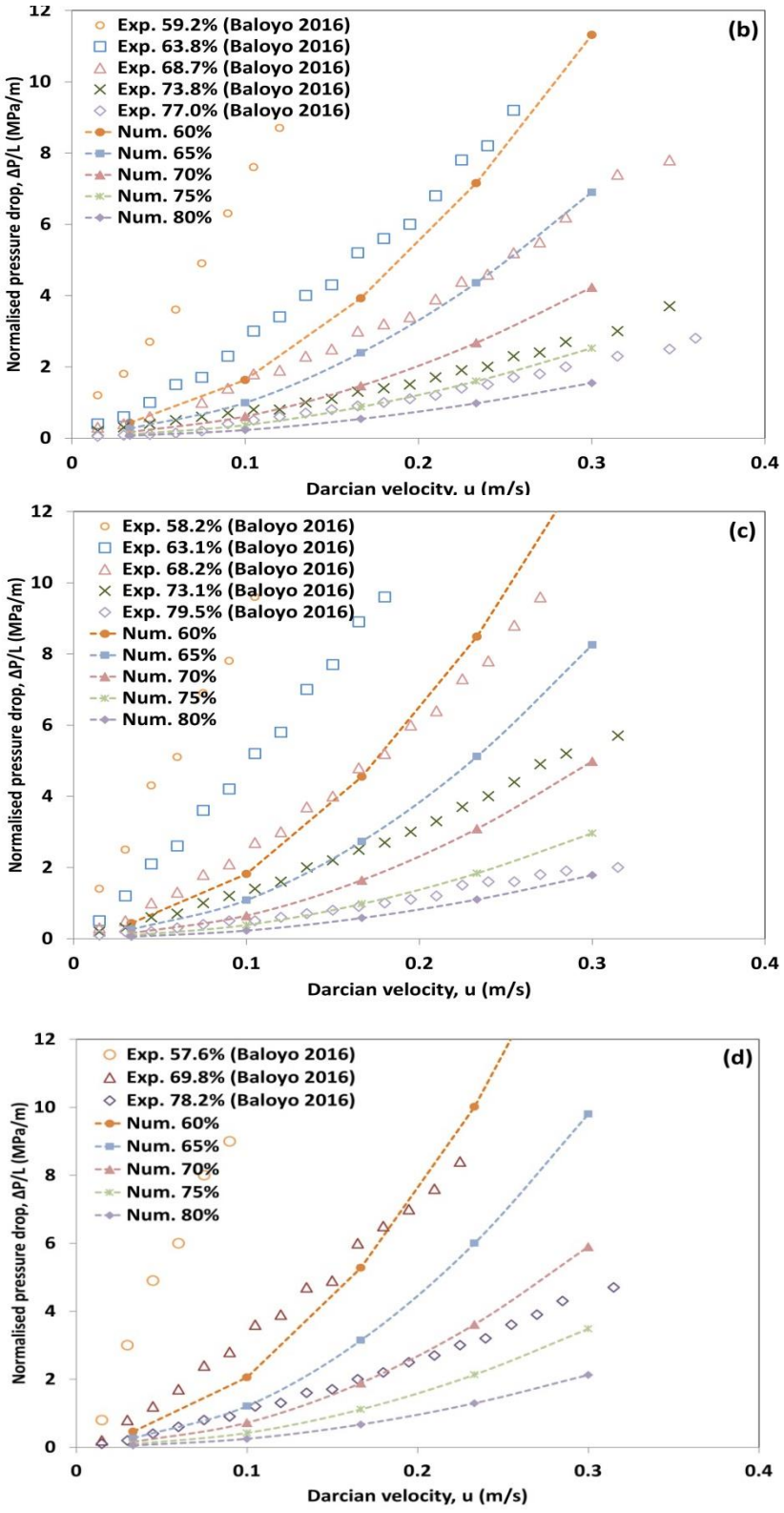

Figure 4-18 (Continuation) Normalised pressure drop compared with experimental data for 3D REVs with a 70 µm metal particle size, different porosities (shown in the figure) and different pore sizes: (a) exp. 250-450 µm and num. 400 µm, (b) exp. 450-710 µm and num. 600 µm, (c) exp. 710-1000 µm and num. 800 µm, and (d) exp. 1000-1500 µm and num. 1000 µm

Permeability and form drag coefficient were obtained following the same procedure as described in Chapter 3. The modified pressure drops ΔP/uL for metal particle sizes of 30 μm, 50 μm and 70 μm were plotted against Darcian velocity u as shown in Figure 4-19, Figure 4-20 and Figure 4-21 respectively. All the plots resulted in a linear trend between the modified pressure drop and Darcian velocity. Permeability and drag form drag coefficient were obtained from the intersect and slope of the lines respectively.

The resulting permeability and form drag coefficient values obtained for the different structures are summarised and presented in Table 4-5. Pore size is indicated at the top row while porosity and metal particle size are indicated in the left columns.

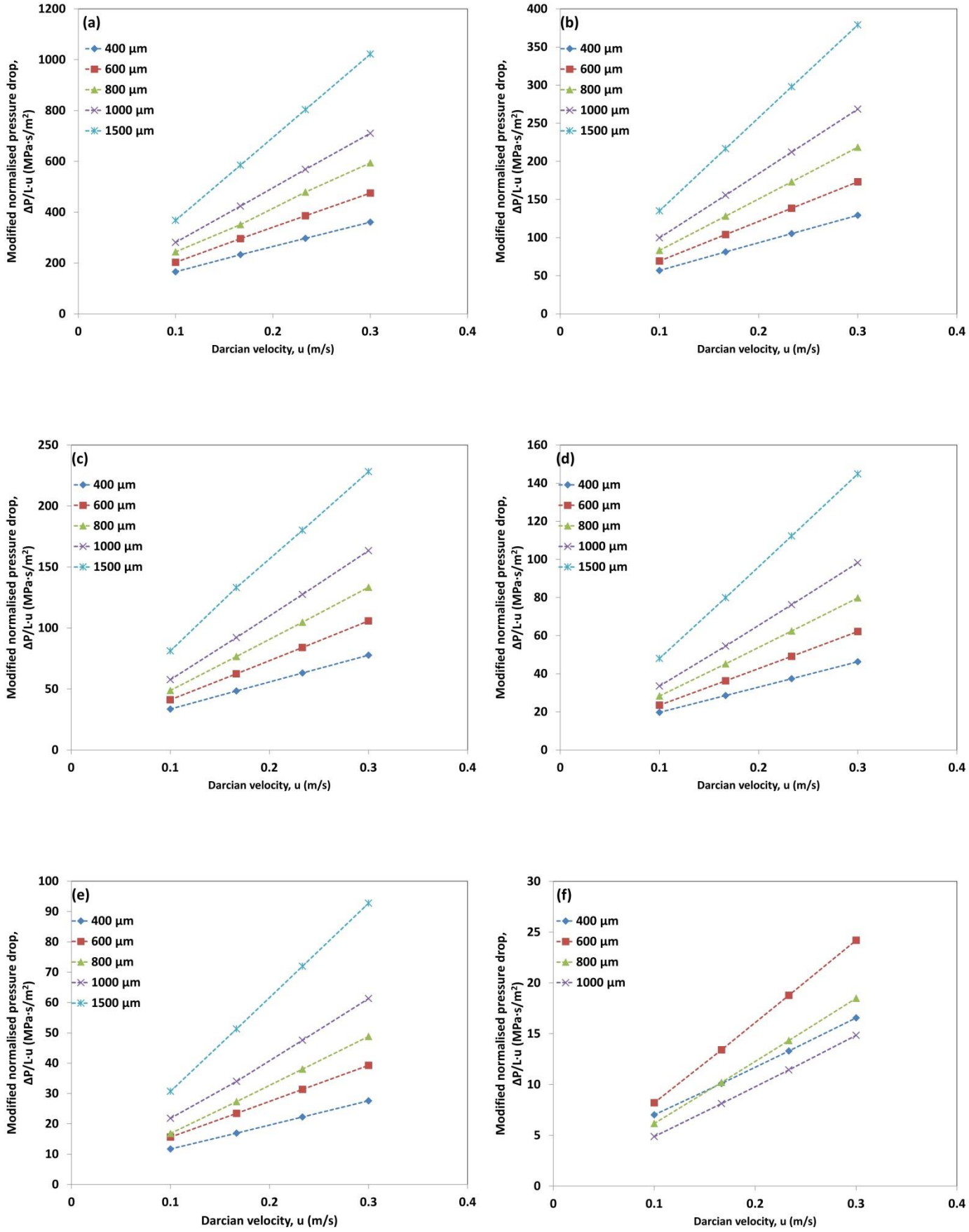

Figure 4-19 Modified normalised pressure drop versus Darcian velocity for samples with different pore sizes (shown on the figure), metal particle size of 30 µm and porosities of: (a) 50%, (b) 60%, (c) 65%, (d) 70%, (e) 75% and (f) 80%

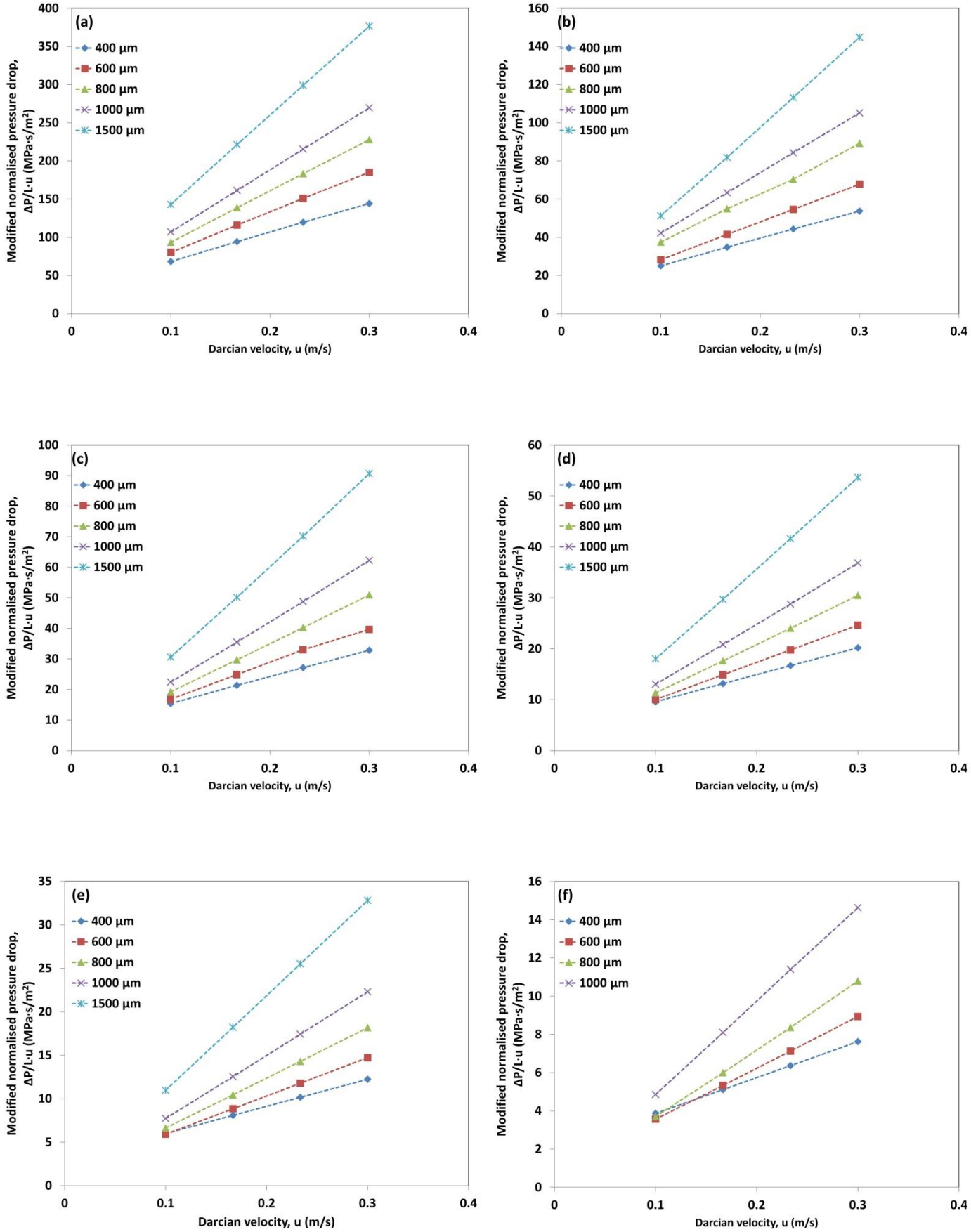

Figure 4-20 Modified normalised pressure drop versus Darcian velocity for samples with different pore sizes (shown on the figure), metal particle size of 50 µm and porosities of: (a) 50%, (b) 60%, (c) 65%, (d) 70%, (e) 75% and (f) 80%

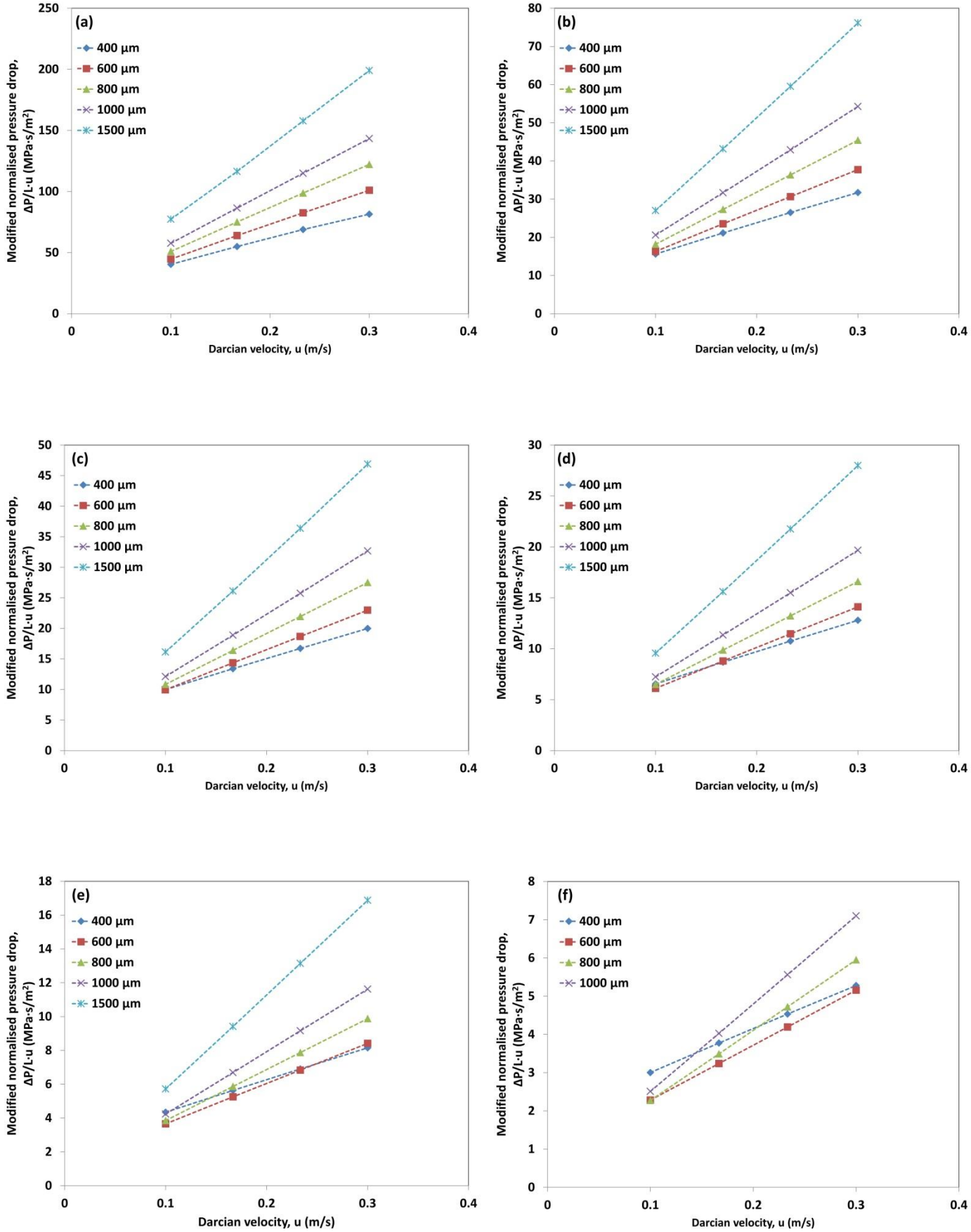

Figure 4-21 Modified normalised pressure drop versus Darcian velocity for samples with different pore sizes (shown on the figure), metal particle size of 70 µm and porosities of: (a) 50%, (b) 60%, (c) 65%, (d) 70%, (e) 75% and (f) 80%

Table 4-5 Permeability and form drag coefficient of the 3D structures

Pore size (μm)		400			600			800			1000			1500		
ε	***Cu diameter [μm]***	**ϕ**	**K [μm^2]**	**C [μm^{-1}]**	**ϕ**	**K [μm^2]**	**C [μm^{-1}]**	**ϕ**	**K [μm^2]**	**C [μm^{-1}]**	**ϕ**	**K [μm^2]**	**C [μm^{-1}]**	**ϕ**	**K [μm^2]**	**C [μm^{-1}]**
	30	13.33	10.30	0.87	20.00	10.16	1.25	26.67	10.69	1.66	33.33	10.53	2.04	50.00	10.53	3.05
50%	50	8.00	23.69	0.33	12.00	25.01	0.48	16.00	24.84	0.62	20.00	24.16	0.75	30.00	24.10	1.10
	70	5.71	42.72	0.21	8.57	42.92	0.25	11.43	43.65	0.32	14.29	43.56	0.39	21.43	40.38	0.57
	30	13.33	32.30	0.32	20.00	34.77	0.48	26.67	35.03	0.63	33.33	33.47	0.79	50.00	31.26	1.14
60%	50	8.00	64.28	0.12	12.00	72.87	0.18	16.00	72.89	0.24	20.00	75.89	0.31	30.00	83.45	0.44
	70	5.71	94.58	0.07	8.57	121.15	0.10	11.43	135.15	0.12	14.29	145.04	0.15	21.43	152.19	0.23
	30	13.33	55.84	0.20	20.00	64.32	0.30	26.67	70.19	0.39	33.33	72.44	0.49	50.00	55.72	0.70
65%	50	8.00	101.98	0.07	12.00	125.66	0.11	16.00	151.75	0.15	20.00	164.91	0.18	30.00	183.10	0.28
	70	5.71	141.86	0.04	8.57	195.47	0.06	11.43	235.58	0.08	14.29	265.12	0.09	21.43	301.78	0.14
	30	13.33	94.64	0.12	20.00	121.62	0.18	26.67	140.02	0.24	33.33	153.48	0.30	50.00	151.94	0.46
70%	50	8.00	157.07	0.04	12.00	221.89	0.07	16.00	275.96	0.09	20.00	311.65	0.11	30.00	345.00	0.17
	70	5.71	204.46	0.03	8.57	309.52	0.04	11.43	397.33	0.05	14.29	462.30	0.06	21.43	554.38	0.09
	30	13.33	155.77	0.07	20.00	192.19	0.11	26.67	289.08	0.15	33.33	269.14	0.19	50.00	285.96	0.29
75%	50	8.00	232.30	0.03	12.00	374.09	0.04	16.00	500.45	0.05	20.00	604.90	0.07	30.00	652.33	0.10
	70	5.71	286.83	0.01	8.57	497.02	0.02	11.43	662.55	0.03	14.29	814.58	0.03	21.43	1052.12	0.05
	30	13.33	249.80	0.04	20.00	540.59	0.05	26.67	934.77	0.06	33.33	1497.57	0.05	50.00	3294.38	0.03
80%	50	8.00	334.53	0.01	12.00	603.24	0.02	16.00	1172.90	0.03	20.00	1385.68	0.05	30.00	2778.06	0.03
	70	5.71	381.13	0.01	8.57	740.50	0.01	11.43	1144.67	0.02	14.29	1549.99	0.02	21.43	2824.68	0.03

4.5.2 Permeability

The permeability values presented in Table 4-5 were plotted against porosity and were compared with the experimental data available from Xiao (2013) and Baloyo (2016). The results for metal particle sizes of 30 μm, 50 μm and 70 μm are shown in Figure 4-22, Figure 4-23 and Figure 4-24, respectively.

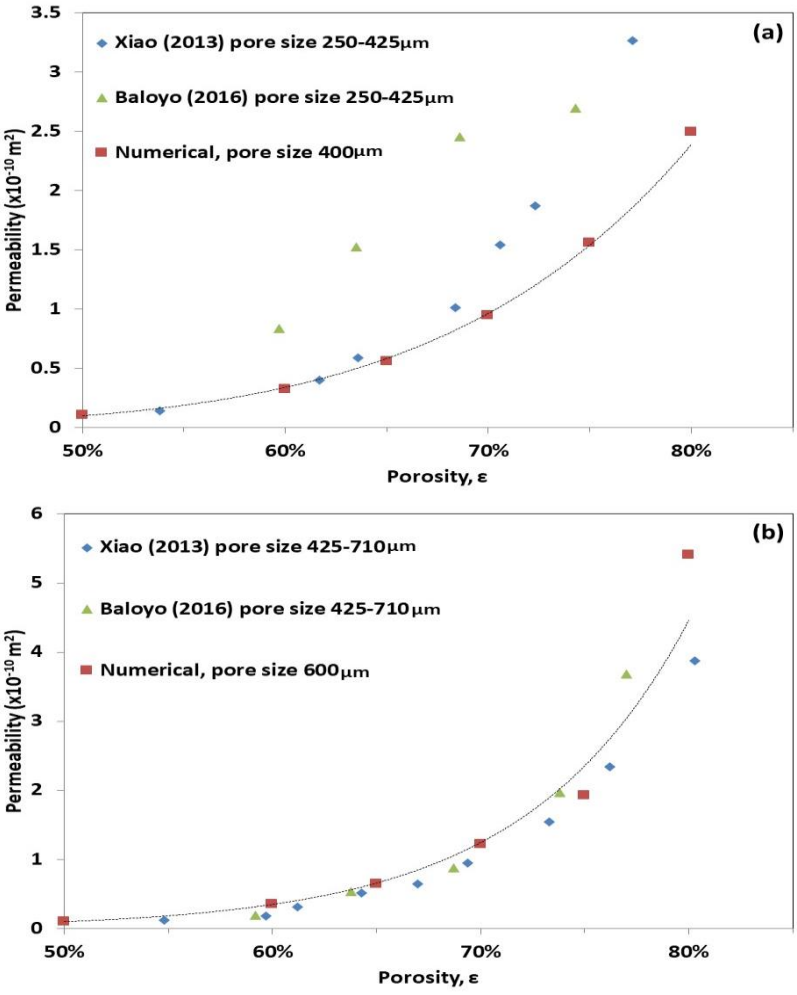

Figure 4-22 Relationship between permeability and porosity (ε) for numerical and experimental (Baloyo 2016, Xiao 2013) data. The REVs have a metal particle size of 30 μm and different pore sizes: (a) exp. 250-450 μm and num. 400 μm, (b) exp. 450-710 μm and num. 600 μm, (c) exp. 710-1000 μm and num. 800 μm, (d) exp. 710-1000 μm and num. 1000 μm, and (e) exp. 1000-1500 μm and num. 1000 μm, (to be continued)

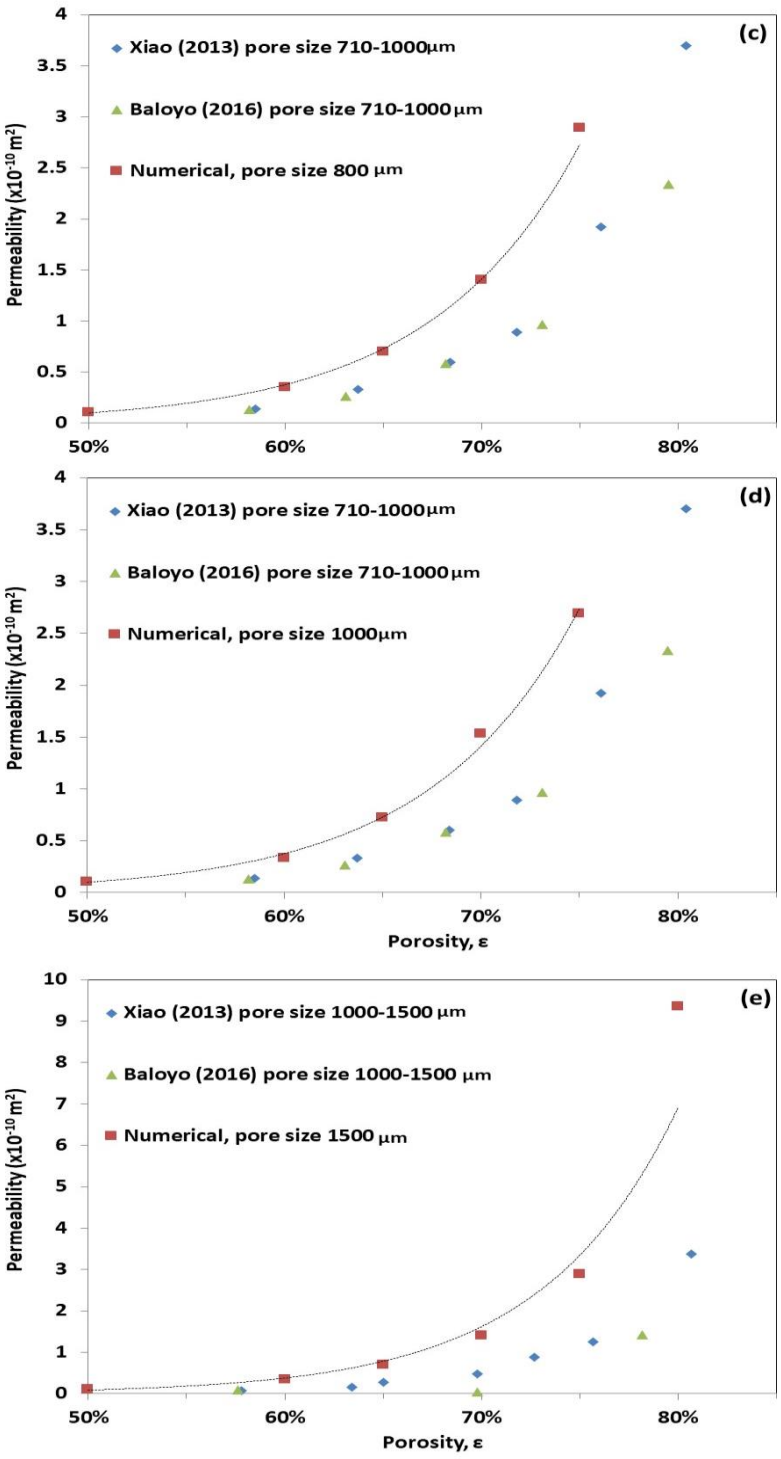

Figure 4-22 (Continuation) Relationship between permeability and porosity (ε) for numerical and experimental (Baloyo 2016**, Xiao** 2013**) data. The 3D REVs have a metal particle size of 30 µm and different pore sizes: (a) exp. 250-450 µm and num. 400 µm, (b) exp. 450-710 µm and num. 600 µm, (c) exp. 710-1000 µm and num. 800 µm, (d) exp. 710-1000 µm and num. 1000 µm, and (e) exp. 1000-1500 µm and num. 1000 µm**

The numerical results showed trends similar to the experimental data, i.e. permeability increases with increasing porosity. This increasing tendency was observed for all 3D REVs. For the smaller pore sizes, i.e. 400 μm and 600 μm, the experimental and numerical trends are very similar. Increasing pore size was shown to increase the difference between the numerical results and the experimental data. The experimental data showed that increasing pore size from 250 - 425 μm to 425 - 710 μm improved permeability significantly. However, increasing pore size to 710 - 1000 μm and then to 1000 - 1500 μm decreased permeability. Baloyo (2016) explained this in terms of pore density and the tortuosity of the material. Other researches however, showed that permeability continues to increase with increasing pore size (Bhattacharya *et al.* 2002, Khayargoli *et al.* 2004).

The relationship between permeability and porosity for a metal particle size of 50 μm can be seen in Figure 4-23. The numerical and experimental values for permeability still have the same increasing trend with porosity. The numerical results and experimental data are in good agreement in some cases. For example, Figure 4-23 (a) shows a similar trend as Xiao's (2013) experimental results. The numerical results in Figure 4-23 (b) are in a similar range as the experimental values. However, the numerical values for permeability deviate from the experimental ones as porosity and pore size increase.

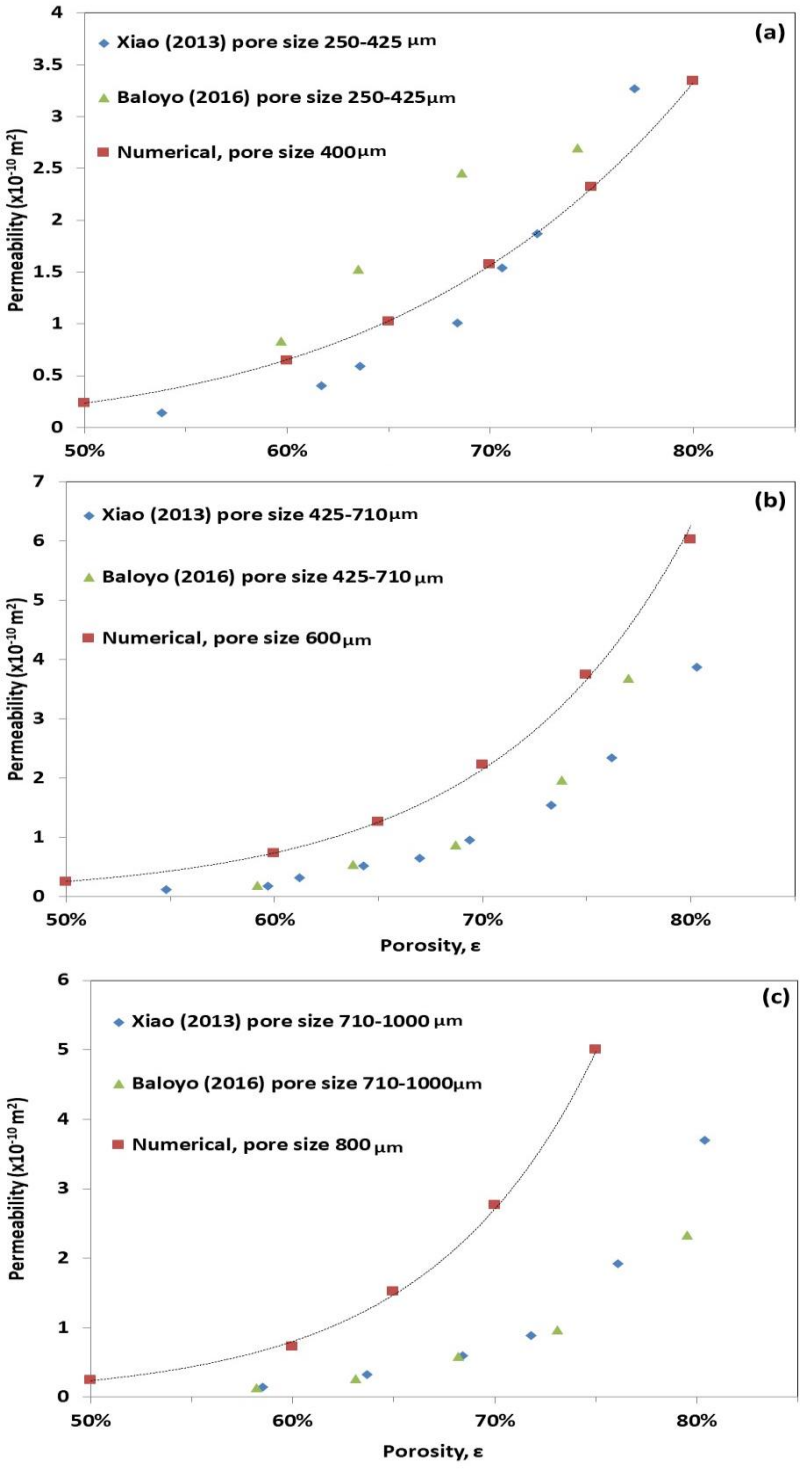

Figure 4-23 Relationship between permeability and porosity (ε) for numerical and experimental (Baloyo 2016, Xiao 2013) data. The 3D REVs have a metal particle size of 50 µm and different pore sizes: (a) exp. 250-450 µm and num. 400 µm, (b) exp. 450-710 µm and num. 600 µm, (c) exp. 710-1000 µm and num. 800 µm, and (d) exp. 710-1000 µm and num. 1000 µm, and (e) exp. 1000-1500 µm and num. 1000 µm, (to be continued)

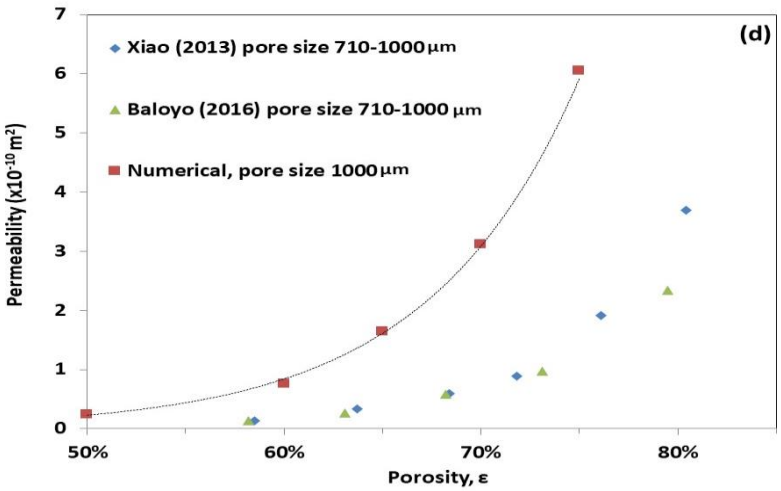

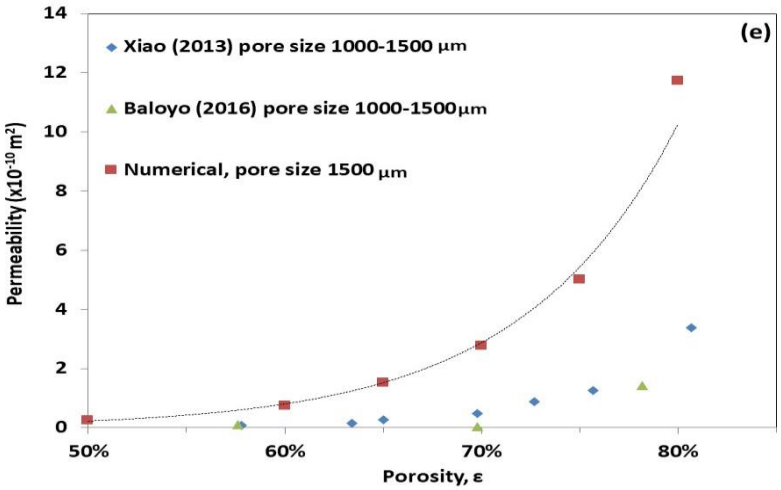

Figure 4-23 (Continuation) Relationship between permeability and porosity (ε) for numerical and experimental (Baloyo 2016**, Xiao** 2013**) data. The REVs have a metal particle size of 50 µm and different pore sizes: (a) exp. 250-450 µm and num. 400 µm, (b) exp. 450-710 µm and num. 600 µm, (c) exp. 710-1000 µm and num. 800 µm, and (d) exp. 710-1000 µm and num. 1000 µm, and (e) exp. 1000-1500 µm and num. 1000 µm**

This relationship between permeability and porosity for the 3D REVs with metal particle size of 70µm is shown in Figure 4-24. The numerical results for the smallest pore size are shown to be in good agreement with the experimental data, while the rest of the results exhibited the same increasing trend with less good agreement. The different behaviour for permeability due to the change in metal particle size can be explained in terms of the increase of radius of the connecting cylinders with metal particle size.

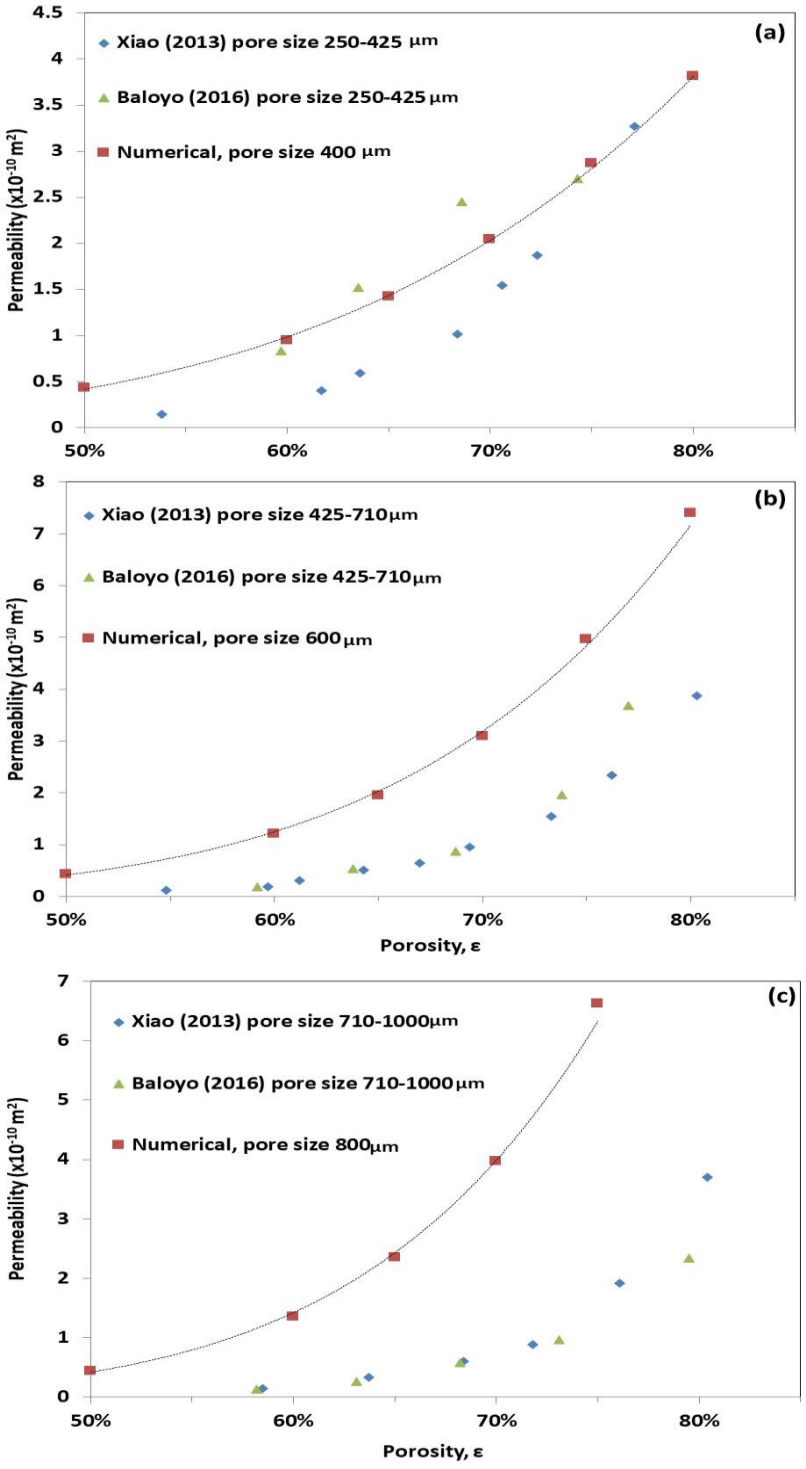

Figure 4-24 Relationship between permeability and porosity (ε) for numerical and experimental (Baloyo 2016, Xiao 2013) data. The 3D REVs have a metal particle size of 70 µm and different pore sizes: (a) exp. 250-450 µm and num. 400 µm, (b) exp. 450-710 µm and num. 600 µm, (c) exp. 710-1000 µm and num. 800 µm, and (d) exp. 710-1000 µm and num. 1000 µm, and (e) exp. 1000-1500 µm and num. 1000 µm, (to be continued)

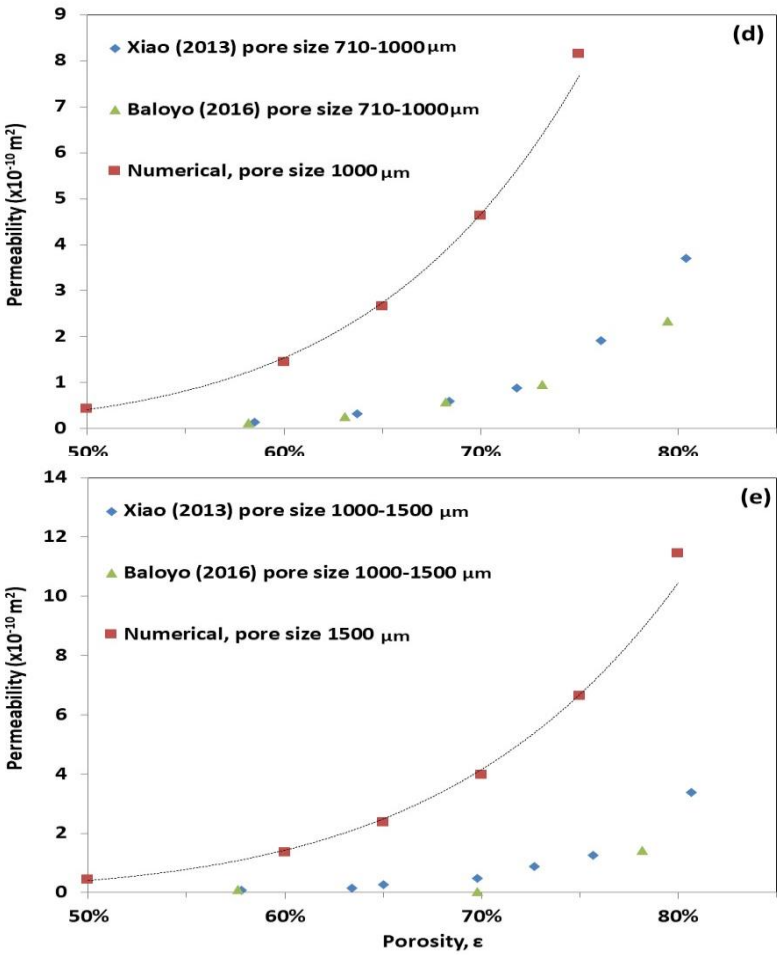

Figure 4-24 (Continuation) Relationship between permeability and porosity (ε) for numerical and experimental (Baloyo 2016, Xiao 2013) data. The 3D REVs have a metal particle size of 70 µm and different pore sizes: (a) exp. 250-450 µm and num. 400 µm, (b) exp. 450-710 µm and num. 600 µm, (c) exp. 710-1000 µm and num. 800 µm, and (d) exp. 710-1000 µm and num. 1000 µm, and (e) exp. 1000-1500 µm and num. 1000 µm

From Figure 4-22 to Figure 4-24 it is evident that permeability increased with pore size. Bhattacharya *et al.* (2002) attributed this increase in permeability to a decrease in tortuosity within the channels of the porous metal with pore size. To further investigate the effect of the pore size, the numerical results of permeability were plotted against pore size as shown in Figure 4-25. Permeability increased with increasing pore size. Khayargoli *et al.*(2004) observed a similar behaviour when studying metal foams with pore diameters ranging from 0.4 mm to 1.5 mm. Abbas (2011) reported that permeability increases with pore size beacuse the smaller filler particles fill the void spaces better.

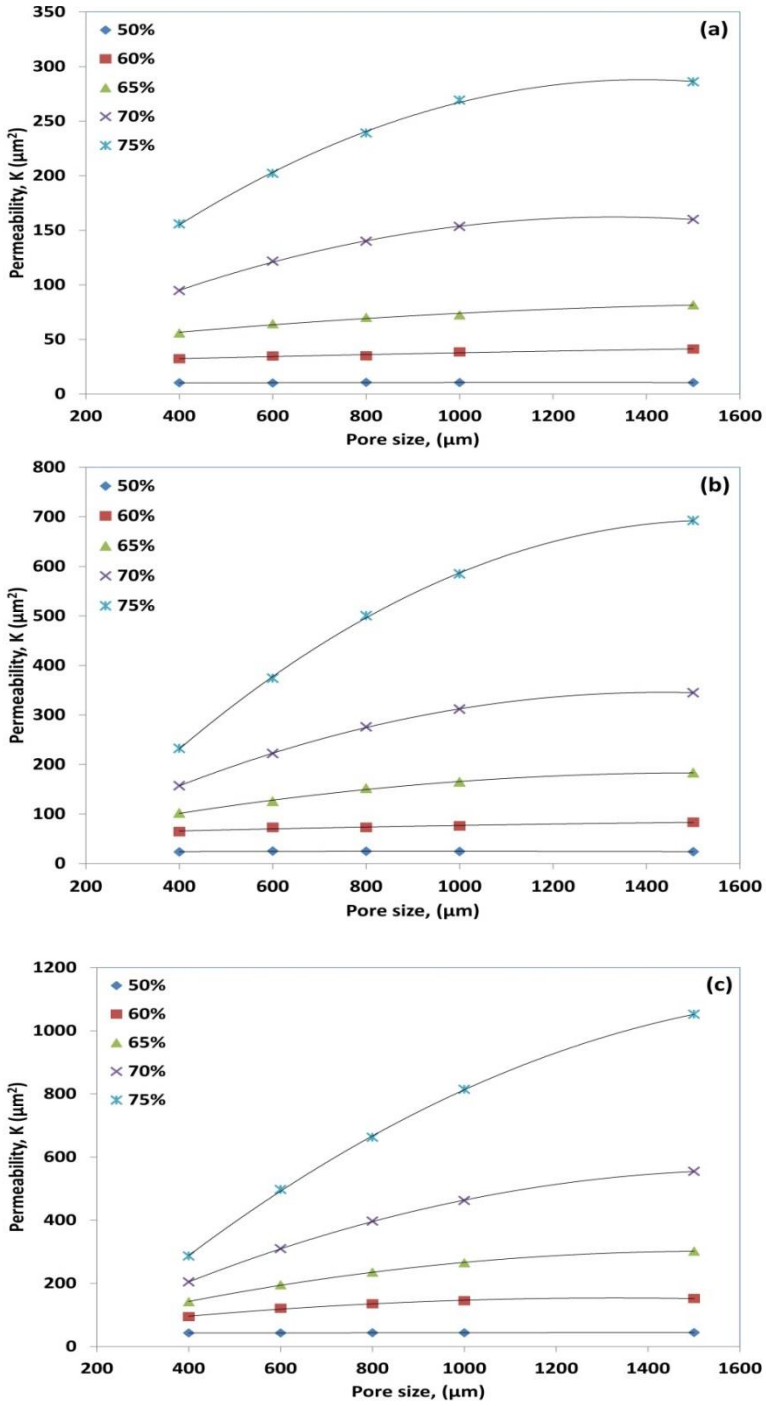

Figure 4-25 Relationship between numerical permeability and pore size with different porosities (shown in figure) and metal particle sizes of: (a) 30, (b) 50 and (c) 70 μm

4.5.3 Form drag coefficient

The form drag coefficient was plotted against porosity for all different 3D REV combinations. The experimental data available for the form drag coefficient is much scarcer than the data for permeability. However, the experimental data are also plotted, whenever available. The results considering 3D REVs with a metal particle size of 30 μm can be seen in Figure 4-26.

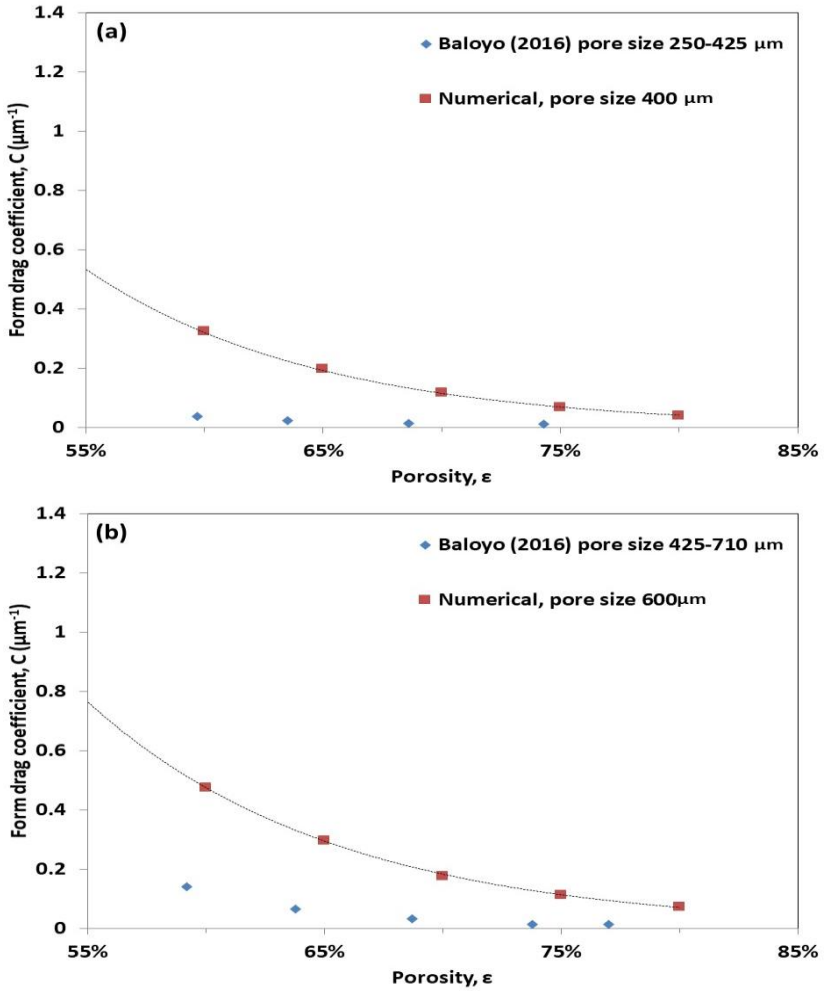

Figure 4-26 Relationship between form drag coefficient (C) and porosity (ε) for numerical and experimental (Baloyo 2016) data. The 3D REVs have a metal particle size of 30 μm and different pore sizes: (a) exp. 250-450 μm and num. 400 μm, (b) exp. 450-710 μm and num. 600 μm, (c) exp. 710-1000 μm and num. 800 μm, and (d) exp. 710-1000 μm and num. 1000 μm, (to be continued)

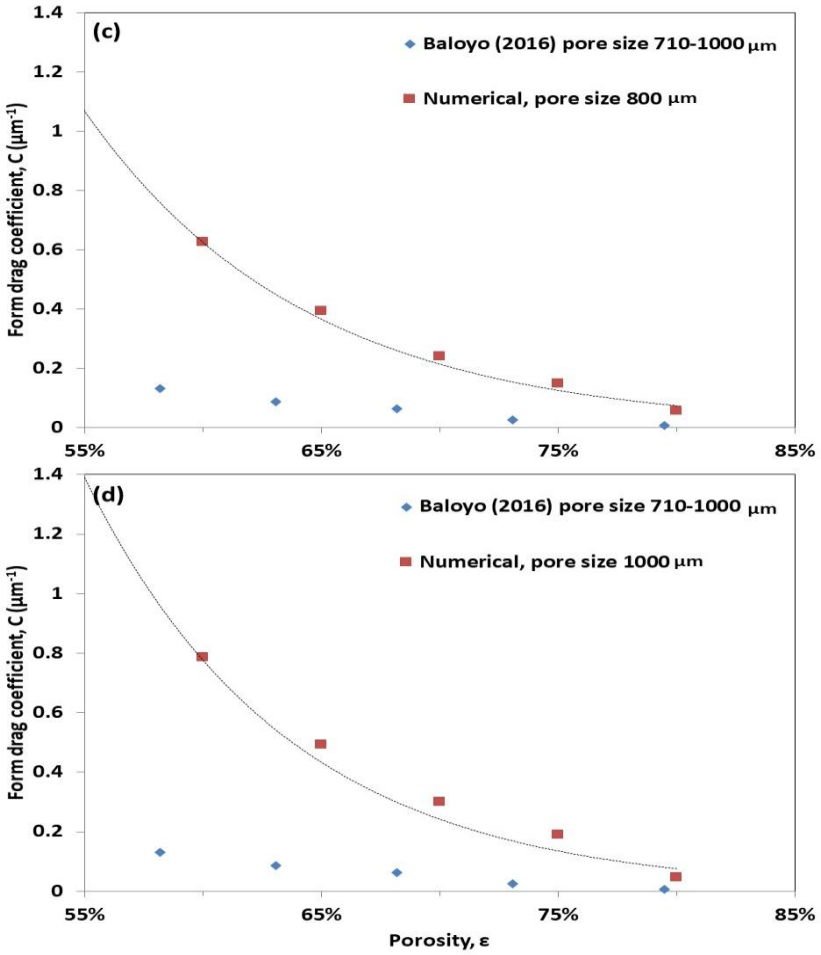

Figure 4-26 (Continuation) Relationship between form drag coefficient (C) and porosity (ε) for numerical and experimental (Baloyo 2016**) data. The 3D REVs have a metal particle size of 30 µm and different pore sizes: (a) exp. 250-450 µm and num. 400 µm, (b) exp. 450-710 µm and num. 600 µm, (c) exp. 710-1000 µm and num. 800 µm, and (d) exp. 710-1000 µm and num. 1000 µm,**

The form drag coefficient exhibited a decreasing trend with increasing porosity. This behaviour agrees with previous studies made on the form drag coefficient for different porous media (Dukhan 2006, Della-Torre *et al.* 2014). Previous researchers contributed the reduction of the form drag to the reduction of the solid matrix, leading to less flow resistance. This phenomenon is also reflected in the 3D unit cells used in the present study. By increasing porosity, the path length was reduced and the cylinder radius was increased, creating less resistance for the water flow. Compared to the experimental data, almost all the numerical results with a metal particle size of 30 µm were shown to be about 3 times larger

and showed a steeper curve. However, as porosity increased, the difference between the two sets of data decreased.

The numerical results also showed that pore size had an effect on the form drag coefficient. Increasing the pore size increased the form drag coefficient. This can be explained in terms of the size difference between the pores and the metal particles used to create the connecting cylinders for the 3D REVs. The increase in form drag coefficient is about 30% with every increment of pore size of 200 μm. The experimental form drag coefficient on the other hand, has less marked increments due to increasing pore size because of the high pore density generated for the small pore sizes. This creates more channels for the fluid to flow leading to less flow resistance.

The numerical and experimental form drag coefficient considering larger metal particle sizes of 50 μ and 70 μm are shown in Figure 4-27 and Figure 4-28, respectively. The numerical results for a metal particle size of 50 μm were closer to the experimental values. The better agreement between the experimental and numerical results is observed in Figure 4-27 (b). However differences between the numerical and experimental values are still noticeable. In the low porosity range, the difference is less than 50%. As porosity increases, the difference decreases.

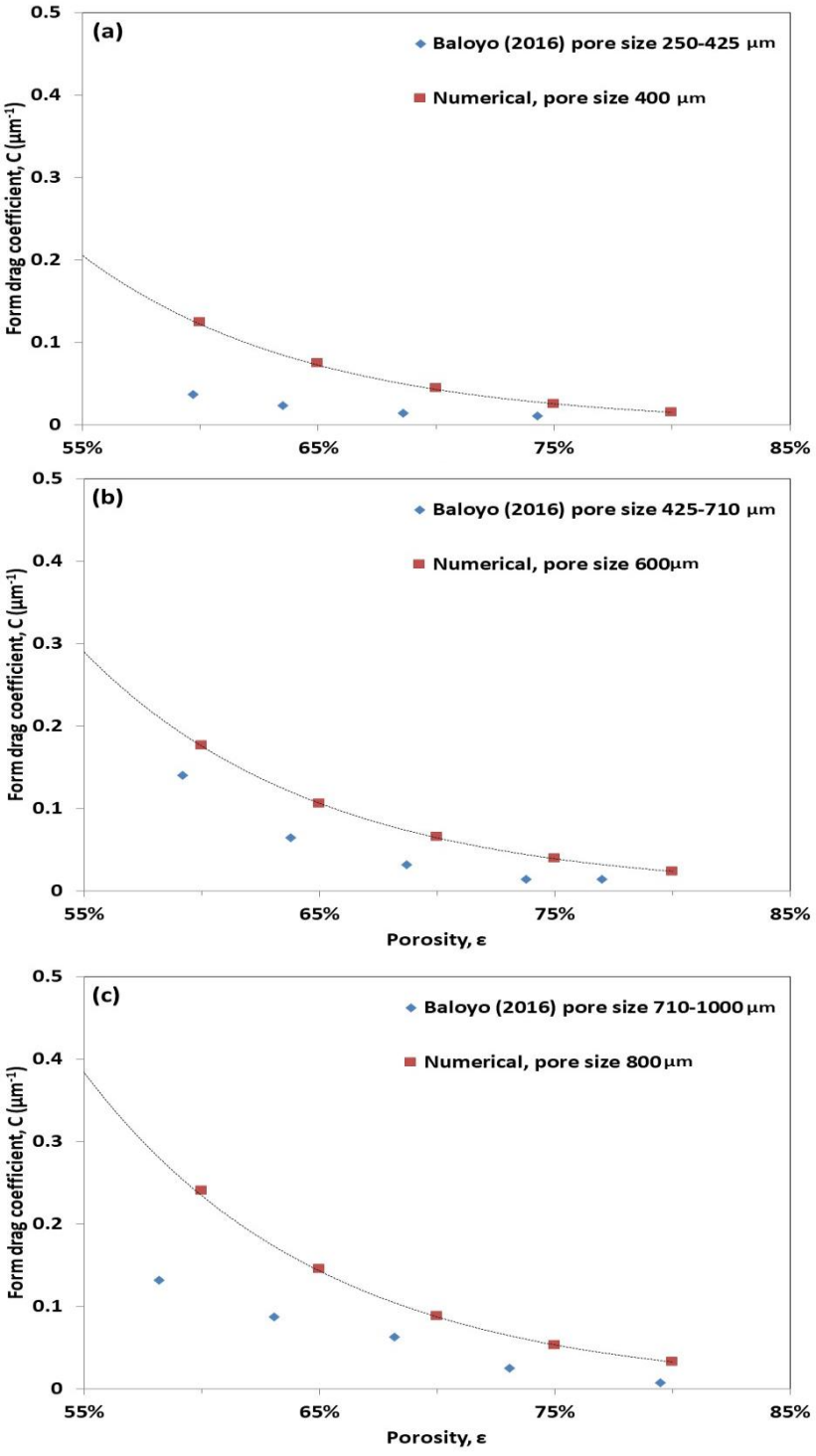

Figure 4-27 Relationship between form drag coefficient (C) and porosity for numerical and experimental (Baloyo 2016) data. The 3D REVs have a metal particle size of 50 µm and different pore sizes: (a) exp. 250-450 µm and num. 400 µm, (b) exp. 450-710 µm and num. 600 µm, (c) exp. 710-1000 µm and num. 800 µm, and (d) exp. 710-1000 µm and num. 1000 µm, (to be continued)

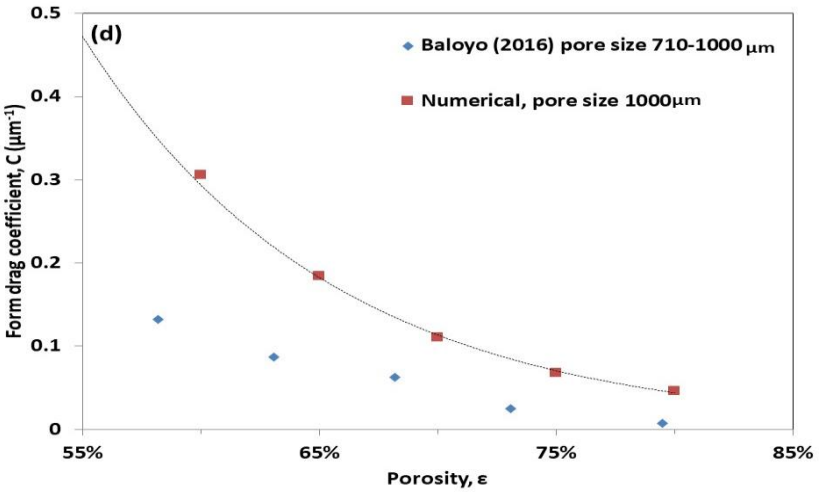

Figure 4-27 (Continuation) Relationship between form drag coefficient (C) and porosity for numerical and experimental (Baloyo 2016**) data. The 3D REVs have a metal particle size of 50 µm and different pore sizes: (a) exp. 250-450 µm and num. 400 µm, (b) exp. 450-710 µm and num. 600 µm, (c) exp. 710-1000 µm and num. 800 µm, and (d) exp. 710-1000 µm and num. 1000 µm**

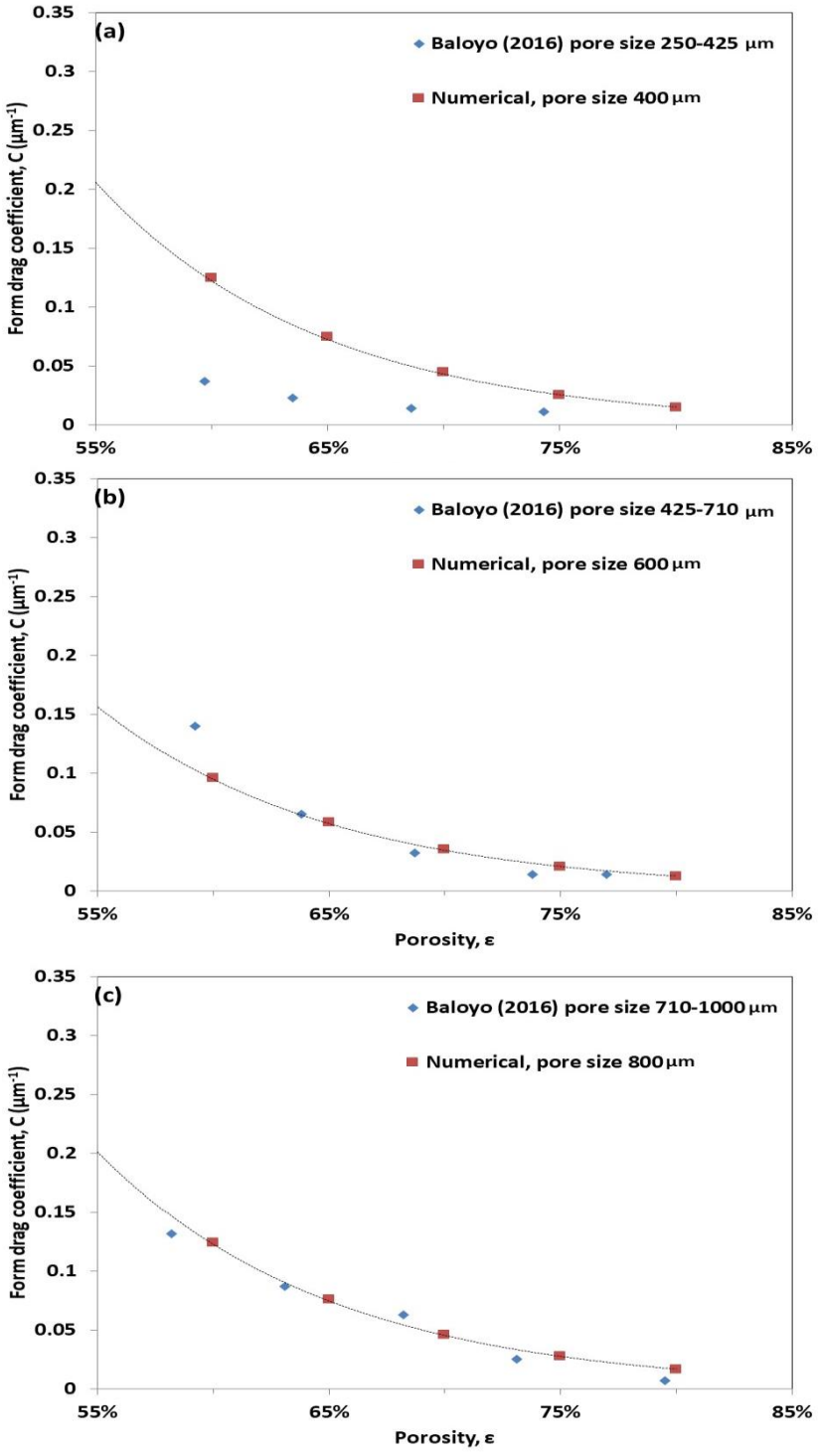

Figure 4-28 Relationship between form drag coefficient (C) and porosity for numerical and experimental (Baloyo 2016) data. The 3D REVs have a metal particle size of 70 µm and different pore sizes: (a) exp. 250-450 µm and num. 400 µm, (b) exp. 450-710 µm and num. 600 µm, (c) exp. 710-1000 µm and num. 800 µm, and (d) exp. 710-1000 µm and num. 1000 µm (to be continued)

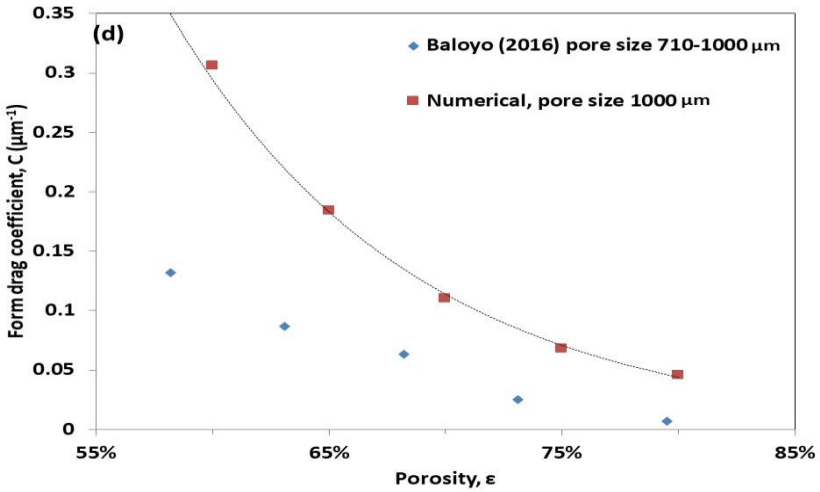

Figure 4-28 (Continuation) Relationship between form drag coefficient (C) and porosity for numerical and experimental (Baloyo 2016**) data. The 3D REVs have a metal particle size of 70 µm and different pore sizes: (a) exp. 250-450 µm and num. 400 µm, (b) exp. 450-710 µm and num. 600 µm, (c) exp. 710-1000 µm and num. 800 µm, and (d) exp. 710-1000 µm and num. 1000 µm**

The numerical results for a metal particle size of 70 µm showed very similar behaviour. With the exception of the REVs with pore size of 400 µm, the numerical results fall almost on the same line as the experimental data. In general, the numerical results exhibited similar behaviour to the experimental values. The numerical results showed that the form drag coefficient increases with pore size. This is further corroborated by the relationship between form drag coefficient and pore size as shown in Figure 4-29. The form drag coefficient increases linearly with pore size.

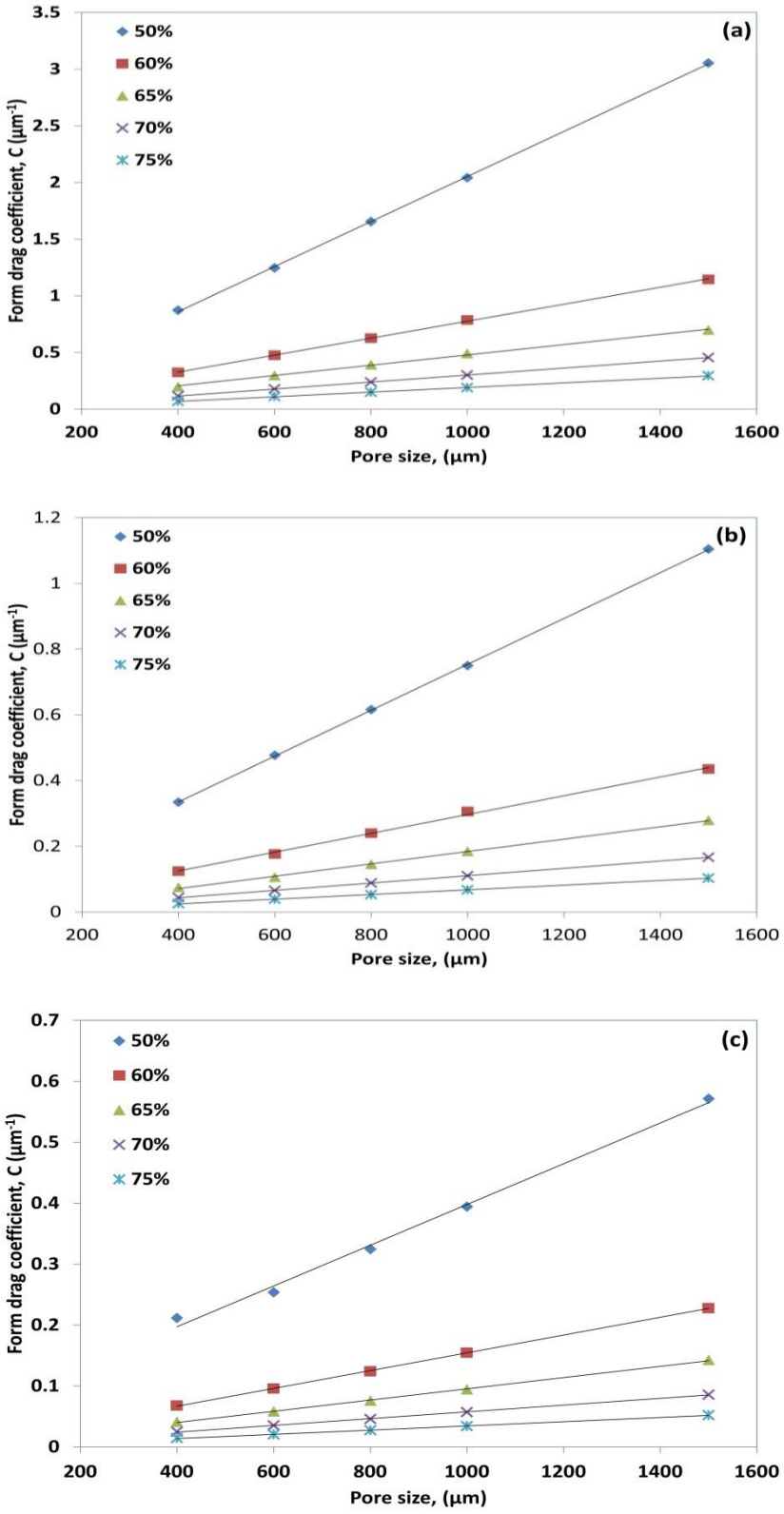

Figure 4-29 Relationship between form drag coefficient and pore size for numerical data with different porosities (shown in figure) and metal particle size of: (a) 30 µm, (b) 50 µm and (c) 70 µm

Increasing pore size, decreasing porosity, or decreasing metal particle size increases the form drag coefficient. Larger pores create smaller openings for the flow stream. Smaller metal particles fill the gaps better than the larger metal particles creating smaller windows. Both situations increase the resistance to the flow by form drag.

4.5.4 Relationship between *K* and *C*

The relationship between permeability K and form drag coefficient C is shown in Figure 4-30. As permeability increases, the form drag coefficient decreases in an exponential fashion. Higher permeability values leads to lower form drag coefficients, or lower permeabilities are related to higher form drag coefficients. As the metal particle size increases, the form drag coefficient decreases at any fixed permeability.

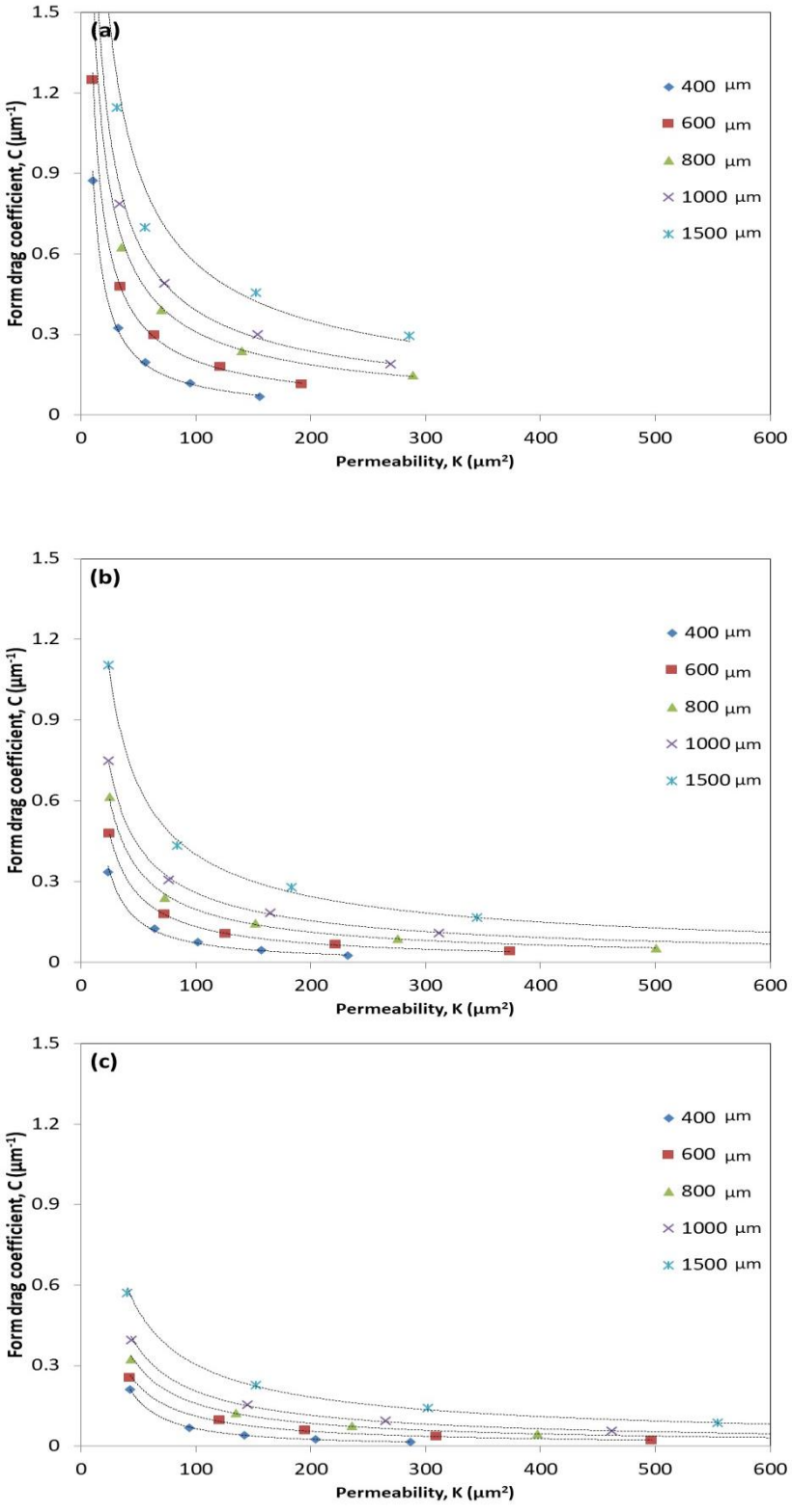

Figure 4-30 Form drag coefficient versus permeability for different pore sizes (shown in the figure) and different metal particle sizes: (a) 30 µm, (b) 50 µm and (c) 70 µm

The relationship between permeability and form drag coefficient is shown alternatively in a logarithmic scale in Figure 4-31. The correlation between permeability and form drag coefficient can be described by:

$$C = \frac{C_f}{K^M} \tag{4.20}$$

The values for the exponential term M and the drag force coefficient C_f are obtained by linear regressions and are presented in Table 4-6. C and K were shown to be highly correlated ($r^2 > 0.99$) for all cases analysed.

Table 4-6 Exponential term and drag force coefficient values for the REVs considering all pore sizes and all metal particle sizes

Metal particle size (μm)	Pore size (μm)	m	C_f	R^2
30	400	0.96	2.63E-05	1
	600	0.80	1.95E-03	1
	800	0.74	1.24E-02	1
	1000	0.72	2.75E-02	1
	1500	0.77	1.09E-02	0.99
50	400	1.17	1.25E-07	0.99
	600	0.94	5.90E-05	1
	800	0.77	3.84E-03	1
	1000	0.70	2.44E-02	1
	1500	0.74	1.50E-02	1
70	400	1.32	2.07E-10	1
	600	1.03	2.84E-06	1
	800	0.81	1.08E-04	1
	1000	0.73	1.00E-03	1
	1500	0.70	2.98E-02	1

Table 4-6 shows that the exponential term obtained for the 3D REVs with different pore sizes and different metal particle sizes are different, rather than having of a constant value of 0.5. The exponential term decreases with pore size for the three metal particle sizes considered.

As the metal particle size increases, however, different behaviours are observed. For the 3D REVs with a pore size of 400 μm to 800 μm, increasing metal particle size led to an increase in the exponential term. For the 3D REVs with a pore size of 1000 μm and 1500 μm, increasing metal particle size can lead to a decrease in the exponential term. The drag force coefficient, on the other hand, increased whit pore size and decreased with metal particle size.

Baloyo (2016) proposed a correlation for water permeability and form drag coefficient in homogeneous LCS porous samples as follows:

$$C = \frac{6.1x10^{-4}}{K^{0.76}} \tag{4.21}$$

This relationship is also shown in Figure 4-31. The numerical results showed a similar tendency as Equation 4.21. However, there is a big difference up to 10 times between the numerical results and Equation 4.21, especially for the large pore size (1500 μm) and small metal particle sizes (30 μm). It should be pointed out that Baloyo (2016) did not consider the effects of pore size and metal particle size on the exponential term and used a fixed value of exponent of 0.76.

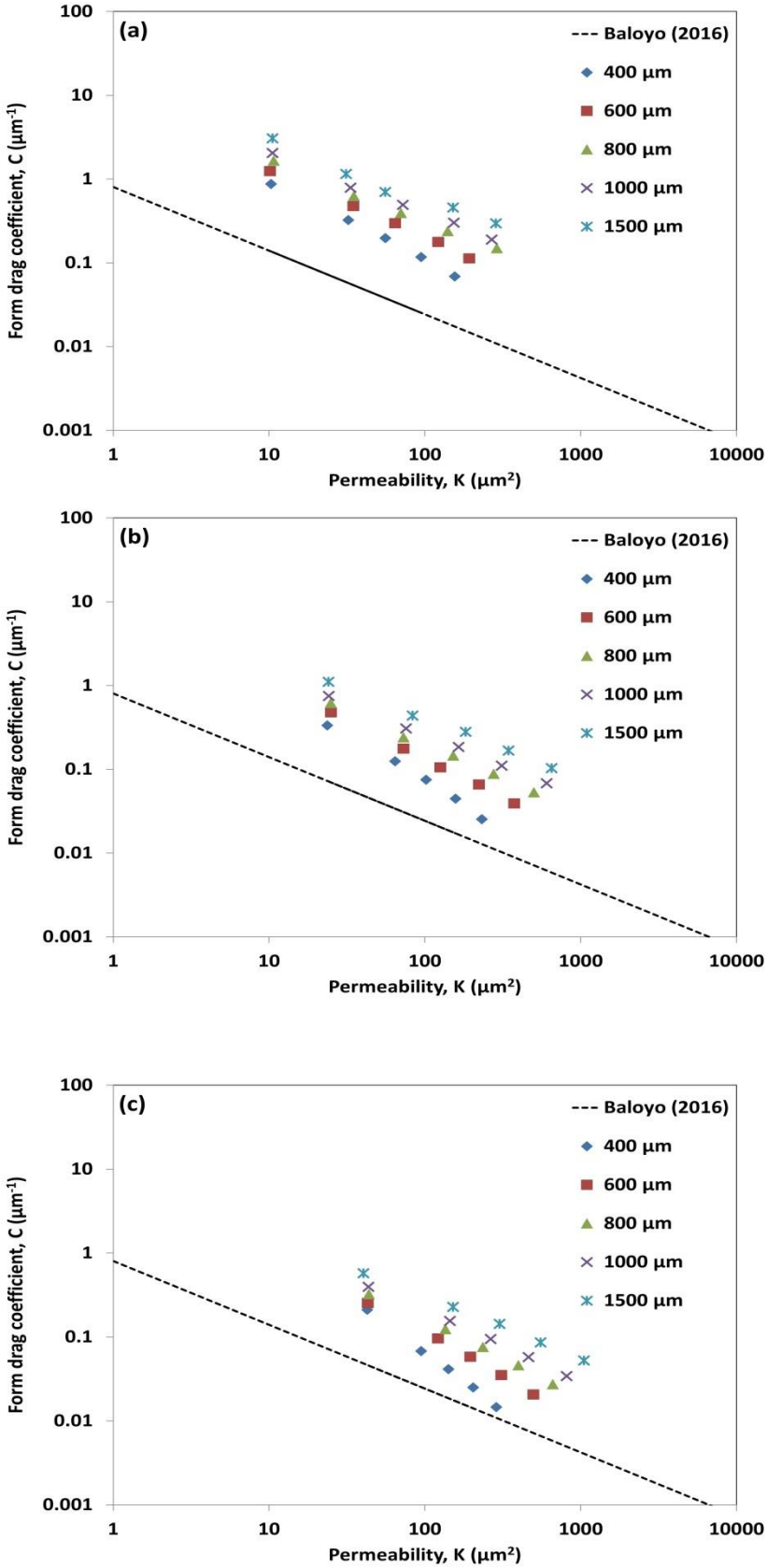

Figure 4-31 Relationship between permeability (K) and the form drag coefficient (C) for the REVs with comparison to the literature with different pore sizes (shown in the figure) and metal particle sizes of: (a) 30 µm, (b) 50 µm and (c) 70 µm

Even though the 3D REVs are created to simulate the porous metals made by the space holder techniques such as the LCS porous copper, there are differences between the numerical and experimental results. There are two possible reasons for the differences. First, some of the parameters such as porosity, pore size and metal particle size were simplified to have fixed values. Second, there is a difference in geometrical structure between the real material and the 3D REVs. However, the 3D REVs are shown to be a suitable model to simulate pressure drop inside the LCS porous copper.

4.6 Heat transfer

4.6.1 Introduction

This section presents and discusses the results obtained from the numerical simulations for heat transfer coefficient calculations. In the numerical analysis, the volumetric flow rate ranged from 0.2 l/min to 1.8 l/min, corresponding to Darcian velocities from 0.03 m/s to 0.3 m/s. A constant heat flux (250 kW/m^2) was applied underneath the REVs. The energy equation was activated and the temperatures throughout the domain were quantified.

In the present study, heat transfer due to forced convection was studied. In the geometry creation process, a heated block was placed underneath the 3D REVs. This block has the same length as the 3D REV and supplies a constant heat flux to the 3D REVs. Water was used to remove heat from the 3D REVs. Newton's cooling law was employed to calculate the heat transfer coefficient, which can be obtained by rearranging equation 2.17:

$$h = \frac{J}{(T_{pl} - T_m)} \tag{4.22}$$

where J is the heat flux from the heated plate per unit area, T_{pl} is the temperature of the heated block, and T_m is the mean temperature at the inlet of the water. In this study, T_m was fixed to 300K. In order to calculate the temperatures throughout the domain, a surface integral was employed from the post processing-reports menu in fluent. Then an area weighted average of the total temperature in every surface was calculated. The temperature at the top of the heated block was chosen as T_{pl}. In the present study, the temperatures were measured at different flow rates for the 3D REVs with different porosities, pore sizes and metal particle sizes. The same ranges of conditions were used as in the pressure drop analysis and the heat transfer coefficients were calculated in all cases. The effects of flow rate, porosity, pore size and metal particle size were investigated.

The heat transfer coefficients calculated in the present study are listed in Table 4-7. Porosity, pore size and metal particle size are the structural parameters that were changed in each simulation. It is difficult to obtain consistent values for the heat transfer coefficients of some of the REVs with porosity of 80%, because of the poor quality of the mesh at the solid-fluid interface. Thus, these results are not included.

Table 4-7 Heat transfer coefficients of REVs structures with different pore size, metal particle size, porosity and flow rate

Pore size (μm)	Metal particle size (μm)	Q (l/min)	Heat transfer coefficient (kW/m^{2}K) at different porosities					
			50%	60%	65%	70%	75%	80%
400	30	0.2	6.14	5.7	5.54	5.37	5.2	5.03
		0.6	13.77	12.8	12.28	11.72	11.07	10.25
		1	17.95	16.61	15.89	15.1	14.19	13.07
		1.4	20.51	18.97	18.13	17.21	16.15	14.87
		1.8	22.23	20.58	19.67	18.67	17.52	16.14
	50	0.2	6.1	5.75	5.55	5.38	5.2	4.97
		0.6	13.68	12.67	12.13	11.53	10.82	9.97
		1	17.75	16.37	15.62	14.78	13.76	12.59
		1.4	20.23	18.66	17.79	16.81	15.6	14.26
		1.8	21.91	20.21	19.28	18.17	16.89	15.45
	70	0.2	6.18	5.72	5.56	5.4	5.19	4.97
		0.6	13.65	12.59	12.02	11.42	10.69	9.85
		1	17.68	16.24	15.44	14.58	13.56	12.36
		1.4	20.15	18.49	17.55	16.54	15.36	13.95
		1.8	21.82	20.03	19.01	17.9	16.62	15.07
600	30	0.2	8.06	7.6	7.37	7.1	6.8	-
		0.6	17.12	15.95	15.38	14.62	13.67	-
		1	21.63	20.09	19.32	18.34	17.1	-
		1.4	24.27	22.54	21.67	20.58	19.19	-
		1.8	26.02	24.17	23.24	22.09	20.62	-
	50	0.2	7.97	7.54	7.28	7.01	6.69	6.38
		0.6	16.95	15.73	15.04	14.28	13.33	12.25
		1	21.36	19.77	18.86	17.87	16.62	15.22
		1.4	23.93	22.16	21.15	20.04	18.65	17.09
		1.8	25.6	23.74	22.69	21.51	20.04	18.39
	70	0.2	7.99	7.5	7.24	6.96	6.65	-
		0.6	16.85	15.58	14.86	14.06	13.08	-
		1	21.18	19.53	18.6	17.55	16.23	-
		1.4	23.73	21.89	20.84	19.67	18.17	-
		1.8	25.41	23.46	22.35	21.11	19.51	-
800	30	0.2	9.29	8.98	8.68	8.37	8.03	7.47
		0.6	19.26	17.97	17.26	16.48	15.52	14.13
		1	22.81	22.16	21.25	20.26	19.05	17.31
		1.4	26.35	24.58	23.22	22.47	21.13	19.23
		1.8	28.05	26.16	25.08	23.93	22.51	20.51
	50	0.2	9.11	8.54	8.21	7.84	7.4	6.82
		0.6	18.25	16.81	16.02	15.19	14.15	12.95
		1	22.81	20.9	19.85	18.73	17.44	16
		1.4	25.57	23.45	22.23	20.96	19.47	17.87
		1.8	27.37	25.11	23.9	22.54	20.93	19.22

(to be continued)

Table 4-7 (Continuation) Heat transfer coefficients of REVs structures with different pore size, metal particle size, porosity and flow rate

Pore size (μm)	Metal particle size (μm)	Q (l/min)	Heat transfer coefficient (kW/m^{2}K) at different porosities					
			50%	60%	65%	70%	75%	80%
800	70	0.2	9.42	8.84	8.52	8.17	7.76	-
		0.6	18.88	17.5	16.67	15.78	14.7	-
		1	23.22	21.5	20.46	19.33	17.97	-
		1.4	25.69	23.81	22.67	21.42	19.92	-
		1.8	27.29	25.33	24.12	22.81	21.23	-
1000	30	0.2	10.76	10.09	9.68	9.33	8.9	8.18
		0.6	20.6	19.41	18.48	17.64	16.63	14.89
		1	25	23.48	22.36	21.35	20.09	17.97
		1.4	27.61	25.83	24.59	23.47	22.08	19.77
		1.8	29.37	27.42	26.09	24.92	23.43	21.01
	50	0.2	10.53	9.89	9.57	9.19	8.74	8.18
		0.6	20.3	18.88	18.11	17.22	16.23	14.87
		1	24.52	22.85	21.89	20.81	19.69	17.95
		1.4	26.85	25.09	24.03	22.87	21.55	19.76
		1.8	28.37	26.54	25.44	24.23	22.73	20.95
	70	0.2	10.45	9.84	9.46	9.08	8.59	7.95
		0.6	20.17	18.69	17.83	16.9	15.76	14.37
		1	24.39	22.59	21.53	20.4	19.01	17.38
		1.4	26.77	24.79	23.63	22.4	20.91	19.16
		1.8	28.35	26.24	25.01	23.72	22.15	20.35
1500	30	0.2	12.51	11.66	11.3	10.86	10.34	9.17
		0.6	22.11	20.75	19.93	18.97	17.91	15.56
		1	26.63	24.49	23.51	22.31	21.03	18.06
		1.4	29.61	26.63	25.55	24.25	22.91	19.77
		1.8	31	28.08	26.97	25.77	24.29	20.77
	50	0.2	12.39	11.54	11.13	10.69	10.12	9.18
		0.6	21.85	20.42	19.55	18.61	17.44	15.56
		1	25.78	24.03	22.96	21.75	20.46	18.26
		1.4	27.97	26.07	24.9	23.71	22.19	19.78
		1.8	29.4	27.49	26.34	25.01	23.39	20.77
	70	0.2	12.11	11.43	11.01	10.56	9.93	9.18
		0.6	20.68	20.12	19.26	18.29	17.07	15.57
		1	25.41	23.65	22.61	21.45	20.03	18.26
		1.4	27.74	25.68	24.51	23.24	21.7	19.79
		1.8	29.44	27.02	25.87	24.45	22.82	20.8

4.6.2 Effect of flow rate

The variations of heat transfer coefficient with flow rate for the 3D REVs with metal particle sizes of 30 μm, 50 μm and 70 μm are shown in Figure 4-32, Figure 4-33 and Figure 4-34, respectively. It can be seen that the heat transfer coefficient is affected by three parameters: the volumetric flow rate, porosity and pore size.

The heat transfer coefficient increases significantly with flow rate in all cases. The increasing trend is not linear but parabolic. The heat transfer coefficient increased more rapidly at flow rates below 1 l/min. For instance, increasing the flow rate from 0.2 l/min to 0.6 l/min led to 100% increase on the heat transfer coefficient. However, at flow rates higher than 1 l/min, the enhancement on the heat transfer coefficient was around 10 to 25%. The relationship between the heat transfer coefficient and the flow rate was similar for different porosities and pore sizes.

Several studies on porous media have reported that increasing flow rate led to an increase on the heat transfer coefficient (Zhang *et al.* 2009, Kopanidis *et al.* 2010, Bai and Chung 2011). It is acknowledged that at higher water flow rates, a turbulent flow occurs within the porous network. This turbulence will cause mixing and greater fluid access to the smaller channels/voids within the porous copper sample (Baloyo and Zhao 2015). This mixing behaviour will increase the heat transfer to the water by forced convection.

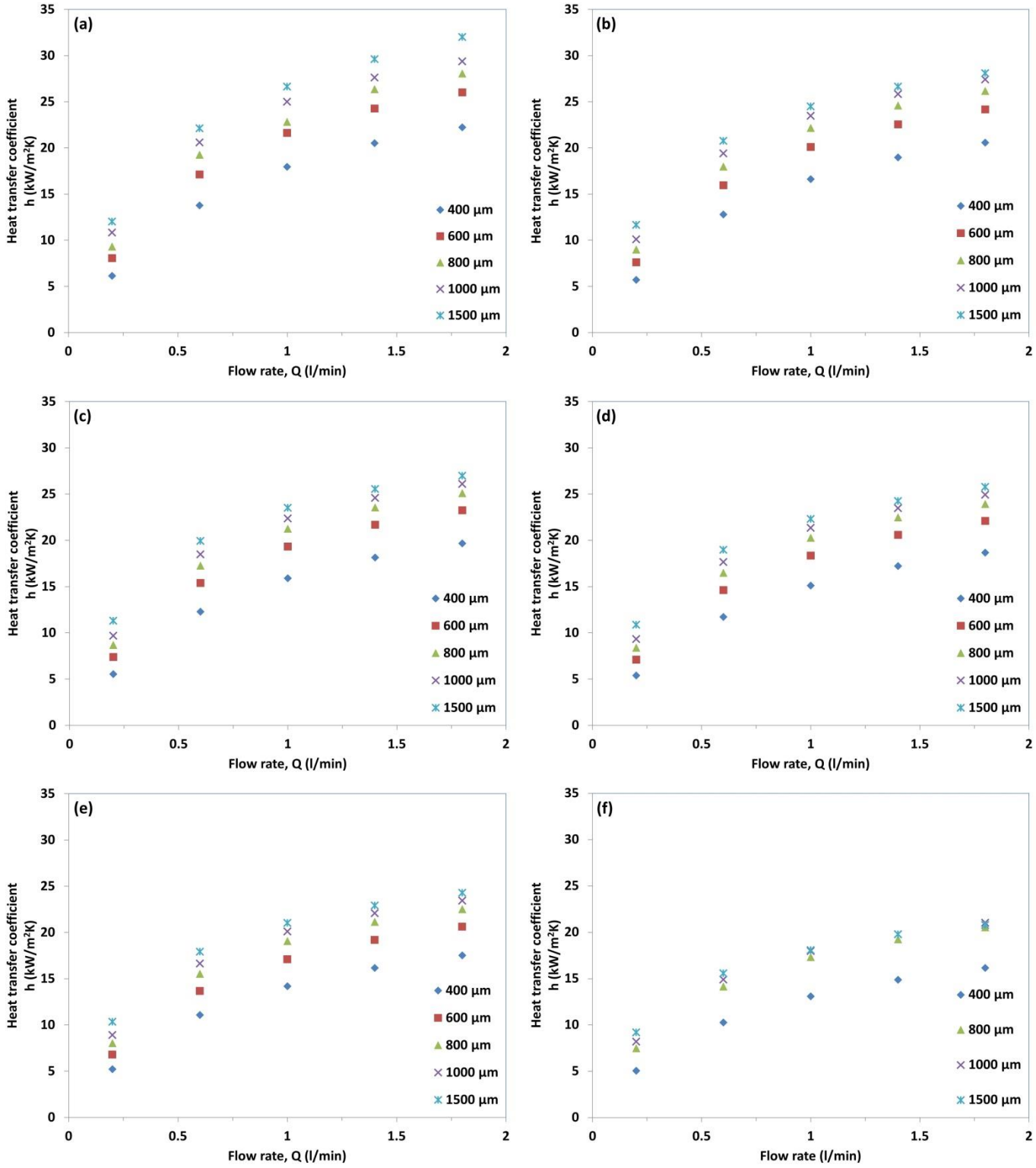

Figure 4-32 Heat transfer coefficient versus volumetric flow rate for REVs with a metal particle size of 30 µm, pore sizes ranging from 400 to 1500 µm (shown in the figure) and different porosities: (a) 50%, (b) 60%, (c) 65%, (d) 70%, (e) 75% and (f) 80%

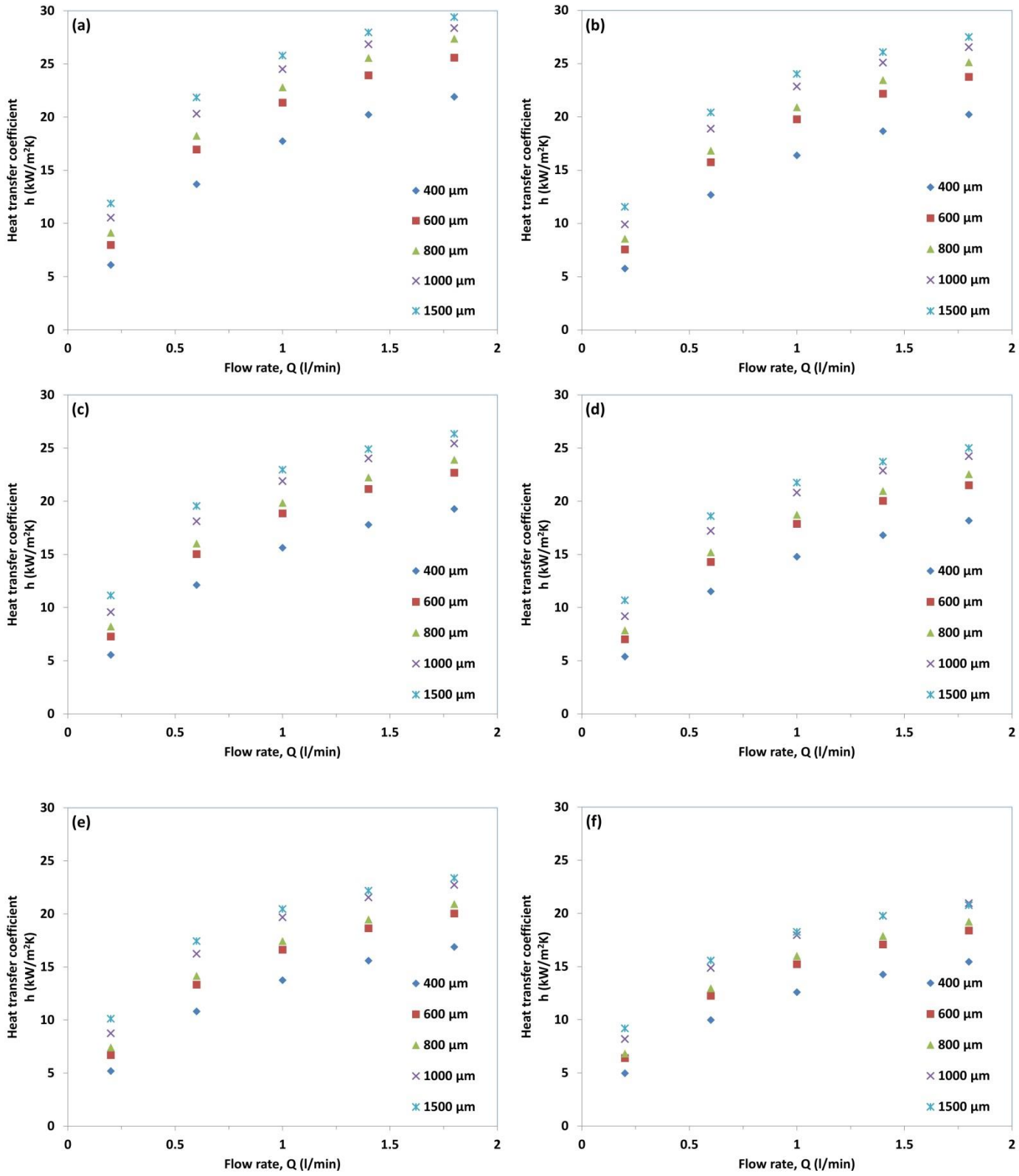

Figure 4-33 Heat transfer coefficient versus volumetric flow rate for REVs with a metal particle size of 50 µm pore sizes ranging from 400 to 1500 µm (shown in the figure) and different porosities: (a) 50%, (b) 60%, (c) 65%, (d) 70%, (e) 75% and (f) 80%

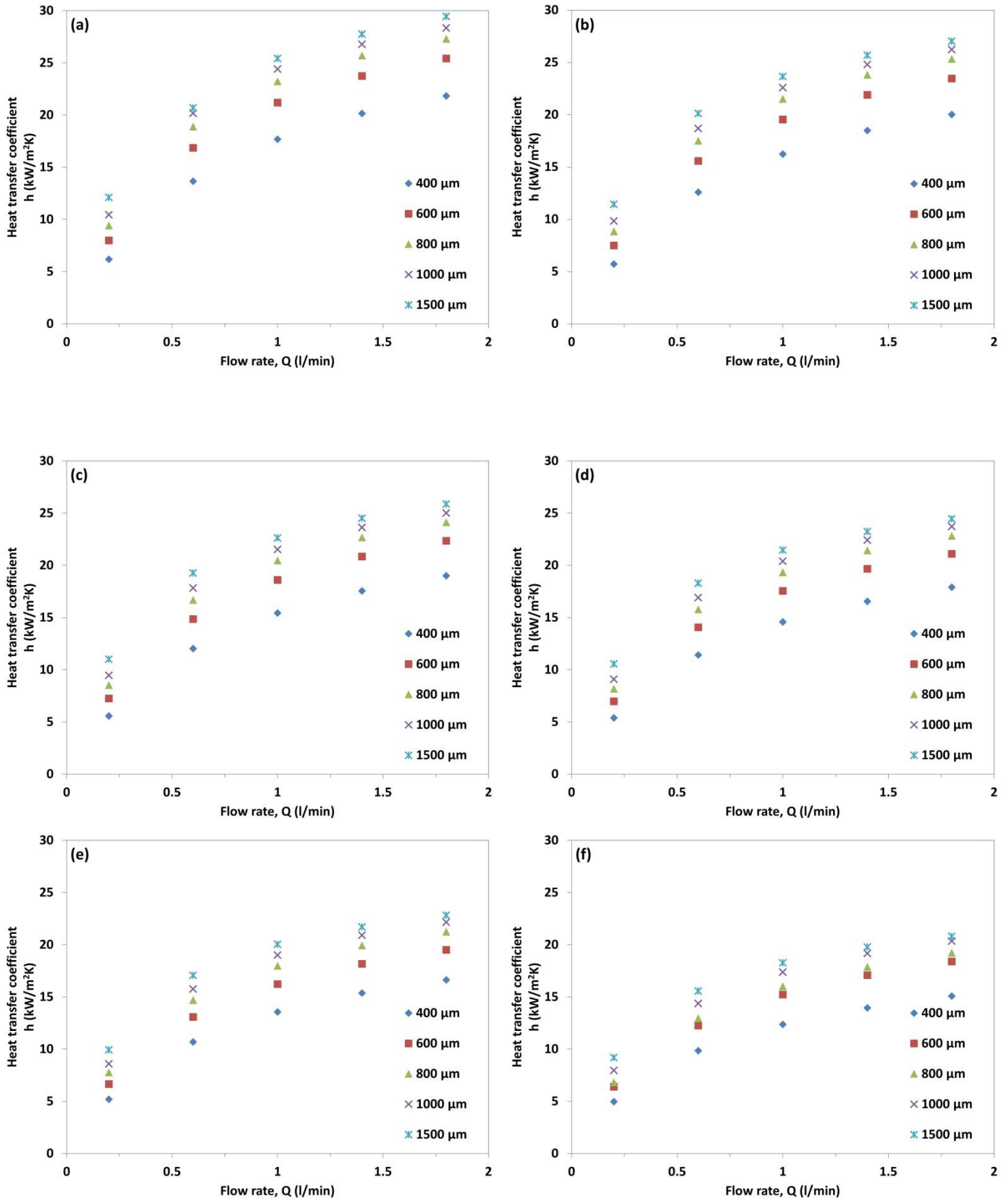

Figure 4-34 Heat transfer coefficient versus volumetric flow rate for REVs with a metal particle size of 70 µm pore sizes ranging from 400 to 1500 µm (shown in the figure) and different porosities: (a) 50%, (b) 60%, (c) 65%, (d) 70%, (e) 75% and (f) 80%

4.6.3 Effect of porosity

Figure 4-35, Figure 4-36 and Figure 4-37 show the variation of heat transfer coefficient with porosity for 3D REVs with metal particle sizes of 30 μm, 50 μm and 70 μm, respectively. The heat transfer coefficient decreases with porosity in all cases. The trend was almost linear, although heat transfer coefficient decreased more rapidly at high porosities. A higher porosity means less solid material for energy transfer due to conduction, and thus less energy to be transferred to the flow by convection.

Mahjoob and Vafai (2008) drew similar conclusions regarding the effect of porosity on the heat transfer coefficient for metal foam heat exchangers. The results also agreed with Xiao and Zhao (2013) and also with Baloyo and Zhao (2015).

Xiao (2013) reported that the highest heat transfer coefficient of the LCS porous copper samples was obtained at 61.2% porosity for the low pore size samples (250-425 μm) and at 65% porosity for the large pore size samples (1000-1500 μm). Baloyo (2016) further studied the effect of porosity on the heat transfer coefficient of homogenous LCS porous copper samples and concluded that the optimum porosity value was 60%. In both studies, porous samples with lower porosities (40% and 50%) exhibited poor performances. This is different from the numerical simulation results obtained in this study. The numerical results showed that the 3D REVs with a porosity of 50% has the best performance.

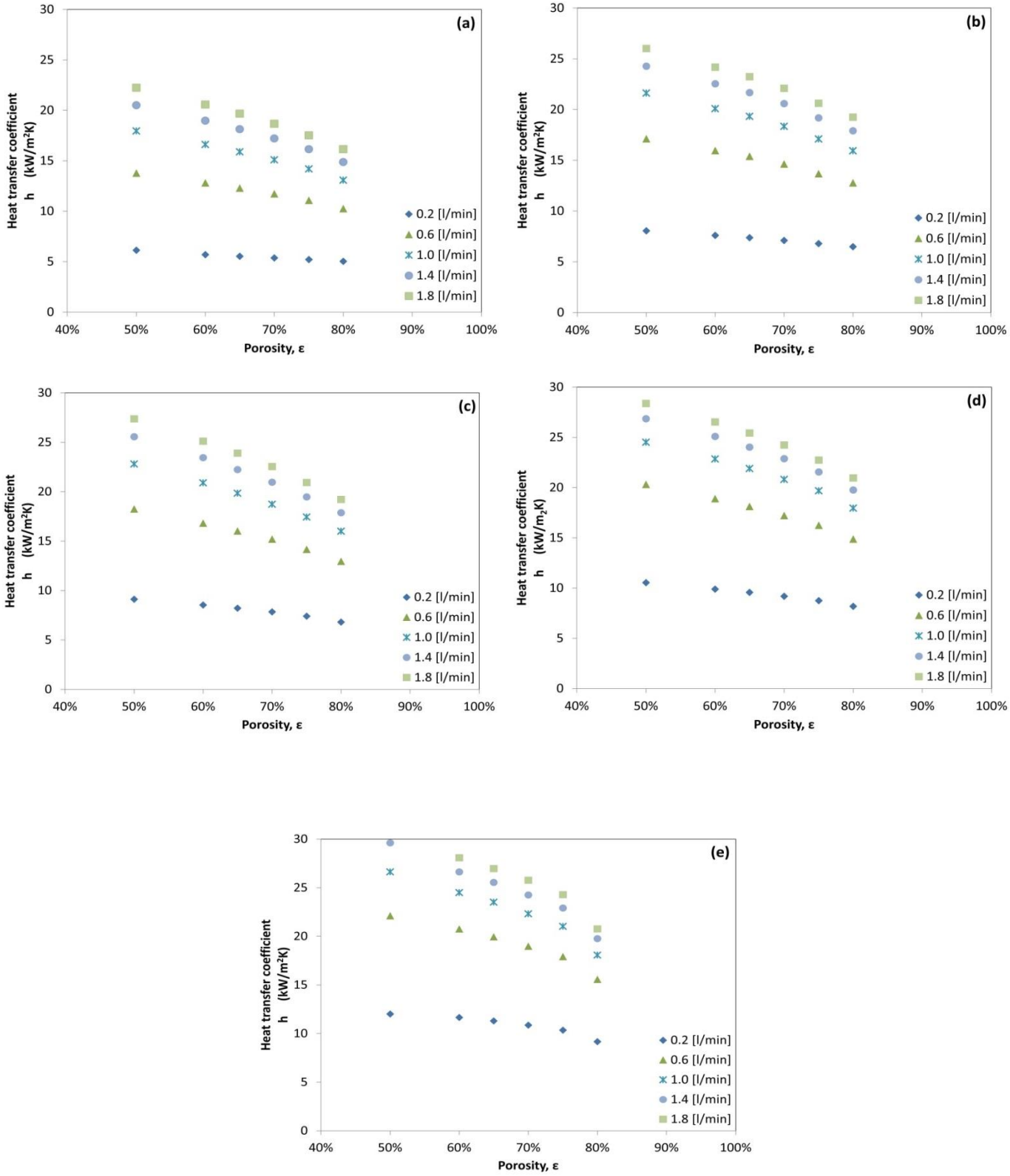

Figure 4-35 Heat transfer coefficient versus porosity of 3D structures with metal particle size of 30 µm at different flow rates (shown in the figures) and pore sizes of: (a) 400 µm, (b) 600 µm, (c) 800 µm, (d) 1000 µm, (e) 1500 µm

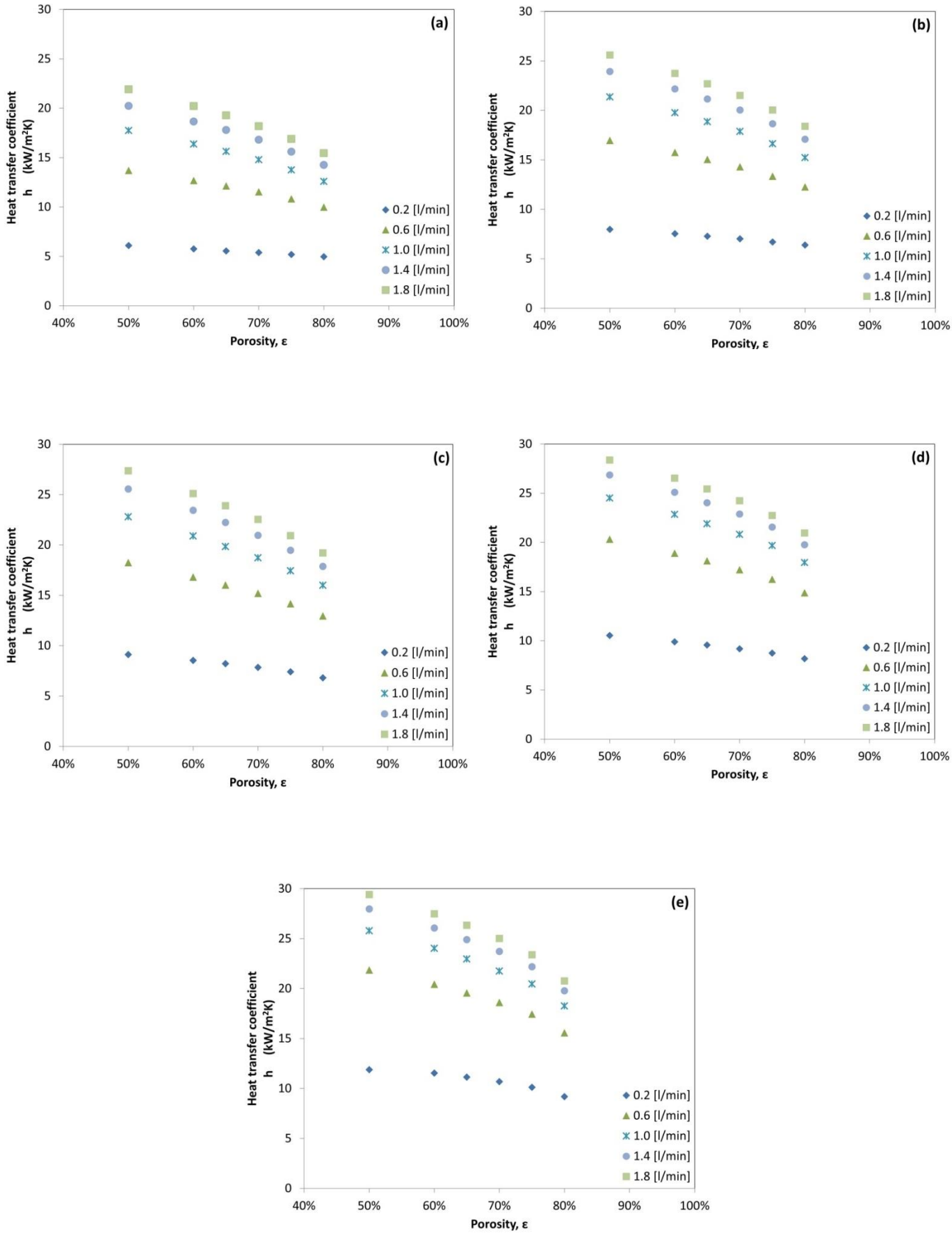

Figure 4-36 Heat transfer coefficient versus porosity of 3D structures with metal particle size of 50 μm at different flow rates (shown in the figures) and pore sizes of: (a) 400 μm, (b) 600 μm, (c) 800 μm, (d) 1000 μm, (e) 1500 μm

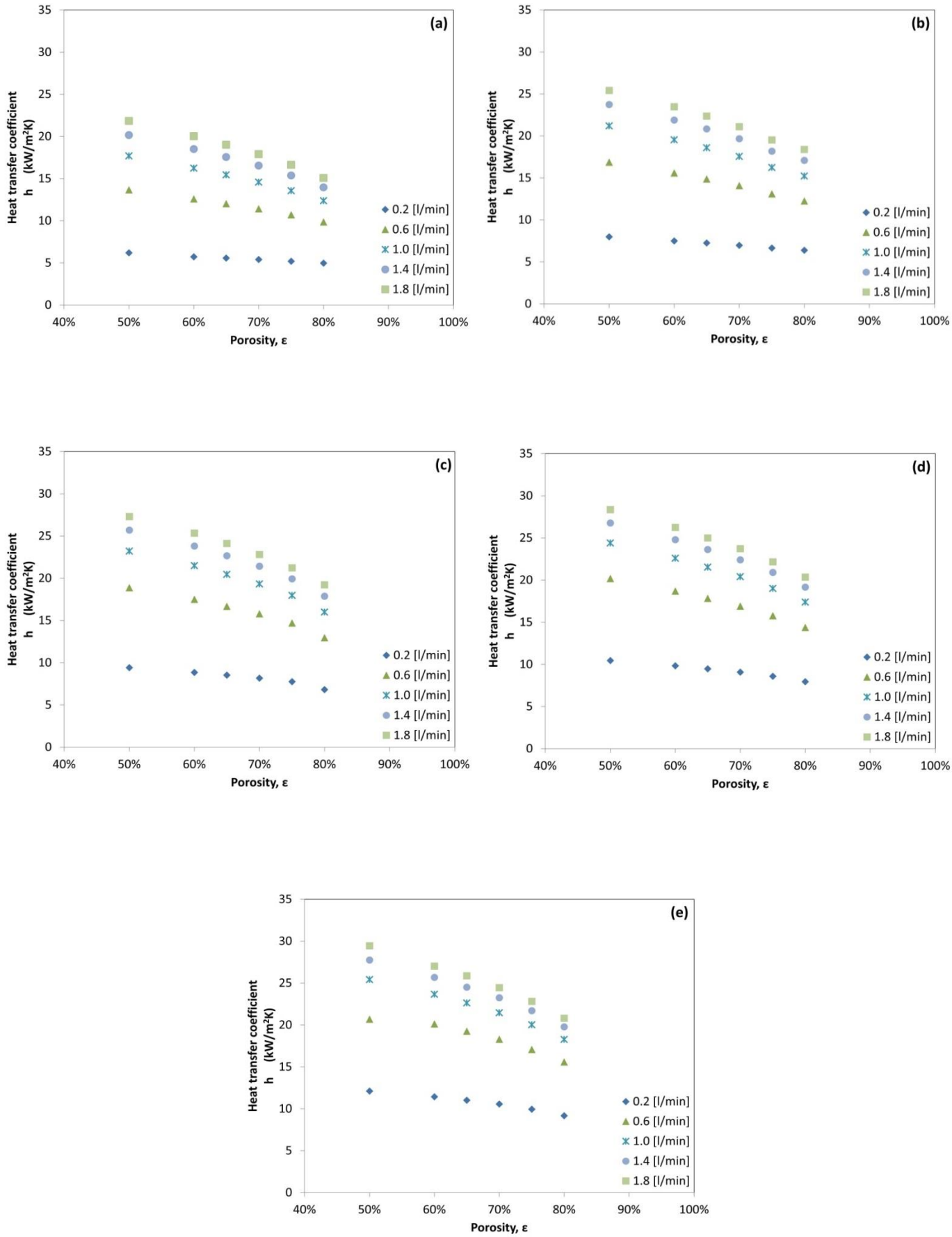

Figure 4-37 Heat transfer coefficient versus porosity of 3D structures with metal particle size of 70 µm at different flow rates (shown in the figures) and pore sizes of: (a) 400 µm, (b) 600 µm, (c) 800 µm, (d) 1000 µm, (e) 1500 µm

As porosity decreases, it is possible to appreciate an increase in the heat transfer coefficient. For example, by comparing the REVs with 80% porosity and 75% porosity, it is observed an increase between 5% to 15% on the heat transfer coefficient. In particular cases like in the REVs with metal particle size of 30 μm and pore size of 1500μm, the observed increment on the heat transfer coefficient was of 17%. However, for the rest of porosities, the observed change in heat transfer coefficient was around 3% for the REVs with the smaller pore size and up to 7% for the REVs with the larger pores.

4.6.4 Effect of pore size

The variations of heat transfer coefficient with pore size for the 3D REV structures with metal particle sizes of 30 μm, 50μm and 70μm were plotted as shown in Figure 4-38, Figure 4-39 and Figure 4-40 respectively. The results show that increasing pore size enhanced the heat transfer coefficient. With a flow rate of 0.2 l/min, changing pore size from 400 μm to 600 μm increases the heat transfer coefficient about 30%. As flow rate increases, the increment of heat transfer coefficient by changing pore size decreases to only 17% in some cases. Changing the pore size further to 800 μm, the increase of heat transfer coefficient is about 18% at the low flow rate and about 7% at the higher flow rate. However, when pore size is increased from 1000 μm to 1500 μm, the heat transfer coefficient starts to stabilise, and even in some cases as in Figure 4-39 (a), the increase in heat transfer coefficient is barely noticeable.

Zhang *et al.* (2009) reported that the best heat transfer performance for the LCS porous structures was achieved with a pore size in the range of 425-710 μm. Larger and smaller pore sizes showed poorer performances. High fluid resistance for the smaller pores or less surface area for the largest pores were cited as the main reasons.

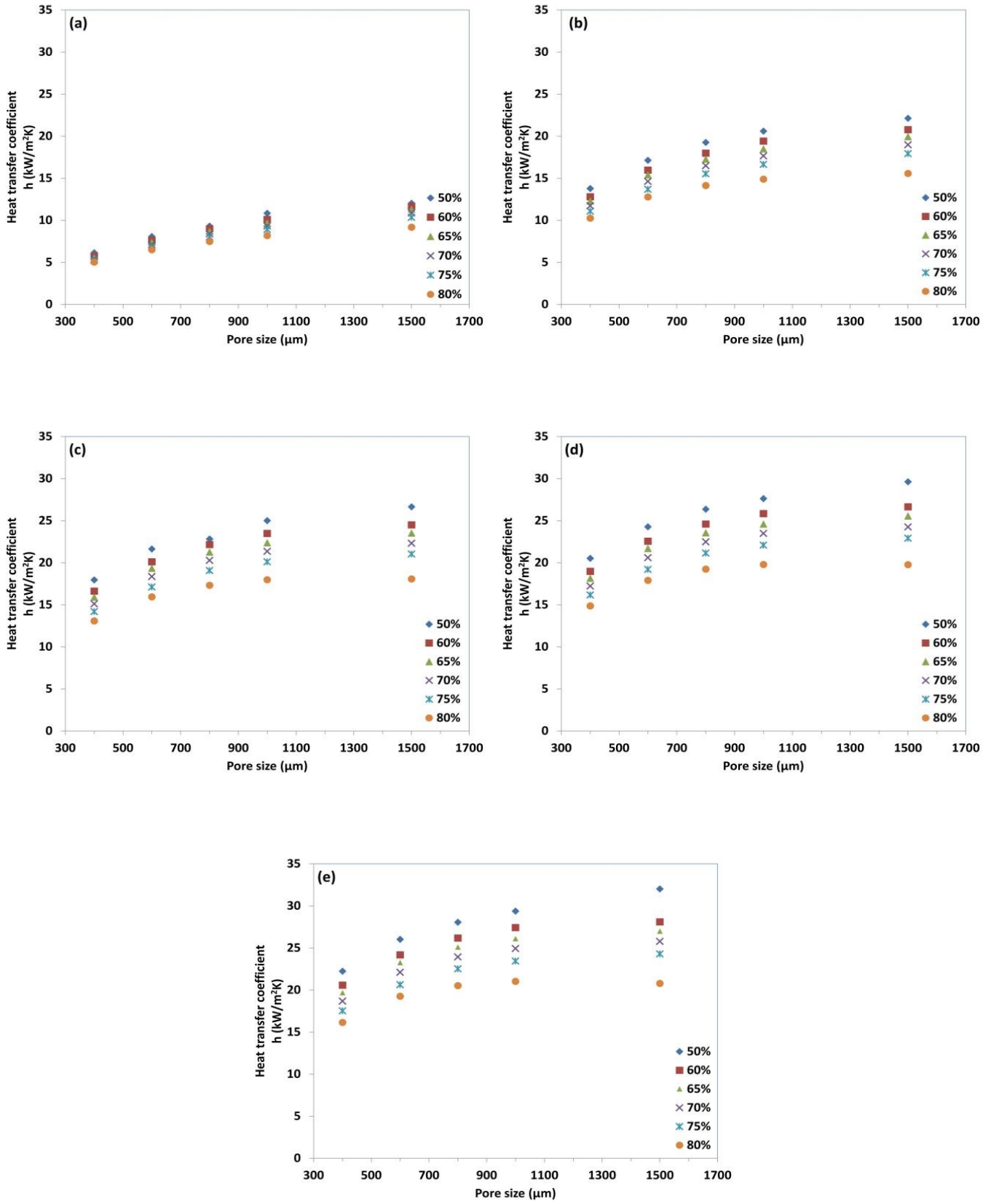

Figure 4-38 Heat transfer coefficient versus pore size with different porosities and metal particle size of 30 µm, variations at different flow rates: (a) 0.2 l/min, (b) 0.6 l/min, (c) 1.0 l/min, (d) 1.4 l/min and (e) 1.8 l/min

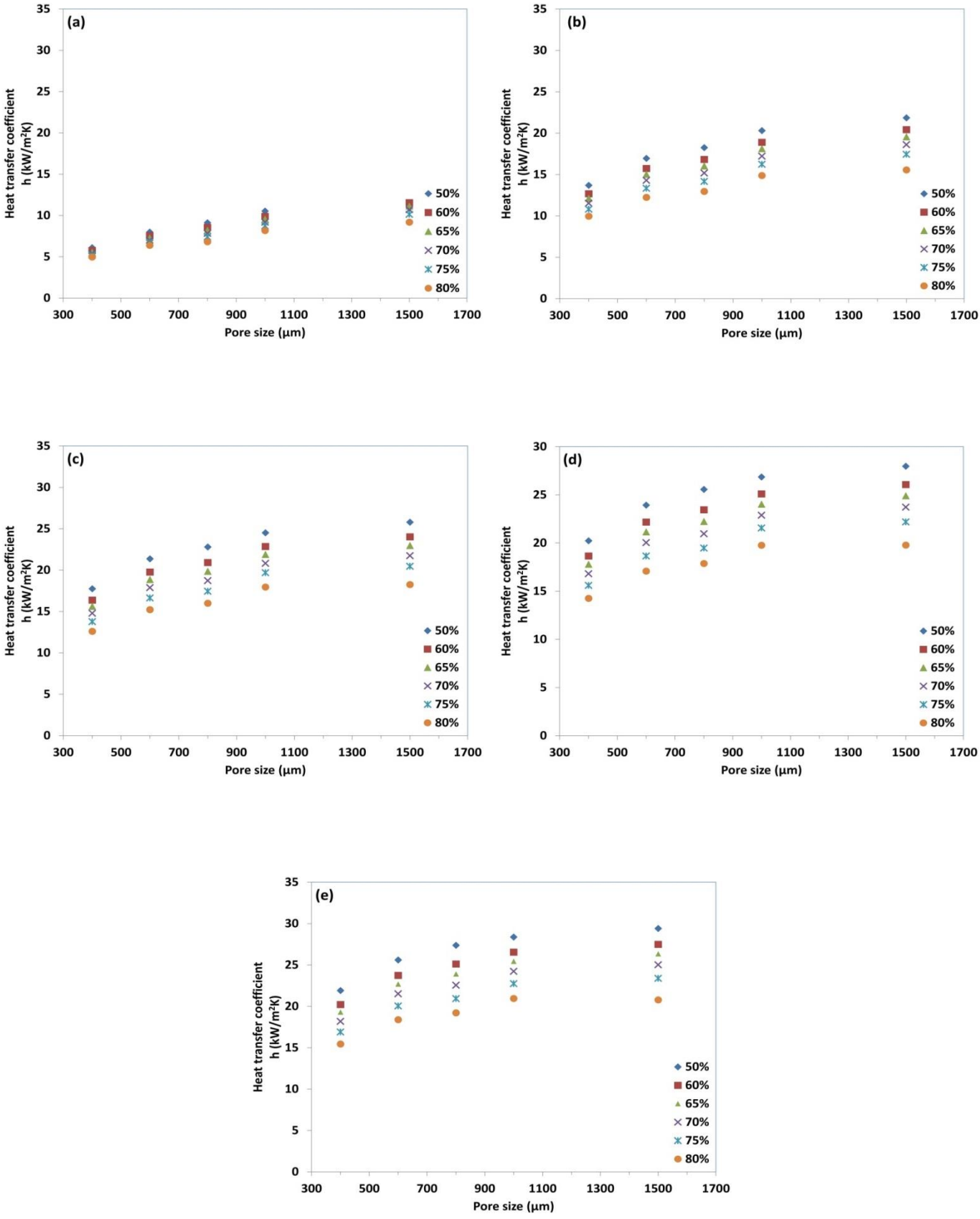

Figure 4-39 Heat transfer coefficient with different porosities versus pore size and metal particle size of 50 µm, variations at different flow rates: (a) 0.2 l/min, (b) 0.6 l/min, (c) 1.0 l/min, (d) 1.4 l/min and (e) 1.8 l/min

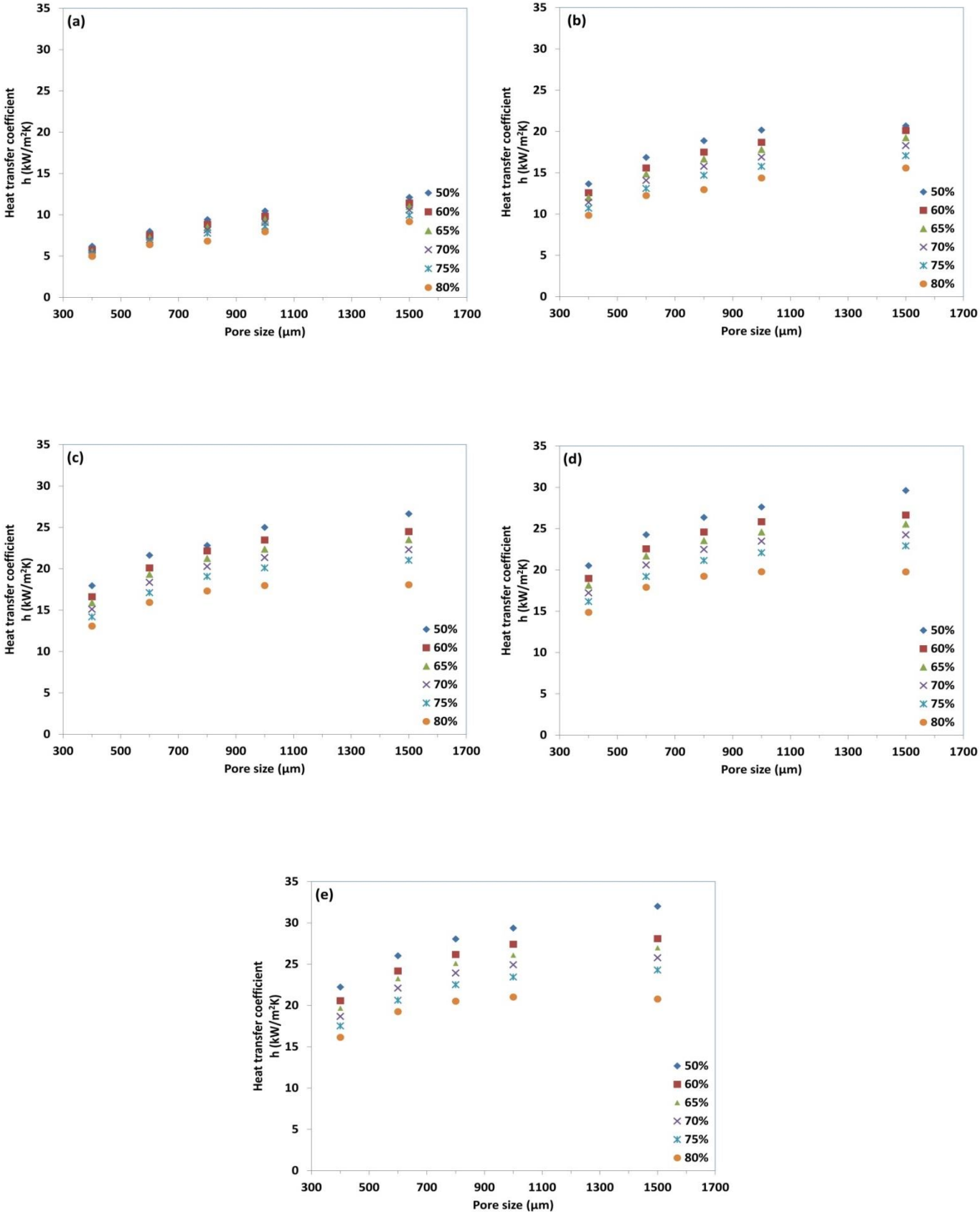

Figure 4-40 Heat transfer coefficient with different porosities versus pore size and metal particle size of 70 µm, variations at different flow rates: (a) 0.2 l/min, (b) 0.6 l/min, (c) 1.0 l/min, (d) 1.4 l/min and (e) 1.8 l/min

4.6.5 Effect of metal particle size

Three different metal particle sizes were studied in the numerical analysis to investigate the effect of copper particle size on the heat transfer performance. The heat transfer coefficients were plotted against porosity in Figure 4-41 to show the effect of the metal particle size at different flow rates.

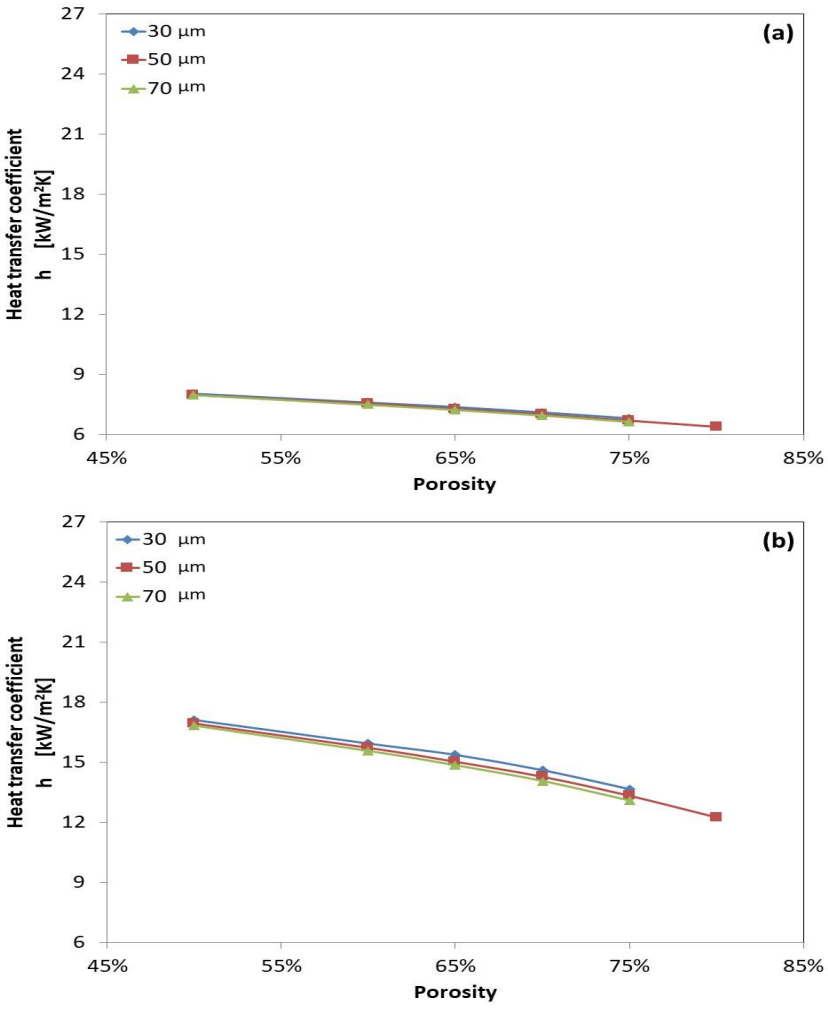

Figure 4-41 Heat transfer coefficient versus porosity for different metal particle sizes (shown in the figure), variations at different flow rates: (a) 0.2 l/min, (b) 0.6 l/min, (c) 1.0 l/min, (d) 1.4 l/min and (e) 1.8 l/min, (to be continued)

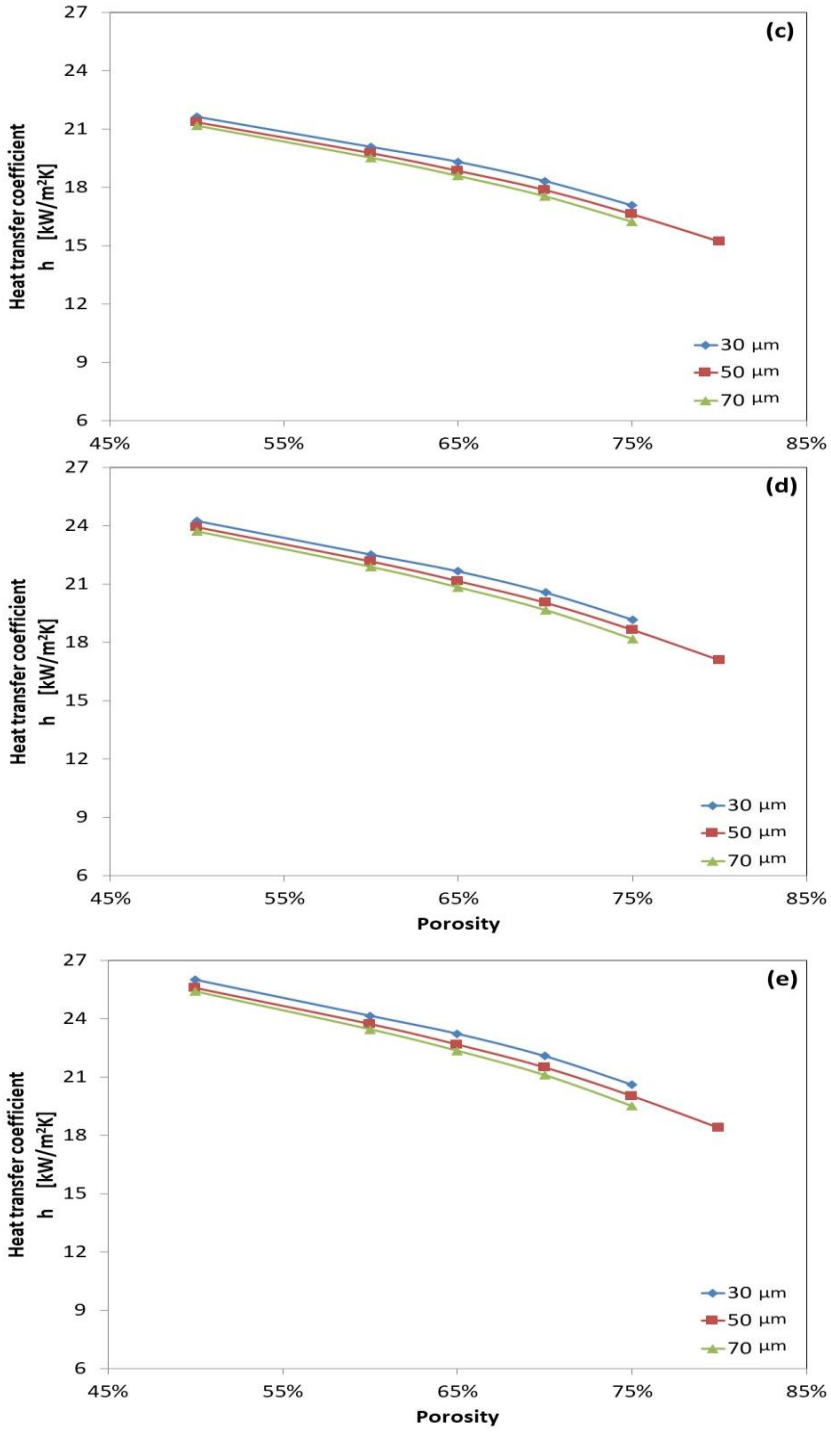

Figure 4-41 (Continuation) Heat transfer coefficient versus porosity for different metal particle sizes (shown in the figure), variations at different flow rates: (a) 0.2 l/min, (b) 0.6 l/min, (c) 1.0 l/min, (d) 1.4 l/min and (e) 1.8 l/min

Xiao (2013) reported that the metal particle size has a significant effect on the heat transfer performance of the LCS porous copper. He showed that increasing the metal particle size

from a range of 50 - 100μm range to a 100 - 300μm decreased the heat transfer response by 20% to 50%. The numerical results also showed that the heat transfer coefficient decreases slightly with metal particle size. However, the difference is barely noticeable in the range of metal particle sizes studied (< 3%). This different behaviour may be caused the experimental samples had large particle size changes (from 50-100μm and 100-300μm), while, the metal particle size change in the present research was small (from 30 μm to 70 μm).

4.6.6 Comparison with experimental data

The numerical results obtained for heat transfer coefficient were compared with experimental data available from Baloyo (2016), as shown in Figure 4-42.

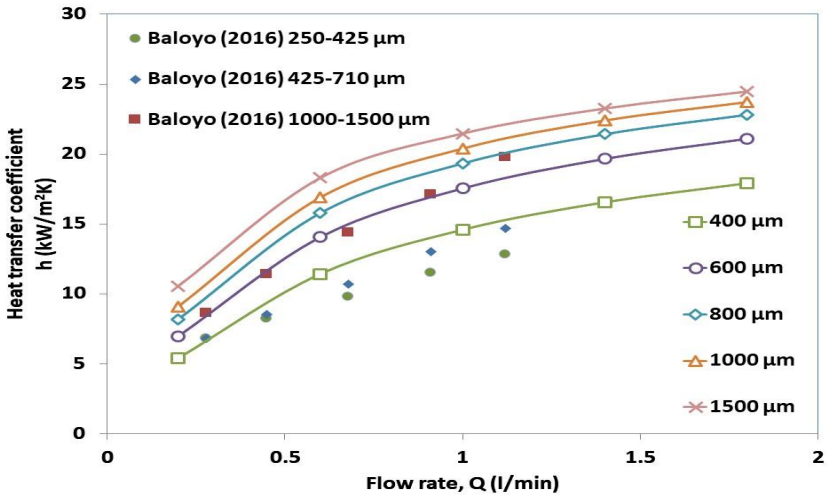

Figure 4-42 Heat transfer coefficient versus volumetric flow rate, comparison with experimental data from homogenous LCS porous structures with porosity close to 70% and different pore sizes (shown in the figure)

Although the flow rate range employed in the experimental work is not as wide as in the numerical analysis, it can be seen that the numerical results followed the same trend as the experimental data, i.e. the heat transfer coefficient increased with increasing flow rate. The numerical and experimental analyses exhibited a similar enhancing effect due to increasing

pore size. However, there are significant differences between the numerical and the experimental results due to different structural characteristics such as porosity, pore size, metal particle size and randomness of the real material. Muramatsu *et al.* (2013) suggested that aligning the pores of the porous structure to create less tortuous channels can greatly improve the heat transfer coefficient. The less tortuous paths of the 3D REVs compared to the real porous copper samples may explain the difference between the numerical and experimental results.

To further compare the results, the numerical heat transfer coefficient was also plotted against the experimental data at different porosities as shown in Figure 4-43. Although there are differences between the experimental and numerical results, they show the same trends in terms of the effect of flow rate.

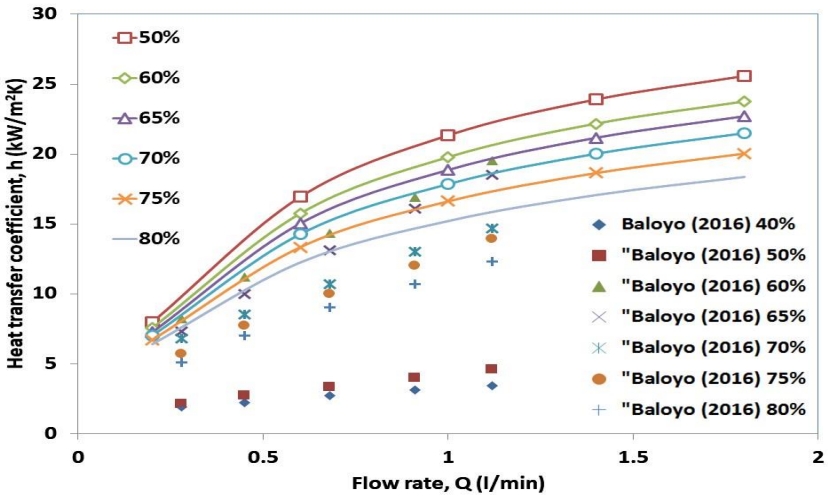

Figure 4-43 Heat transfer coefficient versus volumetric flow rate, comparison with experimental data from homogenous LCS porous structures with pore size in the range of 425-710 µm and different porosities (shown in the figure)

4.6.7 Empirical correlation for heat transfer coefficient

The numerical results for heat transfer coefficient were analysed against different structural parameters of the 3D REVs and flow velocity in the previous sections. It was observed that

increasing flow rate or pore size or decreasing porosity or metal particle size enhanced the heat transfer coefficient. In order to obtain a relationship that encompasses all these 4 variables, a multiple regression is conducted and the following empirical relationship is obtained:

$$h = 13.73 + d_{Cu}(0.0056\varphi - 0.0246) + 129.32u - 225.45u^2 - 19.25\varepsilon \quad (4.23)$$

where d_{Cu} is the diameter of the copper particles, φ is the particle size ratio, u is the Darcian velocity, and ε is the porosity. Equation 4.23 can be used for a Reynolds number ranging from 1 to 500. In total 435 heat transfer coefficient values and their corresponding predictor variables were used and an adjusted correlation factor of $R^2 = 0.96$ was obtained. As the predictor variables are independent from each other, it is assumed that there is no multicollinearity. A multicollinearity test was performed and the variance inflation factor (VIF) was equal or close to 1, confirming that there is no collinearity among the variables. The resulting statistics of the multiple regression as well as the multicollinearity test results can be found in Appendix B.

Xiao and Zhao (2013) also proposed an empirical relationship, for a Reynolds number at pore level ranging from 19 to 95, as follows:

$$h = 226.87(1 - \varepsilon)u^{0.60} + 5.78u^{0.15} \quad (4.24)$$

.

The two empirical correlations, Equations 4.23 and 4.24 were compared using the experimental data for heat transfer coefficients reported in Baloyo (2016), which are listed in Table 4-8. In order to use Equation 4.23, the average pore size in the experimental pore size

range was used to calculate the pore size ratio (φ). The comparison in the middle range porosities (60% to 80%) is shown in Figure 4-44.

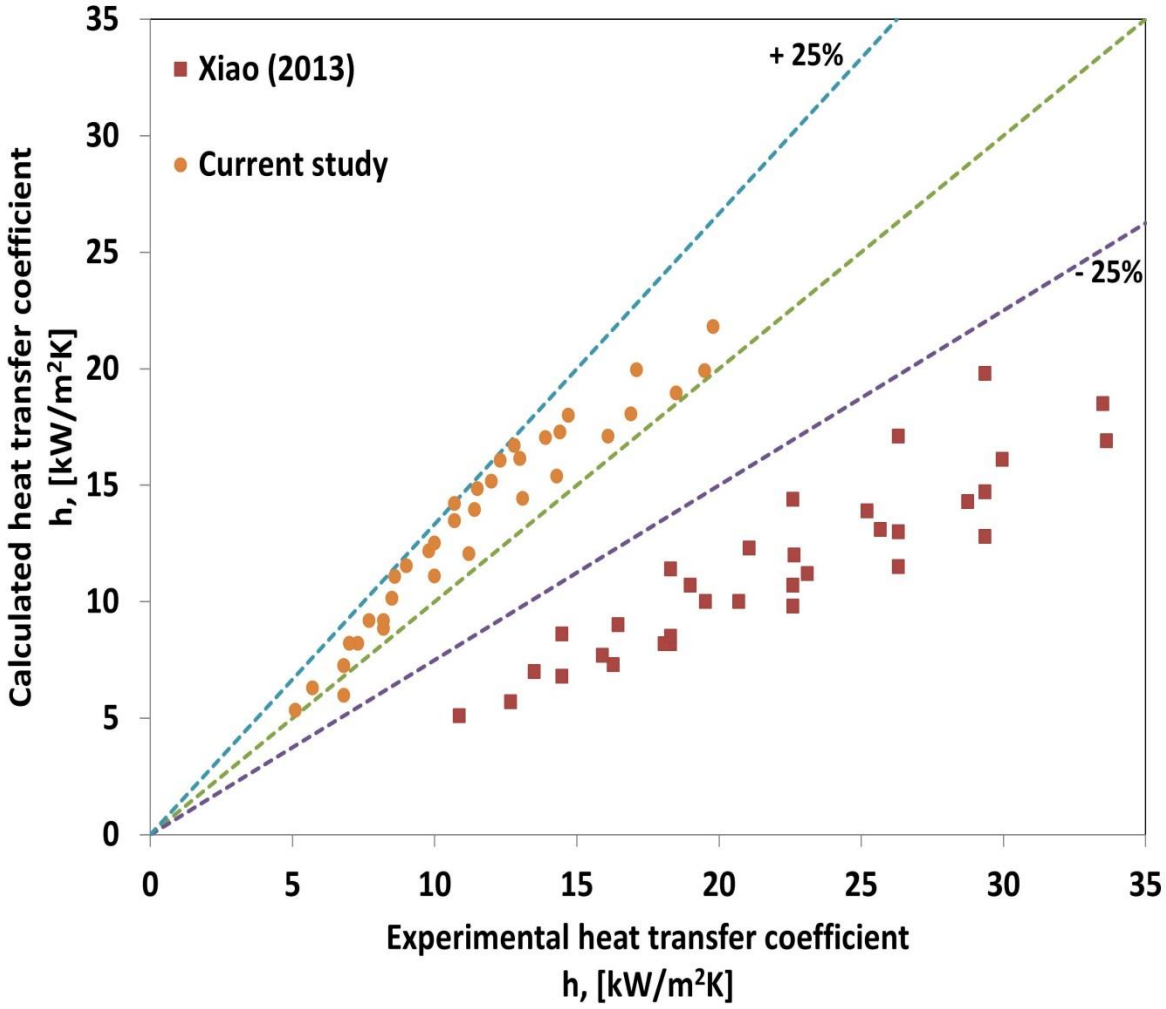

Figure 4-44 Comparison between empirical models and experimental results for heat transfer coefficient on LCS homogeneous porous copper samples

Table 4-8 Experimental heat transfer coefficient for LCS porous copper homogenous samples, (Baloyo 2016)

Pore size (μm)	Metal particle size (μm)	Darcian velocity, u (m/s)	Porosity, ε (%)	Heat transfer coefficient (kW/m^2K)
425 - 710	70	0.05	0.6	8.2
425 - 710	70	0.08	0.6	11.2
425 - 710	70	0.11	0.6	14.3
425 - 710	70	0.15	0.6	16.9
425 - 710	70	0.19	0.6	19.5
425 - 710	70	0.05	0.65	7.3
425 - 710	70	0.08	0.65	10
425 - 710	70	0.11	0.65	13.1
425 - 710	70	0.15	0.65	16.1
425 - 710	70	0.19	0.65	18.5
250 - 425	70	0.05	0.7	6.8
250 - 425	70	0.08	0.7	8.2
250 - 425	70	0.11	0.7	9.8
250 - 425	70	0.15	0.7	11.5
250 - 425	70	0.19	0.7	12.8
425 - 710	70	0.05	0.7	6.8
425 - 710	70	0.08	0.7	8.5
425 - 710	70	0.11	0.7	10.7
425 - 710	70	0.15	0.7	13
425 - 710	70	0.19	0.7	14.7
1000 - 1500	70	0.05	0.7	8.6
1000 - 1500	70	0.08	0.7	11.4
1000 - 1500	70	0.11	0.7	14.4
1000 - 1500	70	0.15	0.7	17.1
1000 - 1500	70	0.19	0.7	19.8
425 - 710	70	0.05	0.7	6.8
425 - 710	70	0.08	0.7	8.5
425 - 710	70	0.11	0.7	10.7
425 - 710	70	0.15	0.7	13
425 - 710	70	0.19	0.7	14.7
425 - 710	70	0.05	0.75	5.7
425 - 710	70	0.08	0.75	7.7
425 - 710	70	0.11	0.75	10
425 - 710	70	0.15	0.75	12
425 - 710	70	0.19	0.75	13.9
425 - 710	70	0.05	0.8	5.1
425 - 710	70	0.08	0.8	7
425 - 710	70	0.11	0.8	9
425 - 710	70	0.15	0.8	10.7
425 - 710	70	0.19	0.8	12.3

It can be seen that Equation 4.23 provides a better correlation than Equation 4.24 for the middle range porosities. The values predicted using Equation 4.23 are within $\pm$ 25% difference from the experimental results while Equation 4.24 predicted values about 50% off in most cases. However, Equation 4.23 diverges from the experimental data for porosities lower than 60%. This may be because the 3D REVs used in this study have 12 contact points. This is different from the LCS porous copper where the number of contact points for each pore is between 2 and 3 at lower porosities such as 40%. Nevertheless, Equation 4.23 can be used as a simple tool to estimate the heat transfer coefficient for the LCS porous copper.

4.7 Summary

This section described a novel procedure for modelling fluid flow through porous metals made by a space holder technique like LCS. The model is based on the construction of a simple unit cell that comprises of an arrangement of cylinders and spheres based on the FCC structure and accounts for the coordination number of the real material. Several REV were created by joining 5 unit cells together in order to perform the numerical analysis.

A number of 3D structures with different porosities of 50%, 60%, 65%, 70%, 75% and 80%, different pore sizes of 400 μm, 600 μm, 800 μm, 1000 μm and 1500μm, and different metal particle sizes of 30μm, 50μm and 70μm were studied. The numerical analysis comprised of two parts, the fluid flow and the heat transfer analysis. For both analyses, copper was used as the solid material and water as fluid. The flow rate was varied from 0.2 l/min to 1.8 l/min.

The pressure drop plots show quadratic correlation with Darcian velocity, following the Forchheimer's equation. The pressure drop increased with increasing flow rate and pore size, decreased with increasing porosity and metal particle size. Permeability and form drag coefficient were obtained from the plots. Permeability increased with increasing porosity or

pore size or metal particle size, and the form drag coefficient decreased when permeability increased. The numerical results of permeability exhibited the same trend as the experimental data, thus showing that the 3D REVs can reasonably represent the porous metal.

The form drag coefficient and permeability have a linear relationship in the logarithmic scale and can be described by a modified Ergun's model. The values for the exponential term and drag force coefficient for different pore sizes, obtained from linear regressions were not constant. The exponential term approached to 0.7 when pore size was increased. The drag force coefficient increased with pore size.

In the heat transfer analysis, the heat transfer coefficients of the REVs were calculated. It was observed that the heat transfer coefficient decreased linearly with increasing porosity, because higher porosity means less heat being transferred to the metal matrix by conduction. Increasing water flow rate increased the heat transfer performance in all cases. Increasing pore size increases the heat transfer coefficient, especially markedly when increasing pore size from 400μm to 600μm. Increasing pore size further led to smaller enhancements on the heat transfer coefficient. Metal particle size had a lesser effect on heat transfer coefficient.

Overall, water flow rate and porosity showed major influences on the heat transfer coefficient. An empirical relationship correlating the heat transfer coefficient with pore size, metal particle size, porosity, Darcian velocity was proposed with the multiple regression giving an adjusted correlation of $R^2 = 0.96$.

5 Conclusions and future work

5.1 Conclusions

5.1.1 Geometry creation

Three different geometric models were created to simulate a porous structure, including 2D patterned struts, 2D random struts, and 3D porous structures based on the FCC structure. The 2D structures were used to calculate pressure drop only, while the 3D structures were used to calculate the pressure drop and heat transfer coefficient.

In the 2D patterned structures, five different strut shapes were used. The strut size was fixed to be 500 μm for the diameter of the circular struts and for the equivalent diameter of triangular, squared, rotated square, and hexagonal struts. The patterned structures consisted of two different arrangements, aligned and staggered. Strut spacing was used to change porosity.

The 2D random structures were created using a program coded in VBA by positioning circular struts with a number of diameters randomly inside the computational domain.

The 3D structures were composed of spheres representing the pores and cylinders connecting the spheres, accounting for the real coordination number of the porous structure. Porosity was achieved by changing the distance between the spheres.

The structural features considered in the geometry creation were: porosities of 50%, 60%, 65%, 70%, 75% and 80%, pore sizes of 400 μm, 600 μm, 800 μm, 1000 μm and 1500 μm, and copper particles of 30 μm, 50 μm and 70 μm.

5.1.2 Fluid flow in 2D patterned structures

There is a quadratic relationship between pressure drop and Darcian velocity. The pressure drop increased with decreasing porosity. The staggered structures had higher pressure

drops than the aligned patterns, increased namely 20% to 40% at low flow rates and up to 95% at higher flow rates. Squared struts had the biggest difference, because of large changes in the strut gap and flow direction. Strut shape also affected pressure drop. The highest values of pressure drop were obtained for the rotated squares, followed by triangles, squares, hexagons and circles. This was attributed to the large projected area of the rotated squares, leading to smaller gaps for the fluid flow.

Permeability increased with increasing porosity due to the increase in strut spacing. Regarding strut shape, the circular struts displayed the highest permeability in the middle range porosity, (60% to 80%), followed by squares, hexagons, triangles and rotated squares for both aligned and staggered arrangements. For the lower porosities (40% and 50%) squared struts had a better performance, followed by hexagons and circles.

The form drag coefficient decreased with increasing porosity. Rotated squares and triangles displayed the highest form drag coefficients in the middle range porosities. For the low range porosities, circular struts had the largest form drag coefficient values followed by hexagons and squares. Staggered arrangements had form drag coefficients between 10% up to 25% higher than the aligned patterns, due to smaller gaps amongst the struts.

The relationship between permeability and form drag coefficient for all the strut shapes is linear in logarithmic scale regardless of the arrangement with the exponential term and force drag coefficient dependent on the strut shape. The smallest value obtained was of 0.65 for the aligned squares which approaches to the 0.5 Ergun's value.

The viscous drag and form drag contributions of the different strut shapes were studied. The relative contribution of form drag increases with increasing flow rate and decreasing porosity. The largest relative contributions of form drag were observed for the staggered squares and the rotated squares in both aligned and staggered patterns. The smallest relative contribution of form drag was obtained for the aligned square struts, mainly because the

aligned squares create directional channels, resulting in less turbulence and less frontal resistance for the flow.

5.1.3 Fluid flow in 2D random structures

The pressure drop showed a quadratic relationship with Darcian velocity, following the Forchheimer equation. The pressure drops for the random structures were about 30% more than for the patterned structures at the low flow rates and about twice at the higher flow rates. The difference can be attributed to the random distribution of struts creating very tortuose paths. The pressure drop values are very sensitive to the structure.

Permeability and form drag coefficient were also calculated for the random structures and the results were in a similar range as with the 2D patterned structures.

The time for the numerical analysis of the random structures, including geometry creation, mesh generation and post processing calculations, was three times longer than for the patterned structures. Therefore, the random structures are not ideal for pressure drop analysis on porous media.

5.1.4 Fluid flow in 3D structures

Pressure drop increased in a quadratic manner with flow rate, following the Forchheimer equation. Decreasing porosity and metal particle size and increasing pore size led to an increase in the pressure drop. The trends agreed well with the experimental data from Baloyo (2016).

Permeability increased with increasing porosity, pore size and metal particle size. The results exhibited similar trends as the experimental data in most cases. Form drag coefficient increased with decreasing porosity, increasing pore size and decreasing metal particle size. The relationship between permeability and form drag coefficient is linear in logarithmic scale. The exponential term and force drag coefficient depend on the pore size and metal particle

size. The exponential term decreases with increasing pore size and approaches 0.7 at larger pore sizes.

5.1.5 Heat transfer in 3D structures

Heat transfer coefficient increased with increasing flow rate in a parabolic fashion. The heat transfer coefficient decreased with increased porosity. The heat transfer coefficient was less affected by pore size and metal particle size. The numerical results agreed reasonably well with experimental results for the LCS porous copper reported in the literature.

An empirical relationship correlating the heat transfer coefficient with Darcian velocity, porosity, pore size and metal particle size was presented with a correlation of 0.96. The correlation worked well with the experimental data of Baloyo (2016).

5.2 Future work

This study focused on the numerical simulation of porous metals made by space holder techniques such as LCS. Only the properties of these materials were considered. Several recommendations for further analysis arising from the current study are outlined as follows:

- Different materials such as aluminium or titanium can be studied by using the unit cells presented in this study to investigate different porous metals.
- The 3D REVs are also suitable for different coolants. Air is often employed in the experimental analysis of LCS porous copper, as well with other porous metals. Therefore, it is important to consider air in future simulations.
- Tailored structures, such as bilayer structures, can also be analysed using the modelling technique presented in the current study. Two groups of different unit cells can be joined together to create the 3D REVs for hybrid structures.

- The range of the parameters studied can be extended. For instance, the effects of higher flow rates or larger metal particle sizes on permeability, form drag coefficient and heat transfer coefficient can be further studied.

References

Abbas, M. N. (2011) 'Modeling of Porosity Equation for Water Flow Through Packed Bed of Monosize Spherical Packing', *Journal of Engineering and Development*, 15(4), pp. 205–226.

Abbood, D. W. (2009) 'An Analytical Model Study for Flow Through Porous Media', in *Thirteenth International Water Technology Conference, IWTC 13*, pp. 873–882.

Adler, P. M., Jacquin, C. G. and Quiblier, J. A. (1990) 'Flow in Simulated Porous Media', *International Journal of Multiphase Flow*, 16(4), pp. 691–712. doi: 10.1016/0301-9322(90)90025-E.

ANSYS (2013) 'ANSYS'. SAS IP, Inc.

Ashby, M. F. *et al.* (2000) *Metal Foams a Design Guide*. 10th Ed. Woburn, MA: Butterworth-Heinemann.

B. Goyeau, Songbe, J.-P. and Gobin, D. (1996) 'Numerical Study of Double-Diffusive Natural Convection in a Porous Cavity Using the Darcy- Brinkman Formulation', *International Journal of Heat and Mass Transfer*, 39(7), pp. 1363–1378.

Bağci, Ö., Özdemir, M. and Dukhan, N. (2014) 'Flow Regimes in Packed Beds of Spheres From pre-Darcy to Turbulent', *Transport in Porous Media*, 104(3), pp. 501–520. doi: 10.1007/s11242-014-0345-0.

Bai, M. and Chung, J. N. (2011) 'Analytical and Numerical Prediction of Heat Transfer and Pressure Drop in Open-Cell Metal Foams', *International Journal of Thermal Sciences*. Elsevier Masson SAS, 50(6), pp. 869–880. doi: 10.1016/j.ijthermalsci.2011.01.007.

Baloyo, J. M. (2016) *Porous Metals with Novel Structures for Optimum Heat Exchange Performance, PhD Thesis*. University of Liverpool.

Baloyo, J. M. and Zhao, Y. (2015) 'Heat Transfer Performance of Micro-Porous Copper Foams with Homogeneous and Hybrid Structures Manufactured by Lost Carbonate Sintering', *MRS Proceedings*, 1779.

Banhart, J. (2000) 'Metallic Foams : Challenges and Opportunities 1 Introduction : Cellular Metals', *Physics*, pp. 13–20.

Banhart, J. (2001) 'Manufacture , Characterisation and Application of Cellular Metals and Metal Foams', *Progress in Materials Science*, 46, pp. 559–632.

Barrande, M., Bouchet, R. and Denoyel, R. (2007) 'Tortuosity of Porous Particles', *Analytical Chemistry*, 79(23), pp. 9115–9121. doi: 10.1021/ac071377r.

Behnam, M., Golezani, A. S. and Lima, M. M. (2011) 'The Effect of Size and Morphology of Iron Powder on Shell Density in Low Carbon Steel Hollow Spheres', *Powder Metallurgy Progress*, 11(3), pp. 185–192.

Beugre, D. *et al.* (2010) 'Lattice Boltzmann 3D Flow Simulations on a Metallic Foam', *Journal of Computational and Applied Mathematics*. Elsevier B.V., 234(7), pp. 2128–2134. doi: 10.1016/j.cam.2009.08.100.

Bhattacharya, A., Calmidi, V. V. and Mahajan, R. L. (2002) 'Thermophysical Properties of High Porosity Metal Foams', *international journal of heat and mass transfer*, 45(June 2001), pp. 1017–1031.

Bianchi, E. *et al.* (2015) 'Numerical Simulation of Heat Transfer in the Near-Wall Region of Tubular Reactors Packed with Metal Open-Cell Foams', *Chemical Engineering Journal*. Elsevier B.V., 264, pp. 268–279. doi: 10.1016/j.cej.2014.11.055.

Bodla, K. K., Weibel, J. A. and Garimella, S. V. (2013) 'Advances in Fluid and Thermal Transport Property Analysis and Design of Sintered Porous Wick Microstructures', *Journal of Heat Transfer*, 135(6), p. 61202. doi: 10.1115/1.4023569.

Boomsma, K. and Poulikakos, D. (2002) 'The Effects of Compression and Pore Size Variations on the Liquid Flow Characteristics in Metal Foams', *Journal of Fluids Engineering*, 124(1), p. 263. doi: 10.1115/1.1429637.

Boomsma, K., Poulikakos, D. and Ventikos, Y. (2003) 'Simulations of Flow Through Open Cell Metal Foams Using an Idealized Periodic Cell Structure', *International Journal of Heat and Fluid Flow*, 24(6), pp. 825–834. doi: 10.1016/j.ijheatfluidflow.2003.08.002.

Boomsma, K., Poulikakos, D. and Zwick, F. (2003) 'Metal Foams as Compact High Performance Heat Exchangers', *Mechanics of Materials*, 35(12), pp. 1161–1176. doi: 10.1016/j.mechmat.2003.02.001.

Boudreau, B. P. (1996) 'The Diffusive Tortuosity of Fine-Grained Unlithified Sediments', *Geochimica et Cosmochimica Acta*, 60(16), pp. 3139–3142. doi: 10.1016/0016-7037(96)00158-5.

Bourantas, G. C. *et al.* (2014) 'Heat Transfer and Natural Convection of Nanofluids in Porous Media', *European Journal of Mechanics - B/Fluids*. Elsevier Masson SAS, 43, pp. 45–56. doi: 10.1016/j.euromechflu.2013.06.013.

Bram, M. *et al.* (2000) 'High-Porosity Titanium, Stainless Steel, and Superalloy Parts', *Advanced Engineering Materials*, 2(4), pp. 196–199. doi: 10.1002/(sici)1527-2648(200004)2:4<196::aid-adem196>3.0.co;2-k.

Chai, Z. *et al.* (2010) 'Non-Darcy Flow in Disordered Porous Media: A Lattice Boltzmann Study', *Computers & Fluids*. Elsevier Ltd, 39(10), pp. 2069–2077. doi: 10.1016/j.compfluid.2010.07.012.

Chiba, H. *et al.* (2004) 'Heat Transfer Capacity of Lotus-Type Porous Copper Heat Sink', *JSME International Journal Series B*, 47(3), pp. 516–521. doi: 10.1299/jsmeb.47.516.

Clyne, T. W. *et al.* (2006) 'Porous Materials for Thermal Management Under Extreme Conditions.', *Philosophical transactions. Series A, Mathematical, physical, and engineering sciences*, 364(1838), pp. 125–46. doi: 10.1098/rsta.2005.1682.

Comiti, J. and Renaud, M. (1989) 'A New Model for Determining Mean Structure Parameters of Fixed Beds From Pressure Drop measurements: Application to Beds Packed with Parallelepipedal Particles', *Chemical Engineering Science*, 44(7), pp. 1539–1545. doi: 10.1016/0009-2509(89)80031-4.

Cooper, J. W., Wang, X. and Mohanty, K. K. (1999) 'Non-Darcy-Flow Studies in Anisotropic Porous Media', *SPE Journal*, (May), pp. 27–30.

Costa, S. C. *et al.* (2015) 'The Thermal Non-Equilibrium Porous Media Modelling for CFD Study of Woven Wire Matrix of a Stirling Regenerator', *Energy Conversion and Management*. Elsevier Ltd, 89, pp. 473–483. doi: 10.1016/j.enconman.2014.10.019.

Costanza-Robinson, M. S., Estabrook, B. D. and Fouhey, D. F. (2011) 'Representative elementary volume estimation for porosity, moisture saturation, and air-water interfacial areas in unsaturated porous media: Data quality implications', *Water Resources Research*,

47(7), pp. 1–12. doi: 10.1029/2010WR009655.

Crowe, C. T., Elger, D. F. and Roberson, J. A. (2005) *Engineering Fluid Mechanics*. 8th Editio. Danvers, MA: John Wiley & Sons, Inc.

Darcy, H. (1856) *Les Fontaines Publiques de la Ville de Dijon*. 1st Ed. Edited by V. Dalmont. Paris, France.

Della-Torre, A. *et al.* (2014) 'CFD Characterization of Flow Regimes Inside Open Cell Foam Substrates', *International Journal of Heat and Fluid Flow*. Elsevier Inc., 50, pp. 72–82. doi: 10.1016/j.ijheatfluidflow.2014.05.005.

Despois, J. and Mortensen, A. (2005) 'Permeability of Open-Pore Microcellular Materials', *Acta Materialia*, 53(5), pp. 1381–1388. doi: 10.1016/j.actamat.2004.11.031.

Diani, A. *et al.* (2014) 'Numerical Analysis of Air Flow through Metal Foams', *Energy Procedia*. Elsevier B.V., 45, pp. 645–652. doi: 10.1016/j.egypro.2014.01.069.

Diao, K. K., Xiao, Z. and Zhao, Y. (2015) 'Specific Surface Areas of Porous Cu Manufactured by Lost Carbonate Sintering: Measurements by Quantitative Stereology and Cyclic Voltammetry', *Materials Chemistry and Physics*. Elsevier B.V, 162, pp. 571–579. doi: 10.1016/j.matchemphys.2015.06.031.

Domingo, A. M. (1997) *Apuntes de Mecanica de Fluidos*. San Francisco, California.

Douglas, J. F., Gasiorek, J. M. and Swaffield, J. A. (2001) *Fluid Mechanics*. 4th Editio. Essex, England: Pearson Education Limited.

Duggirala, R. K. *et al.* (2008) 'Pressure Drop Predictions in Microfibrous Materials Using Computational Fluid Dynamics', *Journal of Fluids Engineering*, 130(7), p. 71302. doi: 10.1115/1.2948363.

Dukhan, N. (2006) 'Correlations for the pressure drop for flow through metal foam', *Experiments in Fluids*, 41(4), pp. 665–672. doi: 10.1007/s00348-006-0194-x.

Dukhan, N. and Al-Rammahi, M. A. (2012) 'Analysis and Experiment for Darcy Flow Convection in Cylindrical Metal Foam', in *Porous Media and Its Applications in Science, Engineering, and Industry*, pp. 191–196. doi: 10.1063/1.4711174.

Dukhan, N., Bağci, Ö. and Özdemir, M. (2014) 'Experimental Flow in Various Porous Media and Reconciliation of Forchheimer and Ergun Relations', *Experimental Thermal and Fluid Science*, 57, pp. 425–433. doi: 10.1016/j.expthermflusci.2014.06.011.

Dukhan, N. and Chen, K.-C. (2007) 'Heat Transfer Measurements in Metal Foam Subjected to Constant Heat Flux', *Experimental Thermal and Fluid Science*, 32(2), pp. 624–631. doi: 10.1016/j.expthermflusci.2007.08.004.

Dukhan, N. and Suleiman, A. S. (2013) 'Simulation of Entry-Region Flow in Open-Cell Metal Foam and Experimental Validation', *Transport in Porous Media*, 101(2), pp. 229–246. doi: 10.1007/s11242-013-0241-z.

Dullien, F. A. L. (1979) *Porous Media. Fluid Transport and Pore Structure*. 1st Ed. New York, NY: Academic Press, Inc.

Ejlali, A., Hooman, K. and Gurgenci, H. (2009) 'Application of High Porosity Metal Foams as Air-Cooled Heat Exchangers To High Heat Load Removal Systems', *International Communications in Heat and Mass Transfer*. Elsevier Ltd, 36(7), pp. 674–679. doi: 10.1016/j.icheatmasstransfer.2009.03.001.

Emanuel, G. (2000) *Analytical Fluid Dynamics*. 2nd Editio. Boca Raton, FL: CRC Press.

Escudier, M. (1998) *The Essence of Engineering Fluid Mechanics*. 1st Editio. Hertfordshire: Prentice Hall Europe.

Eugénio, S. *et al.* (2014) 'Electrodeposition and Characterization of Nickel-Copper Metallic Foams for Application as Electrodes for Supercapacitors', *Journal of Applied Electrochemistry*, 44(4), pp. 455–465. doi: 10.1007/s10800-013-0646-y.

Evans, A. G., Hutchinson, J. W. and Ashby, M. F. (1998) 'Cellular Metals', *Current Opinion in Solid State and Materials Science*, 3(3), pp. 288–303. doi: 10.1016/S1359-0286(98)80105-8.

Faiz, M. (2014) *Comparison of porous media permeability: experimental, analytical and numerical methods, PhD thesis*. Loughborough University.

Fox, R. W., Pritchard, P. J. and McDonald, A. T. (2010) *Introduction to Fluid Mechanics*. 7th Editio. Danvers, MA: John Wiley & Sons, Inc.

Geiger, S., Schmid, K. S. and Zaretskiy, Y. (2012) 'Mathematical Analysis and Numerical Simulation of Multi-Phase Multi-Component Flow in Heterogeneous Porous Media', *Current Opinion in Colloid & Interface Science*. Elsevier Ltd, 17(3), pp. 147–155. doi: 10.1016/j.cocis.2012.01.003.

Ghanbarian, B. *et al.* (2013) 'Tortuosity in Porous Media: A Critical Review', *Soil Science Society of America Journal*, 77(5), p. 1461. doi: 10.2136/sssaj2012.0435.

Gibson, L. J. and Ashby, M. F. (1999) *Cellular Solids*. 2nd Ed. Edited by D. R. Clarke, S. Suresh, and I. M. W. FRS. Cambridge, UK: Cambridge university press.

Haghshenas Fard, M. (2010) 'CFD Modeling of Heat Transfer of CO2 at Supercritical Pressures Flowing Vertically in Porous Tubes', *International Communications in Heat and Mass Transfer*. Elsevier Ltd, 37(1), pp. 98–102. doi: 10.1016/j.icheatmasstransfer.2009.08.004.

Hahn, D. W. and Özişik, M. N. (2012) *Heat Conduction*. 3rd Ed. Hoboken, NJ, USA: John Wiley & Sons, Inc. doi: 10.1002/9781118411285.

Hashim, J., Looney, L. and Hashmi, M. S. J. (1999) 'Metal Matrix Composites : Production by the Stir Casting Method', *Journal of Materials Processing Technology*, 93, pp. 1–7.

Hellström, J. G. I. and Lundström, T. S. (2006) 'Flow Through Porous Media at Moderate Reynolds Number', *International Scientific Colloquium*, (2), pp. 129–134. Available at: http://www.modlab.lv/publications/mmp2006/pdfs/129-134.pdf..

Hill, R. (1963) 'Elastic properties of reinforced solids: Some theoretical principles', *Journal of the Mechanics and Physics of Solids*. Pergamon, 11(5), pp. 357–372. doi: 10.1016/0022-5096(63)90036-X.

Hogg, S. C. *et al.* (2006) 'Microstructural Characterisation of Spray Formed Si-30Al for Thermal Management Applications', *Scripta Materialia*, 55, pp. 111–114. doi: 10.1016/j.scriptamat.2006.02.051.

Hwang, M.-L. and Yang, Y.-T. (2012) 'Numerical Simulation of Turbulent Fluid Flow and Heat Transfer Characteristics in Metallic Porous Block Subjected to a Confined Slot Jet', *International Journal of Thermal Sciences*, 55, pp. 31–39. doi: 10.1016/j.ijthermalsci.2011.11.008.

Iasiello, M. *et al.* (2014) 'Numerical Analysis of Heat Transfer and Pressure Drop in Metal

Foams for Different Morphological Models', *Journal of Heat Transfer*, 136(11), p. 112601. doi: 10.1115/1.4028113.

Incropera, F. P. *et al.* (2007) *Fundamentals of Heat and Mass Transfer*. 7th Ed., *US Patent 5,328,671*. 7th Ed. NJ, EUA: John Wiley & Sons, Inc. doi: 10.1073/pnas.0703993104.

Iversen, N. and Jørgensen, B. B. (1993) 'Diffusion Coefficients of Sulfate and Methane in Marine Sediments: Influence of Porosity', *Geochimica et Cosmochimica Acta*, 57(3), pp. 571–578. doi: 10.1016/0016-7037(93)90368-7.

Jaganathan, S., Vahedi Tafreshi, H. and Pourdeyhimi, B. (2008) 'A Realistic Approach for Modeling Permeability of Fibrous Media: 3-D Imaging Coupled with CFD Simulation', *Chemical Engineering Science*, 63(1), pp. 244–252. doi: 10.1016/j.ces.2007.09.020.

Jambhekar, V. A. (2011) *Forchheimer Porous-Media Flow Models - Numerical Investigation and Comparison with Experimental Data, Master's Thesis*. Universitat Stuttgart.

Janna, W. S. (2016) *Introduction to Fluid Mechanics*. 5th Ed. Edited by T. & F. Group. Boca Raton, FL.

Jiang, P.-X. and Lu, X.-C. (2006) 'Numerical Simulation of Fluid Flow and Convection Heat Rransfer in Sintered Porous Plate Channels', *International Journal of Heat and Mass Transfer*, 49(9–10), pp. 1685–1695. doi: 10.1016/j.ijheatmasstransfer.2005.10.026.

Kaczmar, J. W., Pietrzak, K. and Wlosinski, W. (2000) 'The Production and Application of Metal Matrix Composite Materials', *Journal of Materials Processing Technology*, 106, pp. 58–67.

Karimian, S. a. M. and Straatman, A. G. (2008) 'CFD Study of the Hydraulic and Thermal Behavior of Spherical-Void-Phase Porous Materials', *International Journal of Heat and Fluid Flow*, 29(1), pp. 292–305. doi: 10.1016/j.ijheatfluidflow.2007.07.003.

Khayargoli, P. *et al.* (2004) 'The Impact of Microstructure on the Permeability of Metal Foams', in *Canadian Society for Mechanical Engineering*, pp. 220–228.

Kopanidis, A. *et al.* (2010) '3D Numerical Simulation of Flow and Conjugate Heat Transfer Through a Pore Scale Model of High Porosity Open Cell Metal Foam', *International Journal of Heat and Mass Transfer*. Elsevier Ltd, 53(11–12), pp. 2539–2550. doi: 10.1016/j.ijheatmasstransfer.2009.12.067.

Koponen, A., Kataja, M. and Timonen, J. (1997) 'Permeability and Effective Porosity of Porous Media', *Physical Review E*, 56(3), pp. 3319–3325. doi: 10.1103/PhysRevE.56.3319.

Krishnan, S., Murthy, J. Y. and Garimella, S. V. (2006) 'Direct Simulation of Transport in Open-Cell Metal Foam', *Journal of Heat Transfer*, 128(8), p. 793. doi: 10.1115/1.2227038.

Kundu, P., Kumar, V. and Mishra, I. M. (2014) 'Numerical Modeling of Turbulent Flow Through Isotropic Porous Media', *International Journal of Heat and Mass Transfer*. Elsevier Ltd, 75, pp. 40–57. doi: 10.1016/j.ijheatmasstransfer.2014.03.020.

Lefebvre, L.-P., Banhart, J. and Dunand, D. C. (2008) 'Porous Metals and Metallic Foams: Current Status and Recent Developments', *Advanced Engineering Materials*, 10(9), pp. 775–787. doi: 10.1002/adem.200800241.

Leong, K. C. and Jin, L. W. (2006) 'Effect of Oscillatory Frequency on Heat Transfer in Metal Foam Heat Sinks of Various Pore Densities', *International Journal of Heat and Mass Transfer*, 49(3–4), pp. 671–681. doi: 10.1016/j.ijheatmasstransfer.2005.08.015.

Li, D. and Engler, T. W. (2001) 'Literature Review on Correlations of the Non-Darcy Coefficient', *SPE Permian Basin Oil and Gas Recovery Conference*, (2), pp. 1–8. doi: 10.2118/70015-MS.

Li, X., Wu, X. and He, S. (2014) 'Numerical Investigation of the Turbulent Cross Flow and Heat Transfer in a Wall Bounded Tube Bundle', *International Journal of Thermal Sciences*. Elsevier Masson SAS, 75, pp. 127–139. doi: 10.1016/j.ijthermalsci.2013.08.001.

Liou, M.-F. (2005) *A Numerical Study of Transport Phenomena in Porous Media, PhD thesis*. Case Western Reserve University.

Liu, P. S. and Liang, K. M. (2001) 'Functional Materials of Porous Metals made by P / M , Electroplating and some other Techniques', *Journal of materials science*, 36, pp. 5059–5072.

Lu, G. Q. and Zhao, X. S. (2004) *Nanoporous Materials Science and Enginnering*. 1st Ed. London: Imperial College Press.

Lu, M. (2011) *Mechanical and Acoustic Properties of Porous Steel Manufactured by Lost Carbonate Sintering, PhD Thesis*. University of Liverpool.

Lu, T. J., Stone, H. A. and Ashby, M. F. (1998) 'Heat Transfer in Open-Cell Metal Foams', *Acta Materialia*, 46(10), pp. 3619–3635. doi: 10.1016/S1359-6454(98)00031-7.

Machado, R. (2012) 'Numerical Simulations of Surface Reaction in Porous Media with Lattice Boltzmann', *Chemical Engineering Science*, 69(1), pp. 628–643. doi: 10.1016/j.ces.2011.11.037.

Mahjoob, S. and Vafai, K. (2008) 'A Synthesis of Fluid and Thermal Transport Models for Metal Foam Heat Exchangers', *International Journal of Heat and Mass Transfer*, 51(15–16), pp. 3701–3711. doi: 10.1016/j.ijheatmasstransfer.2007.12.012.

Malham, D. J. A. (2014) *Introductory Fluid Mechanics*. doi: 10.1017/CBO9781107415324.004.

Mancin, S. *et al.* (2010a) 'Heat Transfer During Air Flow in Aluminum Foams', *International Journal of Heat and Mass Transfer*. Elsevier Ltd, 53(21–22), pp. 4976–4984. doi: 10.1016/j.ijheatmasstransfer.2010.05.033.

Mancin, S. *et al.* (2010b) 'Pressure Drop During Air Flow in Aluminum Foams', *International Journal of Heat and Mass Transfer*. Elsevier Ltd, 53(15–16), pp. 3121–3130. doi: 10.1016/j.ijheatmasstransfer.2010.03.015.

Mancin, S. *et al.* (2012) 'Experimental Air Heat Transfer and Pressure Drop Through Copper Foams', *Experimental Thermal and Fluid Science*. Elsevier Inc., 36, pp. 224–232. doi: 10.1016/j.expthermflusci.2011.09.016.

Massey, B. (2006) *Mechanics of Fluids*. 8th Ed. Abingdon, Oxon: Chapman & Hall.

Masuoka, T. and Takatsu, Y. (1996) 'Turbulence Model for Flow Through Porous Media', *International Journal of Heat and Mass Transfer*, 39(13), pp. 2803–2809. doi: 10.1016/0017-9310(95)00353-3.

Matin, M. H. and Pop, I. (2013) 'Forced Convection Heat and Mass Transfer Flow of a Nanofluid Through a Porous Channel with a First Order Chemical Reaction on the Wall', *International Communications in Heat and Mass Transfer*. Elsevier B.V., 46, pp. 134–141. doi: 10.1016/j.icheatmasstransfer.2013.05.001.

Matyka, M., Khalili, A. and Koza, Z. (2008) 'Tortuosity-Porosity Relation in Porous Media Flow', *Physical Review E*, 78(2), p. 26306. doi: 10.1103/PhysRevE.78.026306.

Mauret, E. and Renaud, M. (1997) 'Transport Phenomena in Multi-Particle Systems - I. Limits of Applicability of Capillary Model in High Voidage Beds-Application to Fixed Beds of Fibers and Fluidized Beds of Spheres', *Chemical Engineering Science*, 52(11), pp. 1807–1817. doi: 10.1016/S0009-2509(96)00499-X.

McGlen, R. J., Jachuck, R. and Lin, S. (2004) 'Integrated Thermal Management Techniques for High Power Electronic Devices', *Applied Thermal Engineering*, 24(8–9), pp. 1143–1156. doi: 10.1016/j.applthermaleng.2003.12.029.

Moon, C. and Kim, K. C. (2015) 'Flow and Heat Transfer Characteristics in High Porosity Metal Foams', in *Proceedings of the World Congress on Mechanical, Chemical, and Material Engineering*, pp. 0–6.

Muramatsu, K. *et al.* (2013) 'Heat Transfer and Pressure Drop of Lotus-Type Porous Metals', *Journal of Heat Transfer*, 135(7), p. 72601. doi: 10.1115/1.4023564.

Naaktgeboren, C., Krueger, P. S. and Lage, J. L. (2012) 'Inlet and Outlet Pressure-Drop Effects on the Determination of Permeability and Form Coefficient of a Porous Medium', *Journal of Fluids Engineering*, 134(5), p. 51209. doi: 10.1115/1.4006614.

Nakajima, H. (2007) 'Fabrication, Properties and Application of Porous Metals with Directional Pores', *Progress in Materials Science*, 52(7), pp. 1091–1173. doi: 10.1016/j.pmatsci.2006.09.001.

Nakayama, A. *et al.* (2001) 'A Two-Energy Equation Model for Conduction and Convection in Porous Media', *International Journal of Heat and Mass Transfer*, 44(22), pp. 4375–4379. doi: 10.1016/S0017-9310(01)00069-2.

Ochiai, S. *et al.* (2010) 'Tensile Deformation and Failure Behavior of Open Cell Nickel and Copper Foams', *Materials Transactions*, 51(4), pp. 699–706. doi: 10.2320/matertrans.M2009383.

Ortiz Prado, A., Ortiz Valera, J. A. and Ruiz Cervantes, O. (2013) *Introduccion a la Mecanica del Medio Continuo*. 1st Editio. Mexico City: Universidad Nacional Autonoma de Mexico.

P. de Carvalho, T. *et al.* (2015) 'Experimental and Tomography-Based CFD Investigations of the Flow in Open Cell Metal Foams with Application to Aero Engine Separators', in *Proceedings of ASME Turbo Expo 2015: Turbine Technical Conference and Exposition GT2015*, pp. 1–11.

Papathanasiou, T. D., Markicevic, B. and Dendy, E. D. (2001) 'A Computational Evaluation of the Ergun and Forchheimer Equations for Fibrous Porous Media', *Physics of Fluids*, 13(10), pp. 2795–2804. doi: 10.1063/1.1401811.

Pathak, M. G., Mulcahey, T. I. and Ghiaasiaan, S. M. (2013) 'Conjugate Heat Transfer During Oscillatory Laminar Flow in Porous Media', *International Journal of Heat and Mass Transfer*. Elsevier Ltd, 66, pp. 23–30. doi: 10.1016/j.ijheatmasstransfer.2013.06.060.

Pedras, M. H. J. and de Lemos, M. J. S. (2001) 'On the Mathematical Description and Simulation of Turbulent Flow in a Porous Medium Formed by an Array of Elliptic Rods', *Journal of Fluids Engineering*, 123(4), p. 941. doi: 10.1115/1.1413244.

Phanikumar, M. S. and Mahajan, R. L. (2002) 'Non-Darcy Natural Convection in High Porosity Metal Foams', *International Journal of Heat and Mass Transfer*, 45(18), pp. 3781–3793. doi: 10.1016/S0017-9310(02)00089-3.

Pino Muñoz, D., Bruchon, J. and Drapier, S. (2012) 'Solid-State Sintering Simulation: Surface, Volume and Grain-Boundary Difussions', in *European Congress on Computational Methods in Applied Sciences and Engineering*.

Pisani, L. (2011) 'Simple Expression for the Tortuosity of Porous Media', *Transport in Porous Media*, 88(2), pp. 193–203. doi: 10.1007/s11242-011-9734-9.

Quintard, M. and Whitaker, S. (1994) 'Transport in ordered and disordered porous media II: Generalized volume averaging', *Transport in Porous Media*, 14(2), pp. 179–206. doi: 10.1007/BF00615200.

Robert A. Greenkorn (1983) *Flow Phenomena in Porous Media*. 10th Ed. New York, NY: Marcel Dekker, Inc.

Royal Eugene Collins (1961) *Flow of Fluids Through Porous Materials*. 1st Ed. Edited by V. Nostrand-Reinhold. Princeton, New Jersey.

Saito, M. B. and de Lemos, M. J. S. (2005) 'Interfacial Heat Transfer Coefficient for Non-Equilibrium Convective Transport in Porous Media', *International Communications in Heat and Mass Transfer*, 32(5), pp. 666–676. doi: 10.1016/j.icheatmasstransfer.2004.06.013.

Salak, A., Selecka, M. and Danninger, H. (2005) *Machinability of Powder Metallurgy Steels*. 1st Ed. Cambridge, UK: Cambridge Internationa Science Publishing.

Sayma, A. (2009) *Computational Fluid Dynamics*. 1st Ed. Ventus publishing Aps.

Scheidegger, A. E. (1957) *The Physics of Flow Through Porous Media*. 1st Ed. University of Toronto Press.

Schwartz, D. S. *et al.* (1998) *Porous and Cellular Materials for Structural Applications*. 1 st Ed. Warrendale, PA: Materials Research Society. Available at: http://scholar.google.com/scholar?hl=en&btnG=Search&q=intitle:Porous+and+Cellular+Materials+for+structural+applications#0.

Shapovalov, V. and Boyko, L. (2004) 'Gasar - A New Class of Porous Materials', *Advanced Engineering Materials*, 6(6), pp. 407–410. doi: 10.1002/adem.200405148.

Shaughnessy, E. J. J., Katz, I. M. and Schaffer, J. P. (2005) *Introduction to Fluid Mechanics*. 9th Ed. New York, NY: Oxford University Press.

Sozer, E. and Shyy, W. (2007) 'Modeling of Fluid Dynamics and Heat Transfer Through Porous Media for Liquid Rocket Propulsion', in *43rd Joint Propulsion Conference and Exhibit*. Cincinnati, OH: American Institute of Aeronautics and Astronautics, Inc, pp. 1–11. Available at: http://shyylab.engin.umich.edu/files/papers/AIAA-2007-5549-526.pdf.

Srivastava, V. C. and Sahoo, K. L. (2007) 'Processing, Stabilization and Applications of Metallic Foams. Art of Science.', *Materials Science-Poland*, 25(3), pp. 733–753.

Taheri, M. (2015) *Analytical and Numerical Modeling of Fluid Flow and Heat Transfer through Open-Cell Metal Foam Heat Exchangers, PhD Thesis*. University of Toronto.

Tannehill, J. C., Anderson, D. A. and Pletcher, R. H. (1997) *Computational Fluid Mechanics and Heat Transfer*. 2nd Editio. Philadelphia, PA: Taylor & Francis Group.

Tappan, B. C., Iii, S. A. S. and Luther, E. P. (2010) 'Nanoporous Metal Foams', *Angewandte Chemie International*, 49, pp. 4544–4565. doi: 10.1002/anie.200902994.

Teruel, F. E. and Díaz, L. (2013) 'Calculation of the Interfacial Heat Transfer Coefficient in

Porous Media Employing Numerical Simulations', *International Journal of Heat and Mass Transfer*, 60, pp. 406–412. doi: 10.1016/j.ijheatmasstransfer.2012.12.022.

Teruel, F. E. and Rizwan-uddin (2009) 'Characterization of a Porous Medium Employing Numerical Tools: Permeability and Pressure-Drop from Darcy to Turbulence', *International Journal of Heat and Mass Transfer*, 52(25–26), pp. 5878–5888. doi: 10.1016/j.ijheatmasstransfer.2009.07.017.

Thewsey, D. J. and Zhao, Y. (2008) 'Thermal Conductivity of Porous Copper Manufactured by the Lost Carbonate Sintering Process', *Physica Status Solidi (a)*, 205(5), pp. 1126–1131. doi: 10.1002/pssa.200723121.

Vafai, K. (2005) *Hanbook of Porous Media*. 2nd Ed. Boca Raton, FL: Taylor & Francis Group.

Vafai, K. and Tien, C. L. (1981) 'Boundary and Inertia Effects on Flow and Heat Transfer in Porous Media', *International Journal of Heat and Mass Transfer*, 24, pp. 195–203.

Wang, F. *et al.* (2008) 'Microstructure, Thermo-Physical and Mechanical Properties of Spray-Deposited Si-30Al Alloy for Electronic Packaging Application', *Materials Characterization*, 59(10), pp. 1455–1457. doi: 10.1016/j.matchar.2008.01.012.

Wang, L. *et al.* (2015) 'Volume-averaged macroscopic equation for fluid flow in moving porous media', *International Journal of Heat and Mass Transfer*. Elsevier Ltd, 82, pp. 357–368. doi: 10.1016/j.ijheatmasstransfer.2014.11.056.

Weissberg, H. L. (1963) 'Effective Diffusion Coefficient in Porous Media', *Journal of Applied Physics*, 34(9), pp. 2636–2639. doi: 10.1063/1.1729783.

Whitaker, S. (1986) 'Flow in Porous Media I: A Theoretical Derivation of Darcy's Law', *Transport in Porous Media*, 1(1), pp. 3–25. doi: 10.1007/BF01036523.

Whitaker, S. (1999) *The Method of Volume Averaging*. 4th Ed. Dordrecht / Boston / London: Springer Science+ Business Media. doi: 10.1017/S0022112000211312.

White, F. M. (2011) *Fluid Mechanics*. 7th Ed. New York, NY: Mc Graw Hill.

Xiao, Z. (2013) *Heat Transfer , Fluid Transport and Mechanical Properties of Porous Copper Manufactured by Lost Carbonate Sintering, PhD Thesis*.

Xiao, Z. and Zhao, Y. (2013) 'Heat Transfer Coefficient of Porous Copper with Homogeneous and Hybrid Structures in Active Cooling', *Journal of Materials Research*, 28(17), pp. 2545–2553. doi: 10.1557/jmr.2013.190.

Xin, C. *et al.* (2014) 'Numerical Investigation of Vapor–Liquid Heat and Mass Transfer in Porous Media', *Energy Conversion and Management*. Elsevier Ltd, 78, pp. 1–7. doi: 10.1016/j.enconman.2013.10.047.

Xu, R.-N. and Jiang, P.-X. (2008) 'Numerical Simulation of Fluid Flow in Microporous Media', *International Journal of Heat and Fluid Flow*, 29(5), pp. 1447–1455. doi: 10.1016/j.ijheatfluidflow.2008.05.005.

Yang, J. *et al.* (2013) 'Three-Dimensional Numerical Analysis of Turbulent Flow in Porous Media Formed by Periodic Arrays of Cubic, Spherical, or Ellipsoidal Particles', *Journal of Fluids Engineering*, 136(1), p. 11102. doi: 10.1115/1.4025365.

Yazdchi, K. and Luding, S. (2011) 'On the Validity of the Carman-Kozeny Equation in Random Fibrous Media', *II International Conference on Particle-based Methods -*

Fundamentals and Applications.

Zaragoza, G. and Goodall, R. (2013) 'Metal Foams with Graded Pore Size for Heat Transfer Applications', *Advanced Engineering Materials*, 15(3), pp. 123–128. doi: 10.1002/adem.201200166.

Zhang, L. *et al.* (2009) 'Heat Transfer Performance of Porous Copper Fabricated by the Lost Carbonate Sintering Process', in *Mater. Res. Soc. Symp. Proc*.

Zhang, L. and Zhao, Y. (2008) 'Fabrication of High Melting-Point Porous Metals by Lost Carbonate Sintering Process Via Decomposition Route', *Proceedings of the Institution of Mechanical Engineers, Part B: Journal of Engineering Manufacture*, 222(2), pp. 267–271. doi: 10.1243/09544054JEM832.

Zhao, C. Y. *et al.* (2004) 'The Temperature Dependence of Effective Thermal Conductivity of Open-Celled Steel Alloy Foams', *Materials Science & Engineering*, 367, pp. 123–131. doi: 10.1016/j.msea.2003.10.241.

Zhao, Y. (2003) 'Stochastic Modelling of Removability of NaCl in Sintering and Dissolution Process to Produce Al Foams', *Journal of Porous Materials*, 10(2), pp. 105–111. doi: 10.1023/A:1026079612440.

Zhao, Y. *et al.* (2005) 'Lost Carbonate Sintering Process for Manufacturing Metal Foams', *Scripta Materialia*, 52(4), pp. 295–298. doi: 10.1016/j.scriptamat.2004.10.012.

Zhao, Y. (2013) 'Porous Metallic Materials Produced by P/M Methods', *Journal of Powder Metallurgy & Mining*, 2(3), pp. 2–3. doi: 10.4172/2168-9806.1000e113.

Zhu, T. *et al.* (2014) 'A Study of the Time Constant in Unsteady Porous Media Flow Using Direct Numerical Simulation', *Transport in Porous Media*, 104(1), pp. 161–179. doi: 10.1007/s11242-014-0326-3.

Zill, D. G. and Wright, W. S. (2011) *Calculo de Varias Variables*. 4th Editio. Mexico City: Mc Graw Hill.

Appendix A: Subroutine coded to create random struts in 2D

The subroutine used to create the strut coordinate files used for the 2D random structure creation is presented as follows:

```
' The following subroutine clears the working sheet in order to not repeat values from the previous geometry generated but still using the same input values.
Sub clear()
Dim title(4)
Application.ScreenUpdating = False
Application.DisplayAlerts = False
Sheets(1).Select
s = Sheets.Count
''''''
```

```
    Sheets(s).Select
    ActiveWindow.SelectedSheets.Delete
    s = Sheets.Count
Loop
End Sub
''''''
```

```
    Sheets(s).Select
    ActiveWindow.SelectedSheets.Delete
    s = Sheets.Count
Loop
''''''
```

```
Dim Pore_L As Integer
Dim Pore_H As Integer

Pore_L = L / Aver
Pore_H = H / Aver
''''''
```

```
'These are the iterations for the 5 coordinate lines needed in order to create a strut. These
set of instructions are going to be repeated until the last slot of the reticule is filled with a
strut
    side = Sqr(Pi / Porosity) * Radius(randomValue)
    center = side / 2
    Pore_x(j) = Pore_x(j) + x(j)
    Pore_y = y + center
    If i = 1 Then
       Pore_x(j) = Pore_x(j) + st
    End If
    'In order to draw the pore, ANSYS requires 4 points, the following instructions do so:
    For Point = 1 To 5
       Select Case Point
          Case 1
             px = Pore_x(j)
             py = Pore_y - Radius(randomValue)
          Case 2
             px = Pore_x(j) + Radius(randomValue)
             py = Pore_y
          Case 3
             px = Pore_x(j)
             py = Pore_y + Radius(randomValue)
          Case 4
             px = Pore_x(j) - Radius(randomValue)
             py = Pore_y
          Case Else
             Application.Cells(Row, 1) = idi
             Application.Cells(Row, 2) = 0
```

```
                Row = Row + 1
                Exit For
            End Select
            px = Round(px, 0)
            Application.Cells(Row, 1) = idi
            Application.Cells(Row, 2) = Point
            Application.Cells(Row, 3) = px
            Application.Cells(Row, 4) = py
            Application.Cells(Row, 5) = 0
            Row = Row + 1
        Next Point
        idi = idi + 1
        y = side + y
        If j > Pore_H + 1 Then
            GoTo 500
        End If
        x(j) = side
500
''''''
```

```
        total_circles = total_circles + circle_area
600
''''''
```

```
' Macro1 Macro
    Application.DisplayAlerts = False
    Application.ScreenUpdating = False
    a1 = ThisWorkbook.Name
    Application.Dialogs(xlDialogSaveAs).Show
    a = ThisWorkbook.Name
    If a = a1 Then
        Exit Sub
    End If
    MyPath = ThisWorkbook.Path
    b = Sheets.Count
    For i = 1 To b
        Sheets(i).Select
        ActiveWorkbook.SaveAs Filename:= _
        "" and MyPath and "/" and a and "-" and i and ".txt", FileFormat:=xlText, _
        CreateBackup:=False
    Next i
    ActiveWorkbook.Saved = True
    Application.Quit
 End Sub
```

' The final porosity is calculated manually with the help of the software ANSYS. The final value will be only an approximation to the input value due to the strut overlapping process and the randomness of the structure.

Appendix B: Multiple regression output for the heat transfer coefficient analysis

Model summary	
R Square	0.9638
Standard Error	2.522
Observations	435

ANOVA

	Degrees of freedom
Regression	5
Residual	429
Total	434

Dependent variable:	Heat transfer coefficient
Predictors:	Porosity, Pore size, metal particle size, Darcian velocity
Quadratic predictor:	Darcian velocity

	Coefficients	*Standard Error*	*P-value*	*Collinearity / VIF*
Intercept	13.733	0.79	0	-
Pore size (μm)	0.0056	0.0002	0	0.98
Metal particle size (μm)	-0.026	0.005	0	0.99
u (m/s)	129.32	3.38	0	-
u^2 *(m/s)*	-225.45	10.21	0	-
Porosity (%)	-19.25	0.88	0	0.99

As the P-values for each term of the linear regression have values of zero, it is possible to say that the linear regression is statistically significant. From the previous table, it is possible to see that the predictor with major influence on changing the heat transfer coefficient is the flow rate. Also, it is shown that increasing pore size the heat transfer coefficient will increase as the coefficient is positive. Negative coefficients were obtained for porosity, metal particle size and the quadratic term of flow rate, meaning that increasing values for these predictors will decrease the heat transfer coefficient. In this case, pore size has the biggest negative contribution to enhancing the heat transfer performance with a coefficient of -19.2498.